

Hiroshima University Doctoral Thesis

Age-integrated tectonic model revealing
the deep- to shallow-crustal evolution of
Eastern Ghats Orogenic Belt, India

(インド東ガーツ造山帯の地殻深部から
浅部の進化過程を説明する年代統合
テクトニックモデル)

2017

Department of Earth and Planetary Systems Science,

Graduate School of Science,

Hiroshima University

Amitava Chatterjee

Table of Contents

1. Main Thesis

Age-integrated tectonic model revealing the deep- to shallow-crustal evolution of Eastern Ghats Orogenic Belt, India

(インド東ガーツ造山帯の地殻深部から浅部の進化過程を説明する年代統合テクトニックモデル)

Amitava Chatterjee (チャタジー アミタバ)

2. Thesis Supplements

(1) Zircon U-Pb SHRIMP and monazite EPMA U-Th-total Pb geochronology of granulites of the western boundary, Eastern Ghats Belt, India: new possibility for Neoproterozoic exhumation history. Amitava Chatterjee, Kaushik Das, Sankar Bose, Proloy Ganguly, Hiroshi Hidaka.

Geological Society London, Special Publication, 457 (2017), DOI: <https://doi.org/10.1144/SP457.1>

(2) Age-integrated tectonic modelling across the orogen-craton boundary: Age zonation and shallow- to deep crustal participation during Late Cambrian cratonization of Eastern Ghats Belts, India. Amitava Chatterjee, Kaushik Das, Sankar Bose, Hiroshi Hidaka *Lithos*, (2017) (in press) DOI: 10.1016/j.lithos.2017.07.020.

3. Reference papers

(1) Neoproterozoic transpression and granite magmatism in the Gavilgarh-Tan Shear Zone, central India: Tectonic significance of U-Pb zircon and U-Th-total Pb monazite ages.

Anupam Chattopadhyay, Amitava Chatterjee, Kaushik Das, Arindam Sarkar.

Journal of Asian Earth Science, 147 (2017), 485-501.

DOI:10.1016/j.jseaes.2017.08.018

(2) Mechanism of formation of water-escape structure due to seismogenic fluidization: an experimental revelation.

Prabir Dasgupta and Amitava Chatterjee.

Proceedings of the Indian National Science Academy, under review.

Main thesis

ABSTRACT

The Eastern Ghats Belt (EGB), India is a Proterozoic orogen which co-evolved with its Precambrian neighbors (East Antarctica, Australia, China and parts of Laurentia) during several supercontinental cycles before cratonized with the Archean Proto-India. Such orogen preserves the evidence of deep-crustal tectonothermal events in the orogen-interior. However, the exterior of the orogen (boundary) may preserve the record of both deep- to shallow-crustal events until the final amalgamation process. Hence, the boundary between the orogen and the adjacent craton is the best candidate to understand the comprehensive evolutionary history. To unravel such history of the EGB with respect to the Proto-India during and prior to its amalgamation, the detailed petrological (qualitative and quantitative analyses) and the geochronological investigations are carried out in the present study. The geochronological investigations include high-resolution U-Pb isotopic analyses of zircon (using SHRIMP) and texturally well-constrained U-Th-total Pb analyses of monazite (using EPMA) on the systematically sampled rocks collected in a transect across the western boundary of the EGB. The deep- to shallow-crustal rocks are exposed on the present day erosional surface of the study area. The inherited zircon grains of ~2915–2470 Ma age from the migmatitic quartzofeldspathic gneiss and the mafic granulite represent the protolith ages of the respective rocks. Age of the granulite metamorphism is estimated as ~950–900 Ma by zircon and monazite dating from the charnockitic augen gneisses and aluminous

granulites. A strong decompression-related reaction microtexture and REE chemical signatures in the associated monazite of the reacting garnet suggest that decompression by the exhumation occurred at ~800 Ma during the Rodinia breakup. The zircon grains of the charnockitic augen gneisses also yield the similar age. The results of this study further revealed that along a narrow zone near the thrust-bound margin between the EGB and the Proto-India, the entire crustal segment, from the deep-crustal granulites to the mid-crustal cratonic amphibolites to the shallow-crustal quartz breccia, all were involved actively in the thrust-related tectonics during amalgamation of the EGB at ~550–500 Ma. This youngest imprint of the ~550–500 Ma event erased all the earlier age histories recorded in the zircon and monazite grains of the granulites from the orogen-boundary. The older tectonothermal imprints are only preserved in the rocks farther ~30 km eastward from the thrust boundary, as the thrust-related tectonics had little or no effect in the orogenic interior. The geochronological and petrological evidence from the cratonic rock firmly testify that the amalgamation was achieved during the Gondwana assembly. In the present study, a comprehensive and geochronologically well-constrained tectonic model of the EGB, which encompasses its earliest deep-crustal to the latest shallow-crustal tectonic events up to the stage of final amalgamation is presented by combining all the geochronological data with qualitative and quantitative results of the petrological investigations. The new geochronological data coupled with field evidence and textural evidence from the shallow-crustal rock

finally suggest that the amalgamation related final thrusting was continued, at least, up to Late Cambrian, i.e., post-dating the Kuunga orogeny.

CONTENTS

ABSTRACT	i
CONTENTS	iv
LIST OF FIGURES	viii
LIST OF TABLES	xii
ACKNOWLEDGMENTS	xiii
Chapter 1: INTRODUCTION	1
Chapter 2: BACKGROUND GEOLOGY	11
2.1 Eastern Ghats Belt (EGB)	11
2.2 Bastar Craton (BC)	15
2.3 Nature of the western boundary of the EGB	16
Chapter 3: GENERAL GEOLOGY OF THE WESTERN BOUNDARY	20
3.1 Lithological distribution of the exposed rocks	20
3.1.1 Eastern part (in and around Bhawanipatna town)	20
3.1.2 Western parts	21
3.1.2.1 Area A: in and around Parla village	21
3.1.2.2 Area B: in and around Dharamgarh town	22
3.2 Structural features of the entire study area	23
3.3 Targeted samples for multipurpose investigations	25
Chapter 4: METHODOLOGY	36
4.1 Qualitative petrological analyses	36

4.1.1 Optical Microscopy (OM)	36
4.1.2 Scanning Electron Microscopy (SEM)	36
4.1.3 SEM-Electron Backscatter Diffraction (EBSD)	36
4.2 Quantitative petrological analyses	37
4.2.1 Electron Probe Microanalyzer (EPMA)	37
4.2.2 X-Ray Fluorescence (XRF)	38
4.2.3 X-Ray Diffraction (XRD)	38
4.3 Geochronological analyses	39
4.3.1 Sensitive High-resolution Ion Microprobe (SHRIMP IIe)	39
4.3.2 Electron Probe Microanalyzer (EPMA)	40
Chapter 5: PETROLOGICAL EVOLUTION	42
5.1 Petrography and microstructure	42
5.1.1 Deep-crustal rocks of the EGB	42
5.1.1.1 Charnockitic augen gneiss	42
5.1.1.2 Mafic granulite	44
5.1.1.3 Aluminous granulite	46
5.1.1.4 Meta-ironstone	48
5.1.2 Mid-crustal rocks of the BC	48
5.1.2.1 Migmatitic hornblende gneiss	48
5.1.2.2 Migmatitic quartzofeldspathic gneiss	50
5.1.3 Shallow-crustal marginal rocks	51
5.1.3.1 Foliated quartz breccia	51

5.2 Mineral chemistry	52
5.2.1 Garnet	52
5.2.2 Orthopyroxene	53
5.2.3 Clinopyroxene	54
5.2.4 Plagioclase	54
5.2.5 Spinel	55
5.2.6 Hornblende	55
5.3 Geothermobarometry	55
5.4 Thermodynamic modeling of metamorphic evolution	57
Chapter 6: GEOCHRONOLOGICAL DATA	77
6.1 Zircon U-Pb SHRIMP IIe data	77
6.1.1 Charnockitic augen gneiss	77
6.1.2 Mafic granulite	80
6.1.3 Aluminous granulite	81
6.1.4 Meta-ironstone	83
6.1.5 Migmatitic hornblende gneiss	84
6.1.6 Migmatitic quartzofeldspathic gneiss	85
6.1.7 Foliated quartz breccia	85
6.2 Monazite U-Th-total Pb EPMA data	88
6.2.1 Charnockitic augen gneiss	88
6.2.2 Aluminous granulite	89
6.2.3 Meta-ironstone	91
6.2.4 Foliated quartz breccia	91

6.2.5 Migmatitic quartzofeldspathic gneiss	92
Chapter 7: DISCUSSIONS AND CONCLUSIONS	138
7.1 Significance of the Mesoarchean to Mesoproterozoic ages	138
7.1.1 Mafic granulite	138
7.1.2 Migmatitic hornblende gneiss and migmatitic quartzofeldspathic gneiss	140
7.1.3 Foliated quartz breccia	141
7.2 Significance of the Neoproterozoic to Late Cambrian ages	141
7.2.1 ~1000–900 Ma ages	142
7.2.2 ~850–775 Ma ages	144
7.2.3 ~550–495 Ma ages	146
7.3 Age-zonation across the boundary of orogen	150
7.4 Age-integrated tectonic modeling	152
7.5 Supercontinent correlation	154
7.6 Conclusions	156
References	162

LIST OF FIGURES

Chapter 1

Figure 1: Generalized geological map of the EGB depicting subdivisions into different provinces (Fig. 1a) and isotopic domains (Fig. 1b) according to Dobmeier and Raith (2003) and Rickers et al. (2001), respectively.

Chapter 3

Figure 2: A broad geological map is showing lithological variations in an E-W transect across the EGB-BC boundary. The rectangular boxes mark the precise study areas (eastern part as Fig. 3, south-western part as Fig. 4a and north-western part as Fig. 4b).

Figure 3: A detailed geological map in and around Bhawanipatna town is showing lithological distribution along with the structural data.

Figure 4a: A detailed geological map in and around Parla showing the lithological distribution along with the structural data.

Figure 4b: A detailed geological map in and around Dharamgarh town showing lithological distribution along with the structural data.

Figure 5: Field exposure-scale photographs of the studied rocks.

Figure 6: Structural features of the rocks from the western boundary of the EGB.

Chapter 5

Figure 7: Microphotographs of the three samples of the charnockitic augen gneisses.

Figure 8: Microphotographs of the two samples of the mafic granulites.

Figure 9: Microphotographs of two varieties of the aluminous granulite and the meta-ironstone.

Figure 10: Microphotographs of the migmatitic hornblende gneiss, the migmatitic quartzofeldspathic gneiss and the foliated quartz breccia.

Figure 11: *P-T* pseudosection for the mafic granulite (sample BP12B) constructed in the chemical system $\text{Na}_2\text{O}-\text{CaO}-\text{FeO}-\text{MgO}-\text{Al}_2\text{O}_3-\text{SiO}_2-\text{H}_2\text{O}-\text{TiO}_2-\text{MnO}$.

Chapter 6

Figure 12: Internal structure of zircon grains and U-Pb SHRIMP data plots of the charnockitic augen gneiss (sample BP1).

Figure 13: Internal structure of zircon grains and U-Pb SHRIMP data plots of the charnockitic augen gneiss (sample BP3).

Figure 14: Internal structure of zircon grains and U-Pb SHRIMP data plots of the charnockitic augen gneiss (sample BP2)

Figure 15: Internal structure of zircon grains and U-Pb SHRIMP data plots of the mafic granulites (sample BP12B and BP4).

Figure 16: Internal structure and inclusion study of the zircon grains along with U-Pb SHRIMP analytical plots of the aluminous granulites (sample BP12A and sample BP12C).

Figure 17: Internal structure of zircon grains and U-Pb SHRIMP data plots of the meta-ironstone (sample DG33E).

Figure 18: Internal structure of zircon grains and U-Pb SHRIMP data plots of the migmatitic hornblende gneiss (sample DG33F).

Figure 19: Internal structure of zircon grains and U-Pb SHRIMP data plots of the migmatitic quartzofeldspathic gneiss (sample BP6).

Figure 20: Internal structure of zircon grains and U-Pb SHRIMP data plots of the foliated quartz breccia (sample DG17B).

Figure 21: Internal structure of monazite grains and U-Th-total Pb EPMA monazite data plots of the charnockitic augen gneiss (sample BP1).

Figure 22: X-ray elemental mapping and U-Th-total Pb EPMA dating of monazite grains from the aluminous granulite (sample BP12A).

Figure 23: X-ray elemental mapping and U-Th-total Pb EPMA dating of monazite grains from the aluminous granulite (sample BP12C)

Figure 24: Internal structure of monazite grains and U-Th-total Pb EPMA monazite data plots of the meta-ironstone (sample DG33E) and the foliated quartz breccia (sample DG17B).

Figure 25: Internal structure of monazite grains and U-Th-total Pb EPMA monazite data plots of the migmatitic quartzofeldspathic gneiss (sample BP6)

Chapter 7

Figure 26: Different metamorphic stages on P - T plane correlated with high-resolution and texturally well-constrained geochronological data.

Figure 27: The maximum deposition age of foliated quartz breccia calculated using the detrital monazite geochronological data.

Figure 28: The probability density diagrams showing the spatial variation of the zircon $^{207}\text{Pb}/^{206}\text{Pb}$ ages of different geological events in a transect across the western boundary of the EGB.

Figure 29: The tectonic evolutionary model of the EGB during and before its amalgamation with the Proto-India (marked here as the Bastar Craton).

LIST OF TABLES

Chapter 1

Table 1: Summary of ages recorded previously from the western boundary of the EGB.

Chapter 5

Table 2: Summary of textural and geochronological data of the studied samples.

Table 3: Representative mineral chemical data of the studied rocks.

Table 4: Whole rock XRF data of mafic granulite (sample BP12B).

Chapter 6

Table 5: Analytical results of SHRIMP U-Pb zircon geochronology.

Table 6: Analytical results of EPMA U-Th-total Pb monazite geochronology.

ACKNOWLEDGMENTS

From the core of my heart, I am thankful to my supervisor, Dr. Kaushik Das for his valuable advice and constant support throughout my Ph.D. research. His unique suggestions and consistent encouragement made my Ph.D. research very productive. I am indebted to Prof. Hiroshi Hidaka for giving an excellent opportunity to pursue my Ph.D. at the Hiroshima University. His academic assistance during the span of the Ph.D. was very crucial. I appreciate the thorough guidance from Prof. Sankar Bose during the Ph.D. research. I am grateful to him for his help during the fieldworks in India. I would like to express special thanks to Prof. Jun-ichi Ando for his critical comments to improve my Ph.D. work. I would like to acknowledge Prof. Madhusoodhan Satish-Kumar and Mr. Proloy Ganguly for their constructive comments for the betterment of the Ph.D. research. The help from Dr. Kosuke Kimura during and before SHRIMP analyses are unforgettable. I am thankful to Dr. Yasutaka Hayasaka and Dr. Yasuhiro Shibata for their assistance during EPMA analyses. I would like to thank all the staffs and colleagues of the Department of Earth and Planetary Systems Science, Hiroshima University. This research is funded by Monbukagakusho Honors Scholarship from Japan Student Services Organization (JASSO), 2015-2016, 2017-2018 and Ishihara Endowment Fund from Department of Earth and Planetary Systems Science, Hiroshima University, 2017. Finally, I am grateful for the immense patience and consistent help and encouragement from my parents, brother, and Miss Sayoni Banerjee during my Ph.D. research.

Chapter 1:

INTRODUCTION

Orogenic belts are one of the key crustal domains that record the signature of continental crustal dynamics and its recycling through the geological time. Such orogenic belts eventually culminate and cratonized with pre-existing cratonic crust through accretionary and collisional tectonics (Condie, 2005; Cawood et al., 2009). These orogenic belts, especially of Proterozoic time, are usually known to experience multiple phases of tectonothermal events prior to the final cratonization due to its prolonged trail of tectonic cyclicality during various supercontinent build-up and breakup episodes (Ennih and Liégeois, 2008; St-Onge et al., 2009; Brown, 2007). The margin of the orogenic belt, compared to the orogen's interior, are expected to better preserve the evidence of such multiple tectonothermal histories as the boundary of the orogen participated more actively during the cratonization. Hence, the deep- to shallow-crustal marginal rocks of the orogenic belt can elucidate the understanding of the tectonic evolution of an orogenic belt and the processes of its final amalgamation, (Gray et al., 1997).

Careful analysis of petrological and structural data linked with high-precision and texturally well-constrained geochronological data can help in determining the age-integrated tectonothermal evolution and growth history of ancient orogens prior to and during its amalgamation. Such history can also be used as a tool for transcontinental correlation involving dispersed continental

fragments (Zegers et al., 1998), which were once co-evolved in several Supercontinental cycles since Precambrian time. However, the exercise is difficult as the majority of the high-grade rocks lose primary mineralogical and textural features during multiple phases of metamorphism and deformation since Precambrian time. Generally, it is observed that the bulk rock chemistry, apart from *P-T*-fluid conditions, controls the development and preservation of mineralogical and textural records of different tectonothermal events that a high-grade terrain suffers. The same is applicable for the datable minerals like zircon and monazite from various bulk rock compositions (Kelsey et al., 2008), which often record the different isotopic/chemical signatures in response to different tectonothermal event(s) in a poly-deformed, poly-metamorphosed terrain (Das et al., 2011; Bose et al., 2016a). Thus, the ages of different tectonothermal events can be calculated from the datable minerals which were isotopically or chemically affected by the associated thermal events. Therefore, depending on the different bulk rock compositions for various lithologies, it is rare for a particular rock to record all the age imprints of different tectonothermal pulses. For that reason, it is particularly important to inspect all the possible rock types present at the boundary between the craton and the orogenic belt. Thus, the integration of structural and tectonothermal histories with high-precision geochronological data from deep- to shallow-crustal marginal rocks will not only elucidate the local geological history but also can play a pivotal role for transcontinental correlation.

Such orogen-craton juxtaposition can be found in the Precambrian continental blocks, for example, India. Peninsular India is composed of multiple Archean cratonic blocks which are bordered by several Proterozoic orogenic belts (Southern Granulite Terrain in the south and Eastern Ghats Belt in the east). Eastern Ghats Belt (EGB), being one of such Proterozoic orogenic belts, drew the attention of the geoscientists for the last two decades due to its regional-scale deep-crustal metamorphism and strategic position at least in the three supercontinent reconstructions. The tectonic activities of the EGB culminated through cratonization with the Archean Proto-India [Bastar Craton (BC) and Dharwar Craton in the west, Singhbhum Craton in the north; Fig. 1]. The south of the Godavari rift, i.e., the southern EGB cratonized with the Proto-India in Mesoproterozoic time during Columbia assembly (Vijaya Kumar et al., 2011; Bose et al., 2011; Dasgupta et al., 2017, 2013; Sarkar et al., 2014). However, the cratonization history of the northern EGB with the Proto-India is still debatable, i.e., during Rodinia assembly (~980–940 Ma of Chattopadhyay et al., 2015) or during Gondwana assembly (~550–500 Ma of Ghosh et al., 2016; Dobmeier et al., 2006; Das et al., 2008; Biswal et al., 2007; Bhadra et al., 2004). The amalgamation of the northern EGB with the Proto-India along its northwestern margin was achieved through “hot” over “cold” thrusting (Gupta et al., 2000; Bhadra et al., 2004; Gupta, 2012). The age of this thrusting is intuitively considered as ~550–500 Ma as it is the youngest age recorded, so far, from the boundary and the thrusting is the last tectonic event. (e.g., Gupta et al., 2000; Bhadra et al., 2004; Das et al., 2008; Upadhyay, 2008; Gupta,

2012). However, to delineate the exact age of amalgamation, the attempt could have been made to inspect the adjacent cratonic rocks for petrological and geochronological evidence which may record thermal imprints of thrusting of the “hot” EGB over the “cold” BC during amalgamation. It is noteworthy that the geochronological imprints of ~550–500 Ma are reported from the rocks adjacent to the shear zones (Dobmeier and Raith, 2003), which suggests a unique physico-chemical environment might have prevailed along a narrow area adjacent to these shear zones. However, the understanding of such physico-chemical environment is incomplete due to the lack of high-resolution and texturally well-constrained geochronological data particularly along a geo-transect along these shear zones.

Two older age peaks at ~1100–900 Ma and ~850–775 Ma, apart from the above-mentioned ~550–500 Ma age peak, were recorded from the rocks of the northern EGB. The UHT-HT granulite facies metamorphism in between ~1100–900 Ma is recorded from the rocks of the central part of the EGB (Shaw et al., 1997; Mezger and Cosca, 1999; Upadhyay et al., 2009; Das et al., 2011; Bose et al., 2011; Korhonen et al., 2013), which is succeeded by an imprint at ~850–775 Ma (Sarkar et al., 1989; Shaw et al., 1997; Simmat and Raith, 2008) with unknown tectonic history. However, this ~850–775 Ma tectonothermal event is reported sporadically from different areas within the northern EGB (Bose et al., 2016b). Several similar ages are also reported from the EGB’s Precambrian neighbor (during the Rodinia supercontinent), East Antarctica (Shiraishi et al., 2008; Tong et al., 1995; Black et al., 1987). The documentation

of widespread ~850–775 Ma event from the East Antarctica implies that the EGB also might have experienced the similar tectono-metamorphic pulses, but so far limited from the EGB due to lack of high-resolution geochronological data especially from the marginal rocks. A careful and tactical investigation can be helpful to record the similar age imprints and associated textural development from the marginal rocks of the EGB. Although the tectonic event of ~850–775 Ma is less understood, the recent reports from the Chilka domain suggest a possible decompression of the deep-crust (Bose et al., 2016b).

The evidence of such multiple tectonothermal events ranging in between ~1100–500 Ma are not found along a single transect as these events are spatially separated within the EGB. These areas belong to different domains having variegated metamorphic, structural, and age histories. These issues restrict to establish a petrogenetically, structurally and geochronologically well-integrated unified tectonic evolutionary model of the northern EGB within the above-mentioned time range. Thus, it is necessary to study an “appropriate” area which experienced all these tectonothermal pulses occurred in between ~1100–500 Ma in order to construct the comprehensive tectonic model. As discussed earlier, the most suitable candidates would be the deep- to shallow-crustal rocks of a transect across the postulated boundary between the orogenic belt and its adjacent craton, in which all the evidence of earliest deep-crustal metamorphism to final cratonization might have been preserved.

The deep-crustal granulites, mid-crustal cratonic rock and shallow-crustal sedimentary rock from a transect across the northwestern margin

between the EGB-BC are targeted in this study to understand the metamorphic, structural, and geochronological evolution during and prior to the amalgamation of the EGB with the Proto-India. The high-resolution and texturally well-constrained geochronological data from the systematically sampled rocks are very rare (Mezger and Cosca, 1999 among others, as summarized in Table 1), although the rocks across this transect is well-studied in terms of structural and metamorphic evolution (Bhadra et al., 2004; Biswal et al., 2007; Gupta et al., 2000; Bhattacharya, 2004). The multi-stage tectonic evolutionary model of the EGB (Bhadra et al., 2004; Bhadra and Gupta, 2016; Gupta, 2012; Gupta et al., 2000) cannot be termed age-integrated due to the lack of such geochronological data.

Hence, the present study focuses on the detailed qualitative and quantitative petrological investigations, extensive high-resolution isotopic and texturally well-constrained in-situ geochronological analyses (zircon U-Pb SHRIMP and monazite U-Th-total Pb EPMA) on the deep-crustal granulites, the mid-crustal amphibolites, and the shallow-crustal sedimentary rocks. Finally, an age-integrated crustal-scale tectonic model has been offered by collating all these findings with structural data, which will elucidate the pre- to syn-amalgamation history of the EGB and its status in the supercontinental evolution.

The background geological information corresponding to the EGB and the adjacent craton (BC) is provided in the Chapter 2. This includes the previously reported data of the petrological, structural, and available

geochronological results of these two terrains. Field-based general geology of the entire study area is discussed in the Chapter 3, which provides the mesoscopic description and the field relationship of the studied samples. The methodologies for the multipurpose investigations are outlined in the Chapter 4. The Chapter 5 is dedicated to understand the petrological evolution of the studied rocks, and the results of geochronological analyses of these rocks are presented in the Chapter 6. In the final chapter (Chapter 7), the interpretations of the age data are carried out by combining all the qualitative and quantitative mesostructural and microstructural evidence, which finally lead to establish an age-integrated tectonic model of the EGB with respect to the adjacent Archean Proto-India.

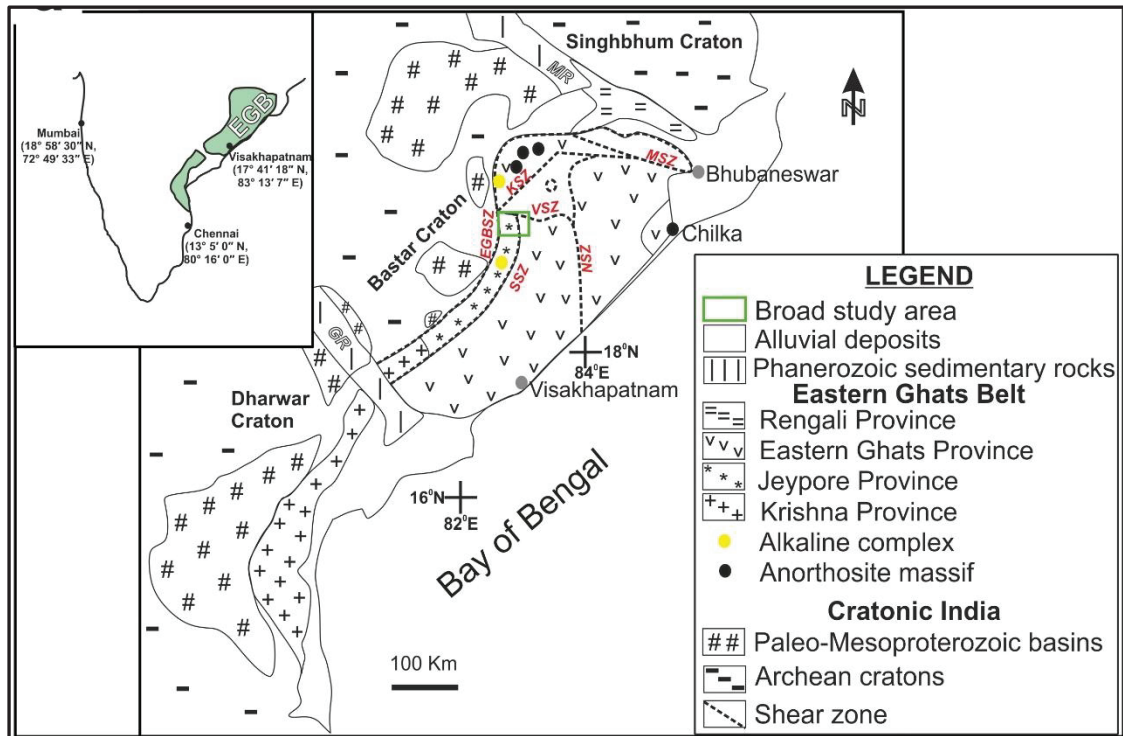


Figure 1a: Generalized geological map of the EGB. Subdivisions of the EGB into different provinces are according to Dobmeier and Raith (2003). Note that the alkaline complexes near the study area are only mentioned in this figure. A green rectangle marks the study area. The entire study area is represented in a broad geological map in figure 2. Inset map shows the position of the EGB with respect to India. Abbreviations used: MR - Mahanadi Rift, EGBSZ - Eastern Ghats Boundary Shear Zone, MSZ - Mahanadi Shear Zone, SSZ - Sileru Shear Zone, KSZ - Koraput-Sonpur Shear Zone, NSZ and VSZ - Nagavalli-Vamasadhara Shear Zone, GR - Godavari Rift.

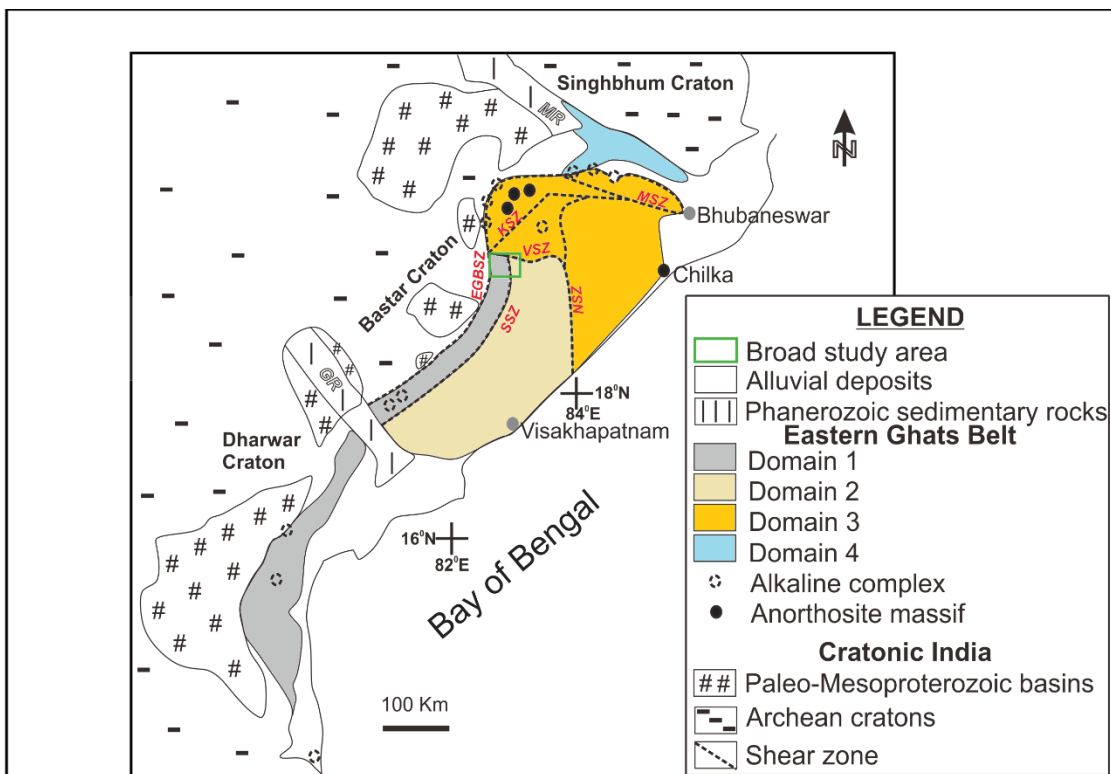


Figure 1b: Generalized geological map of the EGB. Subdivisions of the EGB into different domains are according to Rickers et al. (2001). A green rectangle marks the present study area. The abbreviations used in this figure are same as those in figure 1a.

Table 1: Summary of ages recorded previously from the western boundary of EGB

Tectonothermal event	Location	Age	Method	References
Granulite overprint	Deobhog	~530 Ma	Monazite U-Th-Pb	Simmat and Raith, 2008
Alkaline plutonism	Khariar	552-511 Ma	Zircon U-Pb SHRIMP	Biswal et al., 2007
Alkaline plutonism	Koraput	856 ± 18 Ma	Rb-Sr WR	Sarkar et al., 1989
Granulite metamorphism	Deobhog	~1065-900 Ma	Monazite U-Th-Pb	Simmat and Raith, 2008
Alkaline plutonism	Kunavaram	1384 ± 63 Ma	Zircon U-Pb SHRIMP	Upadhyay and Raith, 2006
Alkaline plutonism	Khariar	~1480 Ma	Zircon U-Pb SHRIMP	Upadhyay et al., 2006
Granite emplacement	Northern part of WCZ	2700-2500 Ma	Zircon U-Pb TIMS	Kovach et al., 2001
Charnockite emplacement	Northern part of WCZ	3400-2700 Ma	Zircon U-Pb TIMS	Kovach et al., 2001
Protolith ages	Domain 1B	3900-3200 Ma	Sm-Nd WR	Rickers et al., 2001

Chapter 2:

BACKGROUND GEOLOGY

2.1 Eastern Ghats Belt (EGB)

The Eastern Ghats Belt (EGB) is an arcuate-shaped ~1000 km long Proterozoic orogenic belt (Figs. 1a and 1b), which is characterized by regional-scale deep-crustal high-temperature/ultra-high temperature (HT-UHT) metamorphism (Lal et al., 1987; Sengupta et al., 1990, 1999; Dasgupta et al., 1995; Bose et al., 2000; Das et al., 2006; Korhonen et al., 2013). The first subdivision of the EGB into different longitudinal zones was based on the distribution of different lithologies (Nanda and Pati 1989; Ramakrishnan et al., 1998). However, such classification failed to explain the complex evolutionary histories of different shear-zone-bound blocks of the EGB.

Rickers et al. (2001) subdivided the EGB into four different domains based on Nd model ages, Rb-Sr isotopic data, and Pb-Pb isotopic data. According to their classification, the western boundary of the EGB belongs to domain 1 (Fig. 1b), which is further subdivided into domain 1A (south of the Godavari Rift) and 1B (north of the Godavari Rift). Nd isotope T_{DM} age of domain 1A for the orthogneisses and paragneisses are approximately 2700–2300 and 3200–2800 Ma, respectively (Rickers et al., 2001), while the metamorphism occurred at approximately 1760–1540 Ma (Mezger and Cosca 1999; Upadhyay et al., 2009; Bose et al., 2011; Sarkar et al., 2014). From domain 1B, the Nd isotope T_{DM} age of orthogneisses range between ~3900 and 3200 Ma, while the

high-grade metamorphism occurred at ~2800 Ma (Kovach et al., 2001). The domain 2 is bounded against domain 1 by the Sileru Shear Zone in the west and the Nagavalli-Vamasadhara Lineament in the east (Fig. 1b). Isotopic signatures revealed homogeneous Nd isotope T_{DM} ages of ~2100–2500 Ma for the metasediments. However, the orthogneisses have highly variable model ages of ~3200–1800 Ma. To the north of domain 2, domain 3 is bounded by the Nagavalli-Vamasadhara Lineament to the south and the Mahanadi Lineament to the north (Fig. 1b), and shows homogeneous Nd isotope T_{DM} ages of ~2200–1800 Ma for both the orthogneisses and the metasediments. Further to the north of the domain 3 up to the southern boundary of the Singhbhum Craton, the domain 4 is situated (Fig. 1b). The metasediments of the domain 4 display Nd isotope T_{DM} ages of ~2800–2200 Ma, whereas the orthogneisses show Nd isotope T_{DM} age of ~3200 Ma. The study area of this research situated at the north of domain 1B (Fig. 1b) according to this subdivision

The latest and most widely used subdivision of the EGB was proposed by Dobmeier and Raith (2003) into four provinces according to the different style and timing of metamorphism and structural evolution. The south of Godavari rift is termed as Krishna Province (Fig. 1a), which is composed of granulite and low- to medium-grade schist belt of common Paleoproterozoic evolution. A short-lived magmatism at ~1720–1700 Ma (Kovach et al., 2001) was followed by a granulite facies metamorphism between ~1620–1540 Ma (Sarkar and Schenk, 2016) in the Krishna Province. The northwestern boundary of the EGB, Jeypore Province (Fig. 1a), extends towards southwest from

Bhawanipatna town to the BC. The high-grade metamorphism occurred at ~2800 Ma (Kovach et al., 2001). Ductile deformation gave rise to well-defined gneissic layering during the peak metamorphic condition. Locally, later overprinting of medium-grade metamorphism recorded along narrow mylonitic shear zones., the central portion of the EGB, the Eastern Ghats Province (Fig. 1a), extend from the east of the Jeypore Province to the Bay of Bengal in the east. The Eastern Ghats Province (EGP) is composed of extremely deformed granulite facies rocks. Alkaline magmatism occurred in this province at ~1500 Ma (Sarkar and Paul, 1998; Aftalion et al., 2000), while granulite facies metamorphism occurred between ~1100–900 Ma (Das et al., 2011; Bose et al., 2011; Korhonen et al., 2013). Extensive evidence of felsic volcanism at ~2800 Ma is reported from the several fault-bounded Rengali Province (Misra et al., 2000; Fig. 1a) along the northern boundary of the EGB). The overall characteristic features of Rengali Province favor its exclusion from the EGB. The present study area is located at the north of Jeypore Province (Fig. 1a).

The predominant granulite facies metamorphism at the Jeypore Province occurred during ~1100–1000 Ma (Upadhyay and Raith, 2006) with an older report of charnockite emplacement at ~3400–2700 Ma (Kovach et al., 2001). This age of metamorphism is broadly equivalent to the age of granulite facies metamorphism (~1100-900 Ma) of Eastern Ghats Province (Shaw et al., 1997; Mezger and Cosca, 1999; Upadhyay et al., 2009; Bose et al., 2011; Das et al., 2011; Korhonen et al., 2013). The younger HT metamorphism at ~950–930 Ma is contemporaneous to the granulite facies metamorphism in parts of the

Rayner Complex, East Antarctica (Kelly et al., 2002; Harley et al., 2013; Morrissey et al., 2015), which implies that, at least, up to ~900 Ma, the EGB was co-evolving with East Antarctica (Bose et al., 2011). Following the UHT-HT events, a comparatively weak age-peak at ~850–800 Ma has been identified sporadically from different parts within the EGB. However, disagreements persist regarding the status of this thermal event. For example, Sarkar et al. (1989) reported the emplacement of alkaline pluton at 856 ± 18 Ma in Koraput, whereas Shaw et al. (1997) suggested the possible granite intrusion occurred at Rayagada during ~800 Ma. Simmat and Raith (2008) reported ~800 Ma monazite chemical ages from Anantagiri and Gokavaram areas. Recent report of ~800 Ma age from the granulites of Chilka domain suggest the possible decompression of the deep-crust (Bose et al., 2016b) before the final amalgamation of the EGB with the Proto-India. Nanda and Pati (1989) opined that during the amalgamation of the EGB with the Proto-India at ~550–500 Ma, the granulite facies rocks were retrogressed to granulite-amphibolite transitional facies along the western boundary. On the other hand, another school of thought invoked that the granulite facies metamorphism was prevailing during the amalgamation with the adjacent BC (Simmat and Raith, 2008; Bhadra et al., 2004; Bhattacharya, 2004; Das et al., 2008; Gupta and Bhattacharya, 2000; Gupta et al., 2000; Neogi and Das, 2000).

2.2 Bastar Craton (BC)

The adjacent Bastar Craton (BC) to the west of the EGB (Fig. 1a and 1b) is composed of tonalite-trondhjemite gneisses of $\sim 3500\text{--}2500$ Ma ages (Sarkar et al., 1993; Ghosh, 2004), granitoids of 2500–2200 Ma ages (Sarkar et al., 1981; Krishnamurthy et al., 1988; Pandey et al., 1989) and greenstone belts (Mondal et al., 2006). Several dolerite, rhyolite, and trachyte dykes have intruded within the craton during ~ 1400 Ma (Mallikarjuna Rao et al., 1995).

These mid-crustal rocks of the BC also acted as a basement of several Mesoproterozoic sedimentary basins (the Singhora Basin, the Khariar Basin, the Ampani Basin, the Sukma Basin, and the Indravati Basin) adjacent to the thrust boundary between the EGB and the BC. These basins are roughly aligned in a northeast-southwest trend. Recently, several geochronological data have been published that helped to unravel the sedimentation history of some the basins. Chronostratigraphic markers, such as rhyolitic ignimbrite, ash beds, bracketed the sedimentation in between $\sim 1600\text{--}1000$ Ma in the Chhattisgarh Basin (Patranabis-Deb et al., 2007, Das et al., 2009; Das et al., 2016; Chakraborty et al., 2015), Khariar Basin and Ampani Basin (Das et al., 2015) Traditionally, the Sukma Basin and Indravati Basin are considered as a part of the Chhattisgarh succession to the north, and the Cuddapah and Pakhal successions to the south (Kale and Phansalkar, 1991). The youngest zircon populations from the Ampani Basin show that the sedimentation was younger than 2079 ± 44 Ma (Saha et al., 2016). The emplacement age of the tuffaceous rock unit from the middle part of the Ampani stratigraphy has recently been dated as 1446 ± 21 Ma, which

suggests that the sedimentation in the Ampani Basin was restricted between ~2050 Ma and 1400 Ma (Saha et al., 2016). It is interesting to note that the basement granite gneiss (incidentally, the closest to the present study area) of sedimentary succession of the Ampani Basin yields an emplacement age of 2489 ± 9 Ma (Saha et al., 2016). The presence of mylonitized pebbles within a conglomerate of the Khariar Basin suggested that the sedimentation was syntectonic which continued up to ~517 Ma (Ratre et al., 2010). Recently, Bhadra and Gupta (2016) invoked that the Khariar Basin evolved through, at least, two phases during the amalgamation of the EGB. They further proposed that the Khariar Basin closed and developed as a foreland fold-thrust belt (accretionary wedge) during the final phase of the orogeny along the northwestern boundary of the EGB. The present study area lies south of the Khariar Basin and east of the Ampani Basin, where both deep-crustal granulitic, mid-crustal cratonic and shallow-crustal sedimentary rocks are exposed.

2.3 Nature of the western boundary of the EGB

Two outcrops of alkaline complexes are exposed near the study area along the western boundary the EGB. These are the Khariar alkaline complex and Koraput alkaline complex (Fig. 1a). However, geochronological data, especially for the Khariar alkaline rocks, are debatable. Aftalion et al. (2000) and Upadhyay and Raith (2006) suggested that the emplacement of alkaline rocks occurred at ~1500 Ma, which were metamorphosed during ~550 Ma. On the contrary, Biswal et al. (2007) invoked that these rocks emplaced in between

576–511 Ma. In the case of Koraput alkaline complex, Sarkar et al. (1989) calculated the emplacement age as 856 ± 18 Ma, whereas Nanda et al. (2008) proposed that these rocks suffered post-intrusion granulite facies metamorphism during ~870–700 Ma (U-Pb zircon age data). Generally, it is observed that the dominant planar fabric is a solid-state deformation structure (Gupta et al., 2005; Das et al., 2008; Nanda et al., 2008; Upadhyay, 2008), which was overprinted by a thrust-related fabric (Das et al., 2008; Upadhyay, 2008). Structural study along the northwestern boundary of the EGB suggests that the tectonic discontinuity between the EGB and the BC is a thrust contact (Neogi and Das, 2000; Dobmeier and Raith, 2003; Biswal et al., 2007), which is geophysically marked by a steep gravity gradient (Subrahmanyam and Verma, 1986). This tectonic discontinuity is characterized by the presence of wide mylonitic belt along this thrust contact (Gupta et al., 2000; Neogi and Das, 2000; Bhadra et al., 2003, 2004). From the microstructural observation, the sense of vergence of the thrust is determined as top-to-the-west (Gupta et al., 2000; Bhadra et al., 2004). On the current erosional surface, the contact zone is defined by the last appearance of granulites on the amphibolite facies cratonic rocks while the actual thrust planes could be buried under the EGB thrust sheets towards the eastern side of the postulated boundary. The BC rocks present within the EGB as “tectonic window” (Bhadra et al., 2004; Bhadra and Gupta, 2016), which may vindicate such possibility. The amalgamation of the EGB with the Proto-India achieved through this final phase of thrusting. The age of the final thrusting is intuitively considered as ~550–500 Ma (Bhadra et al., 2004; Biswal

et al., 2007; Das et al., 2008; Upadhyay, 2008) as thrusting was last deformation event and ~550–500 Ma age is the youngest date recorded from this region. However, zircon grains from the nepheline syenite of this area yielded ~550–500 Ma date (Biswal et al., 2007). This emplacement of the deformed nepheline syenite is claimed as syn-tectonic emplacement during the thrusting (Biswal et al., 2007). Thus, they concluded that the amalgamation of the EGB with the BC occurred during ~550–500 Ma based on such observation due to the thrusting of the “hot” EGB over the “cold” BC (Gupta et al., 2000; Bhadra et al., 2004; Gupta, 2012).

Several age pulses are recorded in between ~1500–500 Ma from the marginal rocks of the EGB. However, the interpretations of these age peaks with the associated tectonothermal events is controversial in the existing literature due to lack of texturally well-constrained and high-resolution geochronological data from the systematically sampled rocks, which restricts to offer a comprehensive and age-integrated unified tectonic model of the northern EGB. As discussed earlier, the most suitable study area for such systematic sampling would be the transect across the craton-orogenic belt boundary, which might preserve the earliest to latest tectonothermal histories of the orogenic belt. Thus, the marginal rocks of the western boundary of the EGB is targeted in the present study for detailed petrological investigations and isotopic and texturally well-constrained geochronological analyses. The combination of microscopic petrological investigations and sophisticated geochronological data with the mesoscopic field evidence finally will be helpful to advance an age-

integrated tectonic model of the EGB. In the following Chapter 3, the field-based general geology of the study area across the western boundary is described in detail, whereas the results of microscopic petrological investigations and geochronological analyses are described in Chapter 4 and 5, respectively.

Chapter 3:

GENERAL GEOLOGY OF THE WESTERN BOUNDARY

3.1 Lithological distribution of the exposed rocks

The study was carried out in a $\sim 60 \times 30$ km transect across the north-western boundary of the EGB, where seven lithologically different rocks are exposed on the surface (Fig. 2). These rocks are charnockitic augen gneiss, mafic granulite, aluminous granulite, meta-ironstone, migmatitic quartzofeldspathic gneiss, migmatitic hornblende gneiss and foliated quartz breccia. The entire field area was subdivided into three parts (Fig. 2) to understand the regional geology and the field relationship of the rocks in detail, i.e., the eastern part (in and around the Bhawanipatna town; Fig. 3), the area A or the south-western part (in and around the Parla village; Fig. 4a), and the area B or the north-western part (in and around the Dharamgarh town; Fig. 4b). The lithological distribution is described in detail for each area in the following sub-sections (3.1.1 and 3.1.2). The structural features of the entire study area are summarized in the sub-section 3.2, whereas detailed mesoscopic to microscopic description of the rocks are discussed in Chapter 5.

3.1.1 Eastern part (in and around Bhawanipatna town)

The area is located ~ 60 km eastward from the postulated western boundary of the EGB (EGBSZ of Gupta et al., 2000; Fig. 2). The geological map in and around the study area is presented in the figure 3. The dominant

rock types of this region are charnockitic augen gneiss and migmatitic quartzofeldspathic gneiss (Fig. 5a and 5b). However, the actual lithological contact between the charnockitic augen gneiss and the migmatitic quartzofeldspathic gneiss is not clear in the field. Thus, the exact contact cannot be determined in and around the mapped area. The migmatitic quartzofeldspathic gneiss is brown-colored which locally hosts isolated lenses of dark-colored mafic granulite (Fig. 5c). The charnockitic augen gneisses have a greasy appearance in the outcrop. The field observation revealed that the both coarse-grained and fine-grained zones occurred within a same body the charnockitic augen gneiss. A sharp boundary differentiates the narrow fine-grained portion from the coarse-grained portion, which possibly indicates that the rock preserves both high-strain zones (fine-grained) and low-strain zones (coarse-grained) (Fig. 5a) in the boundary shear zone.

3.1.2 Western parts

3.1.2.1 Area A: in and around Parla village

This area is located ~15 km eastward from the postulated western boundary of the EGB (EGBSZ of Gupta et al., 2000; Fig. 2). The geological map in and around the study area is presented in figure 4a. The area is dominantly composed of aluminous granulite, mafic granulite, meta-ironstone, migmatitic hornblende gneiss and migmatitic quartzofeldspathic gneiss. The mafic granulite occurs as a continuous band between the aluminous granulite and the migmatitic quartzofeldspathic gneiss (Fig. 4a). This variety of mafic

granulite is dark-colored and contains porphyroblastic garnet grains (Fig. 5d). The leucocratic layers around porphyroblastic garnet grains are mostly composed of plagioclase (Fig. 5d). Two types of aluminous granulite were observed in the field. The brownish white-colored aluminous granulite contains megascopic porphyroblasts of garnet grains (~5 cm in diameter; Fig. 5e), whereas the other variety is dark-brown in color and contains elongated garnet grains of varying sizes (Fig. 5f). The garnet grains of this rock are elongated in shape possibly in response to deformation (Fig. 5f). Locally, the aluminous granulite hosts small bodies of meta-ironstone (Fig. 4a). The meta-ironstone is dark-brown colored rock and contains porphyroblastic garnet (Fig. 5g). In places, pockets of aluminous granulite were found within the migmatitic quartzofeldspathic gneiss (Fig. 4a). The migmatitic hornblende gneiss of the BC occurs within the EGB as a “tectonic window” (Bhadra et al., 2004). The migmatitic hornblende gneiss has a greasy appearance in the outcrop-scale (Fig. 5h). The thrust-plane was inferred based on the field relationship between the migmatitic hornblende gneiss and the adjacent aluminous granulite (Fig. 4a).

3.1.2.2 Area B: in and around Dharamgarh town

The area is located very close to the postulated western boundary of the EGB (~5 km eastward of EGBSZ of Gupta et al., 2000; Fig. 2). The geological map in and around study area is presented in the figure 4b. Major part of the area is composed of the migmatitic quartzofeldspathic gneiss. The foliated quartz breccia occurs as a linear body adjacent to the thrust boundary between the EGB and the BC (Fig. 4b). The pale yellow-colored rock contains the same

regional foliation with an attitude of $0^{\circ}/45^{\circ}$ E (Fig. 5i). Discontinuous and narrow bands of the mafic granulite are hosted within the foliated quartz breccia and the migmatitic quartzofeldspathic gneiss (Fig. 4b). Isolated lenses of the porphyritic charnockite within the migmatitic quartzofeldspathic gneiss was documented from the south of this region (Fig. 4b).

3.2 Structural features of the entire study area

The entire study area is dominantly composed of deformed rocks, such as the migmatitic quartzofeldspathic gneiss, charnockitic augen gneiss, mafic granulite, and aluminous granulite. The early fabric of these high-grade rocks is a banding (S_1) which is defined by the segregated granulite facies minerals. This S_1 banding is attributed to the earliest stage of deformation (D_1). Previous workers carried out high-resolution and extensive structural investigations in this region (Das et al., 2008; Biswal et al., 2007; Bhadra et al., 2004; Gupta et al., 2000). The outcome of their studies pointed out that the S_1 is isoclinally folded during subsequent stage deformation, but with a development of a weak fabric. However, such structures were not observed in the present study. These rocks were intensely deformed by another phase of deformation (D_2), which produced a regional-scale penetrative foliation (S_2). In the present study, D_2 - S_2 corresponds to the D_{3M} - S_{3M} of Bhadra et al. (2004) and Gupta et al. (2000). The S_2 foliation is the dominant fabric of the entire area. Thus, the early structural features prior to S_2 - D_2 were largely obliterated and/or overprinted by S_2 - D_2 . Hence, S_1/S_2 transposed foliation is only identifiable in most of the places

(Figs. 6a and 6b). The S_2 foliation at the eastern part is NW-SE trending and steeply-dipping towards east ($300\text{--}330^\circ/60\text{--}70^\circ$ E). The S_2 foliation is striking almost N-S and moderately dipping towards east near the western boundary ($333^\circ/35^\circ$ E; average of data taken in two areas of western parts; Fig. 6d).

Adjacent to the western boundary of the EGB, two exposures preserve the folded S_1 with the formation of axial planar S_2 fabric. The folds are asymmetric and close to tight in nature which are verging consistently towards the west (Fig. 6c). These axial planar S_2 foliations are low- to moderate dipping (Fig. 6e). The mean orientation of the girdle ($328^\circ/31^\circ$ E; Fig. 6d) which contains the intersection lineation is identical to the mean attitude of the S_2 planes. The S_1 fabric was offset along the S_2 foliation plane (Fig. 6f).

The S_2 foliation being a shear fabric developed due to the D_2 shear deformation is established by studying several kinematic markers, such as the asymmetry of the sigmoidal augen (Fig. 6g) and asymmetrically folded S_1 . The occurrence of the deep-crustal granulites on the mid-crustal amphibolitic gneiss along the shear plane (Fig. 4a) indicates thrusting of the EGB on the BC. The change in regional-scale dip amount of the S_2 foliation from east to west (steeper in the eastern side and gentler near the western boundary) is, thus, due to the westward propagation of the thrust plane. The consistent westward asymmetry of the kinematic markers and westward disruption of the S_1 fabric along the S_2 fabric (Fig. 6f) suggest top-to-the-west sense of thrusting on the shear plane. The structural features described in this study are in accordance to the results obtained by the previous workers of this area (Bhadra et al., 2004;

Gupta et al., 2000; Das et al., 2008; Biswal et al., 2007). The schematic diagram (Fig. 6h) depicts the structural features of the western boundary of the EGB, where the degree of deformation in terms of asymmetry of the interfolial folds and augen, and flattening/elongation of grains decreases from the thrust boundary to the interior of the orogen. The asymmetric folds are more open towards the orogenic interior as the effect of thrust-related deformation was weak towards the interior of the orogen.

3.3 Targeted samples for multipurpose investigations

On the present day erosional surface, seven lithologically different rocks encompassing deep-crustal granulites to shallow-crustal sedimentary rocks were systematically sampled on a transect across the EGB-BC boundary. These deep-crustal granulites include the charnockitic augen gneiss, mafic granulite, aluminous granulite, and meta-ironstone. Several lines of petrological investigations, such as mineralogical evolution, textural relationships, *P-T* estimation, phase diagram modeling are coupled with high-precision and texturally well-constrained geochronological analyses (U-Pb zircon by SHRIMP IIe and U-Th-total Pb monazite by EPMA) to understand the granulite facies metamorphic evolution with time. For such petrological investigation, several thin-sections were prepared. Four thin-sections were used for in-situ monazite geochronology among these thin-sections. The mid-crustal rocks are the migmatitic quartzofeldspathic gneiss and the migmatitic hornblende gneiss. These rocks were targeted to find the petrological and geochronological

signatures during the amalgamation of the EGB with the adjacent BC. Various thin-sections were prepared for petrological investigations and in-situ monazite geochronological analyses. The foliated quartz breccia is present within the granulite package of the EGB occurs as the shallow-crustal component. This rock was studied in terms of petrography, structure, and geochronology to understand its evolution during the process of amalgamation of the EGB. One thin-section of this foliated quartz breccia was prepared for the textural study and in-situ monazite geochronology. Total four mounts were made for U-Pb zircon geochronology encompassing all the deep- to shallow-crustal rocks. One mount was used to identify the polymorph of aluminosilicates inclusions within zircon grains using SEM-EBSD. In the following Chapter 4, the detailed methodologies for multipurpose investigations are discussed.

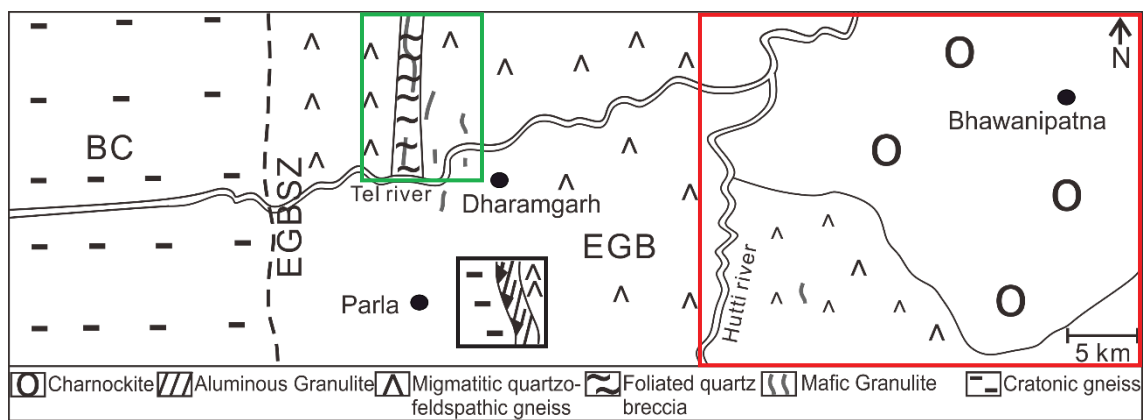


Figure 2: A broad geological map, which shows lithological variation in an E-W transect across the EGB-BC boundary. The postulated boundary between the EGB and the BC is summarized by Gupta et al. (2000) as EGBSZ. The rectangular boxes indicate the precise study areas (eastern area as red box, south-western area as black box and north-western area as green box).

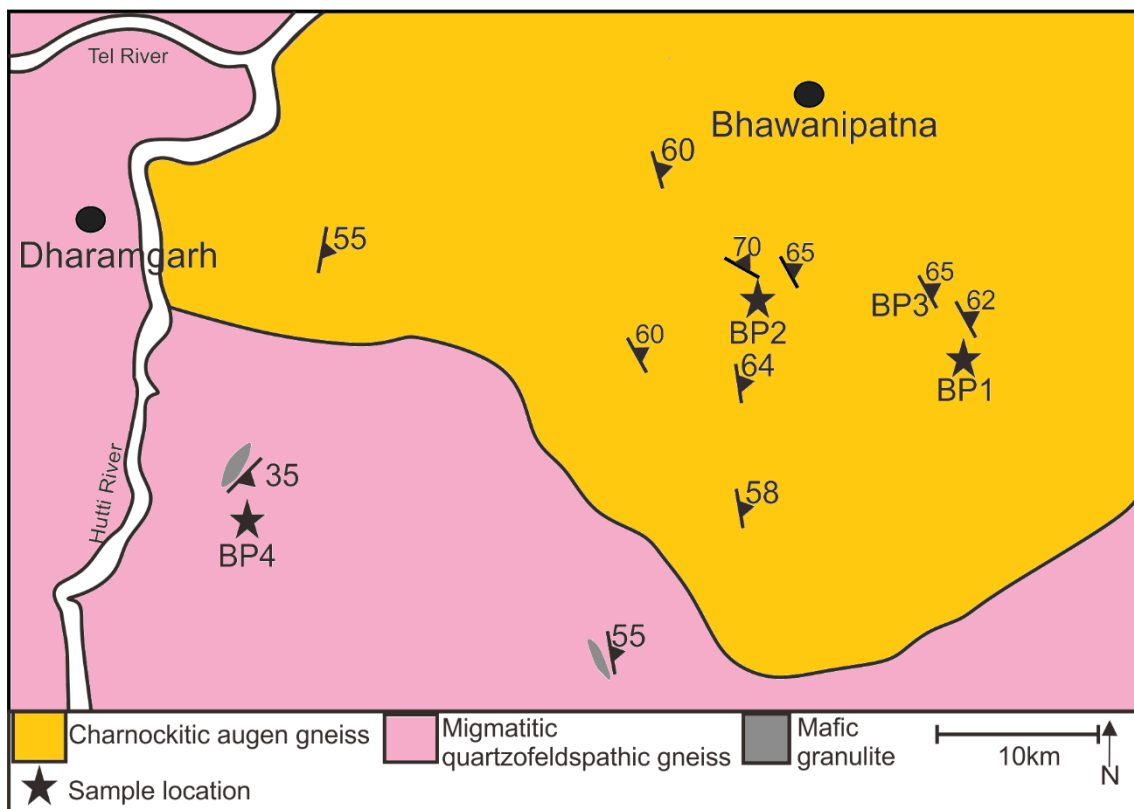


Figure 3: A detailed geological map in and around Bhawanipatna town, which shows the lithological distribution along with the structural data. Note that the structural data presented here as the attitude of the S₂ foliation.

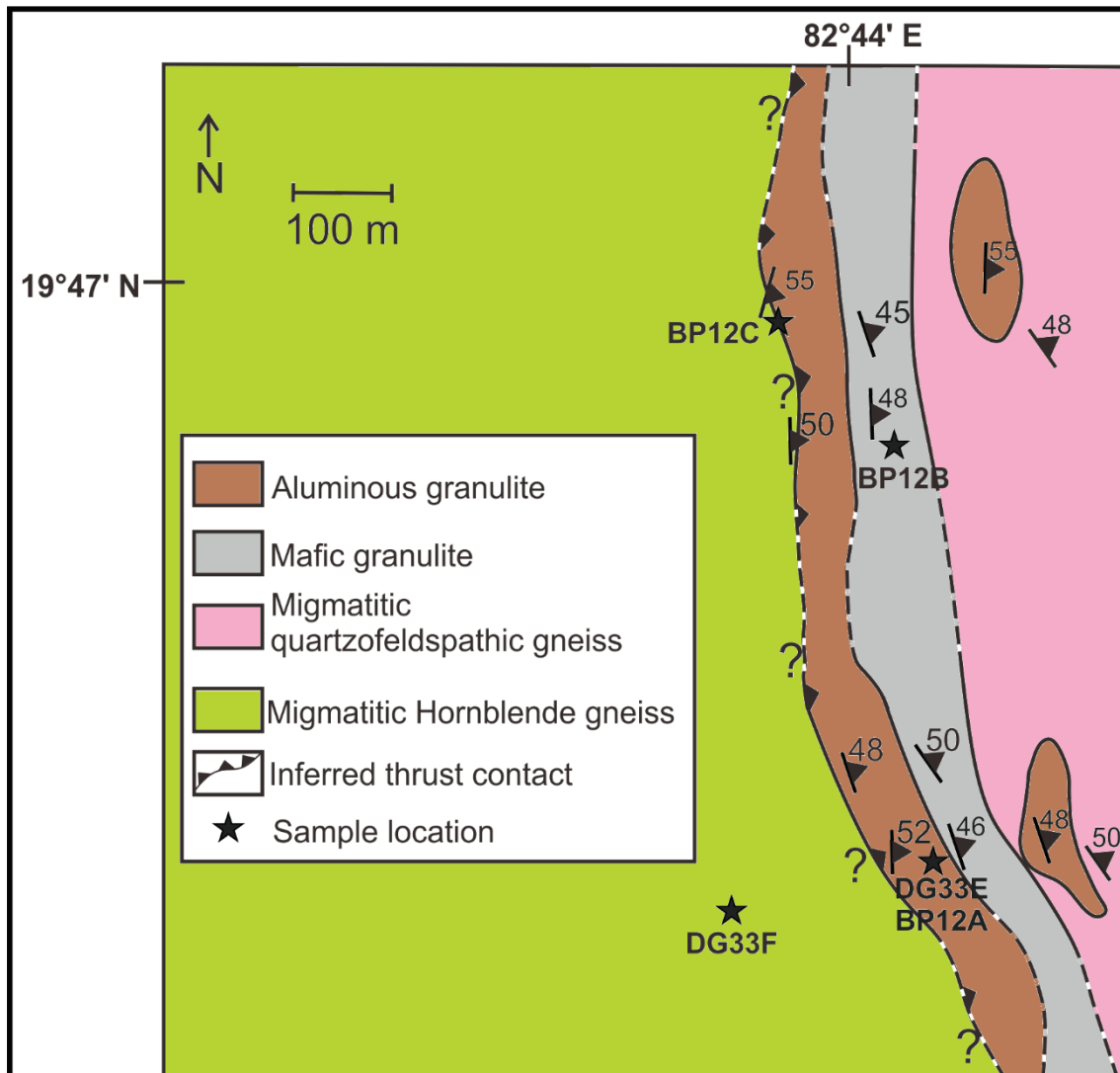


Figure 4a: A detailed geological map in and around the Parla village, which shows the lithological distribution along with the structural data. Note that the dotted line represents the speculated lithological boundary. The structural data plotted in the figure as the attitude of the gneissic (S₂) foliation.

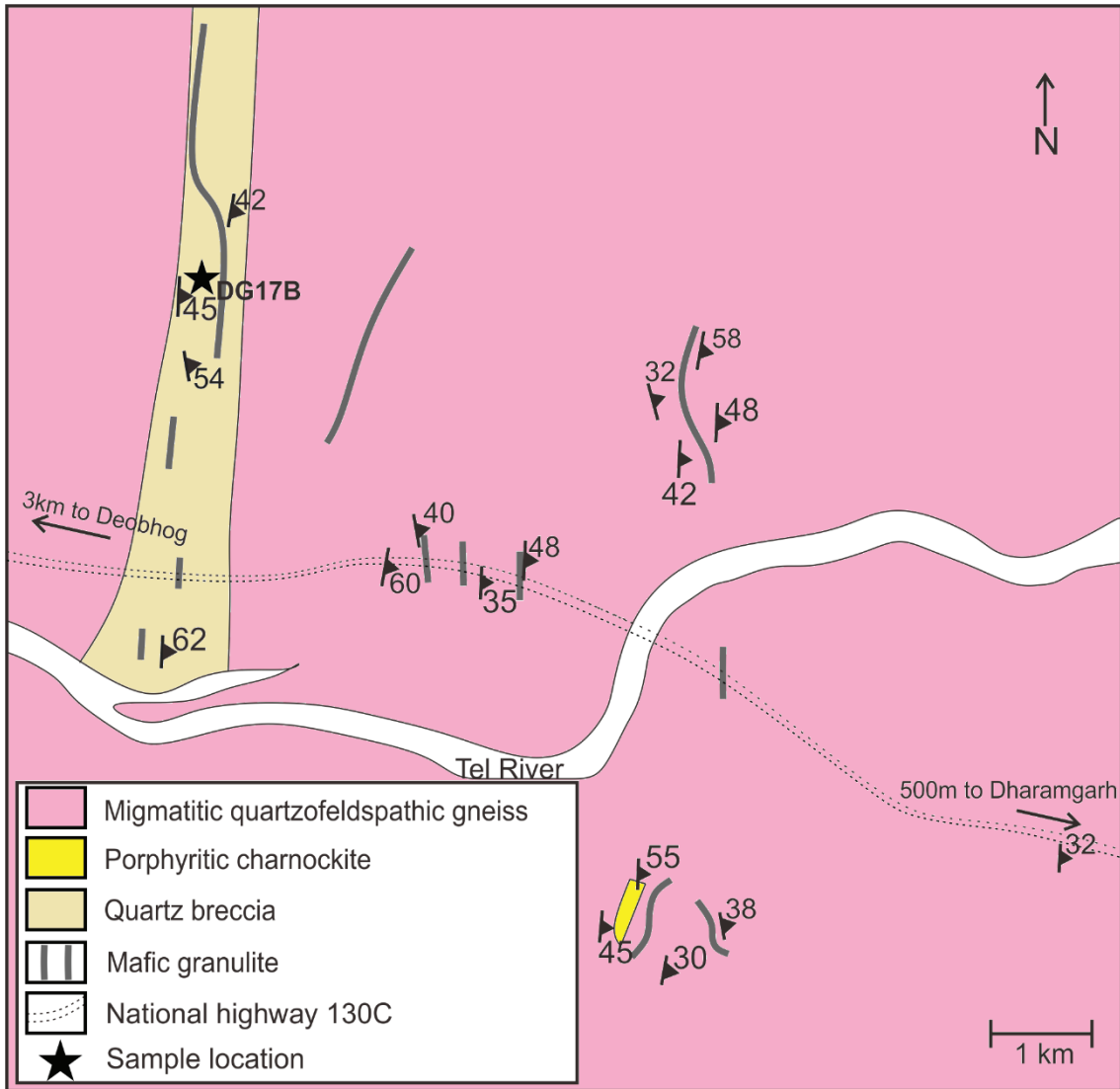


Figure 4b: A detailed geological map in and around the Dharamgarh town, which shows the lithological distribution along with the structural data. Note that the structural data presented here as the attitude of the gneissic (S_2) foliation.

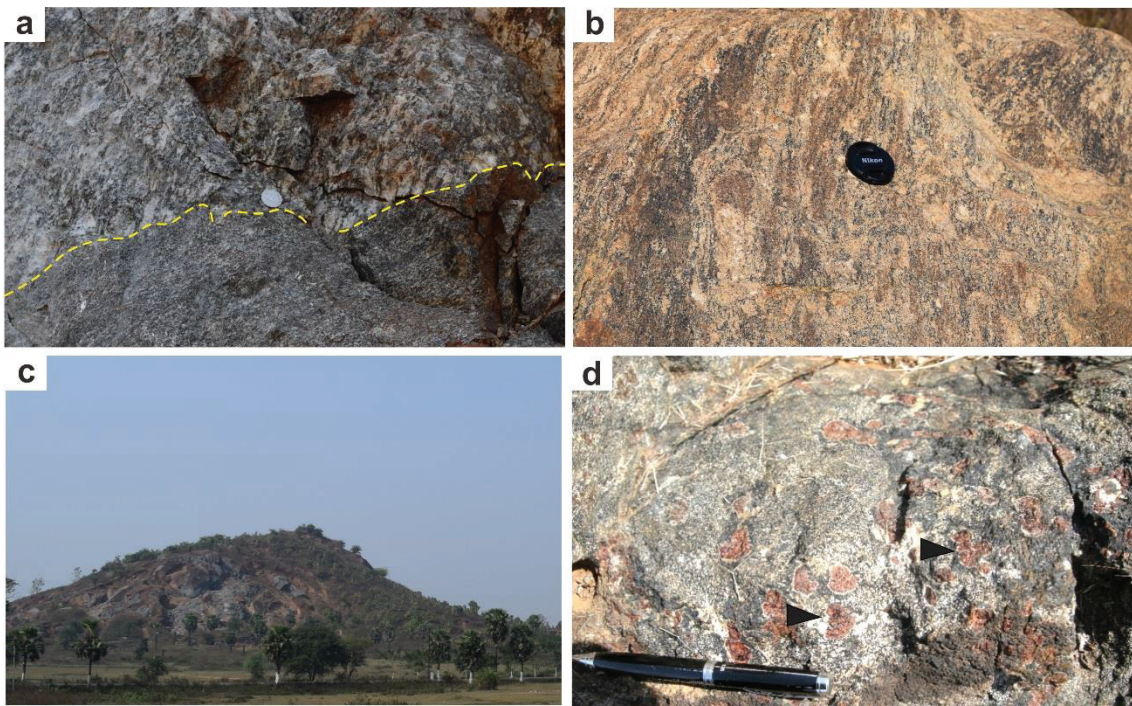


Figure 5 continued in next page

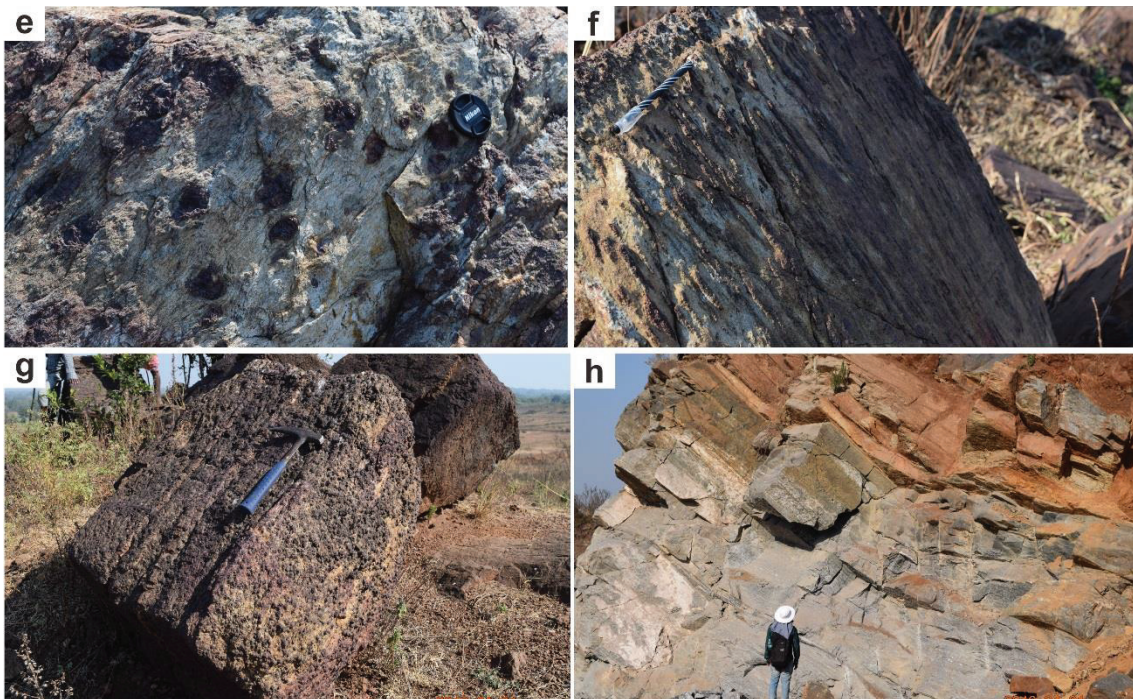


Figure 5 continued in the next page



Figure 5: (a) Field photograph the charnockitic augen gneiss. The dotted line differentiates the low-strain zone from the high-strain zone. (b) Field photograph of the migmatitic quartzofeldspathic gneiss. (c) Field photograph of hillock of the mafic granulite occurs as an isolated outcrop in the field. (d) Field photograph of the mafic granulite at the Parla village showing garnet (solid triangles) porphyroblasts. Note that the length of the pen is c.a. 12 cm. (e) Field photograph of the pegmatoidal aluminous granulite. (f) Field photograph of the deformed variety of aluminous granulite. (g) Field photograph of the meta-ironstone. (h) Field photograph of the migmatitic hornblende gneiss. (i) Field photograph of the foliated quartz breccia.

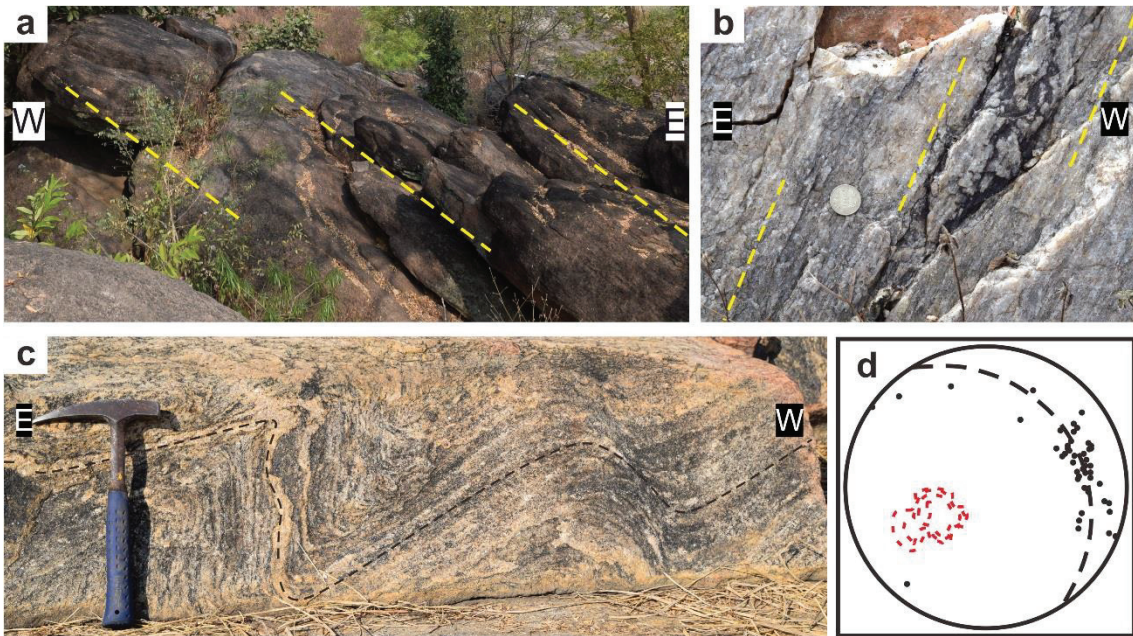


Figure 6 continued in the next page

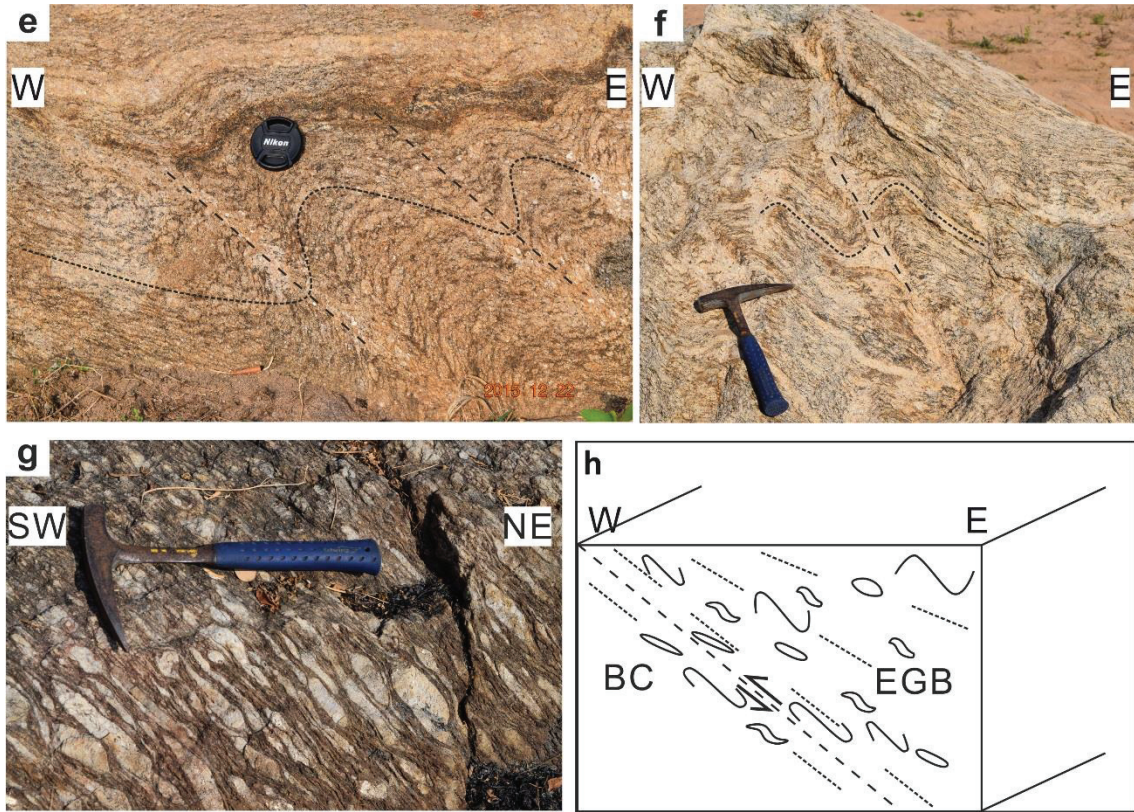


Figure 6: Structural features of the western boundary of the EGB. (a-b) The traces of the regional (S_2) foliation in the migmatitic quartzofeldspathic gneiss and foliated quartz breccia are marked by the dotted line. (c) West-vergent tight asymmetric folds are preserved in the migmatitic quartzofeldspathic gneiss. (d) The stereonet contains the poles of S_2 foliations (red contours) measured in the field, and the intersection lineations (black circles) forming the S_2 plane (dashed line). (e) The asymmetrically folded S_1 fabric cross-cuts the S_2 foliation plane (axial plane $\parallel S_2$ foliation plane). (f) The S_1 fabric is offset along the S_2 foliation plane. Note that the disruption is verging towards the west. (g) Asymmetric sigmoidal augen observed in the charnockitic augen gneiss. (h) Schematic block diagram depicts the structural features of the western boundary of the EGB. The degree of deformation was weak away from the EGB-BC boundary. The dotted lines mark the trace of the regional foliation.

Chapter 4:

METHODOLOGY

4.1 Qualitative petrological analyses

4.1.1 Optical Microscopy (OM)

Several thin-sections of all the rocks were studied under the optical microscope (OM) at the Hiroshima University, Japan to understand the mineralogical assemblages and textural relationship between the different mineral phases.

4.1.2 Scanning Electron Microscopy (SEM)

The Backscatter Electron Images (BSI) of the thin-sections were taken using a JEOL JSM-6390A Scanning Electron Microscope (SEM) equipped with a JED-2300 Energy Dispersive System (EDS) at the Hiroshima University, Japan to understand the textural evolution under high-magnification and identify the tiny and included mineral phases. The BSI and CL techniques under SEM were adopted to observe the zoning pattern, surface condition, fracture distribution and included mineral phases of monazite and zircon grains. The operating voltage was fixed at 15 kV during the qualitative analysis.

4.1.3 SEM-Electron Backscatter Diffraction (EBSD)

The polymorphs of aluminosilicates were identified by the characteristic Kikuchi patterns obtained using SEM-EBSD detector (Nordlys system) equipped with JEOL JSM6390A at Hiroshima University. The samples were polished chemically using colloidal silica for four hours to remove the damaged

layers on the surface. The samples were set on a 70° pre-tilt holder with respect to the incident electron beam to obtain the Kikuchi patterns. CHANNEL 5.0 software of Oxford Instruments HKL was used to index the generated Kikuchi patterns. Data with <math><1^\circ</math> mean angle deviation between the Kikuchi bands were only taken under consideration.

4.2 Quantitative petrological analyses

4.2.1 Electron Probe Microanalyzer (EPMA)

Quantitative mineral chemical analyses, as well as element mapping, were performed using the JEOL JXA 8200 Superprobe at the Natural Science Centre for Basic Research and Development, Hiroshima University. For element X-ray mapping of monazite, the following conditions were maintained during the analyses: beam current 100 nA, step size 0.5 mm, beam diameter 1 μm . The three lines, U- M_α , Th- M_α and Y- L_α , were measured for the U, Th and Y element mapping. The synthetic YAl-garnet was used as a standard material to measure yttrium content. ThO₂ compound silicate glass and natural thorianite were used as a standard material for Th, whereas U₃O₈ compound silicate glass and natural uraninite were used for U. The probe diameter was set in between 1–3 μm and beam current was fixed in between 5–15 nA for the measurement of oxides. For this analysis, the characteristic X-ray lines for all the elements were K_α , and the acquired data were quantified as oxides by ZAF correction. The acceleration voltage was set at 15 kV for both quantitative analysis and element mapping.

4.2.2 X-Ray Fluorescence (XRF)

For whole rock chemical analysis, the representative samples were crushed down to ~5 mm diameter chips using jaw-crusher or oil-press mill, and further smashed down to fine powder (diameter $\leq 250 \mu\text{m}$) using ball-mill or stamp-mill. The powdered sample was dried in oven at 120 °C for 12 hours for evaporation of the surface moisture, and then treated in Superburn for 6 hours at 950 °C to eliminate the structural water. The powdered samples were fused into glass disc using an oven-dried alkali flux, Johnson Matthey Spectroflux 100B [a mixture of lithium tetraborate ($\text{Li}_2\text{B}_4\text{O}_7$) and lithium metaborate (LiBO_2) with a mixing ratio of 2:8] and lithium nitrate (LiNO_3) as oxidising agent. The disc was prepared from 2.000 gm of rock powder, 4.000 gm of flux and 0.60 gm of LiNO_3 as an oxidizer and ~100 μL of 5% LiI solution added to prevent adhesion to the Pt crucible. Whole-rock geochemical analyses for major and trace elements of the samples were carried out by X-ray Fluorescence (XRF) techniques using a Rigaku ZXS system equipped at Hiroshima University. X-ray generated by a 3kW Rh-W dual anode tube was radiated on fused bead samples. The accuracy and precision of this method is outlined in Kanazawa et al. (2001).

4.2.3 X-Ray Diffraction (XRD)

The X-Ray Diffraction (XRD) technique was used for identification of minerals within the clay-supported matrix of foliated quartz breccia. The homogeneously powdered sample was analyzed using Rigaku XRD MultiFlex

installed at Hiroshima University. Cu was used as the target material to generate X-Ray. Cu-K α radiation was generated at 40 kV/40 mA during the analysis.

4.3 Geochronological analyses

4.3.1 Sensitive High-resolution Ion Microprobe (SHRIMP IIe)

The samples were crushed down to ~5mm diameter chips using jaw-crusher or oil-press mill and further smashed down to powder (diameter ~250 μ m) using ball-mill or stamp-mill. Zircon grains were, then, separated by heavy minerals separation method using water from the powdered rock samples. The grains were separated mainly using heavy mineral separation technique by sieving, panning and by magnetic separation methods using hand-held Nd magnet and Frantz Isodynamic Magnetic Separator (Model L1). Special care was taken to avoid any contamination. The separated zircon grains together with the standard zircon grains were then handpicked, mounted in epoxy resin. In the case of the foliated quartz breccia, all the heavy minerals including the zircon grains were mounted together with the standard zircon grains without handpicking. These mounts were finally polished by 1 μ m diamond paste until the grains were properly exposed on the surface. The zircon grains were analyzed for U-Pb dating by SHRIMP IIe at the Hiroshima University. The spot size was about 18 μ m, and seven/five scans through the critical mass ranges were made for data collection. The condition of SHRIMP IIe during the analysis was: Köhler aperture 70 μ m, source slit 80 μ m, collector slit 90 μ m, ESA voltage at 941.70 V, arc voltage at 60 mA, primary current at 2800 V. Counts of $^{196}\text{Zr}_2\text{O}$, ^{204}Pb , ^{206}Pb , ^{207}Pb , ^{208}Pb , ^{238}U , ^{248}ThO , ^{254}UO and background ($^{204.1}\text{Pb}$) were measured

seven times. The analytical technique was adopted from the methodology outlined by Fujii et al. (2008). Two zircon standards, FC1 (1099 ± 0.6 Ma; Paces and Miller, 1993) and SL13 (572 Ma, U concentration = 238 ppm; Claoué-Long et al., 1995) were used for the U-Pb calibration and the calculation of U content in the samples, respectively. During each analytical session, two points on the age-standard were measured before and after measuring five points on the unknown zircon grains. The weighted average ages of the standard were within the error range of the reference zircon grains (1099 ± 0.6 Ma). Based on the method developed by Compston (1999), common Pb was corrected from the measured ^{204}Pb . Finally, Isoplot/Ex 4.15 (Ludwig, 2012) and CONCH (Nelson, 2006) were used for age calculations and various statistical plotting of the age data. Only near-concordant ages ($\leq 5\%$ discordant) were considered for probability density plots and single population weighted average age calculations. Spot dates are quoted at 1σ level, whereas mean ages are given at 95% confidence level.

4.3.2 Electron Probe Microanalyzer (EPMA)

The method outlined in Suzuki and Adachi (1991) was adopted for the in-situ monazite EPMA U-Th-total Pb dating. The obtained raw data were corrected through recalculation methods developed by Fujii et al. (2008) and processed using Isoplot/Ex version 4.15 (Ludwig, 2012). The probe diameter was set at $5 \mu\text{m}$ and beam current was fixed at 200 nA. The acceleration voltage was set at 15 kV. Fifteen characteristic X-ray lines were measured for each element. These lines were Si- $\text{K}\alpha$, Sm- $\text{M}\beta$, Gd- $\text{M}\beta$, Dy- $\text{M}\beta$, Th- $\text{M}\alpha$, U- $\text{M}\beta$, Ca- $\text{K}\alpha$,

La-L α , Ce-L α , Y-L α , P-K α , S-K α , Pr-L β ₁, Nd-L β ₁, Pb-M β . Acquired data were quantified as oxides by ZAF correction. The age standard used in these analyses was Namaqualand monazite (1033 Ma; Hokada and Motoyoshi, 2006). During every analytical session, five to ten points on the age-standard were measured after measuring the unknown monazite grains. The weighted average ages of the standard were within the 1% error range of the quoted value of the reference material (1033 Ma).

Chapter 5:

PETROLOGICAL EVOLUTION

Seven different lithological varieties of are exposed in the three parts of the entire study area. These areas include rocks from different crustal-levels, i.e., the deep-crustal granulites, mid-crustal cratonic gneiss and shallow-crustal sedimentary rocks. The petrographic features, mineralogical assemblages, and corresponding textural relationships are discussed in detail in the following section. These details are summarized in table 2.

5.1 Petrography and microstructure

5.1.1 Deep-crustal rocks of the EGB

5.1.1.1 Charnockitic augen gneiss

Three different varieties of the charnockitic augen gneiss (sample BP1, BP3 and BP2) were studied for petrological and microstructural observations.

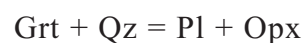
Sample BP1

This rock sample was collected from the southeast of Bhawanipatna town (Fig. 3). The coarse-grained charnockitic augen gneiss is composed of orthopyroxene, K-feldspar, quartz, garnet, biotite, plagioclase, and ilmenite. Augen are composed of K-feldspar. Both porphyroblastic (~800–1000 μm in diameter) and coronal (~5–10 μm in diameter) garnet was observed. The dominant texture of this rock is granoblastic (Fig. 7a). The peak granulite facies metamorphic assemblage is defined by coarse grain orthopyroxene, garnet,

quartz and K-feldspar. The development of coronal garnet (with intergrown quartz) over orthopyroxene resulted from the subsequent cooling event (Fig. 7b). The post-peak granulite facies rehydration event was documented where biotite replaced K-feldspar and garnet (Fig. 7b).

Sample BP3

Another variety of the charnockitic augen gneiss was also collected from the nearby area of sample BP1 which shows additional textures (Fig. 3). This rock contains orthopyroxene (Opx), quartz (Qz), K-feldspar, garnet (Grt), plagioclase (Pl), biotite, and ilmenite. Orthopyroxene, K-feldspar, quartz, and garnet characterized the peak granulite facies metamorphic assemblage. Garnet is both porphyroblastic (~500 μm in diameter) and coronal. The latter variety of garnet was intergrown with quartz and developed around the ilmenite grains (Fig. 7c). The additional textures include the perthitic texture where blebs of plagioclase were found within the K-feldspar host. Another textural feature revealed that the porphyroblastic garnet was destabilized to form orthopyroxene and plagioclase intergrowth (Fig. 7d). Such porphyroblastic garnet break-down texture suggest that destabilization occurred during the post-peak condition. The formation of the intergrowth might had occurred through this reaction:



This reaction can occur either by heating or by decompression in the granulite facies condition. Owing to the fine nature of the product phases, the second possibility seems more feasible. Biotite was produced during post-peak granulite facies rehydration.

Sample BP2

This rock sample was collected near Atangaguda village area which is located at the southwest of Bhawanipatna town (Fig. 3). The medium to fine-grained rock is mineralogically similar to sample BP1 and BP3. However, this rock preserves mesoscopic (Fig. 5a) and microscopic evidence of intense deformation. The microtextures, such as the presence of curved grain boundary, possibly suggest that the rock had experienced dynamic recrystallization (Fig. 7e) in response to deformation. Hence, combination of the field evidence (Fig. 5a), such as presence of high-strain zone adjacent to the low-strain zone, with the microscopic evidence suggest that the rock was deformed possibly by shear stress.

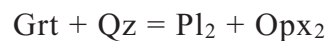
5.1.1.2 Mafic granulite

Two different varieties of the mafic granulite (sample BP12B and BP4) were studied in detail to understand the petrological evolution.

Sample BP12B

This rock sample was collected near the Parla village (Fig. 4a). The coarse-grained gneissic rock contains the porphyroblastic garnet (Fig. 8a). The leucocratic layers around the porphyroblastic garnet are mostly constituted of plagioclase (Fig. 8b), whereas the mesocratic layers are composed of orthopyroxene (Opx_1), clinopyroxene, garnet, ilmenite, hornblende, and biotite \pm zircon. Quartz is rare within the rock. Orthopyroxene (Opx_1), clinopyroxene, plagioclase (Pl_1), quartz and garnet represented the granulite facies

metamorphic assemblage. Garnet and clinopyroxene constituted the porphyroblastic phases (up to 1 cm in diameter), whereas orthopyroxene and plagioclase constituted the finer aggregates (~100–200 μm in diameter). Ilmenite (maximum up to ~100 μm in diameter; Fig. 8a) and relict hornblende₁ occur as inclusions within the porphyroblastic garnet (Fig. 8a). Symplectic intergrowths of orthopyroxene (Opx₂) and plagioclase (Pl₂) were developed on garnet (Fig. 8b), possibly due to the breakdown of the latter in the presence of quartz through this reaction:



This reaction can occur either by heating or by decompression. The textural relationship between reactants and products suggest that the symplectite development was due to decompression. Textural data further implied that the plagioclase-rich leucocratic layer around the garnet grains was formed due to the decompression melting. Additionally, the incipient late-hornblende₂ formed at the site of symplectite intergrowth (Fig. 8b). The prominent growth of late-hornblende₂ on clinopyroxene (Fig. 8c) suggests that the late-hornblende₂ was formed during the post-peak rehydration. Thus, this rock preserves mineral assemblages of both peak granulite facies and post-peak granulite-amphibolite facies transitional facies.

Sample BP4

This dark colored medium-grained rock was sampled at a place ~25 km southeast of the Dharamgarh town (Fig. 3), where it occurs as an isolated exposure (Fig. 5c). The rock is composed of orthopyroxene, clinopyroxene,

plagioclase, garnet, ilmenite, hornblende and quartz. Plagioclase (~3–5 mm in diameter) and garnet (~1 mm long and ~0.5 mm wide) are present within the finer matrix which is composed of orthopyroxene, clinopyroxene, ilmenite and quartz. Garnet also occurs as corona with intergrown quartz (Fig. 8d) around ilmenite and clinopyroxene which were formed at the peak granulite facies condition. Hence, the textural relationship suggests that such coronal garnet and quartz intergrowth was possibly produced during post-peak granulite facies cooling. Microstructural observation, especially curved grain boundary, revealed that the rock was deformed and recrystallized dynamically.

5.1.1.3 Aluminous granulite

Two varieties of aluminous granulite (sample BP12A and BP12C) were studied to understand the textural and microstructural development.

Sample BP12A

This sample was collected from a location close to the above-described mafic granulite (sample BP12B; Fig. 4a). The coarse-grained rock contains garnet, along with euhedral sillimanite, quartz, hemo-ilmenite, and magnetite ± zircon. Garnet, sillimanite, quartz, magnetite and hemo-ilmenite represent the peak granulite facies metamorphic assemblage (Fig. 9a). The garnet is porphyroblastic in nature. The core of the porphyroblastic garnet contains an intergrowth of garnet, quartz, sillimanite, and hemo-ilmenite (Fig. 9b). The core possibly grew syn-kinematically with the matrix foliation. The core of the garnet is surrounded by the thick intergrowth-free garnet rim, which grew post-

kinematically (Fig. 9b). The elongated finer-grained matrix minerals of quartz, sillimanite and hemo-ilmenite defines the foliation. Sillimanite also occurs as a coarse grain variety in the matrix, which appeared to bend against the garnet. The sillimanite away from the porphyroblastic garnet exhibits post-kinematic growth. The latter variety of sillimanite transformed to fibrolite during post-peak granulite facies metamorphism (Fig. 9c). The garnet and quartz in this rock contain abundant secondary fluid inclusions, whereas primary fluid inclusions are rare. In addition, exsolution lamellae of ilmenite was found within the hemo-ilmenite, which presumably formed due to cooling during the post-peak condition (Fig. 9a).

Sample BP12C

This sample was collected from the nearby area of the sample BP12A (Fig. 4a). The mineralogy is similar to the sample BP12A. Outcrop-scale evidence, such as presence of elongated garnet grains may suggest that this is a highly deformed variety of aluminous granulite. Combination of several mesoscopic evidence of shearing (discussed in the section 3.2) with the limited microstructural evidence, such as the weakly developed shape-asymmetry of the garnet suggest that it suffered the same shear deformation (Fig. 9d). The disposition of the thrust plane between the EGB and the BC was inferred by combining the field occurrence of this deep-crustal sheared rock adjacent to the mid-crustal cratonic rocks (Fig. 4a). The absence of K-feldspar indicated that the metamorphic condition during the granulite facies was K-feldspar-invariant, or partial melts were completely lost. However, no evidence was found in favor

of either partial melting or K-feldspar invariance. The presence of both magnetite and hematite indicated that oxygen fugacity was close to the hematite-magnetite (HM) buffer.

5.1.1.4 Meta-ironstone

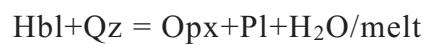
The coarse-grained meta-ironstone was sampled near the Parla village (Fig. 4a). The rock is dominantly composed of magnetite, hematite, garnet, spinel, and quartz. The presence of porphyroblastic magnetite and garnet characterized the granoblastic texture of granulite facies metamorphic condition. Hematite replaced magnetite grains along the intragranular fracture planes (Fig. 9e) due to oxygen enrichment along the fractures. Spinel occurs as inclusion within the magnetite-hematite and garnet. Rarely, quartz was observed to form around the garnet (Fig. 9e).

5.1.2 Mid-crustal rocks of the BC

5.1.2.1 Migmatitic hornblende gneiss

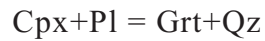
The medium to coarse-grained migmatitic hornblende gneiss was collected near the Parla village (Fig. 4a). This rock is composed of hornblende, clinopyroxene, plagioclase, orthopyroxene, quartz, K-feldspar, hematite, ilmenite and garnet. The gneissic foliation was defined by the alternate layers of mafic and felsic minerals. Mafic layers are dominantly composed of hornblende, clinopyroxene, plagioclase and orthopyroxene (Fig. 10a). Minor amount of quartz and K-feldspar were observed in the mafic layers. Presence of

porphyroblastic hornblende and equilibrium texture between hornblende and clinopyroxene (Fig. 10a) suggest that the hornblende and clinopyroxene formed at the amphibolite facies condition. The progradation from the amphibolite facies assemblage to amphibolite-granulite transition facies was evident by the appearance of orthopyroxene on hornblende in the mafic layer (Fig. 10a). The progradation reaction can be as follows:



The liberation of H₂O/melt could cause either by simple dehydration reaction or by dehydration melting reaction. In this case, textural evidence of dehydration melting, such as presence of leucocratic melt-mat, was not seen. Thus, the reaction is considered as a dehydration reaction. The presence of plagioclase, K-feldspar and quartz characterizes the felsic layers. Both quartz and feldspar exhibit undulose extinction and the grain boundary of feldspar is curved. The foliation-parallel quartz ribbon and deformed plagioclase suggest plastic deformation. However, the adjacent amphiboles and pyroxene did not show evidence of plastic deformation. Thus, it is plausible that the plastic deformation of quartz and feldspar occurred at intermediate temperature (Stipp et al., 2002; Rosenberg and Stünitz, 2003), which was possibly corresponded to the temperature of amphibolite-granulite transitional facies condition. Locally, small amount of garnet is found in the felsic layers. Clinopyroxene is present within the garnet grains as inclusion (Fig. 10b). The garnet is present around the clinopyroxene and plagioclase as thick or thin corona. The formation of

garnet from clinopyroxene in the presence of plagioclase can be explained by the following reaction:



This reaction can occur either due to compression or cooling. The kinetic factors (rate of reaction) is slow in case of retrograde cooling, which favors coronal texture of the product phase during retrograde cooling. Presence of the coronal garnet around the clinopyroxene and plagioclase possibly suggests that the garnet grew during retrograde cooling.

5.1.2.2 Migmatitic quartzofeldspathic gneiss

This sample was collected from the west of the Dharamgarh town on the National Highway 130C (Fig. 4b). The medium-grained rock is essentially composed of quartz, K-feldspar, plagioclase, garnet, biotite and ilmenite. Garnet is porphyroblastic in nature (Fig. 10c). Garnet porphyroblasts are ~500–700 μm in diameter. The granulite facies porphyroblastic garnet was replaced by biotite during post-peak rehydration (Fig. 10c). Inclusions of quartz grains are present within the garnet grains (Fig. 10c). Feldspar was decomposed to sericite. The anti-perthitic texture is present, where thin blebs of K-feldspar occurred within the host plagioclase (Fig. 10d).

5.1.3 Shallow-crustal marginal rocks

5.1.3.1 Foliated quartz breccia

The coarse-grained foliated quartz breccia was sampled from ~5 km northwest of the location of sample BP6 (Fig. 4b). The rock is dominantly composed of quartz, and was previously considered to be a component of the granulite package of the EGB (Metapelite/Quartzite package of Gupta et al., 2000). Microscopic observation revealed that this is a clastic rock where clasts of quartz grains are highly angular, poorly sorted, and randomly oriented in the thin-section scale (Fig. 10e). Such texture can form either due to brecciation of a foliated quartzite or deposition of quartz-rich immature sediments with low-degree of transportation. Characteristic textural evidence of a cataclastic quartzites, such as irregular fracturing in the individual grains, extensive intersecting micro-fracturing and mortar texture (Spry, 1969; House and Gray, 1982; Sibson, 1986) were not observed. Moreover, the adjacent rocks were not showing any evidence of cataclasis (e.g., the granulites). Adding to that, the presence of kaolinitic clayey matrix in the interstitial space between the larger quartz grains was confirmed by the powder X-ray diffraction analysis (Fig. 10f), which is completely missing in the adjacent feldspar-bearing rocks. The decomposition of feldspar as the origin of kaolinitic clayey matrix was ruled out as the adjacent granulites are devoid of kaolinitic clay. Thus, sedimentary origin of this rock was, further, validated by the presence of clayey matrix which did not formed due to the decomposition of feldspar. Hence, all line of

evidence led to infer that this is not a component of the granulite package of the EGB, but a clastic sedimentary rock.

This clayey matrix-supported quartz breccia might have deposited in a small basin formed adjacent to the progressing thrust-front (e.g., Schwans, 1988; DeCelles and Giles, 1996). The brecciation of the nearby source rocks occurred possibly as a consequence of the thrusting, and supplied the highly angular clasts as they experienced low degree of transportation.

5.2 Mineral chemistry

The mineral chemical data of four rocks were generated using the EPMA. These data were used for conventional geothermobarometric calculations and for understanding the chemical characters of some major minerals of the rocks. In the following subsections, mineral chemical data of the individual minerals of these rocks is described. The representative mineral chemical data of the individual rocks are summarized in the Table 3.

5.2.1 Garnet

In mafic granulite (sample BP12B), core of the porphyroblastic garnet of granulite facies metamorphic assemblage exhibited minor compositional variation ($\text{Alm}_{53-60}\text{Prp}_{17-21}\text{Grs}_{16-25}\text{Sps}_{1-4}$). These garnet grains broke down along the rims to produce symplectite intergrowth of plagioclase and orthopyroxene. Thus, the composition of these rims is slightly different than the cores ($\text{Alm}_{59-64}\text{Prp}_{12-18}\text{Grs}_{18-23}\text{Sps}_{3-4}$). Consequently, the X_{Mg} value between the core to rim also vary (rim: 0.16–0.23; core: 0.23–0.28). Garnet of aluminous

granulite (sample BP12A) documented a slight compositional variation between core and rim (rim: $\text{Alm}_{71-72}\text{Prp}_{22-23}\text{Grs}_4\text{Sps}_3$; core: $\text{Alm}_{72-73}\text{Prp}_{20-21}\text{Grs}_4\text{Sps}_3$). The X_{Mg} value increases from the core to rim (core = 0.22 and rim = 0.23–0.25). Garnet in meta-ironstone (sample DG33E) displayed no discernible zoning from core to rim ($\text{Alm}_{71-75}\text{Prp}_{17-20}\text{Grs}_{5-10}\text{Sps}_1$). Hence, the variation in the X_{Mg} value was not observed between the core and rim ($X_{\text{Mg}} = 0.19\text{--}0.21$). Compared to the porphyroblastic garnet of granulite facies condition, the garnet in the migmatitic hornblende gneiss (sample DG33F) of the BC is richer in grossular content (Grs_{25-26}). However, this sample also exhibited very weak compositional zoning between core and rim of the garnet ($\text{Alm}_{62-65}\text{Prp}_{5-6}\text{Grs}_{25-26}\text{Sps}_4$). Consequently, the X_{Mg} value almost remain constant between the core to (rim: 0.06–0.08; core: 0.06–0.07).

5.2.2 Orthopyroxene

In mafic granulite (sample BP12B), the porphyroblastic orthopyroxene of granulite facies metamorphic assemblage displayed no compositional variation in terms of Fe-Mg distribution from core to rim ($X_{\text{Mg}} = 0.49\text{--}0.50$). The compositional variation was observed in terms of Al content between core and rim (core: 1.15–1.35 wt% Al_2O_3 ; rim: 0.84–1.1 wt% Al_2O_3). Blebs of orthopyroxene of symplectite intergrowth are variably aluminium-rich (0.94–1.47 wt% Al_2O_3) and slightly Mg-poor ($X_{\text{Mg}} = 0.45\text{--}0.50$) than the porphyroblastic phases. Orthopyroxene in migmatitic hornblende gneiss (sample DG33F) is Mg-poor than the mafic granulite ($X_{\text{Mg}} = 0.39\text{--}0.40$). However, the Fe-Mg distribution is homogenous from core to rim.

5.2.3 Clinopyroxene

The granulite facies porphyroblastic clinopyroxene from mafic granulite (sample BP12B) displayed very weak compositional variation from core to rim (rim: $X_{Mg} = 0.58-0.63$, $X_{Fe} = 0.37-0.42$, $X_{Ca} = 0.84-0.9$; core: $X_{Mg} = 0.57-0.62$, $X_{Fe} = 0.38-0.43$, $X_{Ca} = 0.86-0.91$). The porphyroblastic clinopyroxene in the mafic layer of migmatitic hornblende gneiss (sample DF33F) exhibited slight variation in Fe-Mg distribution from core to rim (rim: $X_{Mg} = 0.52-0.56$, $X_{Fe} = 0.42-0.48$; core: $X_{Mg} = 0.51-0.55$, $X_{Fe} = 0.45-0.49$). Slight enrichment of Ca was observed in the rim with respect to the core (rim: $X_{Ca} = 0.87-0.89$; core: $X_{Ca} = 0.84-0.88$). The included clinopyroxene within the garnet in the felsic layer of migmatitic hornblende gneiss is Mg-poor ($X_{Mg} = 0.32-0.35$) but Fe-rich ($X_{Fe} = 0.65-0.68$) than the porphyroblastic clinopyroxene. The Fe distribution is nearly homogenous, from core to rim. However, very weak compositional zoning between Mg and Ca was noticed from core to rim (rim: $X_{Mg} = 0.34-0.35$, $X_{Ca} = 0.88-0.89$; core: $X_{Mg} = 0.32-0.35$, $X_{Ca} = 0.87-0.9$).

5.2.4 Plagioclase

The anorthitic plagioclase associated with the granulite facies metamorphic assemblage in mafic granulite (sample BP12B) displayed wide compositional variation in the core ($Ab_{22-46}An_{54-77}Or_{0-1}$), as well as, in the rim ($Ab_{12-30}An_{70-88}$). The anorthitic plagioclase associated with the symplectite intergrowth is compositionally similar with the rimmal portion of the plagioclase of granulite facies metamorphic assemblage ($Ab_{9-29}An_{71-91}Or_{0-1}$). The migmatitic hornblende gneiss (sample DG33F) contains albitic plagioclase

in the felsic layer, which did not show any compositional zoning ($\text{Ab}_{60}\text{An}_{36-38}\text{Or}_{3-4}$) from core to rim. The plagioclase in the mafic layer of migmatitic hornblende gneiss is also compositionally homogenous ($\text{Ab}_{54-56}\text{An}_{41-43}\text{Or}_{3-4}$). However, the calcium content of these plagioclase grains is higher than the felsic layer.

5.2.5 Spinel

The spinel in meta-ironstone (sample DG33E) is compositionally hercynitic, which is a product of complete solid solution between hercynite and spinel ($\text{Hc}_{80-72}\text{Spl}_{15-24}$). The spinel grains included within the garnet grains are more magnesian ($X_{\text{Mg}} = 0.23$) compared to the spinel grains included within the magnetite-hematite ($X_{\text{Mg}} = 0.14-0.16$).

5.2.6 Hornblende

The porphyroblastic hornblende in the mafic layer of migmatitic hornblende gneiss (sample DG33F) did not show appreciable compositional variation from core to rim ($X_{\text{Mg}} = 0.43-0.45$). Total Al in the T site also remains constant in between core and rim (1.9–2). TiO_2 concentration in the hornblende is varying in the range of 2.4–2.7 wt%.

5.3 Geothermobarometry

The mafic granulite (sample BP12B) had been chosen as the representative rock to calculate P - T condition during different stages of the metamorphic evolution due to its suitable mineral assemblages and textural development associated at different stages. The textural evolution and

development of corresponding mineral assemblages in response to the metamorphic conditions were discussed in detail in the previous section.

Several conventional geothermobarometers were used for the quantitative *P-T* estimation of each stages.

The granulite facies metamorphic assemblage was stabilized at 898 ± 4 °C, 10–11 Kbar as estimated by the garnet-orthopyroxene thermometry (Lee and Ganguly, 1988) and the garnet-clinopyroxene-plagioclase-quartz barometry (Moecher et al., 1988). The geobarometric calculation for the granulite facies condition by the garnet-orthopyroxene-plagioclase-quartz barometer (Perkins and Chipera, 1985) yielded 10.77 ± 0.05 kbar, which is in accordance with the calculated value obtained by the garnet-clinopyroxene-plagioclase-quartz barometer. However, the garnet-orthopyroxene thermometry of Harley (1984) yielded a lower temperature as 749 ± 3 °C for granulite facies metamorphism. The granulite facies temperature was calculated by the garnet-clinopyroxene thermometer as 730 ± 7 °C (Ellis and Green, 1979). Followed by the granulite facies condition, the garnet-orthopyroxene-plagioclase-quartz barometer (Newton and Perkins, 1982) estimated the decompression occurred at a pressure of 7.5 ± 0.04 kbar. The temperature during the decompression was calculated from the garnet-orthopyroxene (from the symplectite texture) thermometry as 826 ± 12 °C (Lee and Ganguly, 1988) and 677 ± 12 °C (Harley, 1984). The error values in the *P-T* calculations are the external error of the data-set, without considering the intrinsic error values of the corresponding geothermobarometers.

5.4 Thermodynamic modeling of metamorphic evolution

The P - T evolution of the granulites from the western margin of the EGB was characterized by estimating the P - T conditions using several conventional geothermobarometers. The mafic granulite (sample BP12B) was exclusively targeted to understand the P - T evolution as it exhibits pre- to post- peak granulite facies textural evidence. The conventional geothermobarometric data were superimposed on the pseudosection modeling to determine the exact position of each stage of metamorphism on a P - T plane. The software, *Perple_X* (Connolly and Petrini, 2002; version 6.7.7), was used for the pseudosection modeling. The pseudosection modeling was carried out using the bulk rock composition obtained by whole rock XRF analysis (Table 4).

A model chemical system of Na_2O - CaO - FeO - MgO - Al_2O_3 - SiO_2 - H_2O - TiO_2 - MnO (NCFMASHTMn) was chosen for the pseudosection modeling depending on the bulk rock composition and mineral assemblage. Fe_2O_3 was excluded as a variable since the presence of Fe^{3+} in ferromagnesian phases is minor particularly in this rock. The following mineral phases were included for the pseudosection modeling: garnet (Grt), hornblende (Hbl), clinopyroxene (Cpx), orthopyroxene (Opx), plagioclase (Pl), quartz (Qz), ilmenite (Ilm), rutile (Rt) and water (H_2O). Mineral phase diagram was calculated as a function of P - T using the technique of free energy minimization (Connolly, 2005). The *perplex_option.dat* file (Holland and Powell, 1998) was used for constraining the solution properties of these mineral phases. The following activity models were used for the corresponding mineral phases: garnet and clinopyroxene

(Holland and Powell, 1998), clinoamphibole (Dale et al., 2005), orthopyroxene (Holland and Powell, 2003) and plagioclase (Newton et al., 1980). Rutile, ilmenite, and quartz were considered as pure phases. The mineral phases at the higher temperature side of the pseudosection may be metastable with respect to the assemblage involving melt. The absence of melt model for the metabasite system hinders this assessment. However, the several experimental studies and natural observations revealed that the topological variation of the phase relationships and their change in position of the field boundaries are negligible when mineral assemblages coexist with the fluid (H₂O) or melt (Wolf and Wyllie, 1994; Vielzeuf and Schmidt, 2001; Pattison, 2003).

The resultant phase diagram revealed that the garnet is the only mineral phase which is stable across all the mineral stability fields (Fig. 11). The inclusion of relict hornblende and ilmenite within the porphyroblastic garnet grains suggest that the porphyroblastic garnet of peak granulite facies might have produced from hornblende during prograde metamorphism by dehydration (Fig. 11). Thus, the pre-peak granulite facies metamorphic condition (M₁) was assumed to lie in the field consist of orthopyroxene, hornblende, garnet, clinopyroxene, plagioclase, quartz, and ilmenite. However, the position of M₁ could not be plotted on the *P-T* space due to lack of data in the present study. The mineral assemblage of orthopyroxene₁ + clinopyroxene + garnet + plagioclase₁ + ilmenite ± quartz characterized the peak granulite facies metamorphic assemblage (M₂). The stability field for this mineral assemblage is tiny on the *P-T* space for this bulk composition. The exact position of the M₂

within a P - T range was validated by the conventional P - T estimation (~ 900 °C temperature and ~ 11 – 10 Kbar pressure). The formation of symplectite intergrowth of orthopyroxene₂ and plagioclase₂ around the garnet grains in the expense of quartz was due to the near-isothermal decompression. This near-isothermal decompression upto ~ 825 °C temperature and ~ 7.5 Kbar pressure characterizes the M_3 event (Fig. 11). The formation of the incipient late-hornblende also observed at the site of garnet breakdown. The precise position of M_3 on the P - T plane was determined by combining the mineralogical assemblage with the conventional P - T calculation and observed dispositions of the pyrope isopleths of garnet (Fig. 11). Followed by the M_3 event, the M_4 metamorphic event is characterized by the appearance of late-hornblende on clinopyroxene was due to rehydration during retrogression from granulite facies to granulite-amphibolite transitional facies. However, a speculative metamorphic P - T path was constructed accordingly for the M_4 event due to the absence of precise P - T data for this event (Fig. 11).

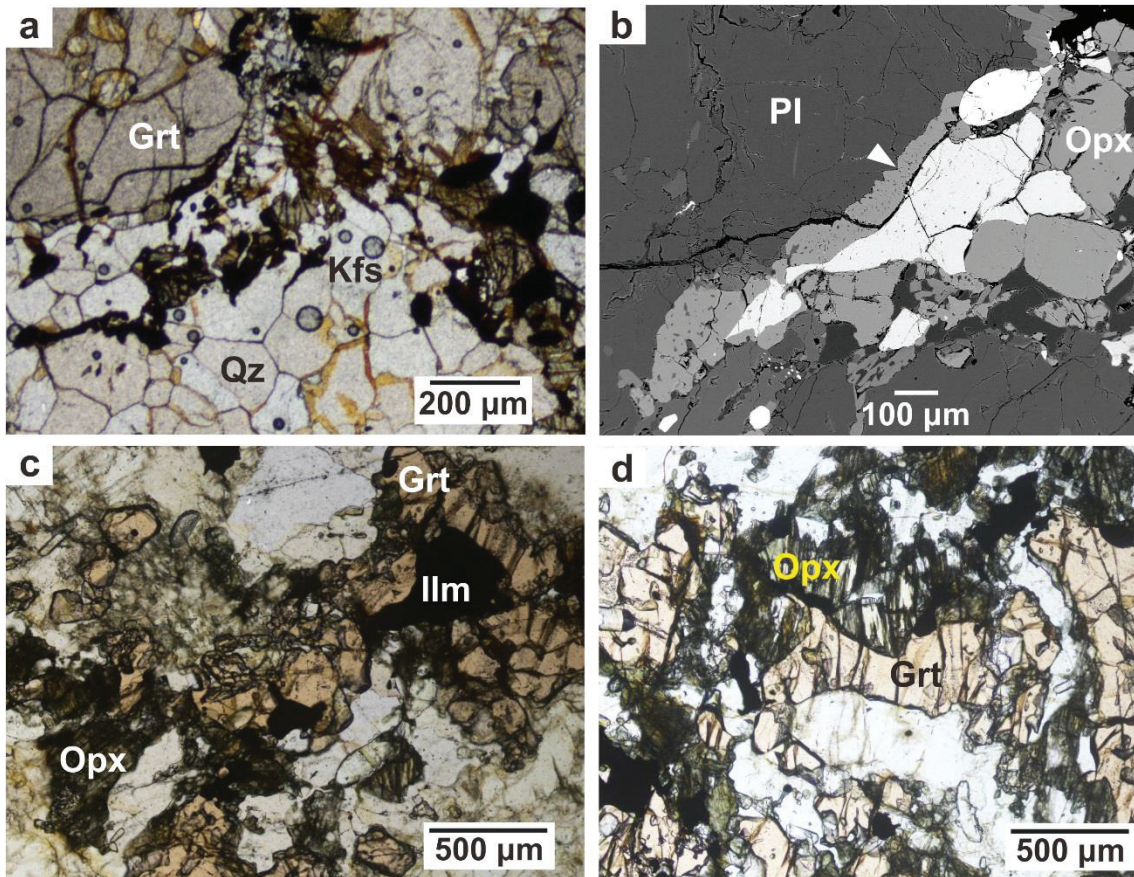


Figure 7 continued in the next page

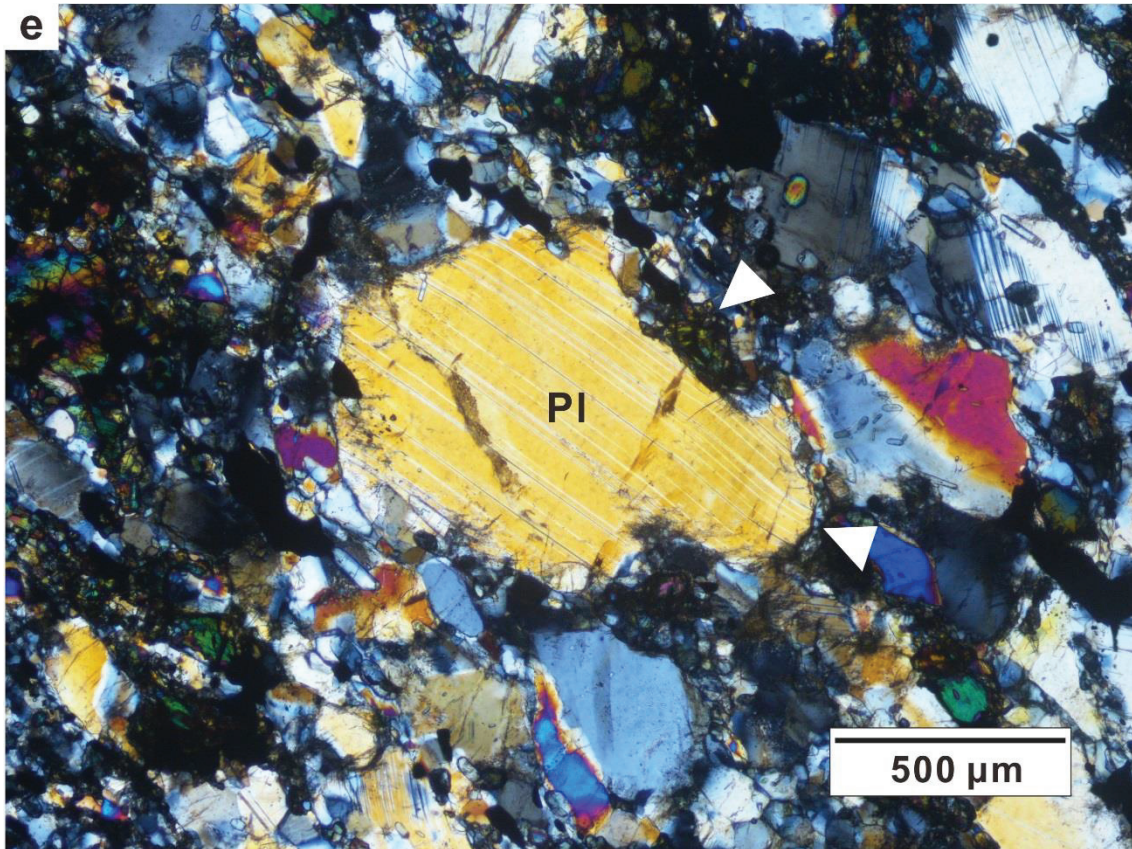


Figure 7: The microphotographs of the three samples of charnockitic augen gneiss. (a) The OM (PPL) image of sample BP1 represents the granoblastic texture of peak metamorphic assemblage is composed of garnet (Grt), quartz (Qz), K-feldspar (Kfs). (b) The SEM-BSI image shows development of the coronal garnet and quartz intergrowth (black triangle) associated with the orthopyroxene (Opx) and plagioclase (Pl). (c) The OM (PPL) image represents the formation of coronal garnet (Grt) around ilmenite (Ilm) and orthopyroxene (Opx) in the sample BP3. (d) Porphyroblastic garnet (Grt) broke down to orthopyroxene (Opx) due to decompression. (e) The OM (CPL) microphotograph of grain-size refinement texture marked by the presence of both porphyroclastic plagioclase (Pl) and recrystallized fine grain aggregate surrounding the porphyroclasts (white triangles) in the sample BP2.

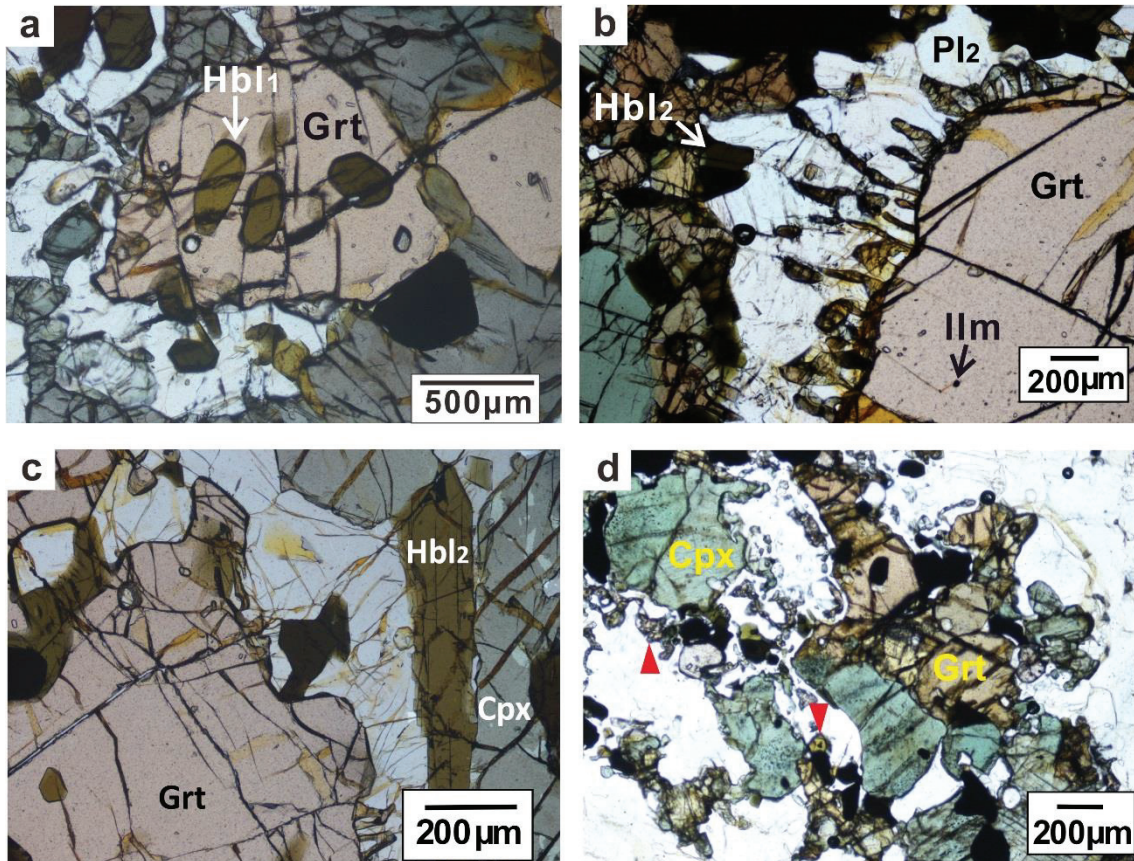
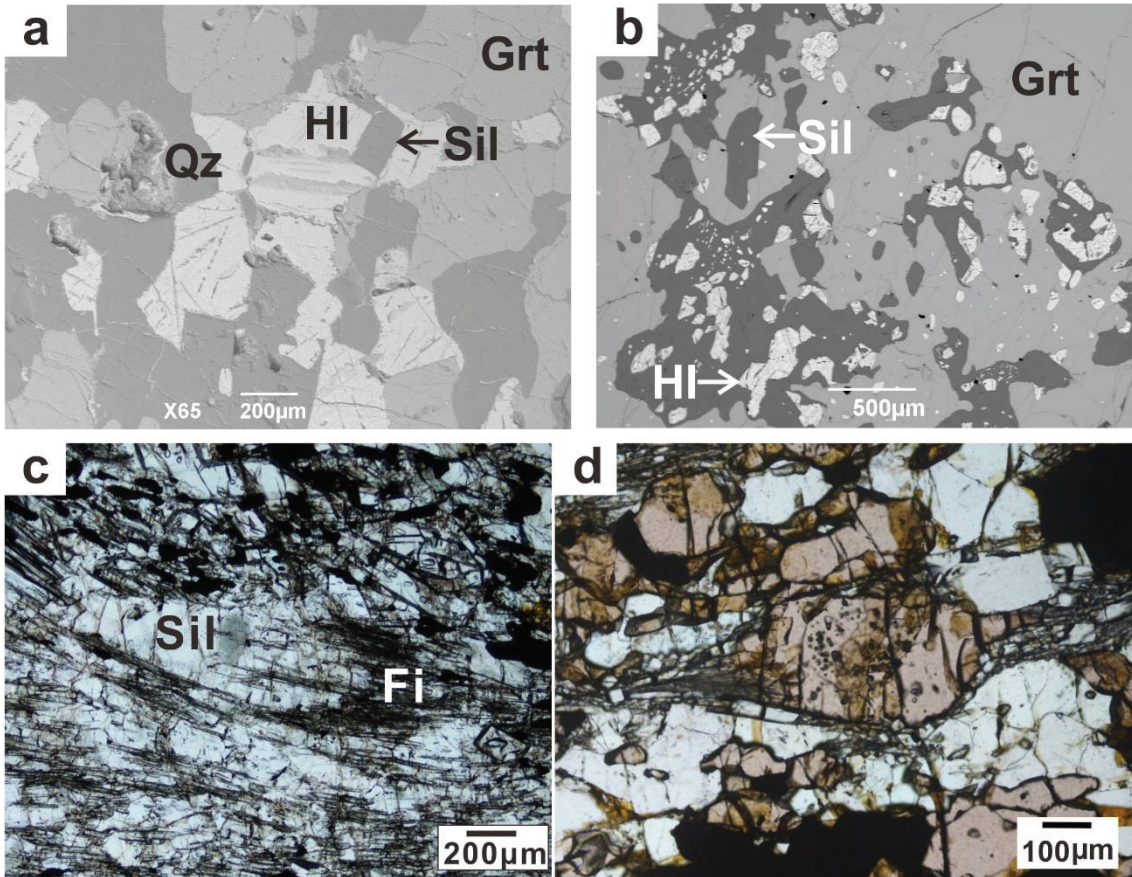


Figure 8: The OM microphotographs (PPL) of the two samples of mafic granulites (sample BP12B and BP4). (a) The inclusion of early-hornblende (Hbl_1) within the porphyroblastic garnet grain (Grt) is observed in the sample BP12B. (b) The garnet (Grt) broke down to symplectitic orthopyroxene₂ (blebs-like intergrowth) and plagioclase₂ (Pl_2). Incipient late-hornblende₂ (Hbl_2) formed at the site of the symplectite intergrowth. (c) The prominent growth of late-hornblende₂ (Hbl_2) on clinopyroxene is observed. (d) Garnet present as porphyroblastic phase and coronal intergrowth (red triangle) around clinopyroxene (Cpx) in Sample BP4.



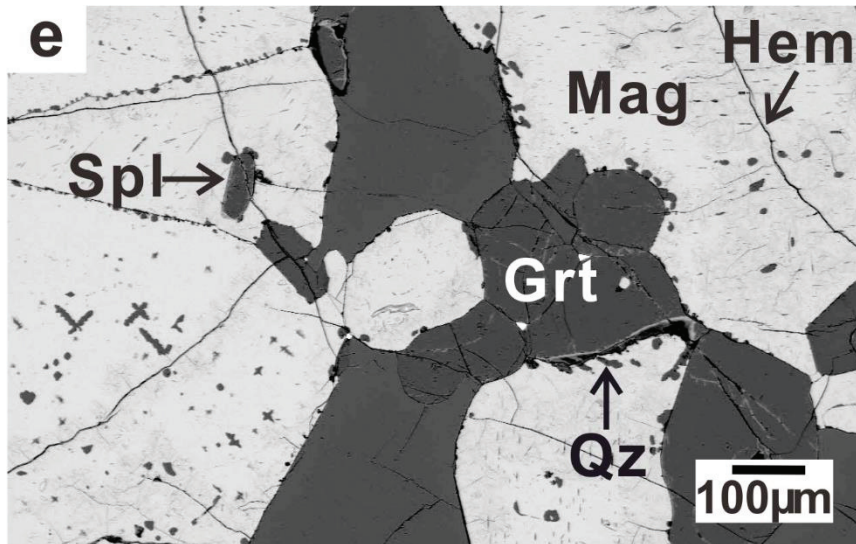


Figure 9: The microphotographs of two varieties of aluminous granulite (sample BP12A and BP12C) and meta-ironstone (sample DG33E). (a) The SEM- BSI microphotograph is showing the overall mineralogical assemblage of aluminous granulite (sample BP12A), which is composed of hemo-ilmenite (HI), quartz (Qz), sillimanite (Sil) and garnet (Grt). (b) The SEM- BSI microphotograph represents the intergrowth at the core of the porphyroblastic garnet, which comprises of sillimanite (Sil), quartz (Qz) and hemo-ilmenite (HI). (c) The OM image (PPL) is showing that away from the porphyroblastic garnet grains, bladed sillimanite (Sil) transforming into fibrolite (Fi). (d) The OM image (PPL) of sample BP12C shows porphyroclastic garnet developing weak shape-asymmetry due to shearing. (e) The SEM- BSI microphotograph of sample DG33E shows that the hematite (Hem) formed along the intragranular fracture planes within the magnetite (Mag). Spinel (Spl) is included within magnetite-hematite. Coronal quartz (Qz) formed around the garnet (Grt).

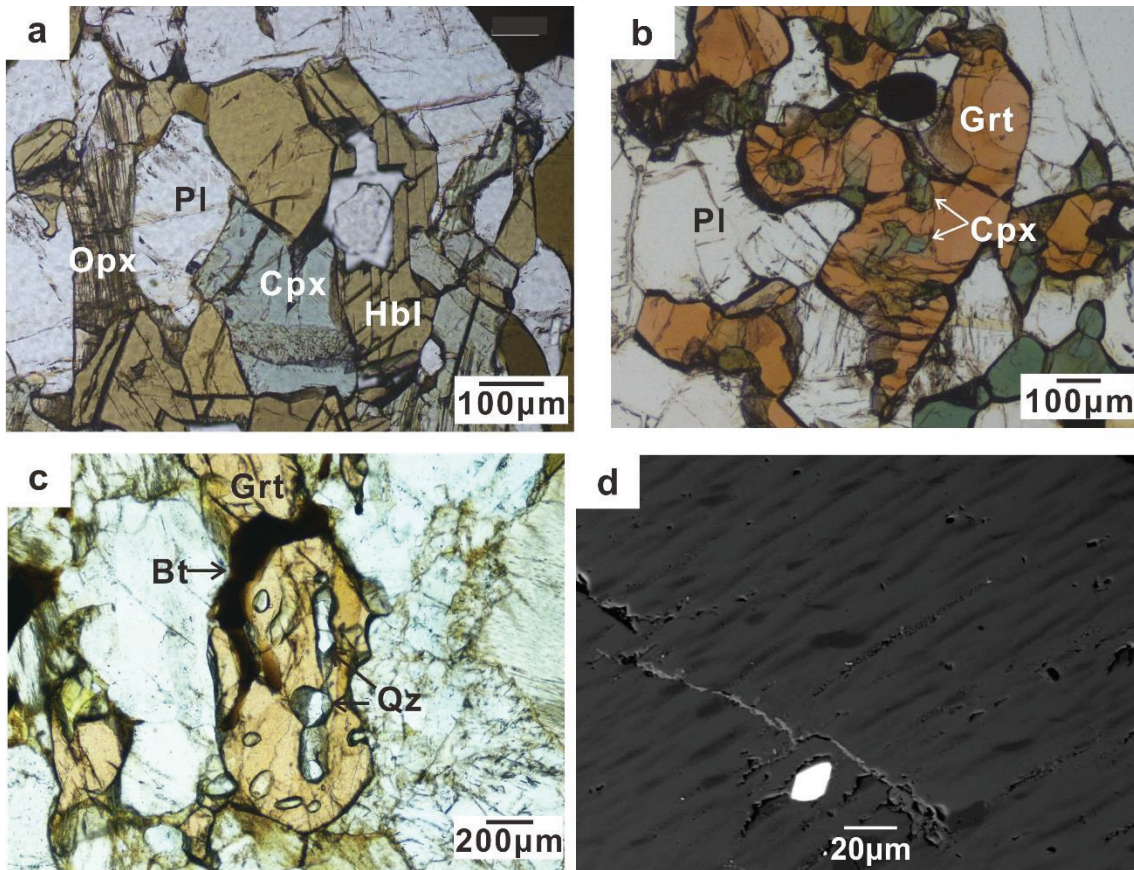


Figure 10 continued in the next page

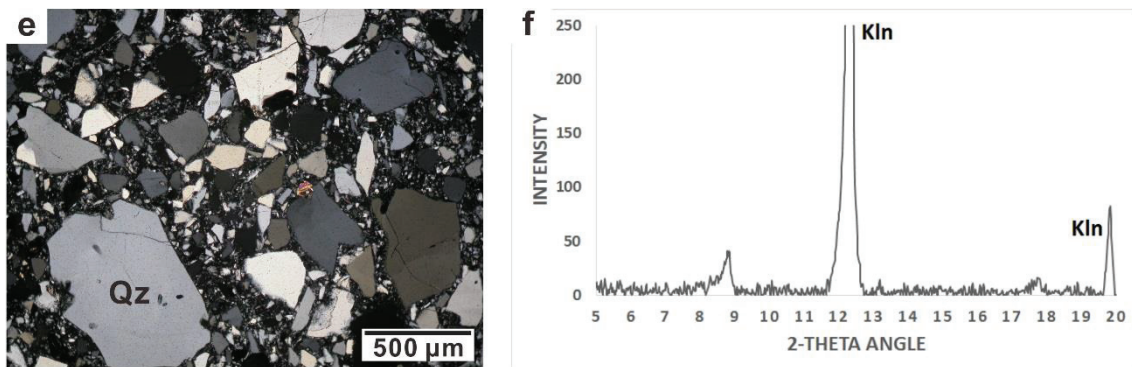


Figure 10: (a) The OM microphotograph (PPL) shows representative mineral assemblage in the mafic layer of migmatitic hornblende gneiss (sample DG33F), which is composed of hornblende (Hbl), clinopyroxene (Cpx), plagioclase (Pl) and orthopyroxene (Opx). (b) The OM microphotograph (PPL) shows that the clinopyroxene (Cpx) included within the garnet grains (Grt) in the felsic layer of the same rock. (c) The OM microphotograph (PPL) of the migmatitic quartzofeldspathic gneiss (sample BP6) shows that the porphyroblastic garnet (Grt) of peak metamorphic assemblage contains inclusions of quartz (Qz). Biotite (Bt) was formed at the boundary of the garnet grain. (d) The SEM- BSI microphotograph of the same rock shows anti-perthite texture where the blebs of guest K-feldspar present within the host plagioclase. (e) The OM microphotograph (CPL) of foliated quartz breccia (sample DG17B) shows highly angular, poorly sorted quartz grains. (f) The characteristic XRD peaks of kaolinitic (Kln) clayey matrix in sample DG17B.

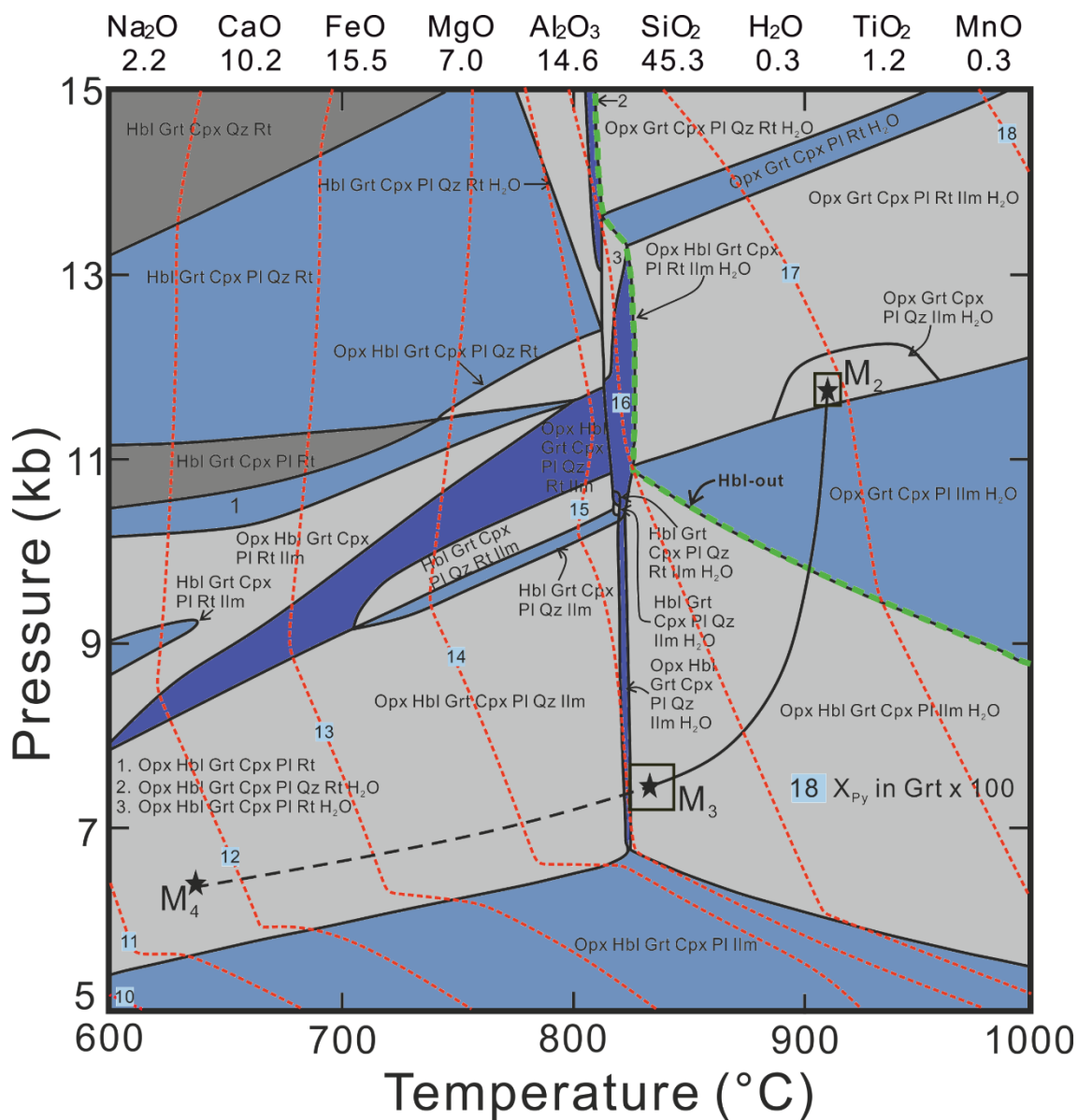


Figure 11: P - T pseudosection for mafic granulite (sample BP12B) constructed in the system Na_2O - CaO - FeO - MgO - Al_2O_3 - SiO_2 - H_2O - TiO_2 - MnO . The bulk rock composition is mentioned on the top the phase diagram. The stability fields of different variance are shown by blue and gray shades. The pre-peak granulite facies metamorphic is considered as M_1 . The peak granulite facies metamorphic assemblage is denoted as M_2 in the figure. The exact positions of M_2 and M_3 within specific P - T ranges (marked by rectangular boxes) were deduced from the combination of conventional P - T calculations and X_{Py} isopleths of garnet which was superimposed in the figure. The M_4 represent the granulite-amphibolite transitional facies. The green dashed-line represents the hornblende (Hbl)-out line.

Table 2: Summary of textural and geochronological data of the studied samples

Sample name	GPS coordinates	Mineralogy	Textural features	Additional information	$^{207}\text{Pb}/^{206}\text{Pb}$ SHRIMP Age	U-Th-total Pb EPMA Age
Charnockitic augen gneiss (sample BP1)	19°51.579' N 83°09.063' E	Opx-Kfs-Qz- Grt-Bt-Pl-Ilm	Porphyroblastic assemblage of Opx-Kfs-Qz-Grt represents peak metamorphic assemblage whereas development of coronal Grt+Qz intergrowth represents subsequent cooling event. Bt formed during the rehydration event.	Not available.	942 ± 11 Ma - Age of granulite facies metamorphism. A spot age of 773 ± 22Ma - Age of decompression.	948 ± 6 Ma - Age of granulite facies metamorphism. 772 ± 13 Ma - Age of decompression. Two apparent peaks at ~840 Ma and ~910 Ma - Probably discrete geological events or mixed ages.
Charnockitic augen gneiss (sample BP3)	19°51.499' N 83°10.298' E	Opx-Qz-Kfs- Grt-Pl-Bt-Ilm	Peak metamorphic assemblage is characterized by Opx-Kfs-Qz-Grt. Coronal Grt+Qz intergrowth represents cooling. Perthitic texture observed. Porphyroblastic Grt decompressed to produce Opx+Pl. Bt is a product of rehydration.	Not available.	951 ± 10 Ma - Age of granulite facies metamorphism. One spot age at 1034 ± 16 Ma -Age of UHT metamorphism (?). A spot age of 841 ± 21 - Age of decompression. One spot age of 884 ± 21 Ma - Mixed age.	Not available.

Table 2 continued

Sample name	GPS coordinates	Mineralogy	Textural features	Additional information	$^{207}\text{Pb}/^{206}\text{Pb}$ SHRIMP Age	U-Th-total Pb EPMA Age
Charnockitic augen gneiss (sample BP2)	19°49.907' N 83°06.405' E	Opx-Kfs-Qz-Pl- Ilm-Grt	Dominant texture is granoblastic. Porphyroclasts of Opx and Pl also noticed.	Highly deformed due to shearing. Refinement of grain size occurred.	928 ± 26 Ma - Age of granulite facies metamorphism.	Not available.
Mafic granulite (sample BP12B)	19°46.918' N 82°44.155' E	Opx-Cpx-Pl-Grt- Ilm-Hbl-Bt±Qz	Inclusion of relict Hbl ₁ present within Grt. Opx ₁ -Cpx-Pl ₁ -Grt represent peak metamorphic assemblage. Hbl ₂ -Bt is product of post peak cooling and rehydration. Symplectite intergrowth of Opx ₂ and Pl ₂ around Grt developed due to destabilization of Grt during decompression.	Granulite facies <i>P-T</i> estimated as: T= ~900 C ₀ and P= ~11-10 kbar. Near- isothermal decompression <i>P-</i> T estimated as: T= ~825 C and P= ~7.5 kbar.	Single population weighted mean age of 521 ± 16 Ma	No monazite grains found from two thin sections.

Table 2 *continued*

Sample name	GPS coordinates	Mineralogy	Textural features	Additional information	$^{207}\text{Pb}/^{206}\text{Pb}$ SHRIMP Age	U-Th-total Pb EPMA Age
Mafic granulite (sample BP4)	19°49.224' N 82°52.533' E	Opx-Cpx-Pl-Grt- Ilm-Hbl-Qz	Porphyroblastic texture composed of Pl and Grt whereas coronal Grt+Qz intergrowth also reported, which probably represent a cooling event.	Evidence of dynamic recrystallization by preserving curved grain boundaries is seen.	Spot ages ranging in between 2468 ± 7 Ma and 2915 ± 4 Ma - Protolith ages.	Not available.
Aluminous granulite (sample BP12A)	19°46.645' N 82°44.15' E	Grt-Sil-Qz-Hem- Ilm-Mag-Zrn	Porphyroblastic Grt is documented, where the core contains an intergrowth of Grt-Sil-Qz-Ilm. The fine grained matrix of Qz, Sil and hemo-ilmenite show a foliation. Coarser Sil transforming to Fi along its both end. Exsolution lamellae of Ti-rich phase found within hemo-ilmenite.	Purely potash-free bulk indicates that the metamorphic condition during the peak was K-feldspar invariant, or partial melts were completely lost.	Spot age of 505 ± 32 Ma - Age of granulite-amphibolite facies transitional metamorphism.	519 ± 5 Ma - Age of granulite-amphibolite facies transitional metamorphism.

Table 2 continued

Sample name	GPS coordinates	Mineralogy	Textural features	Additional information	$^{207}\text{Pb}/^{206}\text{Pb}$ SHRIMP Age	U-Th-total Pb EPMA Age
Aluminous granulite (sample BP12C)	19°46.943' N 82°43.827' E	Grt-Sil-Qz-Hem-Porphyroclastic Grt Ilm-Mag-Zrn	observed. Highly sheared variety. Grt and Sil shares straight boundary between them. Sil, Qz, Ilm shows a foliation parallel growth.	Presence of both magnetite and hematite indicates oxygen fugacity was close to the HM buffer. Inclusion of Fe present within the Zrn.	Single population weighted mean age of 532 ± 21 Ma - Age of granulite-amphibolite facies transitional metamorphism.	524 ± 5 Ma - Age of granulite-amphibolite facies transitional metamorphism. ~ 800 Ma - Age of decompression. Two spot ages at 928 ± 41 Ma and 913 ± 31 Ma - Age of granulite metamorphism. One spot age as 891 ± 57 Ma - Mixed age.
Meta-ironstone (sample DG33E)	19°46.75' N 82°44.15' E	Mag-Hem-Grt-Sp1-Qz	The granoblastic texture is characterised by porphyroblastic Mag and Grt. Hematite is replacing the magnetite grains along the intragranular fracture planes. Grt is often surrounded by Qz.	Not available	Single population weighted mean age of 521 ± 18 Ma	Single population weighted mean age of 499 ± 5 Ma

Table 2 continued

Sample name	GPS coordinates	Mineralogy	Textural features	Additional information	$^{207}\text{Pb}/^{206}\text{Pb}$ SHRIMP Age	U-Th-total Pb EPMA Age
Migmatitic hornblende gneiss (sample DG33F)	19°46.74' N 82°43.68' E	Hbl-Cpx-Pl- Opx-Qz-Kfs- Hem-Ilm-Grt	Mafic layer is defined by the equilibrium texture between Hbl and Cpx. Appearance of Opx on Hbl also documented in the mafic layer. Formation of Grt+Qz in expense of Cpx+Pl in the felsic layer.	Formation of Opx from Hbl marks the progradation from amphibolite facies to amphibolite-granulite transitional facies during thrusting of "hot" EGB on "cold" BC.	Discordia line on concordia diagram define upper-intercept age as 2425 ± 32 Ma and lower-intercept age as 545 ± 34 Ma.	-
Foliated quartz breccia (sample DG17B)	19°54.97' N 82°41.44' E	Qz-Kln-Kfs- Mnz-Zrn	Highly angular and poorly sorted Qz. Interstitial space between the larger Qz is either filled by Kln matrix. Inclusion of Kfs documented in Qz.	Immature clastic sedimentary rock deposited in an incipient basin between the larger Qz is developed adjacent to the thrust-front.	Detrital Zrn supplied from multiple provenance of ~530 Ma, dominant age cluster is of 509 ± 4 Ma. Other age peaks at ~2100-850 Ma and between ~2100-3200 Ma ages. Maximum depositional age for sedimentation was $484 \pm 10 - 18$ Ma.	Weighted mean age of most Ma, ~1350 Ma, ~930 Ma and ~700 Ma.

*Minerals abbreviation are used as prescribed by Whitney and Evans (2010).

Table 3: Representative mineral compositions of the studied rocks

Rock type Sample number	Mafic granulite BP12B																	
	Grt			Opx			Cpx			Pl								
Minerals	Por-C	Por-R	Por-R	Por-C	Por-R	Sym	Sym	Por-C	Por-R	Por-R	Por-R	Por-C	Por-R	Sym	Sym			
Texture																		
Wt%																		
SiO ₂	38.77	38.62	38.03	38.53	50.78	50.62	50.15	51.49	49.48	51.37	50.76	51.89	48.89	54.67	45.48	50.65	44.86	50.79
TiO ₂	0.12	0.11	0.09	0.06	0.08	0.087	0.07	0.07	0.37	0.32	0.26	0.16	0.00	0.03	0.01	0.03	0.02	0.00
Al ₂ O ₃	21.48	21.51	21.15	21.32	1.35	0.837	1.21	1.42	3.37	2.55	2.34	2.04	32.32	28.36	34.23	31.22	34.99	31.26
Cr ₂ O ₃	0.01	0.00	0.03	0.01	0.02	0.016	0.00	0.07	0.03	0.02	0.00	0.03	0.00	0.00	0.00	0.00	0.00	0.00
FeO	25.94	24.97	28.41	27.72	30.39	30.33	31.83	29.93	13.57	12.58	14.62	12.34	0.21	0.189	0.41	0.39	0.65	0.66
MnO	0.70	0.71	1.49	1.82	0.58	0.588	0.55	0.63	0.23	0.23	0.19	0.24	0.01	0	0.00	0.02	0.00	0.00
MgO	4.48	5.35	3.13	4.74	16.51	16.47	15.02	17.04	10.13	11.54	11.12	11.99	0.01	0.006	0.00	0.00	0.01	0.00
CaO	8.73	9.03	7.72	6.36	0.78	0.585	0.71	0.54	21.95	21.95	20.43	21.98	15.77	11.23	17.91	13.95	18.52	14.76
Na ₂ O					0.02	0	0.00	0.00	0.31	0.43	0.28	0.37	2.46	5.287	1.36	3.33	1.04	3.32
K ₂ O	0.03	0.01	0.00	0.01	0.00	0	0.00	0.02	0.00	0.00	0.00	0.00	0.17	0.099	0.07	0.06	0.03	0.08
Total	100.3	100.3	100.04	100.56	100.52	99.53	99.54	101.20	99.43	100.98	100.02	101.03	99.84	99.87	99.46	99.65	100.12	100.86
Oxygen	12	12	12	12	6	6	6	6	6	6	6	6	8	8	8	8	8	8
Si	3.02	3.00	3.01	3.01	1.96	1.97	1.97	1.97	1.90	1.93	1.94	1.95	2.24	2.47	2.11	2.31	2.07	2.30
Ti	0.01	0.01	0.01	0.00	0.00	0.00	0.00	0.00	0.01	0.01	0.01	0.00	0.00	0.00	0.00	0.00	0.00	0.00
Al	1.97	1.97	1.97	1.97	0.06	0.04	0.06	0.06	0.15	0.11	0.11	0.09	1.75	1.51	1.87	1.68	1.91	1.67
Cr	0.00	0.00	0.00	0.00	0.00	0.00	0.00	0.00	0.00	0.00	0.00	0.00	0.00	0.00	0.00	0.00	0.00	0.00
Fe	1.69	1.62	1.88	1.81	0.98	0.99	1.05	0.96	0.44	0.40	0.47	0.39	0.01	0.01	0.02	0.01	0.02	0.02
Mn	0.05	0.05	0.10	0.12	0.02	0.02	0.02	0.02	0.01	0.01	0.01	0.01	0.00	0.00	0.00	0.00	0.00	0.00
Mg	0.52	0.62	0.37	0.55	0.95	0.96	0.88	0.97	0.58	0.65	0.63	0.67	0.00	0.00	0.00	0.00	0.00	0.00
Ca	0.73	0.75	0.65	0.53	0.03	0.02	0.03	0.02	0.90	0.88	0.84	0.88	0.77	0.54	0.89	0.68	0.92	0.72
Na	0.00	0.00	0.00	0.00	0.00	0.00	0.00	0.00	0.02	0.03	0.02	0.03	0.22	0.46	0.12	0.30	0.09	0.29
K	0.00	0.00	0.00	0.00	0.00	0.00	0.00	0.00	0.00	0.00	0.00	0.00	0.01	0.01	0.00	0.00	0.00	0.00
Total	7.99	8.01	8.00	8.00	4.01	4.00	4.00	4.00	4.02	4.02	4.01	4.02	5.00	5.01	5.02	4.99	5.02	5.01
X _{Mg}	0.24	0.28	0.16	0.23	0.49	0.49	0.46	0.50	0.57	0.62	0.58	0.63						

Table 3 continued

Rock type		Migmatitic hornblende gneiss															
Sample		DG33F															
Minerals	Texture	Grt		Opx		Cpx			Pl			Hbl					
		C	R	Por-C	Por-R	Por-C	Por-R	Inc-R	Inc-C	M-C	M-R	F-C	F-R	C	R		
Wt%																	
SiO ₂		37.30	37.14	49.28	49.28	50.43	51.41	49.14	48.67	58.27	58.16	58.01	57.90	39.75	40.85		
TiO ₂		0.00	0.02	0.09	0.09	0.33	0.19	0.08	0.09	0.00	0.00	0.02	0.03	2.52	2.55		
Al ₂ O ₃		19.63	20.08	0.74	0.73	1.90	1.49	1.51	1.90	25.60	25.23	26.45	25.99	11.13	10.90		
Cr ₂ O ₃		0.04	0.01	0.06	0.03	0.06	0.00	0.05	0.04	0.00	0.00	0.00	0.00	0.06	0.07		
FeO		30.82	29.63	34.84	34.66	15.74	15.84	20.65	21.66	0.14	0.27	0.20	0.30	20.48	20.33		
MnO		1.59	1.61	0.82	0.78	0.45	0.38	0.32	0.33	0.05	0.00	0.00	0.00	0.15	0.22		
MgO		1.27	1.40	12.68	12.89	9.49	9.86	6.30	5.90	0.00	0.00	0.00	0.00	7.53	7.80		
CaO		9.38	9.32	0.87	0.80	21.00	21.14	20.56	20.39	7.31	7.58	8.64	8.43	11.10	11.01		
Na ₂ O				0.02	0.00	0.45	0.41	0.36	0.40	6.67	6.78	6.22	6.35	1.64	1.52		
K ₂ O				0.01	0.00	0.02	0.00	0.00	0.01	0.59	0.48	0.61	0.54	1.69	1.68		
Total		100.03	99.20	99.40	99.25	99.86	100.71	98.98	99.39	98.62	98.50	100.14	99.54	96.04	96.93		
Oxygen		12	12	6	6	6	6	6	6	8	8	8	8	22	22		
Si		3.02	3.01	1.97	1.97	1.95	1.96	1.96	1.94	2.64	2.64	2.60	2.61	5.93	6.01		
Ti		0.00	0.00	0.00	0.00	0.01	0.01	0.00	0.00	1.37	1.35	0.00	0.00	0.28	0.28		
Al		1.87	1.92	0.04	0.03	0.09	0.07	0.07	0.09	0.00	0.00	1.40	1.38	1.96	1.89		
Cr		0.00	0.00	0.00	0.00	0.00	0.00	0.00	0.00	0.00	0.00	0.00	0.00	0.01	0.01		
Fe ²⁺		2.08	2.01	1.17	1.16	0.51	0.51	0.69	0.72	0.01	0.01	0.01	0.01	2.17	2.08		
Mn		0.11	0.11	0.03	0.03	0.01	0.01	0.01	0.01	0.00	0.00	0.00	0.00	0.02	0.03		
Mg		0.15	0.17	0.76	0.77	0.55	0.56	0.37	0.35	0.00	0.00	0.00	0.00	1.68	1.71		
Ca		0.81	0.81	0.04	0.03	0.87	0.87	0.88	0.87	0.35	0.37	0.41	0.41	1.78	1.74		
Na				0.00	0.00	0.03	0.03	0.03	0.03	0.59	0.60	0.54	0.55	0.47	0.43		
K				0.00	0.00	0.00	0.00	0.00	0.00	0.03	0.03	0.03	0.03	0.32	0.32		
Total		8.05	8.03	4.01	4.01	4.02	4.01	4.02	4.02	4.99	4.99	4.99	4.99	14.62	14.50		
X _{Mg}		0.07	0.08	0.39	0.40	0.52	0.53	0.35	0.33					0.44	0.45		

Table 3 continued

Rock type Sample	Meta-ironstone DG33E				Spl			Aluminous granulite BP12A			
	Por-C	Por-C	Por-M	Por-R	Inc*	Inc"	Inc"	Por-C	Por-C	Por-R	Por-R
Minerals	Grt				Grt			Grt			
Texture	Por-C	Por-C	Por-M	Por-R	Inc*	Inc"	Inc"	Por-C	Por-C	Por-R	Por-R
Wt%											
SiO ₂	38.13	38.13	37.53	38.32				38.10	38.19	38.28	38.05
TiO ₂	0.00	0.02	0.00	0.01	0.039	0.12	0.05	0.01	0.00	0.04	0.03
Al ₂ O ₃	21.11	21.16	20.96	21.64	59.43	57.93	57.26	21.60	21.68	21.77	21.59
Cr ₂ O ₃	0.01	0.00	0.04	0.00	0.201	0.09	0.07	0.02	0.05	0.04	0.01
FeO	33.98	34.01	32.35	34.21	35.5	39.03	38.36	33.38	33.35	31.81	32.54
MnO	0.43	0.42	0.35	0.37	0.022	0.05	0.03	1.39	1.36	1.38	1.32
MgO	5.02	4.70	4.35	4.98	5.91	3.648	4.07	5.29	5.15	5.84	5.50
CaO	1.94	2.60	3.63	1.83				1.43	1.36	1.32	1.27
Total	100.62	101.03	99.20	101.37	101.10	100.86	99.83	101.21	101.13	100.47	100.30
Oxygen	12	12	12	12	4	4	4	12	12	12	12
Si	3.01	3.00	3.00	3.00				2.99	3.00	3.00	3.00
Ti	0.00	0.00	0.00	0.00	0.00	0.00	0.00	0.00	0.00	0.00	0.00
Al	1.97	1.96	1.98	2.00	1.95	1.94	1.93	2.00	2.00	2.01	2.01
Cr	0.00	0.00	0.00	0.00	0.00	0.00	0.00	0.00	0.00	0.00	0.00
Fe	2.24	2.24	2.17	2.24	0.83	0.93	0.92	2.19	2.19	2.09	2.15
Mn	0.03	0.03	0.02	0.02	0.00	0.00	0.00	0.09	0.09	0.09	0.09
Mg	0.59	0.55	0.52	0.58	0.24	0.15	0.17	0.62	0.60	0.68	0.65
Ca	0.16	0.22	0.31	0.15				0.12	0.11	0.11	0.11
Total	8.01	8.01	8.01	8.00	3.02	3.03	3.03	8.01	8.00	7.99	8.00
X _{Mg}	0.21	0.20	0.19	0.21	0.23	0.14	0.16	0.22	0.22	0.25	0.23

Por - Porphyroblastic, Sym- symplectite intergrowth, C- core, R- rim
Inc"- inclusion in magnetite/hematite, Inc*- inclusion in garnet
M- mafic layer, F- felsic layer

Table 4: Whole rock XRF data of mafic granulite (sample BP12B)

SiO ₂	45.33
TiO ₂	1.166
Al ₂ O ₃	14.628
FeO*	15.506
MnO	0.304
MgO	7.042
CaO	10.206
Na ₂ O	2.167
K ₂ O	0.201
P ₂ O ₅	0.171
H ₂ O	0.25
Total	96.971

FeO*= recalculated from measured Fe₂O₃

Chapter 6:

GEOCHRONOLOGICAL DATA

The geochronological investigations were carried out using zircon U-Pb systematics by SHRIMP IIe and monazite U-Th-total Pb systematics by EPMA. The geochronological data of individual rock are summarized in table 2.

6.1 Zircon U-Pb SHRIMP IIe data

Seven different rocks were analyzed in SHRIMP IIe after separating zircon grains. Analytical data of the individual samples are presented in Table 5.

6.1.1 Charnockitic augen gneiss

Samples BP1

Total forty-three points were measured from out the thirty-eight zircon grains separated this sample. Most of the grains were oval shaped with aspect ratio ~2: 1 (length ~100 μm and breadth ~50 μm). The SEM-CL images revealed that most of the grains preserved a dark oscillatory zoned core which were surrounded by brighter oscillatory zoned or homogenous rim (Fig. 12a). However, few grains exhibited sector zoning [Fig. 12a(II)]. The U and Th contents from analyzed spots varied widely from 141 to 1564 ppm and from 61 to 598 ppm, respectively (Table 5). The Th/U ratio ranged between 0.10 and 1.93 (Table 5), and the Th/U vs. age plot ($^{207}\text{Pb}/^{206}\text{Pb}$ near-concordant age) did

not reveal any pattern (Fig. 12b). All the analyzed on the Tera-Wasserburg diagram (Fig. 12c) defined a discordia line with 1514 ± 180 Ma as the upper intercept and 877 ± 34 Ma as the lower intercept (MSWD = 3.1). MSWD was high because of the wide scatter of data points near the lower intercept, whereas the upper intercept yielded large error due to lack of data-points near the upper intercept. The concordia diagram was rescaled between 1100–700 Ma using the same data-set, which exhibited that core of the zircon grains ranged between approximately 990 and 850 Ma, whereas the overgrown rims were relatively well-constrained and ranged between ~950 and ~900 Ma (Fig. 12d). In few occasions, the cores yielded younger ages than the rims as they were subsequently reset in response to the younger thermal event(s) during the formation of the ~950–900 Ma rim. A single spot date of 773 ± 22 Ma ($^{207}\text{Pb}/^{206}\text{Pb}$ date with 98% concordance, Th/U = 0.45) was recorded from the dark-CL core of a grain [Fig. 12a(I)].

Sample BP3

Thirty-four points were analyzed from twenty-four zircon grains of this sample. The grains were oval in shape, with varying length and width ranging in between ~100 and 300 μm and ~50 and 100 μm , respectively (Fig. 13a). The SEM-CL images revealed that a few grains contained dark core which were surrounded by bright overgrowth (Fig. 13a), whereas some grains preserved the thin luminous overgrowth along the rim. The grains were mostly chaotically zoned and occasionally preserved homogenous dark core. Oscillatory-zoned zircon grains were rare. The U and Th contents from the analyzed spots ranged

widely between 44 and 1771 ppm, and 63 and 356 ppm, respectively.

Consequently, the Th/U ratios also varied extensively (0.08–1.88; Table 5). No pattern emerged from Th/U vs. age plots ($^{207}\text{Pb}/^{206}\text{Pb}$ near-concordant age; Fig. 13b). All the analyzed data were plotted on a Tera-Wasserburg diagram [Fig. 13c(I)]. Eighteen spots, analyzed from both core and rim, yielded near-concordant data, which formed a single-population age cluster with a weighted average mean age as 951 ± 10 Ma [$^{207}\text{Pb}/^{206}\text{Pb}$ age, $n = 15$, $\text{MSWD} = 1.8$; Fig. 13c(II)]. Two spots yielded younger $^{207}\text{Pb}/^{206}\text{Pb}$ dates as 884 ± 21 and 841 ± 21 Ma, while an older spot date as 1034 ± 16 Ma was also reported.

Sample BP2

Twenty-three zircon grains from this sample were measured. Most of the grains were oval in shape. The SEM-CL images revealed that the grains were irregularly and patchy zoned. Occasionally, the very thin overgrowth along the rim was observed (Fig. 14a). The aspect ratios of the grains were $\sim 2:1$ (~ 200 μm in length and ~ 100 μm in width; Fig. 14a). The U and Th contents varied from 36 to 233 ppm and from 56 to 433 ppm, respectively (Table 5). The Th/U ratios ranged in between 0.8 and 2.7 (Table 5). Th/U vs. age data ($^{207}\text{Pb}/^{206}\text{Pb}$ near-concordant age) were plotted in figure 14b, which did not show any correlation between the associated thermal event(s) and ratio. Only nine near-concordant data-points were obtained from the thirty-seven analyzed points. The Tera-Wasserburg plot of all the data-points exhibited a small spread along the concordia line [Fig. 14c(I)]. The weighted average mean age from the

overgrowth domain yielded the single-population age as 928 ± 26 Ma [$^{207}\text{Pb}/^{206}\text{Pb}$ age, $n = 9$, MSWD = 0.70; Fig. 14c(II)].

6.1.2 Mafic granulite

Sample BP12B

The majority of the zircon grains were rounded in shape with a diameter about ~ 50 μm . Occasionally, inclusions of orthopyroxene were found within the zircon grains. The dark homogenous to patchy zoned cores were surrounded by a thin homogenous but luminous-CL rim (Fig. 15a) in most of the grains.

Unfortunately, such overgrown rims, in most of the cases, were too thin to be measured using the SHRIMP. The elongated and irregular shaped zircon grains were rarely observed. U and Th contents varied between 681–144 ppm and 138–33 ppm, respectively with Th/U ratio in the range 0.38–0.1 (Table 5). Total twenty-one points were analyzed from fifteen zircon grains. The Tera-Wasserburg plot of all data points yielded a single age group on concordia line [Fig. 15b(I)]. Single population weighted mean age was calculated from the eight near-concordant data points as 521 ± 16 Ma [$n = 8$, MSWD = 0.34 and probability = 0.93; Fig. 15b(II)]. From the core to rim, the spot dates did not vary significantly (Fig. 15a).

Sample BP4

Thirty-three points from twenty zircon grains were measured from this sample. All the grains were oval in shape, with length and width of ~ 150 – 200 μm and ~ 100 μm , respectively. Most of the grains exhibited homogeneous-CL

response. Rarely, core-rim structure was observed. Such grains contained irregular to oscillatory-zoned core which were surrounded by either oscillatory-zoned or homogenous overgrowth (Fig. 15c). U (75–3385 ppm) and Th (72–446 ppm) varied widely (Table 5). Th/U ratios ranged between 2.382 and 0.132 (Table 5). Twenty-six data-points were observed as near-concordant, from thirty-three analyzed points. The Tera-Wasserburg plot showed that the majority of the analyzed data-point were distributed on the concordia line near the upper intercept (Fig. 15d). The youngest spot $^{207}\text{Pb}/^{206}\text{Pb}$ date was 2468 ± 7 Ma, whereas the oldest spot $^{207}\text{Pb}/^{206}\text{Pb}$ date was 2915 ± 4 Ma.

6.1.3 Aluminous granulite

Sample BP12A

Total sixteen points were measured on fourteen bulk-separated zircon grains. Most of the grains were very small and irregular-shaped (aspect ratio $\sim 2:1$). Thus, only single analytical point per grain could be measured (Fig. 16a). Rarely, the rounded to sub-rounded grains were observed. The elongated grains were extremely scanty. Such grains had length and width of $\sim 80\text{--}100$ μm and $\sim 30\text{--}50$ μm , respectively. The majority of the grains contained the inclusions of quartz and/or aluminosilicate (Fig. 16a). The SEM-EBSD analysis revealed that the obtained Kikuchi pattern of these included phase of aluminosilicate was best matched with the Kikuchi pattern of the sillimanite (7-9 bands with Mean Angle Deviation $< 1^\circ$; Fig. 16b). The sillimanite of this rock is dominantly fibrous in nature, i.e., fibrolite. Thus, it is logical to consider that these

included aluminosilicates are fibrolite. Similar inclusion within the zircon grains of sample BP12C were also documented. The significance of the inclusion of fibrolite within the zircon grain is discussed later during the interpretation of the age data.

Most of the zircon grains exhibited a dark homogenous CL-response. The SEM-CL images further revealed that rarely grains with brighter core graded outward into a thin darker rim. U content varied in between 370 and 218 ppm, whereas Th content was low (5–1 ppm) (Table 5). Th/U ranged between 0.01 and 0.02. The Tera-Wasserburg concordia plot of all the data exhibited the single-population $^{238}\text{U}/^{206}\text{Pb}$ age distribution (Fig. 16c). Only one $^{207}\text{Pb}/^{206}\text{Pb}$ spot date of 505 ± 32 Ma retrieved as near-concordant (concordance 105%, Th/U = 0.02) from a tiny and rounded zircon grain with homogenous CL-response (16a).

Sample BP12C

Sixteen zircon grains were extracted from this variety of aluminous granulite. Morphologically, most of the grains were oval to rounded in shape where the diameter was varying from ~50 to ~30 μm (Fig. 16d). Inclusions of sillimanite (fibrolite) (Fig. 16d and 16e) and/or quartz were present within most of the zircon grains. The majority of the grains had homogenous and uniform CL response. The SEM-CL images revealed that thin homogenous overgrowth mantled the core of few grains. CL images further revealed that the boundary between the core and rim was corroded. However, these overgrowths are too thin to allow dating using the SHRIMP. It was rarely observed that few grains

exhibit patchy, sector zoning pattern (Fig. 16d). U and Th contents ranged between 1122–201 ppm and 32–2 ppm, respectively. Th/U ratio was consistent in a range between 0.05–0.01 (Table 5). Out of eighteen analyzed points, six near-concordant data-points were retrieved and only these data were considered for the statistical age interpretations. All the data plotted on the Tera-Wasserburg concordia diagram reflected a single age-population [Fig. 16f(I)]. The single population weighted mean age was calculated as 532 ± 21 Ma from these near-concordant age data [$n = 6$, MSWD = 0.56 and probability = 0.73; Fig. 16f(II)].

6.1.4 Meta-ironstone

Zircon grains of this rock morphologically varied from irregular to sub-rounded, and rarely tabular. The aspect ratios of irregular grains were diverse (~2:1–3:1). The sub-rounded grains had a diameter of $\sim 50\mu\text{m}$, while tabular grains were larger ($\sim 150 \times 75 \mu\text{m}$) compared to irregular and sub-rounded grains (Fig. 17a). The majority of the grains exhibited homogenous dark-CL response. The SEM-CL images further documented that rarely grains preserved luminous patchy core which was mantled by a darker rim (Fig. 17a). U and Th contents were 799–494 ppm for U and 94–85 ppm for Th. Th/U ratios varied between 0.11 and 0.18 (Table 5). Only one point per grain was measured for U-Pb dating. Out of the thirteen zircon grains, total thirteen points were analyzed. All the thirteen data-points on the Tera-Wasserburg diagram defined a continuous spread of age data between ~ 560 and ~ 480 Ma [Fig. 17b(I)]. Out of

the thirteen data-points, ten near-concordant data points yielded a single-population weighted age as 521 ± 18 Ma [$n = 10$, MSWD = 0.76; Fig. 17b(II)].

6.1.5 Migmatitic hornblende gneiss

Total sixty-nine points were measured from thirty-nine zircon grains. The majority of the grains were observed as euhedral, subhedral and tabular in shape, and their size varied in length (~ 150 – 200 μm) and width (~ 50 – 100 μm). The cores of these grains commonly exhibited homogeneous dark-CL response, which graded outward into a relatively luminous rim (Fig. 18a). The SEM-CL images further revealed that the boundary between core and rim was, occasionally, corroded. Some zircon grains preserved the xenocrystic cores rarely, which were surrounded by an oscillatory zoned overgrown rim. The irregularly shaped grains of varying sizes exhibited chaotic and convolute zoning pattern (Fig. 18a). U content ranged widely from 75 to 1243 ppm, whereas Th content varied between 26 and 435 ppm. Consequently, the Th/U ratio also varied drastically between 1.1–0.11 (Table 5). All data points were plotted on the Tera-Wasserburg concordia diagram, which yielded a discordia line with 2425 ± 32 Ma as upper intercept and 545 ± 34 Ma as lower intercept (MSWD = 0.25; Fig. 18b). Probability density diagram all the concordant data ($n = 12$) shows two dominant $^{207}\text{Pb}/^{206}\text{Pb}$ age-peaks at ~ 2400 Ma ($n = 10$) and ~ 570 Ma ($n = 2$; Fig. 18c). This ~ 550 Ma age was recorded from the homogenous bright-CL rim. It was observed that the boundary between the core and rim was corroded (Fig. 18a).

6.1.6 Migmatitic quartzofeldspathic gneiss

Thirty points were measured from twenty-one bulk-separated zircon grains from this sample. All the grains were oval shaped with length and width varying from ~200 to ~250 μm and from ~80 to ~100 μm , respectively. Most of the grains showed the core-rim structure (Fig. 19a). The SEM-CL images revealed that the homogeneous and oscillatory-zoned bright core was rimmed by dark homogenous (sometimes oscillatory-zoned; Fig. 19a) mantle and/or rim. The U content of the grains varied between 3664 ppm and 75 ppm. Th content ranged between 66 and 1553 ppm (Table 5). Th/U ratio varied between 0.06 and 0.88 (Table 5). Out of thirty analyzed points, twelve data-points were found to be near-concordant where the spot dates ranged between 2345 ± 4 and 2515 ± 11 Ma. All the analyzed points plotted on the Tera-Wasserburg concordia diagram defined the discordia line with the upper intercept at 2448 ± 19 Ma ($n = 11$) and lower intercept at 560 ± 19 Ma ($n = 1$; MSWD = 1.7; Fig. 19b). The dark-CL rim of a single grain yielded the spot date of 525 ± 9 Ma ($^{207}\text{Pb}/^{206}\text{Pb}$ date with 102% concordance), whereas the brighter core of the same grain yielded the spot date of 2487 ± 5 Ma ($^{207}\text{Pb}/^{206}\text{Pb}$ date with 98% concordance).

6.1.7 Foliated quartz breccia

The detrital zircon grains with diverse morphological varieties were recorded from this sample. The zircon grains were observed to be oval and sub-rounded in shape. The prismatic, euhedral, as well as, irregularly shaped zircon

grains were rarely seen (Fig. 20a). The aspect ratios of the majority of the grains were ~2:1 (~100 × ~50 μm). The zoning patterns of these detrital zircon grains were also diverse. The SEM-CL images revealed that most of the grains preserved the oscillatory zoned brighter core, which was mantled by the darker-CL rim (Fig. 20a). The zircon grains occasionally preserved xenocrystic core which emitted dark-CL signals. The complex growth zoning and homogenous CL-response were rarely documented (Fig. 20a). U and Th contents of the individual zircon grains varied widely (1390–70 ppm for U and 753–22 ppm for Th). Hence, Th/U ranged extensively between 0.02 and 1.45 (Table 5). The total sixty-two points were analyzed from thirty-two zircon grains. All the measured data points plotted on the Tera-Wasserburg concordia diagram exhibited the wide scatter of age data on the concordia line, especially from ~3200–2100 Ma and ~850–500 Ma (Fig. 20b). Thus, the upper intercept and lower intercepts of the discordia line could not be determined precisely, which made it difficult to construct a meaningful discordia line. All the near-concordant data (n = 28; 90–110% concordance) on the probability density diagram unveiled the multiple age-peaks at ~530 Ma (n = 2), ~850 Ma (n = 2) and between ~3200–2100 Ma (n = 24; Fig. 20c). The Neoproterozoic ages were recorded from the rim having homogenous CL-response (Fig. 20a).

Varying degrees of reverse discordance in U-Pb zircon dates were reported from the two samples of aluminous granulite (sample BP12A and BP12C) and one sample of mafic granulite (sample BP12B). The reports of

reverse discordance during zircon analyses are widespread in the published literatures (Kelly and Harley, 2005; Kusiak et al., 2013 and references therein). There are several reasons for the generation of reverse discordant age data. The reverse discordance can be caused by local unsupported radiogenic Pb gain (Williams et al., 1984; Compston, 1999), compositional artefacts (Wiedenbeck, 1995), or by matrix sputtering effects due to differential ion yield of the zircon mounts (McLaren et al., 1994; Black et al., 1986). In this study, differential ion yield of the zircon mounts can be ruled out as both unknown and standard zircon grains were placed in the same mount. Hence, the matrix sputtering effect was not responsible for the reverse discordance. The possibility of common Pb contamination for reverse discordance is eliminated due to the absence of high ^{204}Pb count during the analyses. Radiogenic Pb can be accommodated within the partially metamictized zircon domains (Mezger and Krogstad, 1997; Geisler et al., 2003). Mobilization of such excess radiogenic Pb can be facilitated from the metamictized domain either by fluids or through annealing at elevated temperatures, whereas unmetamictized part witnessed no Pb movement (Mezger and Krogstad, 1997). Kusiak et al. (2013) demonstrated that concentration of radiogenic Pb in micro-domains produces spuriously older dates, which validated the micron-scale Pb disturbance. Similar indicators of micron-scale radiogenic Pb disturbance have been documented in other studies (Compston, 1999; McFarlane et al., 2006). On the other hand, the ingress of aqueous fluid at granulite-amphibolite transitional facies can disturb the intragranular isotopic system by enhancing the Pb diffusion, which can cause

normal and reverse discordance (Carson et al., 2002). Thus, in this study, the possibility of micron-scale redistribution of radiogenic Pb for the reverse discordance seems to be the most suitable explanation.

6.2 Monazite U-Th-total Pb EPMA data

In-situ monazite grains from five different rock types were analyzed in EPMA by U-Th-total Pb systematics. Analytical data of these rock samples are presented in Table 6.

6.2.1 Charnockitic augen gneiss

Eight monazite grains from the thin section were selected, and the total of sixty-one spots were analyzed from the core, mantle, and rim regions (Table 6). The grains were morphologically oval to rounded in shape with the aspect ratio of ~3:1 (~100 μm in length and ~30 μm in width). The majority of the grains exhibited compositional zoning between core and rim, where the dark-BSI core was surrounded by brighter rim (Figs. 21a and 21c). Compositionally homogenous grains were rare. The spot dates varied between 689 ± 20 and 984 ± 27 Ma. The oldest date of 984 ± 27 Ma was recorded from the dark-BSI core, whereas the youngest date of 689 ± 20 Ma was measured from the brighter rim. A representative grain (grain 17; Table 6) was chosen as it exhibited compositional zoning (Fig. 21a) and preserved multiple age-peaks. The grain was observed to present as the inclusion within the plagioclase outside the porphyroblastic garnet. The brighter rim yielded the youngest spot date of 723

± 21 Ma, but the darker core and mantle exhibited the oldest pool age as ~ 940 Ma. Another representative grain was found as the inclusion within the porphyroblastic garnet (Fig. 21b), which yielded the pool age of ~ 950 Ma (Fig. 21c). Two dominant pool ages of 772 ± 13 Ma ($n = 13$, MSWD = 4.1; Fig. 21d) and 950 ± 6 Ma ($n = 14$, MSWD = 0.46; Fig. 21e) were obtained from all the analyzed points. Apart from these age-peaks, two age-peaks at ~ 840 and ~ 910 Ma were also yielded.

6.2.2 Aluminous granulite

Sample BP12A

Three in-situ monazite grains were selected from the thin section of this rock. Two of them were ~ 15 μm in length and ~ 10 μm in width and occur as the inclusions within the garnet. The other grain was larger, with a diameter of about 30 μm , and occurred as the inclusion within the quartz in the matrix of the rock (Fig. 22a). A total of eleven points were analyzed from these three grains (Table 6). The SEM-BSI image of the larger monazite grain (grain 3; Table 6) revealed compositional zoning which was confirmed with the U-Th-Y X-ray maps (Fig. 22b). The grain was compositionally homogenous in terms of the Y and U distribution. However, enrichment of Th occurs along the rim compared to the homogenous core. In figure 22c, the representative grain exhibits variable spot dates. The single-population weighted mean age was calculated as 519 ± 5 Ma ($n = 11$, MSWD = 2.7; Fig. 22d), although the spot dates ranged between 510 ± 8 and 534 ± 10 Ma.

Sample BP12C

The monazite grains were more abundant in the variety of aluminous granulite. The seven monazite grains were mapped for U, Th, and Y distributions before the geochronological analysis. The total of forty-two points within these grains were analyzed according to the zoning pattern and U, Th, and Y distributions (Table 6). The monazite grains had the varying length (~20 to 100 μm) and width (~10 to 35 μm). Most of these grains were subhedral and elliptical in shape, but the irregularly shaped grain was also observed. The monazite grains from the matrix, as well as, the grains enclosed within the peripheral regions of garnet, were selected. Some of these garnet porphyroblasts preserved the included minerals, such as quartz, in between the interior and the exterior zones. No zoning in terms of U and Y concentration was observed in the matrix monazite grains. On the other hand, the included monazite grains at the rim of garnet (grain 1; Fig. 23a) exhibited elemental zoning in terms of Th and Y distribution [Fig. 23b(I-III)], possibly due to elemental redistribution with the host garnet which was a source for the Y enrichment during the breakdown of garnet. One of such representative monazite grain preserved Y-rich zone which was poor in Th content. However, the rest of the grain shows homogenous Y and Th distribution [Fig. 23b(III)]. Six points were analyzed on that grain, where the spot dates ranged between 512 ± 15 and 797 ± 41 Ma (Fig. 23c). The latter (oldest) date was acquired from the high-Y rich region, whereas the rest of the grain (homogenous in terms of low-Y content) recorded dates as ~ 520 Ma. Another included monazite grain yielded a spot date of 745 ± 43 Ma,

with three older spot dates of 891 ± 57 , 913 ± 31 and 928 ± 41 Ma. The dominant single-population weighted average age recorded from the rock as 524 ± 5 Ma ($n = 37$, MSWD = 1.6; Fig. 23d), which is similar to that of the other aluminous granulite (sample BP12A). The age spectrum recorded from this rock is shown in figure 23e.

6.2.3 Meta-ironstone

Eight in-situ monazite grains were selected from the thin-section for geochronological analysis. The grains were small in size ($\sim 10 \times 5 \mu\text{m}$) and highly irregular in shape (Fig. 24a). The majority of the grains were homogeneous in terms of the zoning pattern as revealed by the SEM-BSI images. However, some were observed as zoned grains (Fig. 24a). Most of the monazite grains were found at the boundary of garnet grains or within the garnet grains as inclusion. However, no significant difference in the spot dates were recorded from the individual grains. The spot dates varied between 455 ± 54 Ma and 529 ± 64 Ma. The total twenty-one points were measured from the eight grains, which yielded a single population weighted mean age as 499 ± 5 Ma ($n = 21$, MSWD = 1.11, probability = 0.33). The probability density diagram in figure 24b displays the single age-peak at ~ 500 Ma.

6.2.4 Foliated quartz breccia

Total twenty-eight points were measured from seven grains of the thin-section. Out of seven grains, five irregular shaped grains were small ($\sim 30\text{--}40$

μm in length and $\sim 20\text{--}30\ \mu\text{m}$ in width). Rest of the grains were bigger in size and morphologically elongated (aspect ratio $\sim 2:1$). The SEM-BSI images of the individual grains displayed the distinct compositional zoning (Fig. 24c). Individual spots for age dating were selected according to the different zoning pattern. Textural investigation revealed that the monazite grains were either located within the quartz grain as the inclusion or present within the kaolinitic matrix. The representative monazite grain, which preserved all the age-peaks of the rock, showed that the core yielded the oldest age as $2120 \pm 44\ \text{Ma}$, surrounded by the mantle of $1365 \pm 71\ \text{Ma}$ and then rimmed by a younger $\sim 500\ \text{Ma}$ domain (Fig. 24c). The spot dates varied between $2120 \pm 44\ \text{Ma}$ and $494 \pm 20\ \text{Ma}$. The probability density diagram consist of all the data points exhibits the strongest peak at $\sim 500\ \text{Ma}$ [$n = 23$; Fig. 24d(I)]. The weighted average pool age as $509 \pm 4\ \text{Ma}$ [$n = 23$, MSWD = 1.15, probability = 0.28; Fig. 24d(II)] was calculated from the $\sim 500\ \text{Ma}$ data-points.

6.2.5 Migmatitic quartzofeldspathic gneiss

Seven grains were selected for the in-situ analysis. Total forty-eight points were measured from these seven grains (Table 6). The grains were oval with aspect ratios of $\sim 2:1$ ($\sim 200\ \mu\text{m}$ in length and $\sim 100\ \mu\text{m}$ in width). The measured points were chosen in terms of the different zoning pattern in the SEM-BSI images. However, no major difference in the spot dates was found irrespective of the zoning pattern (e.g., grain 17; Fig. 25a). The spot dates

ranged between 478 ± 23 and 523 ± 8 Ma. All the data represented the single population weighted mean age as 511 ± 3 Ma ($n = 48$, MSWD = 1.9; Fig. 25b).

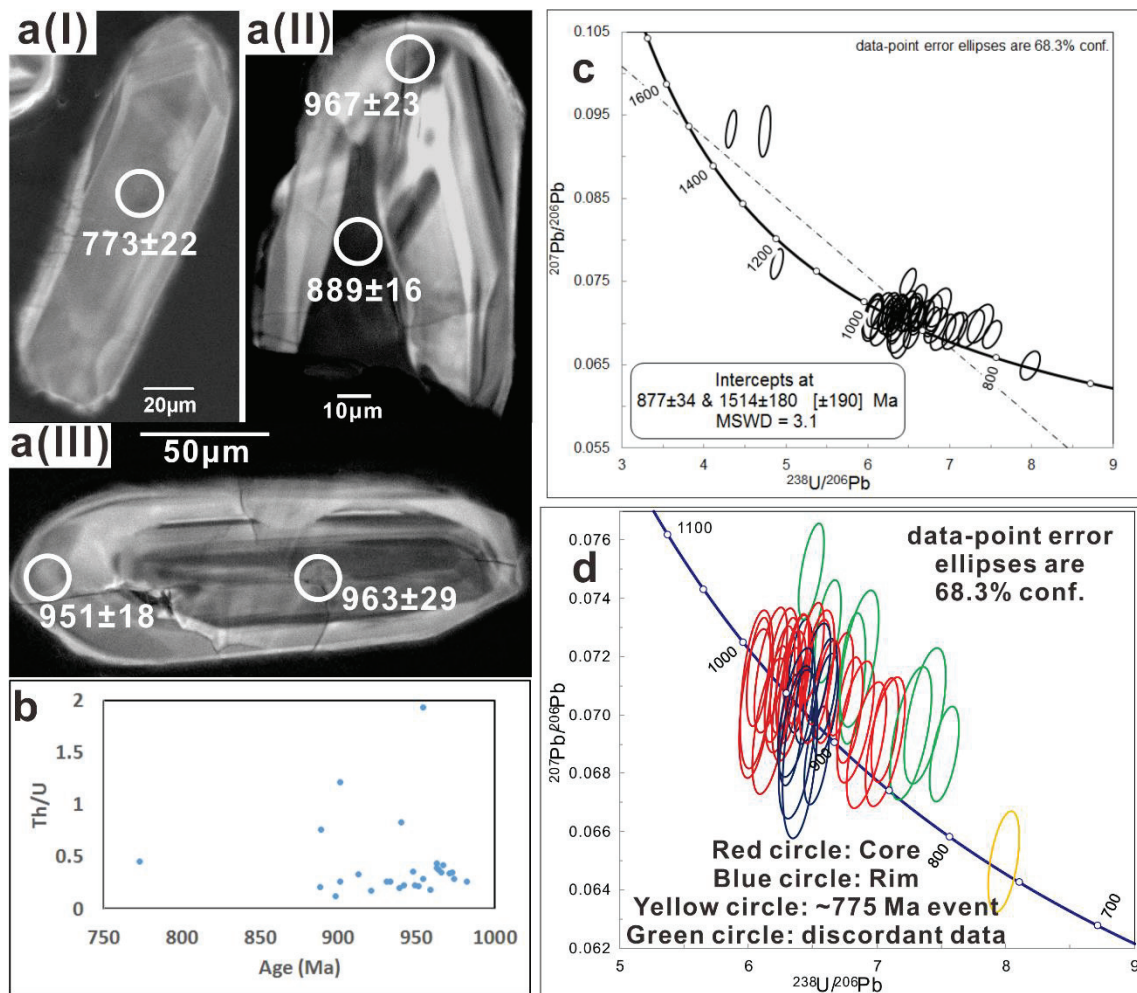


Figure 12: Internal structure of zircon grains and U-Pb SHRIMP analytical plots of the charnockitic augen gneiss (sample BP1). a(I)-a(III) The SEM-CL images of representative zircon grains are exhibiting different zoning pattern with spot date. (b) Th/U vs. age plot ($^{207}\text{Pb}/^{206}\text{Pb}$ near-concordant dates). (c) Tera-Wasserburg Concordia diagram of all analyzed data is showing the age spread between ~ 1500 and 775 Ma. (d) Magnified representation (~ 700 – 1100 Ma) on the concordia diagram is showing the widespread core age along with a well-constrained younger rim.

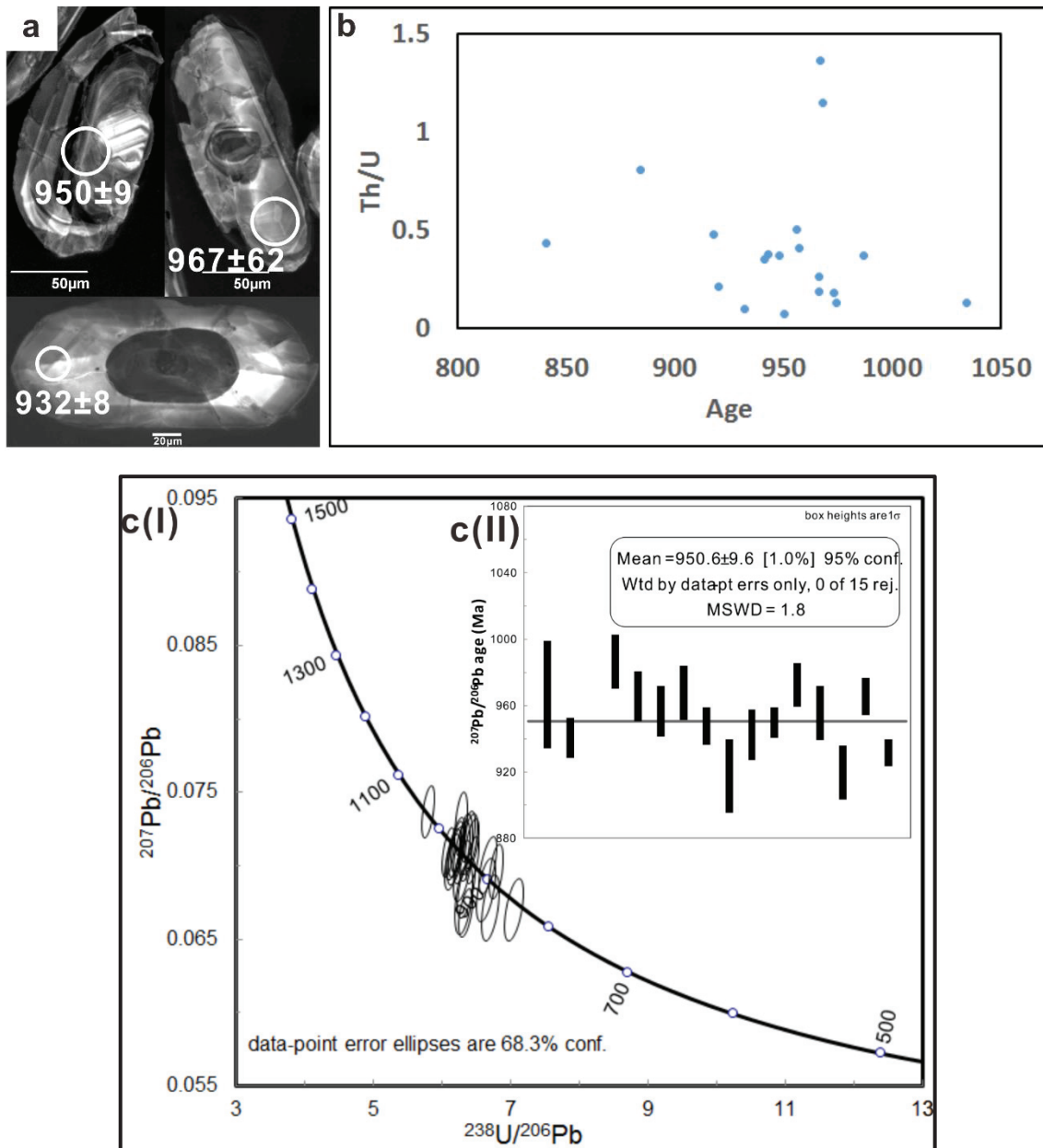


Figure 13: Internal structure of zircon grains and U-Pb SHRIMP analytical plots of the charnockitic augen gneiss (sample BP3). (a) The SEM-CL images of representative zircon grains exhibiting different zoning pattern with spot date. (b) Th/U vs. age plot ($^{207}\text{Pb}/^{206}\text{Pb}$ near-concordant dates). c(I) Tera-Wasserburg Concordia diagram is showing most of the data clustering at approximately 950 Ma. c(II) Single-population weighted-average age recorded from this rock as 951 ± 10 Ma.

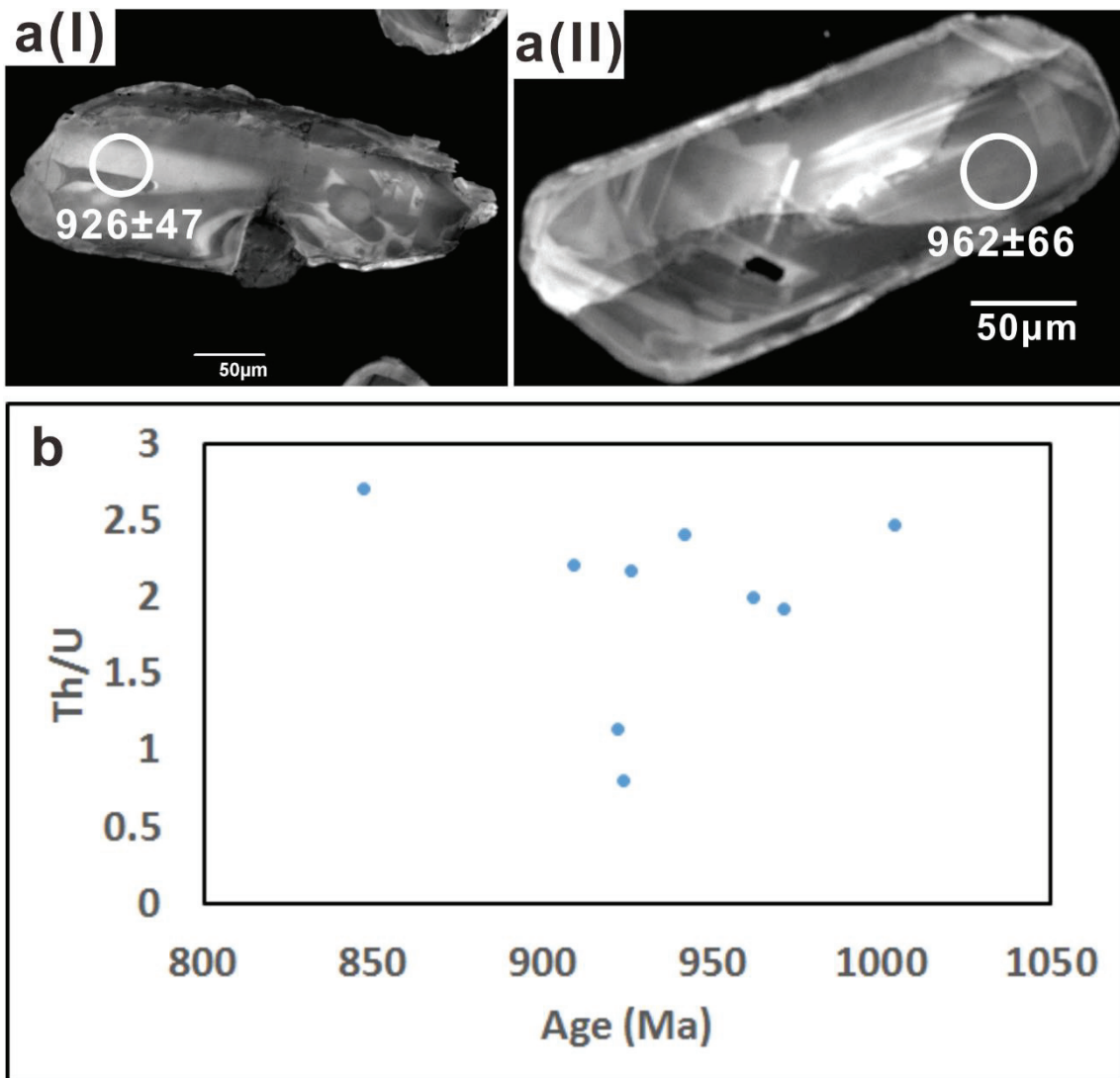


Figure 14 continued in the next page

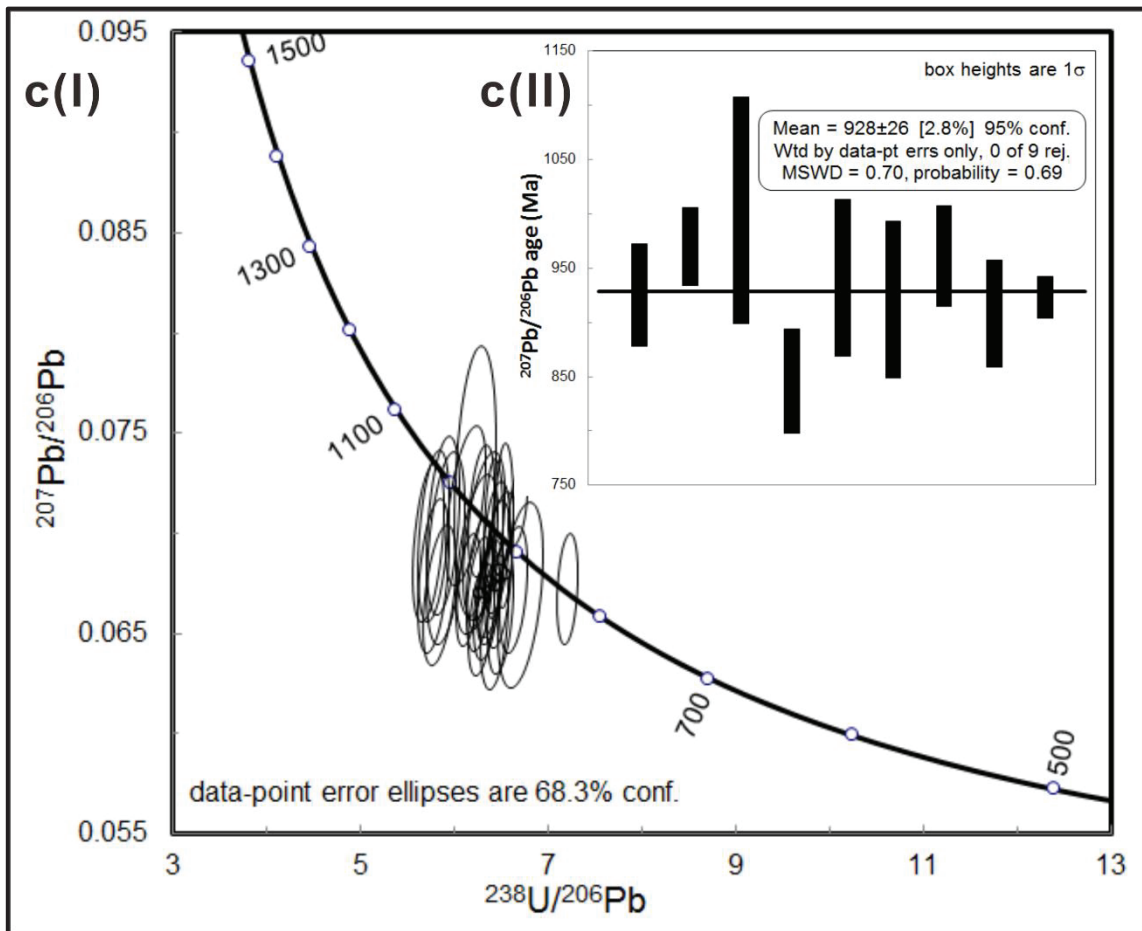


Figure 14: Internal structure of zircon grains and U-Pb SHRIMP analytical plots of the charnockitic augen gneiss (sample BP2). a(I) and a(II) The SEM-CL images of representative zircon grains exhibiting different zoning pattern with spot date. (b) Th/U vs. age plot ($^{207}\text{Pb}/^{206}\text{Pb}$ near-concordant dates). c(I) Tera-Wasserburg Concordia diagram is showing all the data clustering at approximately 930 Ma. c(II) Single-population weighted-average age recorded from this rock as 928 ± 26 Ma.

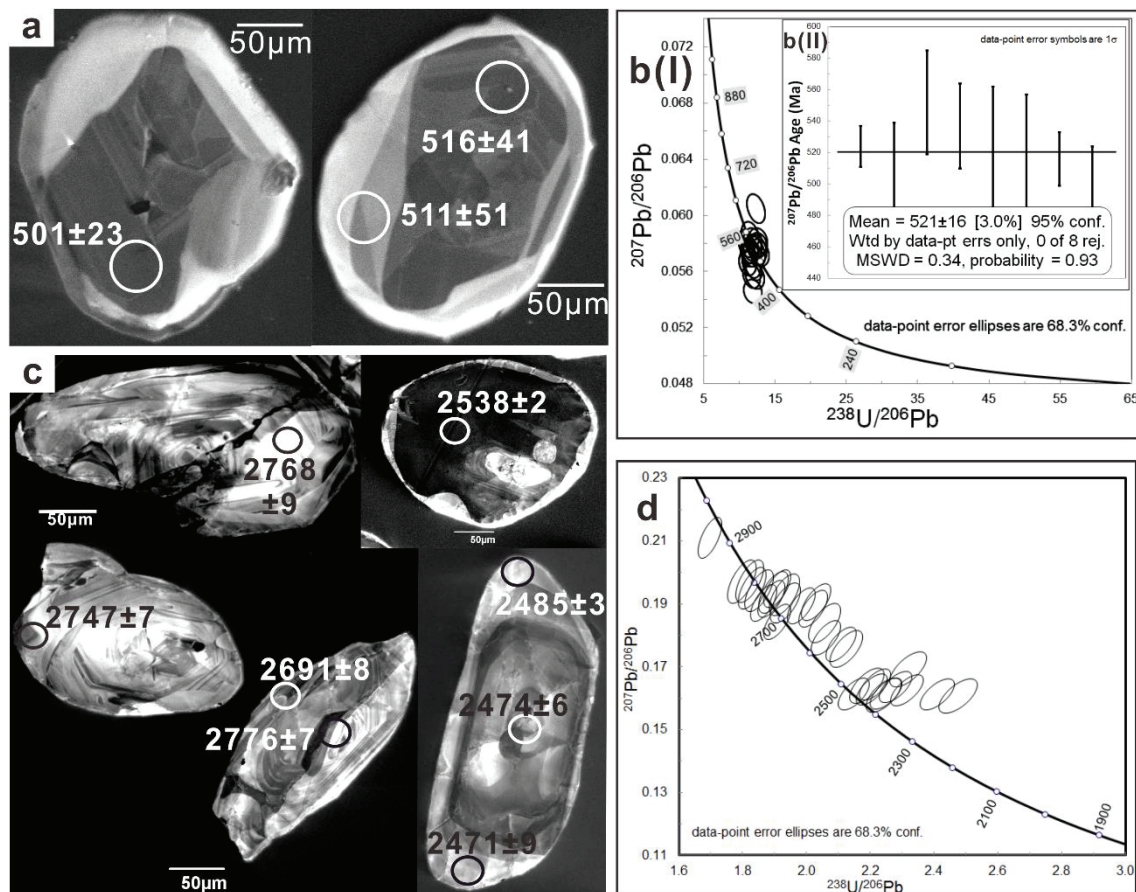


Figure 15: Internal structure of zircon grains and U-Pb SHRIMP analytical plots of the mafic granulites. (a) The SEM-CL images of representative zircon grains from sample BP12B exhibiting different zoning pattern with spot date. b(I) Tera-Wasserburg concordia plot is showing all data points cluster around ~ 520 Ma. b(II) Single-population weighted-average age recorded from this rock as 521 ± 16 Ma. (c) The SEM-CL images of representative zircon grains from the sample BP4 exhibiting different zoning pattern with spot date. (d) Tera-Wasserburg concordia diagram is showing a spread of age data between ~ 2900 Ma and ~ 2400 Ma.

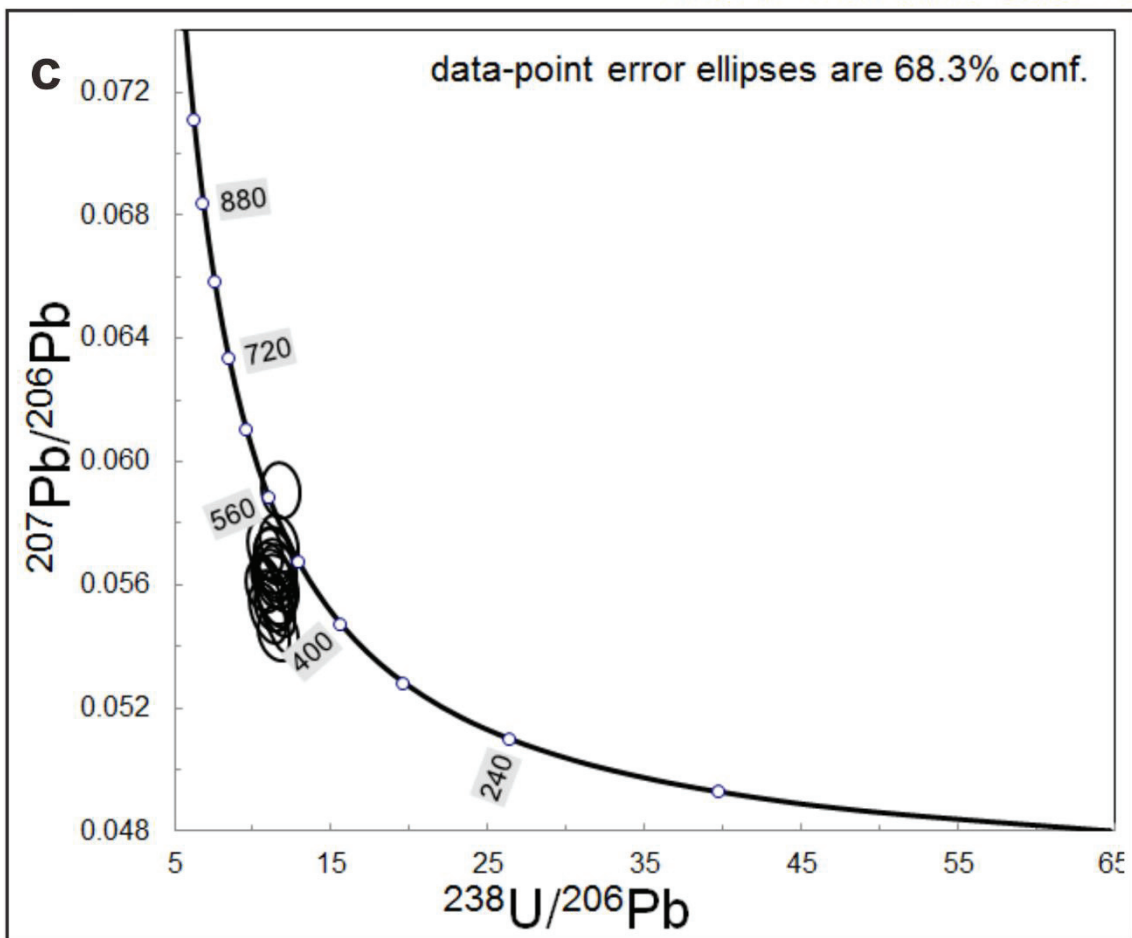
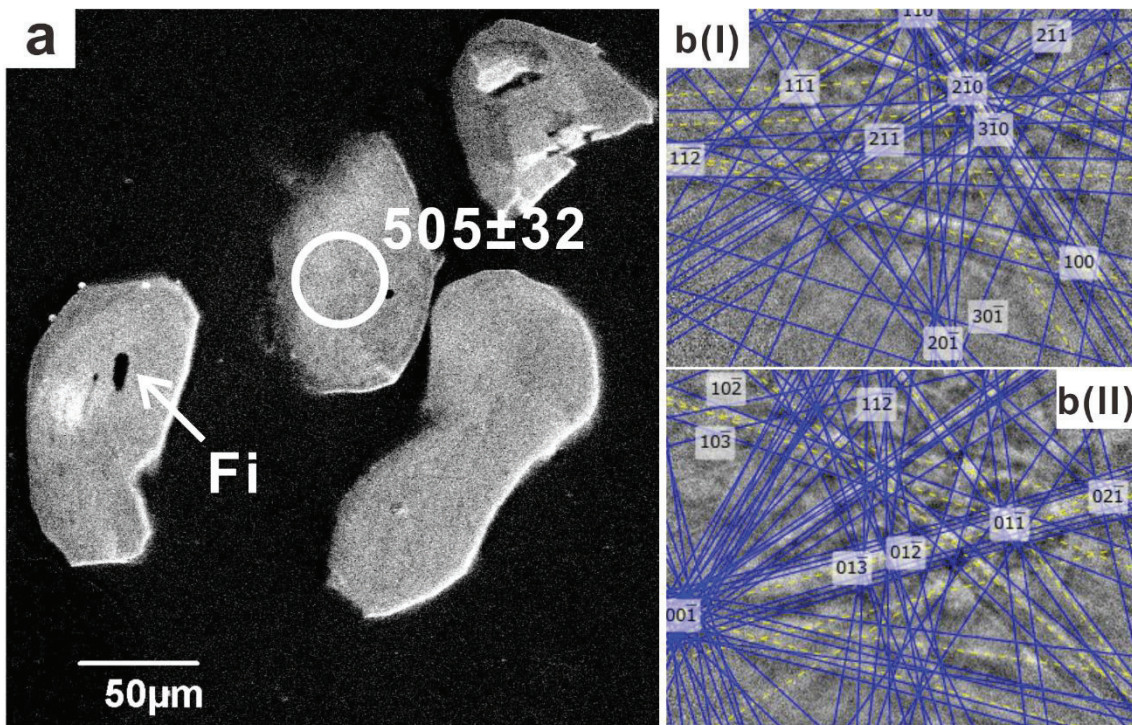


Figure 16 continued in the next page

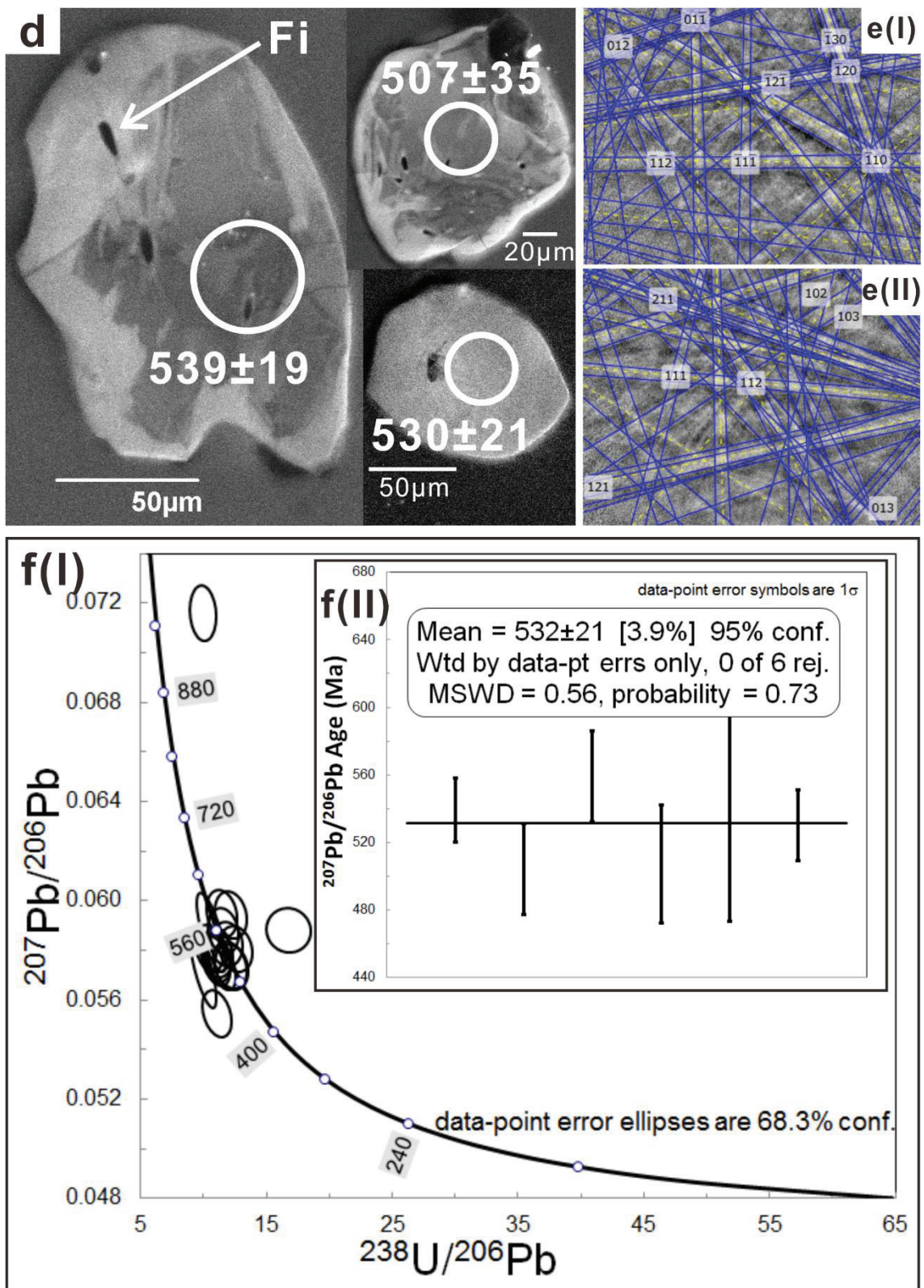


Figure 16: Internal structure and inclusion study of the zircon grains along with U-Pb SHRIMP analytical plots of the aluminous granulites (sample BP12A and sample

BP12C). (a) The SEM-CL images of representative zircon grains from sample BP12A are exhibiting different zoning pattern with spot date. Inclusions of fibrolite (Fi) found within the zircon grain. b(I-II) Representative Kikuchi pattern obtain from the included fibrolite (7 bands matched with sillimanite; MAD 0.72° and 0.85°, respectively) c) Tera-Wasserburg concordia plot of sample BP12A. (d) The SEM-CL images of representative zircon grains from sample BP12C are exhibiting different zoning pattern with spot date. Inclusions of fibrolite (Fi) found within the zircon grain. e(I-II) Representative Kikuchi pattern obtain from the included fibrolite (7 bands matched with sillimanite, MAD 0.7°; 9 bands matched with sillimanite, MAD 0.67°, respectively) f(I) Tera-Wasserburg concordia plot is showing all data points cluster around ~530 Ma. f(II) Single-population weighted-average age recorded from this rock as 532 ± 21 Ma.

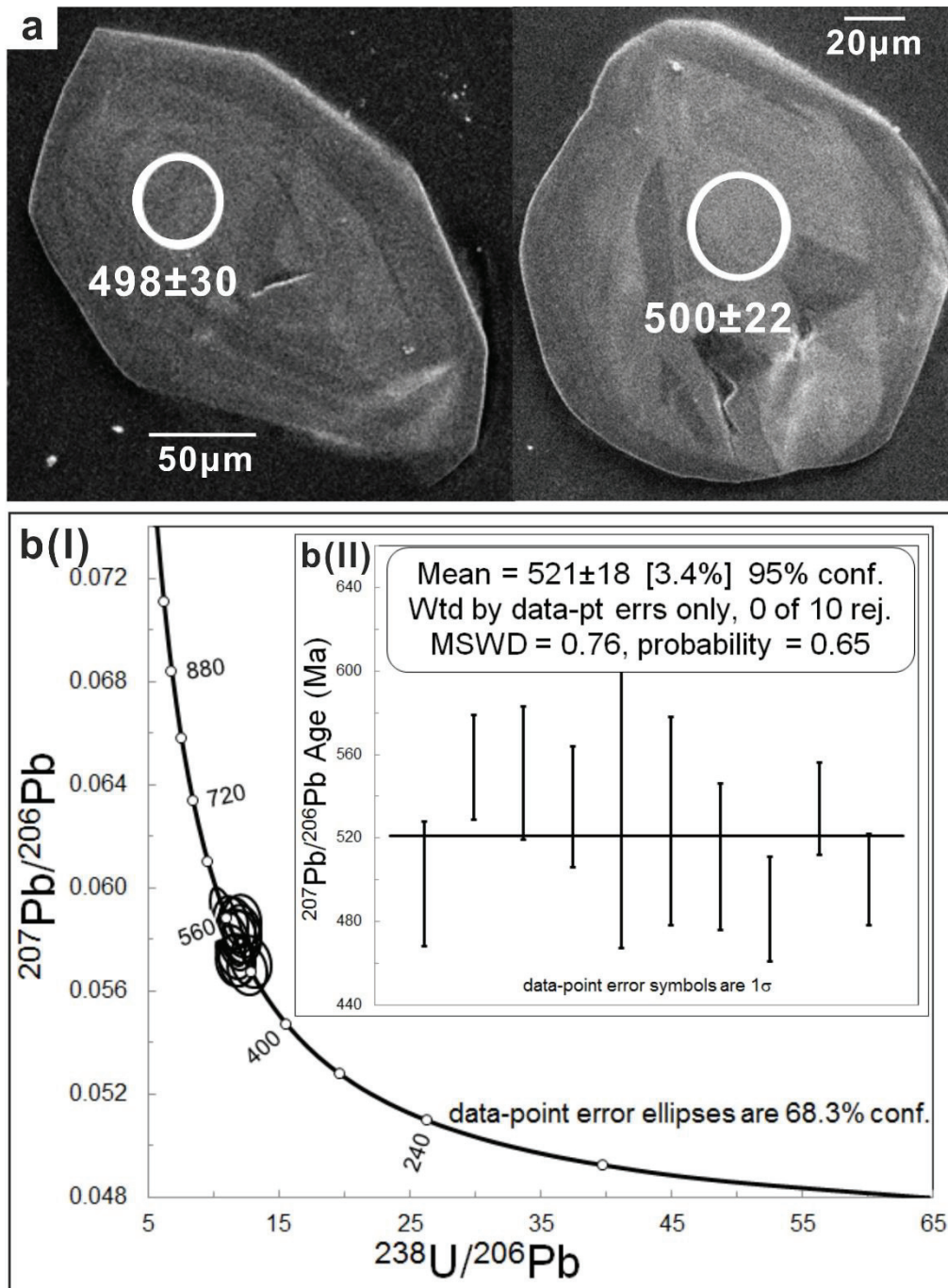


Figure 17: Internal structure of zircon grains and U-Pb SHRIMP analytical plots of the meta-ironstone (sample DG33E). (a) The SEM-CL images of representative zircon grains are exhibiting different zoning pattern with spot date. b(I) Tera-Wasserburg concordia plot is showing all data points cluster around ~525 Ma. b(II) Single-population weighted-average age recorded from this rock as 521 ± 18 Ma.

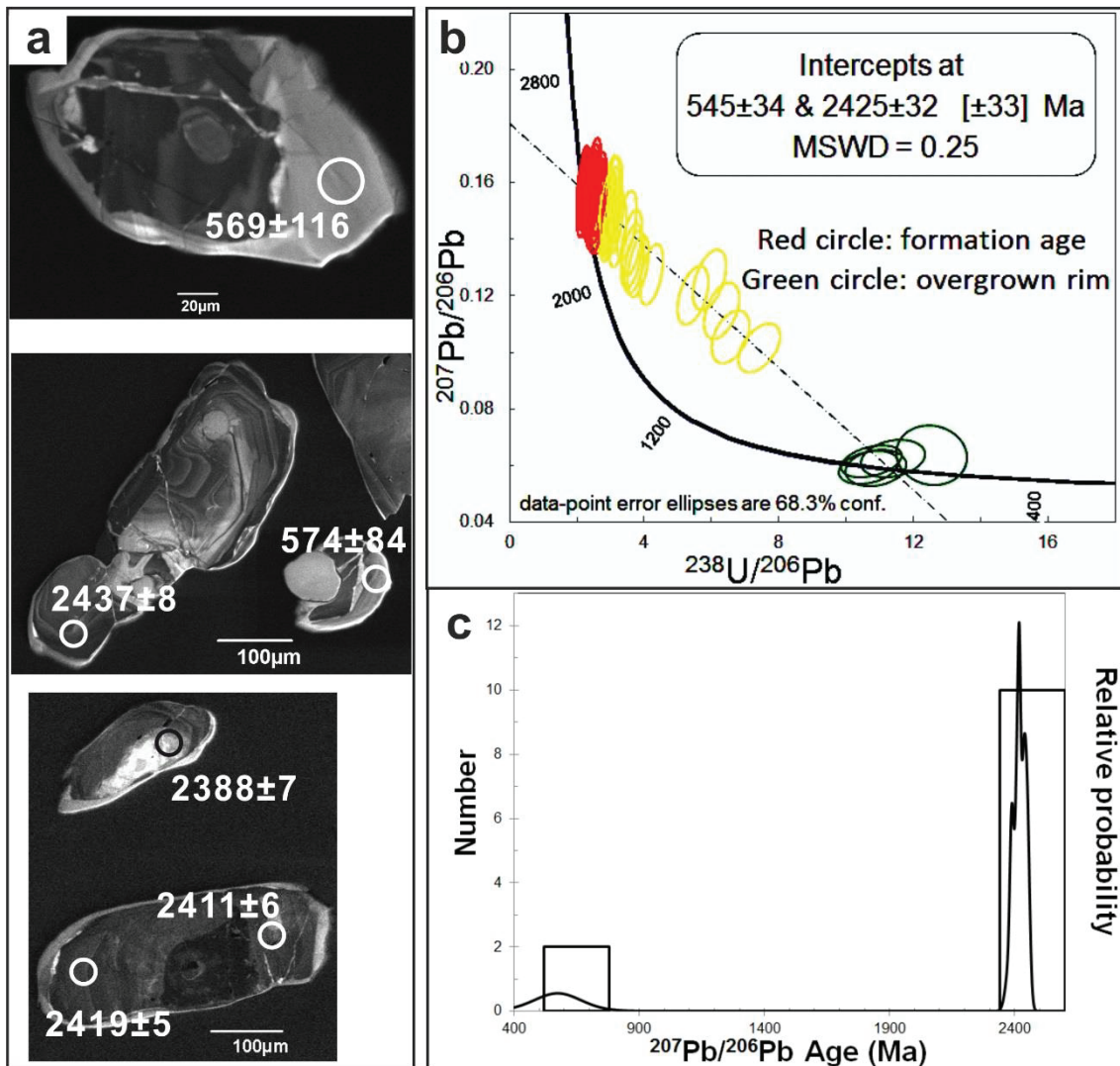


Figure 18: Internal structure of zircon grains and U-Pb SHRIMP analytical plots of the migmatitic hornblende gneiss (sample DG33F). (a) The SEM-CL images of representative zircon grains are exhibiting different zoning pattern with spot date. The core of the zircon grains yields mostly ~2400 Ma date whereas the rim exhibits ~550 Ma spot dates. (b) Tera-Wasserburg concordia plot reveals the upper intercept around ~2425 Ma and lower intercept around ~545 Ma as defined by the discordia line. (c) Probability density plot of the near-concordant data point showing two age-peaks at ~2400 Ma and ~550 Ma.

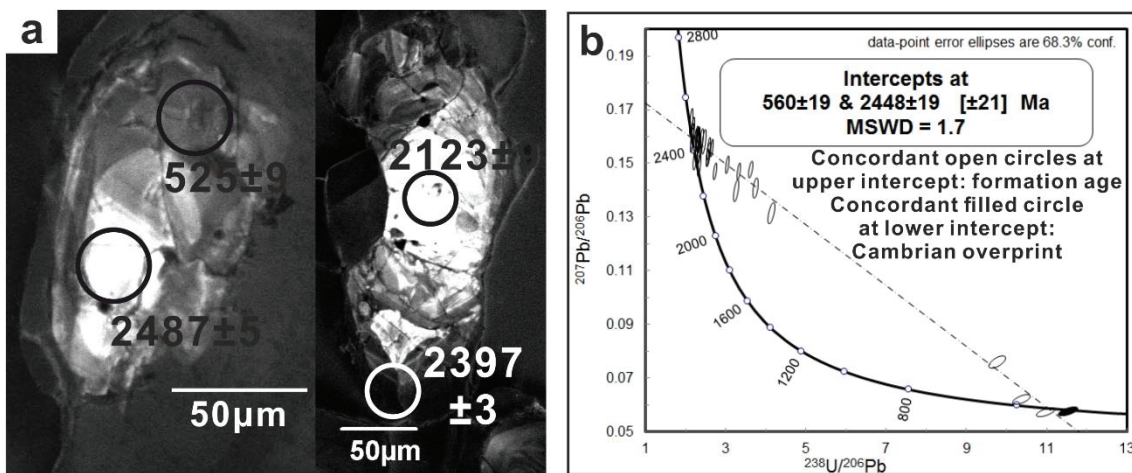


Figure 19: Internal structure of zircon grains and U-Pb SHRIMP analytical plots of the migmatitic quartzofeldspathic gneiss (sample BP6). (a) The SEM-CL images of representative zircon grains are showing different zoning pattern with spot dates. (b) The Tera-Wasserburg concordia diagram showing the widespread clusters with the discordia line with upper intercept age between approximately 2500 and 2350 Ma. A single concordant spot date of 525 ± 9 Ma marks the lower intercept.

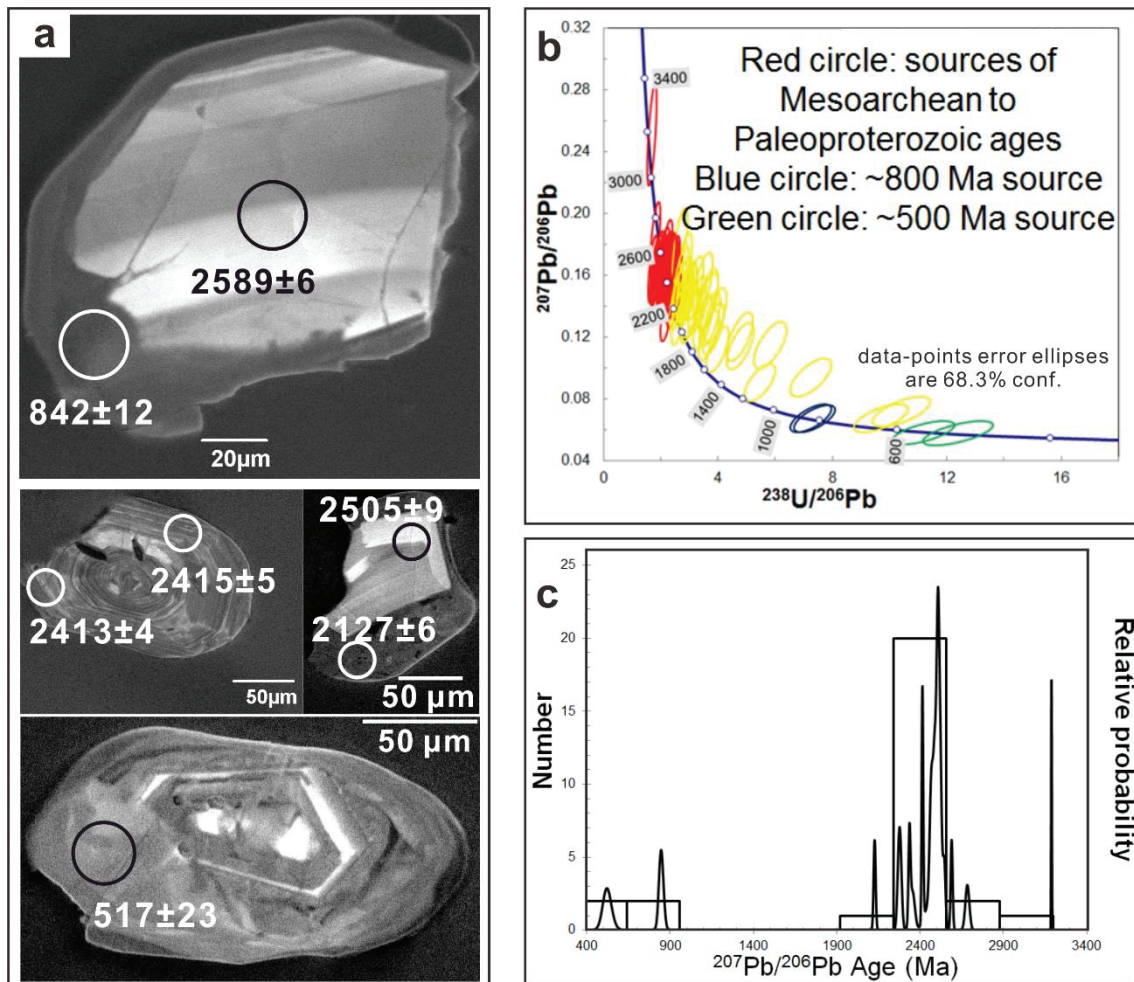


Figure 20: Internal structure of zircon grains and U-Pb SHRIMP analytical plots of the foliated quartz breccia (sample DG17B). (a) The SEM-CL images of representative zircon grains are showing wide varieties of zoning pattern. The Neoproterozoic spot dates (~850 Ma and ~520 Ma) are recorded mostly from the rim of Paleoproterozoic to Archean zircon grains. (b) The Tera-Wasserburg concordia plot reveals the wide scattering of age data ranging from ~3200 Ma to ~500 Ma, suggesting multiple sources of sedimentation. (c) Probability density plot of near-concordant ages are showing multiple peaks at ~530 Ma, ~850 Ma and between ~3200–2100 Ma.

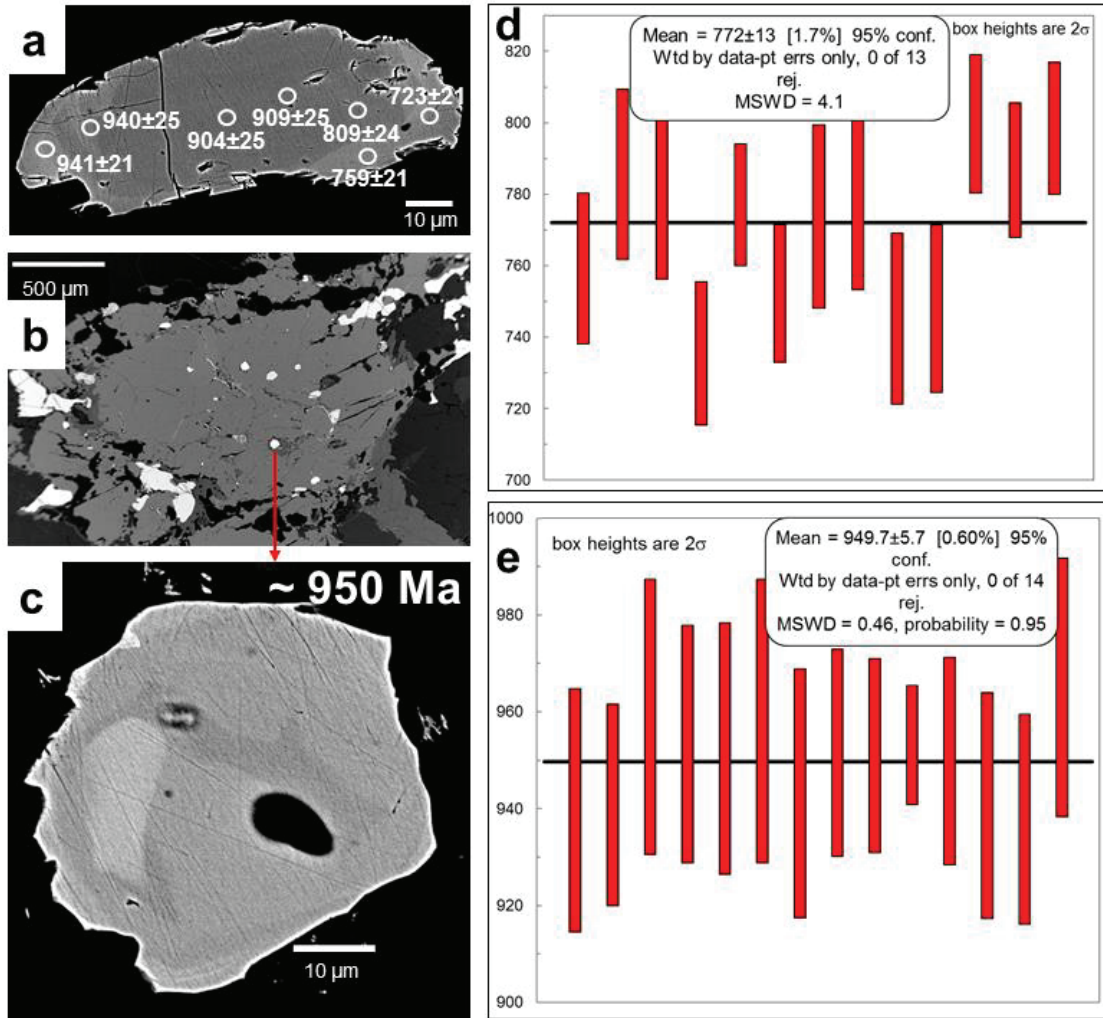


Figure 21: Internal structure of the monazite grains and U-Th-total Pb EPMA monazite dating plots of the charnockitic augen gneiss (BP1). (a) The SEM-BSI image of a representative monazite grain is showing compositional zoning with the spot dates ranging between ~941 and ~723 Ma. (b) Another representative monazite grain occurs as the inclusion within the porphyroblastic garnet. (c) Single cluster pool age of ~950 Ma recorded from the grain. (d) The weighted average mean age calculated from the matrix monazite is 772 ± 13 Ma. (e) The weighted average mean age calculated from the included monazite is 950 ± 6 Ma.

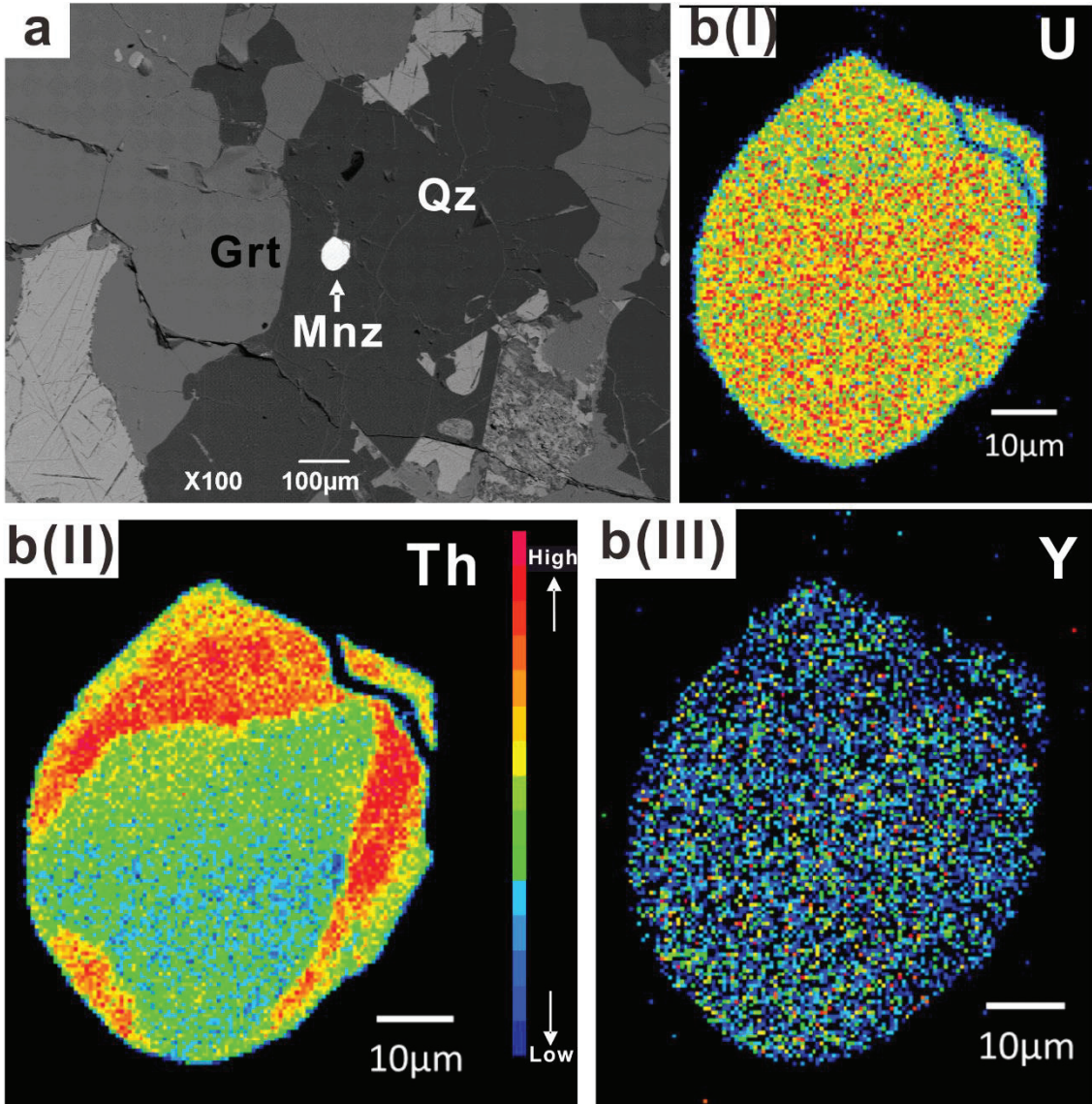


Figure 22 continued in the next page

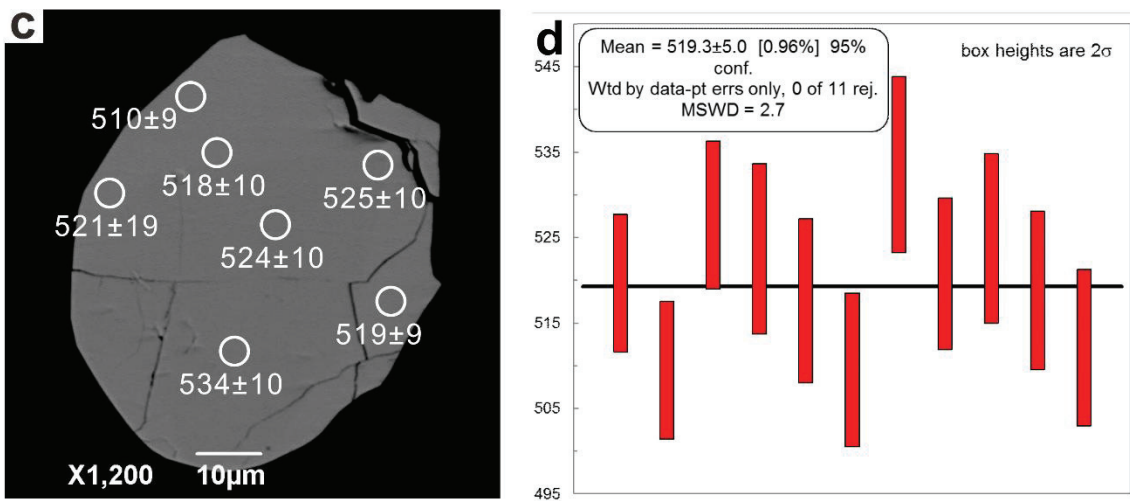


Figure 22: X-ray elemental mapping and U-Th-total Pb EPMA dating plots of the monazite grains from the aluminous granulite (sample BP12A). (a) The SEM-BSI image reveal that the monazite (Mnz) is included within the quartz (Qz). b(I)-b(III) Element maps of the analyzed monazite for U, Th, and Y. The concentration level of the elements is shown on the right side of the subfigure b(II). (c) The SEM-BSI image of the monazite grain is showing the spot dates. (d) The single population weighted average age is calculated as 519 ± 5 Ma.

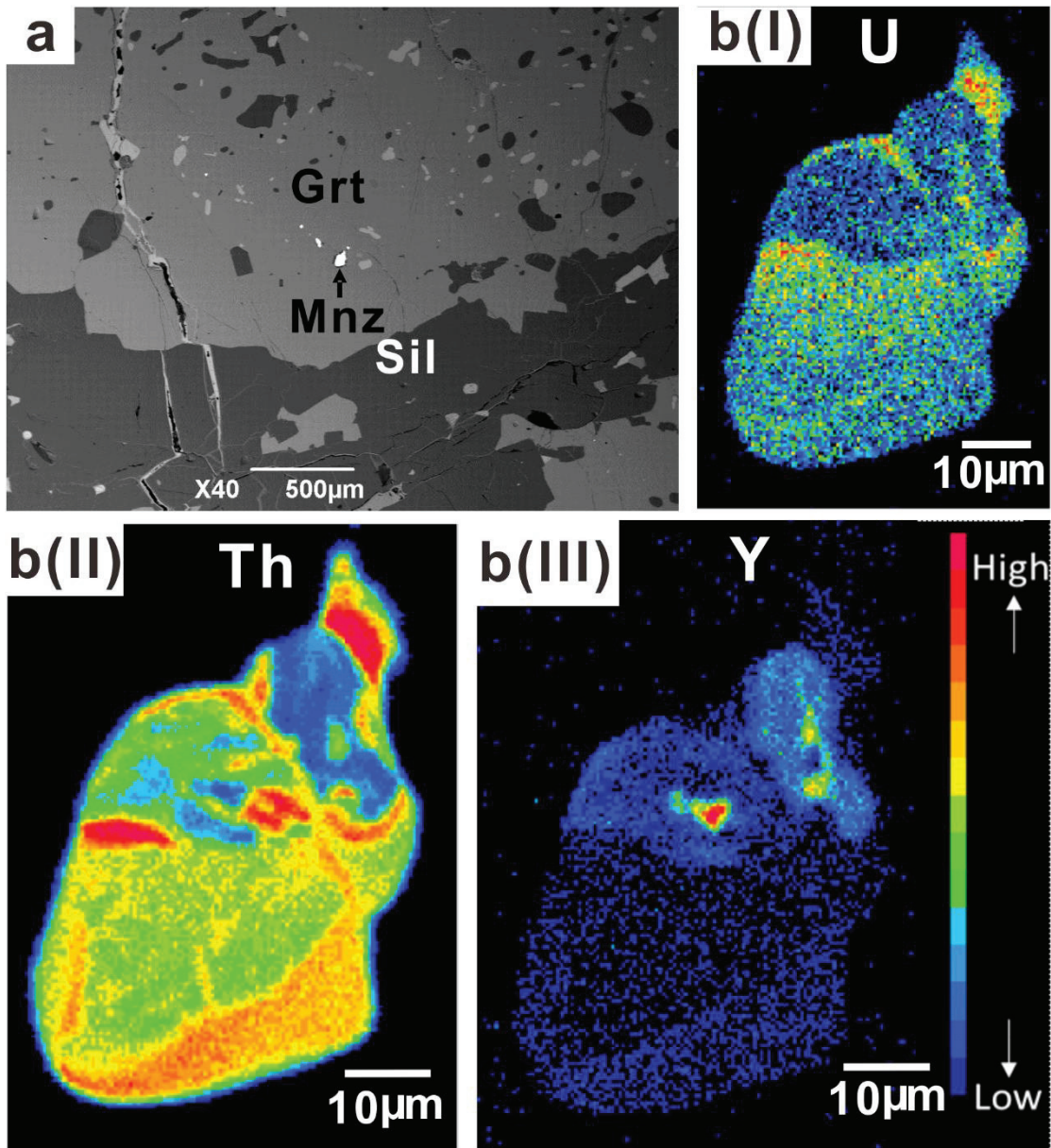


Figure 23 continued in the next page

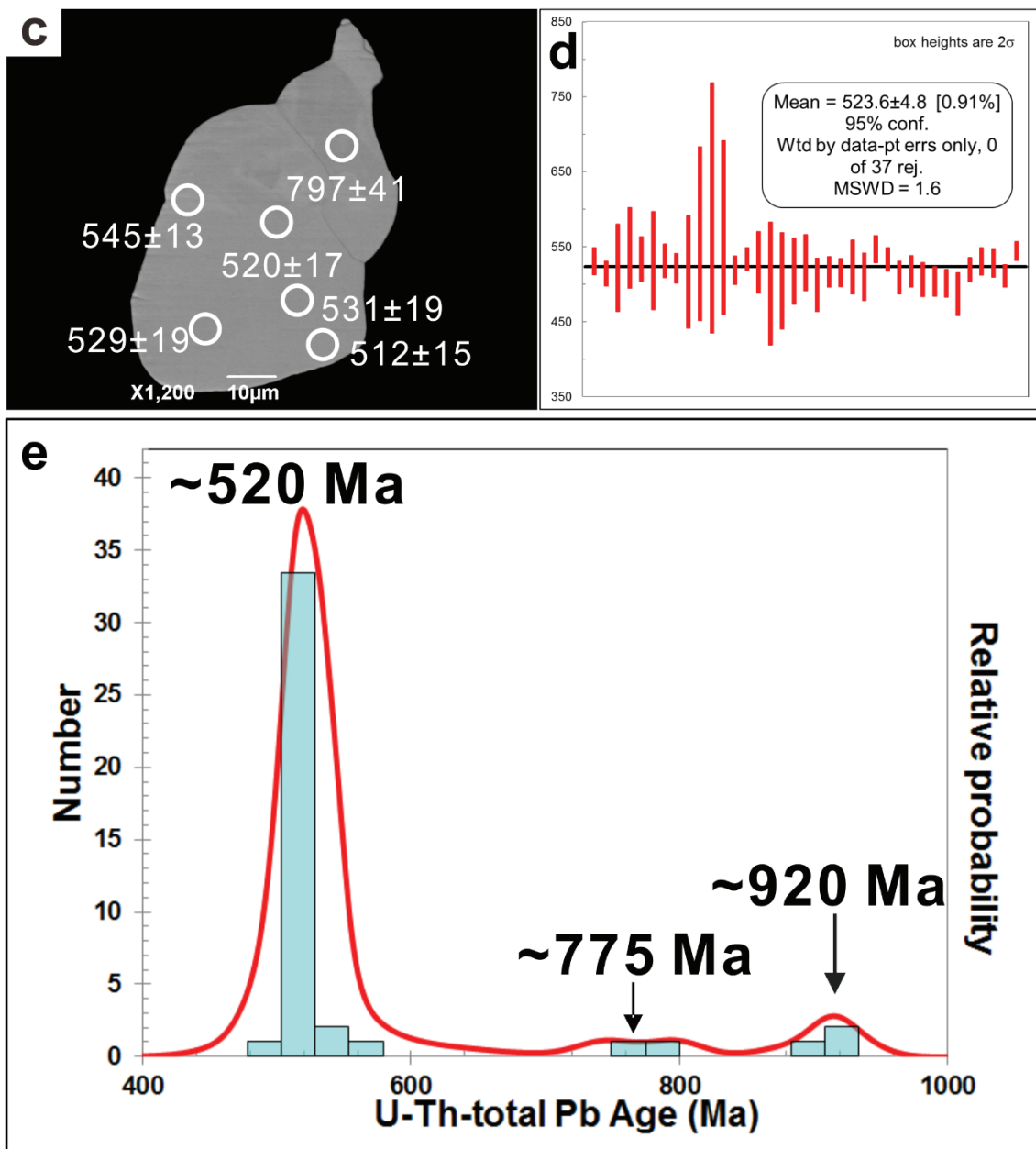


Figure 23: X-ray elemental mapping and U-Th-total Pb EPMA dating plots of monazite grains from the aluminous granulite (sample BP12C) (a) The SEM-BSI image reveal that the monazite (Mnz) is included within the rim of the garnet (Grt). b(I)-b(III) Element maps of the analyzed monazite for U, Th, and Y. The concentration levels of the elements are shown on the right-hand side of subfigure b(III). (c) The SEM-BSI image of the monazite grain is showing compositional zoning with the spot dates. (d) The most dominant weighted average of age is calculated as. (e) Probability density plot of spot dates showing a strong peak at approximately 520 Ma, with two minor peaks at ~920 and ~775 Ma.

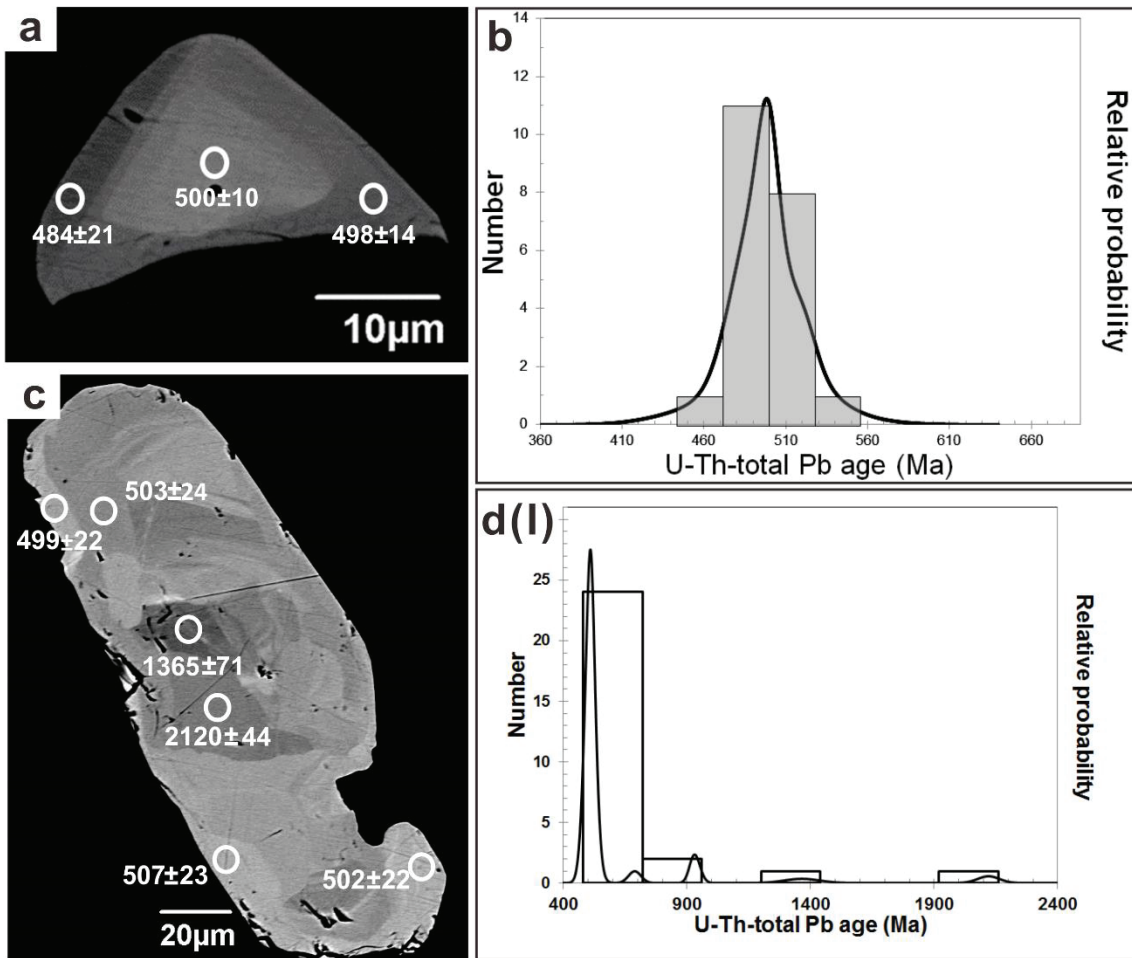


Figure 24 continued in the next page

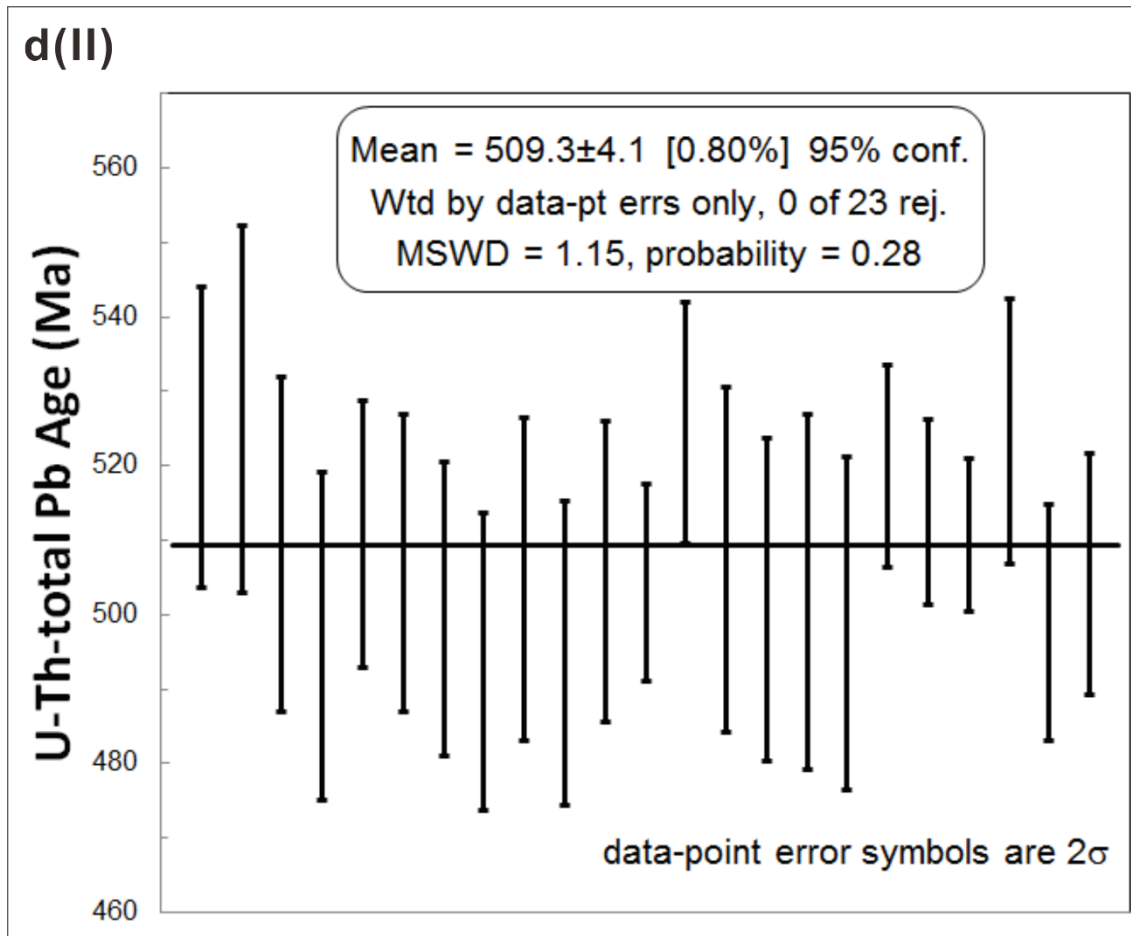


Figure 24: Internal structure of the monazite grains and U-Th-total Pb EPMA monazite dating plots of meta-ironstone (sample DG33E) and the foliated quartz breccia (sample DG17B). (a) The SEM-BSI image of a representative monazite grain is showing compositional zoning with the spot dates. (b) The probability density plot of all data points yields a single population age-peak at ~500 Ma. (c) The SEM-BSI image of a representative monazite grain is showing compositional zoning with the spot dates. The representative monazite grain preserves the core of ~2100 Ma, which is mantled by ~1350 Ma zone and then surrounded by the rim of ~500 Ma. d(I) The probability density plot is showing strongest age peak at ~500 Ma ($n = 23$) with minor peaks ~2100 Ma ($n = 1$), ~1350 Ma ($n = 1$), ~930 Ma ($n = 2$), ~700 Ma ($n = 1$). d(II) The weighted average age is calculated from the most dominant age cluster as 509 ± 4 Ma.

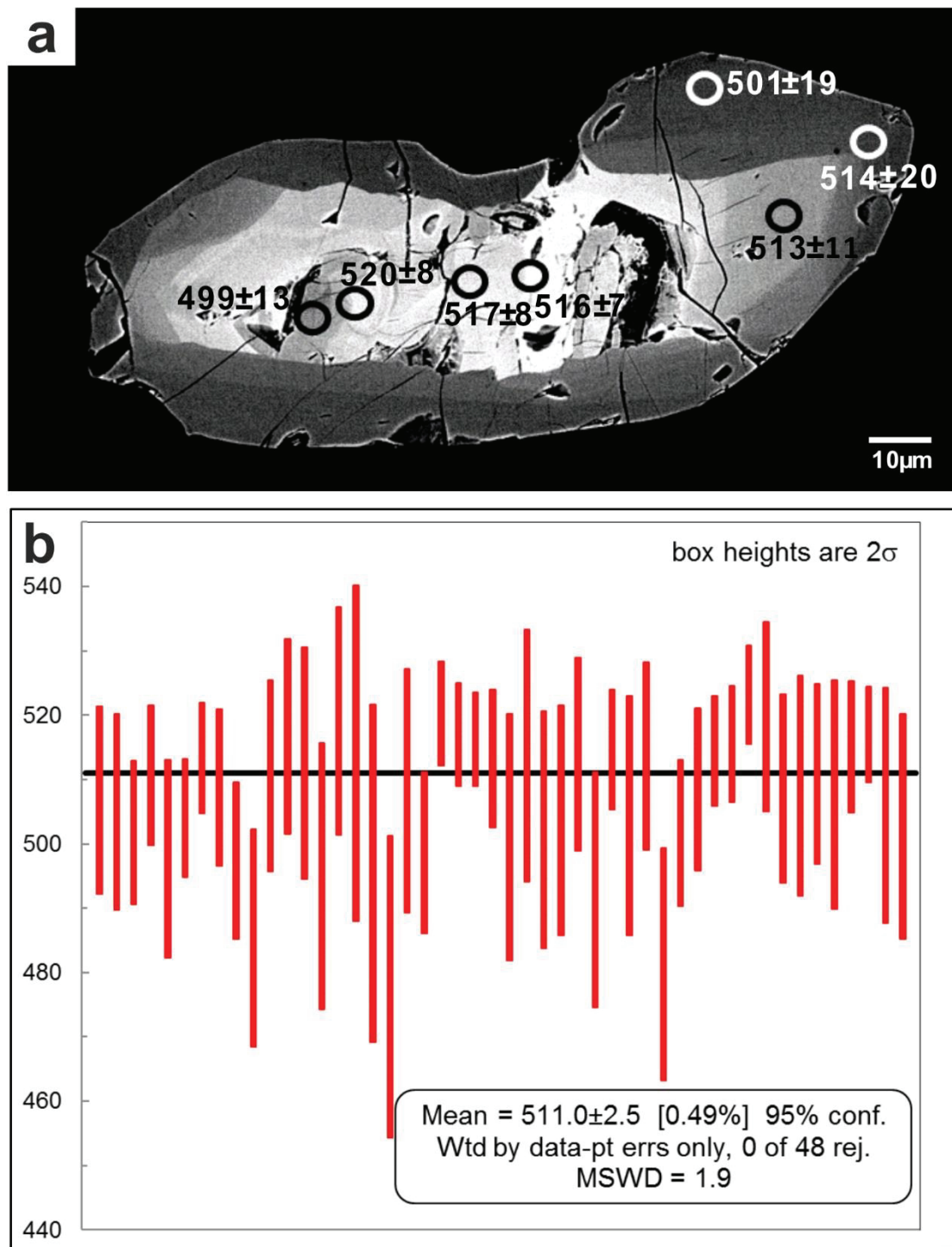


Figure 25: Internal structure of monazite grains and U-Th-total Pb EPMA monazite dating plots of the migmatitic quartzofeldspathic gneiss (sample BP6). (a) The SEM-BSI image of a representative monazite grain is showing compositional zoning with the spot dates. (b) The single population weighted average age is calculated as 511 ± 3 Ma.

Table 5: Analytical results of SHRIMP U-Pb zircon geochronology

Points	U (ppm)	Th (ppm)	Total Pb (ppm)	Th/U	$^{207}\text{Pb}/^{206}\text{Pb}$	$\pm 1\sigma$	$^{208}\text{Pb}/^{206}\text{Pb}$	$\pm 1\sigma$	$^{207}\text{Pb}/^{235}\text{U}$	$\pm 1\sigma$	$^{206}\text{Pb}/^{238}\text{U}$	$\pm 1\sigma$	% conc.	$^{207}\text{Pb}/^{206}\text{Pb}$ age (Ma)	$\pm 1\sigma$
Charnokitic augen gneiss (Sample no. BP1)															
BP1-01	704	593	167	0.84	0.077	0.001	0.268	0.001	2.173	0.001	0.204	0.002	107	1124	14
BP1-02	822	203	126	0.25	0.073	0.001	0.096	0.001	1.519	0.001	0.151	0.002	90	1011	16
BP1-03	476	598	74	1.26	0.069	0.001	0.205	0.002	1.357	0.002	0.142	0.001	94	913	20
BP1-04	651	134	97	0.21	0.069	0.001	0.059	0.001	1.448	0.001	0.153	0.002	103	888	17
BP1-05	384	126	62	0.33	0.069	0.001	0.101	0.002	1.513	0.002	0.158	0.002	104	913	23
BP1-06	898	205	142	0.23	0.071	0.000	0.068	0.001	1.568	0.001	0.161	0.002	101	949	13
BP1-07	623	137	93	0.22	0.071	0.001	0.069	0.001	1.476	0.001	0.151	0.002	95	951	18
BP1-08	271	107	45	0.39	0.071	0.001	0.129	0.002	1.555	0.002	0.158	0.002	98	963	29
BP1-08	778	79	97	0.10	0.069	0.001	0.028	0.001	1.259	0.001	0.133	0.001	91	889	15
BP1-10	286	119	46	0.42	0.071	0.001	0.115	0.002	1.536	0.002	0.156	0.002	97	967	23
BP1-11	356	153	79	0.43	0.093	0.002	0.133	0.003	2.707	0.003	0.211	0.002	83	1489	31
BP1-12	621	161	97	0.26	0.072	0.000	0.078	0.001	1.555	0.001	0.157	0.002	96	982	12
BP1-23	212	149	35	0.70	0.071	0.001	0.219	0.003	1.443	0.003	0.147	0.001	92	965	31
BP1-24	1196	229	181	0.19	0.075	0.000	0.064	0.000	1.592	0.000	0.154	0.002	87	1067	9
BP1-25	488	165	81	0.34	0.071	0.001	0.100	0.001	1.621	0.001	0.164	0.002	101	971	20
BP1-26	463	174	75	0.38	0.071	0.001	0.101	0.001	1.568	0.001	0.160	0.002	99	964	19
BP1-13	700	143	106	0.20	0.070	0.001	0.074	0.001	1.470	0.001	0.152	0.002	97	939	18
BP1-14	448	130	70	0.29	0.072	0.001	0.088	0.001	1.546	0.001	0.157	0.002	96	974	20
BP1-15	750	408	120	0.54	0.071	0.001	0.159	0.001	1.460	0.001	0.149	0.001	93	959	17
BP1-16	515	233	67	0.45	0.065	0.001	0.137	0.001	1.122	0.001	0.125	0.001	98	773	22
BP1-17	531	153	80	0.29	0.071	0.001	0.086	0.001	1.483	0.001	0.152	0.002	95	954	16
BP1-18	320	74	50	0.23	0.070	0.001	0.066	0.001	1.536	0.001	0.158	0.002	100	942	20
BP1-19	301	301	86	1.00	0.093	0.001	0.338	0.002	2.970	0.002	0.231	0.002	90	1495	14
BP1-20	416	139	64	0.33	0.071	0.001	0.100	0.001	1.507	0.001	0.153	0.002	94	971	18
BP1-21	707	535	122	0.76	0.072	0.001	0.223	0.001	1.533	0.001	0.154	0.002	93	991	14

Table 5 continued

Points	U (ppm)	Th (ppm)	Total Pb (ppm)	Th/U	$^{207}\text{Pb}/^{206}\text{Pb}$	$\pm 1\sigma$	$^{208}\text{Pb}/^{206}\text{Pb}$	$\pm 1\sigma$	$^{207}\text{Pb}/^{235}\text{U}$	$\pm 1\sigma$	$^{206}\text{Pb}/^{238}\text{U}$	$\pm 1\sigma$	% conc.	$^{207}\text{Pb}/^{206}\text{Pb}$ age (Ma)	$\pm 1\sigma$
BP1-22	432	115	63	0.27	0.070	0.001	0.082	0.001	1.426	0.021	0.147	0.001	95	933	20
BP1-33	942	166	133	0.18	0.070	0.000	0.050	0.001	1.408	0.022	0.146	0.002	96	921	11
BP1-34	748	261	122	0.35	0.072	0.000	0.100	0.001	1.599	0.025	0.162	0.002	99	973	12
BP1-35	1564	291	233	0.19	0.071	0.000	0.056	0.000	1.508	0.022	0.154	0.002	96	959	8
BP1-36	573	207	93	0.36	0.071	0.001	0.105	0.001	1.543	0.026	0.158	0.002	100	948	17
BP1-37	465	164	72	0.35	0.071	0.001	0.106	0.001	1.505	0.026	0.153	0.002	95	966	18
BP1-39	191	145	33	0.76	0.069	0.001	0.221	0.003	1.478	0.038	0.156	0.002	105	889	41
BP1-40	271	523	61	1.93	0.071	0.001	0.493	0.004	1.612	0.036	0.165	0.002	103	954	33
BP1-41	233	194	44	0.83	0.070	0.001	0.245	0.003	1.602	0.034	0.165	0.002	105	940	29
BP1-42	305	133	51	0.44	0.071	0.001	0.133	0.002	1.569	0.031	0.160	0.002	99	963	26
BP1-1-01	336	372	47	1.11	0.069	0.001	0.105	0.001	1.317	0.023	0.138	0.002	91	910	17
BP1-2-01	281	120	47	0.43	0.070	0.001	0.126	0.001	1.555	0.028	0.162	0.002	106	917	19
BP1-3-01	502	131	79	0.26	0.070	0.000	0.081	0.001	1.517	0.025	0.157	0.002	101	931	12
BP1-6-01	282	127	43	0.45	0.072	0.001	0.140	0.001	1.445	0.025	0.146	0.002	89	984	16
BP1-5-01	249	125	36	0.50	0.070	0.001	0.156	0.001	1.309	0.023	0.136	0.002	88	928	17
BP1-13-01	141	172	28	1.22	0.069	0.001	0.391	0.003	1.493	0.033	0.157	0.002	104	901	30
BP1-24-01	500	129	70	0.26	0.069	0.000	0.083	0.001	1.348	0.023	0.142	0.002	95	901	13
BP1-17-01	492	61	68	0.12	0.069	0.000	0.035	0.001	1.375	0.022	0.145	0.002	97	898	11
Charnockitic augen gneiss (Sample no. BP3)															
BP3A-01	175	239	36	1.37	0.071	0.001	0.419	0.004	1.553	0.031	0.158	0.002	98	967	32
BP3A-02	456	160	72	0.35	0.070	0.000	0.109	0.001	1.509	0.018	0.155	0.002	99	941	12
BP3A-03	716	95	107	0.13	0.072	0.000	0.039	0.001	1.536	0.019	0.156	0.002	96	974	14
BP3A-04	631	107	130	0.17	0.134	0.001	0.073	0.001	3.661	0.043	0.198	0.002	54	2154	9
BP3A-05	919	119	151	0.13	0.074	0.001	0.033	0.001	1.756	0.024	0.173	0.002	99	1034	16
BP3A-06	397	149	64	0.38	0.072	0.001	0.118	0.001	1.560	0.021	0.157	0.002	95	987	16
BP3A-07	143	100	27	0.70	0.070	0.002	0.209	0.004	1.637	0.041	0.171	0.002	111	918	45
BP3A-08	607	114	100	0.19	0.071	0.001	0.055	0.001	1.669	0.022	0.170	0.002	105	966	15

Table 5 continued

Points	U (ppm)	Th (ppm)	Total Pb (ppm)	Th/U	$^{207}\text{Pb}/^{206}\text{Pb}$	$\pm 1\sigma$	$^{208}\text{Pb}/^{206}\text{Pb}$	$\pm 1\sigma$	$^{207}\text{Pb}/^{235}\text{U}$	$\pm 1\sigma$	$^{206}\text{Pb}/^{238}\text{U}$	$\pm 1\sigma$	% conc.	$^{207}\text{Pb}/^{206}\text{Pb}$ age (Ma)	$\pm 1\sigma$
BP3A-09	353	191	59	0.54	0.067	0.001	0.166	0.002	1.456	0.020	0.158	0.002	113	833	17
BP3A-10	517	213	87	0.41	0.071	0.001	0.125	0.001	1.607	0.021	0.164	0.002	102	957	15
BP3A-11-1	305	131	50	0.43	0.073	0.001	0.131	0.002	1.604	0.028	0.160	0.002	94	1012	27
BP3A-11-2	128	173	28	1.35	0.071	0.001	0.397	0.004	1.673	0.035	0.172	0.002	108	948	35
BP3A-12-1	309	356	61	1.15	0.071	0.001	0.343	0.002	1.586	0.021	0.161	0.002	100	968	16
BP3A-13-1	487	181	81	0.37	0.071	0.000	0.116	0.001	1.585	0.019	0.163	0.002	103	948	11
BP3A-14	274	131	43	0.48	0.070	0.001	0.148	0.002	1.418	0.022	0.148	0.001	97	918	22
BP3A_3_01	401	152	67	0.38	0.071	0.001	0.118	0.001	1.580	0.025	0.163	0.002	103	943	15
BP3A_3_02	126	177	27	1.40	0.067	0.001	0.452	0.004	1.498	0.039	0.162	0.002	115	843	43
BP3A_3_03	100	159	22	1.59	0.065	0.002	0.519	0.005	1.393	0.044	0.155	0.002	119	782	56
BP3A_5_01	145	186	30	1.28	0.068	0.001	0.409	0.003	1.485	0.031	0.159	0.002	110	863	29
BP3A_5_02	507	225	82	0.44	0.069	0.000	0.113	0.001	1.492	0.024	0.158	0.002	107	885	15
BP3A_5_02	357	155	53	0.43	0.067	0.001	0.122	0.002	1.314	0.023	0.142	0.002	102	841	21
BP3A_1_01	245	98	38	0.40	0.067	0.001	0.111	0.002	1.384	0.026	0.149	0.002	106	844	25
BP3A_02_1	1771	136	273	0.08	0.071	0.000	0.024	0.000	1.574	0.023	0.161	0.002	101	950	9
BP3A_07_1	453	84	69	0.19	0.072	0.000	0.054	0.001	1.548	0.024	0.157	0.002	97	973	13
BP3A_07_2	326	165	55	0.51	0.071	0.001	0.157	0.001	1.558	0.025	0.159	0.002	100	956	16
BP3A_08_1	297	63	46	0.21	0.070	0.001	0.064	0.001	1.529	0.025	0.159	0.002	103	920	16
BP3A_08_2	595	159	95	0.27	0.071	0.000	0.081	0.001	1.584	0.024	0.161	0.002	100	966	11
BP3A_10_1	554	165	93	0.30	0.069	0.000	0.092	0.001	1.601	0.025	0.167	0.002	109	913	14
BP3A-22-01	1225	125	174	0.10	0.070	0.000	0.032	0.000	1.452	0.021	0.150	0.002	97	932	8
BP3A-22-02	129	243	30	1.88	0.067	0.001	0.585	0.004	1.520	0.035	0.163	0.002	114	853	36
BP3A-12-01	311	64	52	0.21	0.070	0.001	0.056	0.001	1.660	0.027	0.173	0.002	112	920	17
BP3A-15-01	333	269	60	0.81	0.068	0.001	0.312	0.002	1.408	0.025	0.149	0.002	101	884	21
BP3A-16-01	44	68	9	1.55	0.058	0.003	0.464	0.008	1.229	0.067	0.154	0.002	175	528	113
BP3A-18-01	313	228	57	0.73	0.068	0.001	0.226	0.001	1.535	0.025	0.163	0.002	110	880	16

Table 5 continued

Points	U (ppm)	Th (ppm)	Total Pb (ppm)	Th/U	$^{207}\text{Pb}/^{206}\text{Pb}$	$^{208}\text{Pb}/^{206}\text{Pb}$	$^{207}\text{Pb}/^{235}\text{U}$	$^{206}\text{Pb}/^{238}\text{U}$	% conc.	$^{207}\text{Pb}/^{206}\text{Pb}$ age (Ma)	$\pm 1\sigma$	$\pm 1\sigma$	$\pm 1\sigma$	$\pm 1\sigma$
Charnokitic augen gneiss (Sample no. BP2)														
BP2-01	123	310	34	2.52	0.067	0.762	0.006	1.584	0.049	122	0.003	0.171	838	44
BP2-02	60	74	13	1.23	0.066	0.363	0.008	1.581	0.077	125	0.003	0.173	821	88
BP2-03	112	278	31	2.48	0.068	0.742	0.007	1.624	0.056	119	0.003	0.173	867	53
BP2-04	82	144	20	1.76	0.070	0.523	0.007	1.671	0.062	111	0.003	0.173	926	60
BP2-05	85	221	24	2.60	0.070	0.779	0.007	1.680	0.058	113	0.003	0.175	918	53
BP2-06	81	213	23	2.63	0.070	0.795	0.008	1.655	0.064	108	0.003	0.170	942	64
BP2-07	99	205	22	2.07	0.067	0.637	0.007	1.379	0.057	107	0.004	0.149	837	65
BP2-08	106	129	23	1.22	0.063	0.351	0.010	1.496	0.097	146	0.004	0.173	702	123
BP2-09	74	161	18	2.18	0.070	0.648	0.006	1.530	0.053	103	0.004	0.159	926	47
BP2-10	103	141	21	1.37	0.069	0.416	0.005	1.526	0.050	107	0.004	0.160	899	42
BP2-11	48	92	11	1.92	0.071	0.571	0.006	1.611	0.050	101	0.004	0.164	971	36
BP2-12	83	172	21	2.07	0.069	0.613	0.007	1.621	0.067	111	0.004	0.170	908	65
BP2-13	42	57	8	1.36	0.062	0.408	0.010	1.269	0.080	129	0.003	0.147	689	119
BP2-14	98	242	25	2.47	0.073	0.752	0.011	1.612	0.095	96	0.004	0.161	1004	104
BP2-15	160	433	37	2.71	0.067	0.838	0.006	1.288	0.034	99	0.001	0.139	847	48
BP2-16	101	178	21	1.76	0.071	0.526	0.005	1.476	0.024	93	0.002	0.150	969	24
BP2-17	73	176	18	2.41	0.070	0.737	0.009	1.492	0.057	98	0.002	0.154	942	72
BP2-18	92	105	18	1.14	0.070	0.341	0.007	1.501	0.056	101	0.002	0.156	922	72
BP2-19	114	127	19	1.11	0.064	0.334	0.006	1.204	0.047	114	0.001	0.137	728	77
BP2-1-01	54	66	11	1.22	0.058	0.368	0.006	1.233	0.059	172	0.002	0.154	536	95
BP2-2-01	79	84	15	1.06	0.067	0.349	0.004	1.400	0.040	107	0.002	0.151	846	48
BP2-2-02	111	264	28	2.38	0.067	0.757	0.004	1.477	0.037	114	0.002	0.160	839	39
BP2-3-01	126	293	31	2.33	0.067	0.744	0.004	1.460	0.032	110	0.002	0.157	851	30
BP2-3-02	163	273	35	1.67	0.067	0.513	0.003	1.452	0.033	112	0.002	0.157	842	32
BP2-6-01	78	129	17	1.65	0.066	0.538	0.005	1.411	0.045	117	0.002	0.156	795	55
BP2-7-01	95	208	24	2.19	0.066	0.715	0.004	1.445	0.037	119	0.002	0.159	799	40
BP2-9-01	80	160	19	2.00	0.071	0.637	0.005	1.564	0.045	99	0.002	0.159	962	46

Table 5 continued

Points	U (ppm)	Th (ppm)	Total Pb (ppm)	Th/U	$^{207}\text{Pb}/^{206}\text{Pb}$	$\pm 1\sigma$	$^{208}\text{Pb}/^{206}\text{Pb}$	$\pm 1\sigma$	$^{207}\text{Pb}/^{235}\text{U}$	$\pm 1\sigma$	$^{206}\text{Pb}/^{238}\text{U}$	$\pm 1\sigma$	% conc.	$^{207}\text{Pb}/^{206}\text{Pb}$ age (Ma)	$\pm 1\sigma$
BP2-10-01	36	56	8	1.56	0.060	0.003	0.509	0.009	1.241	0.074	0.150	0.002	149	605	121
BP2-12-01	123	171	24	1.39	0.065	0.001	0.451	0.004	1.312	0.038	0.147	0.002	115	767	48
BP2_15_01	74	176	19	2.38	0.066	0.002	0.780	0.005	1.409	0.043	0.154	0.002	113	815	52
BP2_15_02	82	84	16	1.02	0.068	0.001	0.321	0.003	1.498	0.036	0.160	0.002	110	870	36
BP2_18_01	95	224	25	2.36	0.067	0.001	0.754	0.004	1.510	0.037	0.163	0.002	115	846	38
BP2-17-01	74	95	15	1.28	0.068	0.002	0.423	0.005	1.454	0.050	0.155	0.002	107	870	61
BP2-17-02	108	229	26	2.12	0.067	0.001	0.660	0.004	1.447	0.037	0.158	0.002	115	823	40
BP2_20_01	73	161	18	2.21	0.069	0.002	0.723	0.005	1.486	0.044	0.155	0.002	102	909	49
BP2_13_01	100	217	24	2.17	0.064	0.002	0.707	0.005	1.351	0.040	0.154	0.002	125	734	51
BP2_16_01	233	187	41	0.80	0.070	0.001	0.256	0.002	1.488	0.027	0.154	0.002	100	924	19
Mafic granulite (Sample no. BP12B)															
BP12B.3.1	681	67	51	0.10	0.058	0.000	0.030	0.001	0.638	0.046	0.080	0.006	95	524	13
BP12B.4.1	251	40	21	0.16	0.057	0.001	0.049	0.002	0.691	0.051	0.087	0.006	106	510	31
BP12B.4.2	280	50	23	0.18	0.056	0.001	0.052	0.002	0.668	0.050	0.086	0.006	112	472	41
BP12B.5.1	260	47	21	0.18	0.056	0.001	0.054	0.002	0.657	0.048	0.085	0.006	120	442	32
BP12B.7.1	221	62	17	0.28	0.057	0.001	0.082	0.002	0.616	0.046	0.078	0.005	96	505	34
BP12B.7.2	200	48	16	0.24	0.058	0.001	0.078	0.001	0.638	0.046	0.080	0.006	92	537	25
BP12B.8.1	380	47	31	0.12	0.059	0.001	0.041	0.002	0.703	0.052	0.087	0.006	97	552	33
BP12B.9.1	269	64	23	0.24	0.057	0.001	0.075	0.001	0.698	0.050	0.088	0.006	107	510	19
BP12B.10.1	198	41	17	0.21	0.058	0.001	0.067	0.002	0.728	0.054	0.091	0.006	106	530	38
BP12B.11.1	302	57	26	0.19	0.057	0.001	0.059	0.001	0.699	0.051	0.090	0.006	116	477	26
BP12B.11.2	233	68	21	0.29	0.058	0.002	0.092	0.004	0.724	0.057	0.091	0.006	108	520	59
BP12B.12.1	246	25	19	0.10	0.058	0.001	0.031	0.001	0.677	0.049	0.084	0.006	97	537	27
BP12B.13.1	144	33	11	0.23	0.058	0.001	0.075	0.003	0.643	0.049	0.081	0.006	98	511	51
BP12B.13.2	351	75	27	0.21	0.058	0.001	0.069	0.002	0.636	0.048	0.080	0.006	96	516	41
BP12B.14.1	233	62	19	0.27	0.061	0.001	0.092	0.003	0.676	0.051	0.081	0.006	81	622	41
BP12B.14.2	364	138	31	0.38	0.055	0.001	0.121	0.001	0.633	0.046	0.084	0.006	131	396	25

Table 5 continued

Points	U (ppm)	Th (ppm)	Total Pb (ppm)	Th/U	$^{207}\text{Pb}/^{206}\text{Pb}$	$\pm 1\sigma$	$^{208}\text{Pb}/^{206}\text{Pb}$	$\pm 1\sigma$	$^{207}\text{Pb}/^{235}\text{U}$	$\pm 1\sigma$	$^{206}\text{Pb}/^{238}\text{U}$	$\pm 1\sigma$	% conc.	$^{207}\text{Pb}/^{206}\text{Pb}$ age (Ma)	$\pm 1\sigma$
BP12B.15.1	317	53	26	0.17	0.058	0.000	0.053	0.001	0.670	0.048	0.084	0.006	101	516	17
BP12B.15.2	260	49	21	0.19	0.056	0.001	0.057	0.003	0.656	0.050	0.084	0.006	111	470	51
BP12B.16.1	300	95	25	0.32	0.056	0.001	0.098	0.002	0.632	0.047	0.082	0.006	116	440	34
BP12B.17.1	282	53	23	0.19	0.057	0.001	0.059	0.001	0.671	0.049	0.085	0.006	105	501	23
BP12B.18.1	348	47	29	0.14	0.057	0.001	0.044	0.001	0.686	0.050	0.087	0.006	107	500	21
Mafic granulite (Sample no. BP4)															
BP4-01	400	198	213	0.50	0.176	0.001	0.137	0.001	11.427	0.194	0.471	0.008	95	2616	6
BP4-02	258	110	160	0.43	0.195	0.001	0.116	0.001	14.717	0.251	0.547	0.009	101	2786	6
BP4-03	418	172	184	0.41	0.161	0.001	0.109	0.001	8.964	0.152	0.404	0.007	89	2466	6
BP4-04	138	72	82	0.52	0.193	0.001	0.143	0.002	13.790	0.246	0.518	0.008	97	2768	9
BP4-05	248	149	160	0.60	0.197	0.001	0.163	0.001	14.948	0.259	0.549	0.009	101	2804	7
BP4-06	806	182	371	0.23	0.169	0.001	0.071	0.000	10.078	0.169	0.431	0.007	91	2552	5
BP4-07	173	86	102	0.50	0.191	0.001	0.134	0.001	13.601	0.235	0.518	0.008	98	2747	7
BP4-08	229	131	128	0.57	0.184	0.001	0.158	0.001	12.352	0.217	0.487	0.008	95	2691	8
BP4-09	330	231	209	0.70	0.194	0.001	0.196	0.001	14.103	0.243	0.527	0.009	98	2776	7
BP4-10	169	88	108	0.52	0.197	0.001	0.140	0.001	15.146	0.266	0.557	0.009	102	2804	8
BP4-11	635	126	296	0.20	0.161	0.001	0.054	0.000	9.921	0.169	0.446	0.007	96	2468	7
BP4-12	415	293	269	0.71	0.194	0.001	0.199	0.001	14.497	0.250	0.541	0.009	100	2780	7
BP4-13	698	307	354	0.44	0.164	0.001	0.127	0.001	10.351	0.177	0.457	0.007	97	2500	7
BP4_01_1	152	72	86	0.47	0.189	0.001	0.135	0.001	12.883	0.201	0.495	0.007	95	2732	6
BP4_01_2	1192	180	535	0.15	0.163	0.000	0.045	0.000	9.700	0.145	0.432	0.006	93	2484	3
BP4_02_1	313	181	219	0.58	0.211	0.000	0.164	0.001	17.177	0.261	0.590	0.009	103	2915	4
BP4_03_1	272	145	169	0.53	0.191	0.001	0.152	0.001	14.099	0.217	0.537	0.008	101	2747	5
BP4_04_1	308	229	153	0.74	0.161	0.001	0.229	0.001	9.241	0.143	0.415	0.006	91	2471	6
BP4_05_1	409	308	260	0.75	0.185	0.000	0.223	0.001	13.353	0.203	0.525	0.008	101	2694	4
BP4_10_01	230	348	139	1.51	0.164	0.001	0.420	0.001	9.911	0.154	0.439	0.006	94	2495	6
BP4_10_02	1266	322	620	0.25	0.164	0.000	0.089	0.000	10.244	0.153	0.452	0.007	96	2502	3

Table 5 continued

Points	U (ppm)	Th (ppm)	Total Pb (ppm)	Th/U	$^{207}\text{Pb}/^{206}\text{Pb}$	$\pm 1\sigma$	$^{208}\text{Pb}/^{206}\text{Pb}$	$\pm 1\sigma$	$^{207}\text{Pb}/^{235}\text{U}$	$\pm 1\sigma$	$^{206}\text{Pb}/^{238}\text{U}$	$\pm 1\sigma$	% conc.	$^{207}\text{Pb}/^{206}\text{Pb}$ age (Ma)	$\pm 1\sigma$
BP4_6_01	238	126	139	0.53	0.190	0.001	0.153	0.001	13.190	0.202	0.505	0.007	96	2739	5
BP4_8_01	204	99	115	0.49	0.191	0.001	0.137	0.001	12.974	0.201	0.493	0.007	94	2750	5
BP4_15_01	954	124	478	0.13	0.163	0.000	0.037	0.000	10.899	0.164	0.485	0.007	103	2485	3
BP4_15_02	218	194	119	0.89	0.162	0.001	0.257	0.001	9.923	0.155	0.445	0.007	96	2474	6
BP4_15_03	102	243	76	2.38	0.161	0.001	0.705	0.003	10.370	0.170	0.466	0.007	100	2471	9
BP4_16_01	333	114	174	0.34	0.177	0.000	0.101	0.000	11.599	0.177	0.474	0.007	95	2628	4
BP4_12_01	3385	446	1776	0.13	0.168	0.000	0.039	0.000	11.712	0.174	0.505	0.007	104	2538	2
BP4_17_01	838	115	394	0.14	0.163	0.000	0.039	0.000	10.203	0.154	0.454	0.007	97	2488	3
BP4_19_01	292	179	183	0.61	0.192	0.001	0.180	0.001	14.016	0.214	0.530	0.008	99	2759	4
BP4_16_02	454	225	250	0.50	0.179	0.000	0.140	0.000	12.013	0.183	0.486	0.007	96	2648	4
BP4_20_01	286	155	175	0.54	0.195	0.001	0.161	0.001	14.104	0.217	0.524	0.008	98	2786	5
Aluminous granulite (Sample no. BP12A)															
BP12A.1.1	264	4	21	0.02	0.054	0.001	0.002	0.001	0.646	0.047	0.086	0.006	137	388	29
BP12A.2.1	218	2	18	0.01	0.055	0.002	0.002	0.005	0.685	0.059	0.090	0.006	129	428	90
BP12A.3.1	288	3	23	0.01	0.057	0.001	0.004	0.001	0.695	0.050	0.088	0.006	111	491	22
BP12A.3.2	267	2	21	0.01	0.056	0.001	0.003	0.001	0.677	0.049	0.088	0.006	118	457	27
BP12A.4.1	258	5	20	0.02	0.057	0.001	0.010	0.002	0.677	0.050	0.086	0.006	105	505	32
BP12A.5.1	283	5	23	0.02	0.055	0.001	0.003	0.001	0.673	0.049	0.088	0.006	127	427	24
BP12A.6.1	264	2	21	0.01	0.057	0.000	0.004	0.001	0.688	0.049	0.088	0.006	114	477	18
BP12A.6.2	279	2	22	0.01	0.057	0.001	0.004	0.002	0.691	0.051	0.088	0.006	111	489	30
BP12A.7.1	370	4	29	0.01	0.056	0.000	0.002	0.001	0.665	0.048	0.087	0.006	123	436	20
BP12A.8.1	233	2	18	0.01	0.056	0.001	0.000	0.003	0.667	0.051	0.086	0.006	116	458	49
BP12A.9.1	252	2	20	0.01	0.059	0.001	0.005	0.001	0.692	0.050	0.085	0.006	92	569	19
BP12A.10.1	247	4	20	0.02	0.056	0.001	0.007	0.001	0.675	0.049	0.087	0.006	114	471	21
BP12A.11.1	326	5	27	0.02	0.056	0.002	0.004	0.004	0.692	0.055	0.090	0.006	125	445	65
BP12A.12.1	348	2	29	0.01	0.055	0.001	-0.001	0.003	0.696	0.053	0.092	0.006	135	417	48
BP12A.13.1	241	2	20	0.01	0.057	0.001	0.002	0.002	0.731	0.054	0.093	0.007	115	497	35

Table 5 continued

Points	U (ppm)	Th (ppm)	Total Pb (ppm)	Th/U	$^{207}\text{Pb}/^{206}\text{Pb}$	$\pm 1\sigma$	$^{208}\text{Pb}/^{206}\text{Pb}$	$\pm 1\sigma$	$^{207}\text{Pb}/^{235}\text{U}$	$\pm 1\sigma$	$^{206}\text{Pb}/^{238}\text{U}$	$\pm 1\sigma$	% conc.	$^{207}\text{Pb}/^{206}\text{Pb}$ age (Ma)	$\pm 1\sigma$
BP12A.14.1	294	3	25	0.01	0.056	0.001	0.003	0.001	0.721	0.053	0.093	0.007	127	452	27
BP12A.15.1	277	1	23	0.00	0.056	0.001	0.002	0.002	0.693	0.052	0.089	0.006	118	468	39
BP12A.16.1	229	2	18	0.01	0.055	0.001	-0.001	0.003	0.665	0.052	0.087	0.006	125	429	57
Aluminous granulite (Sample no. BP12C)															
BP12C.1.1	604	13	47	0.02	0.058	0.001	0.006	0.001	0.677	0.049	0.084	0.006	97	539	19
BP12C.2.1	307	16	29	0.05	0.072	0.001	0.028	0.001	0.998	0.072	0.101	0.007	64	975	20
BP12C.3.1	1122	32	61	0.03	0.059	0.000	0.007	0.001	0.484	0.035	0.060	0.004	67	561	15
BP12C.4.1	279	13	21	0.05	0.059	0.001	0.015	0.001	0.674	0.049	0.082	0.006	87	583	28
BP12C.5.1	394	6	29	0.02	0.058	0.001	0.004	0.001	0.639	0.047	0.080	0.006	93	532	26
BP12C.5.2	424	14	32	0.03	0.057	0.001	0.010	0.001	0.647	0.047	0.082	0.006	101	504	27
BP12C.6.1	328	16	26	0.05	0.059	0.001	0.016	0.001	0.704	0.051	0.087	0.006	96	559	27
BP12C.7.1	252	11	19	0.04	0.057	0.001	0.013	0.002	0.655	0.048	0.083	0.006	101	507	35
BP12C.8.1	388	15	36	0.04	0.057	0.002	0.014	0.005	0.796	0.068	0.101	0.007	123	503	87
BPC12.9.1	224	2	19	0.01	0.058	0.001	0.001	0.002	0.728	0.055	0.091	0.006	109	519	41
BP12C.10.1	225	2	19	0.01	0.058	0.001	0.002	0.002	0.729	0.055	0.092	0.006	110	514	45
BP12C.11.1	273	14	22	0.05	0.058	0.002	0.019	0.003	0.703	0.055	0.089	0.006	107	513	59
BP12C.12.1	209	2	17	0.01	0.060	0.001	0.007	0.002	0.717	0.053	0.087	0.006	92	586	29
BP12C.13.1	484	14	40	0.03	0.058	0.000	0.010	0.001	0.715	0.051	0.090	0.006	106	523	18
BP12C.14.1	232	12	19	0.05	0.055	0.001	0.013	0.002	0.689	0.052	0.090	0.006	130	430	40
BP12C.14.2	262	14	23	0.05	0.059	0.002	0.019	0.005	0.765	0.065	0.094	0.007	104	558	85
BP12C.15.1	201	3	17	0.01	0.058	0.001	0.005	0.001	0.724	0.052	0.091	0.006	105	530	21
BP12C.16.1	554	13	49	0.02	0.058	0.001	0.009	0.002	0.766	0.057	0.096	0.007	110	534	34
Meta-ironstone (Sample no. DG33E)															
DG33E.1.1	576	92	43	0.16	0.057	0.001	0.055	0.001	0.612	0.050	0.078	0.006	97	498	30
DG33E.2.1	571	92	49	0.16	0.059	0.001	0.067	0.001	0.715	0.058	0.088	0.007	99	554	25
DG33E.3.1	621	91	50	0.15	0.059	0.001	0.058	0.002	0.684	0.056	0.085	0.007	95	551	32
DG33E.4.1	508	89	41	0.18	0.058	0.001	0.056	0.001	0.676	0.055	0.084	0.007	98	535	29

Table 5 continued

Points	U (ppm)	Th (ppm)	Total Pb (ppm)	Th/U	$^{207}\text{Pb}/^{206}\text{Pb}$	$\pm 1\sigma$	$^{208}\text{Pb}/^{206}\text{Pb}$	$\pm 1\sigma$	$^{207}\text{Pb}/^{235}\text{U}$	$\pm 1\sigma$	$^{206}\text{Pb}/^{238}\text{U}$	$\pm 1\sigma$	% conc.	$^{207}\text{Pb}/^{206}\text{Pb}$ age (Ma)	$\pm 1\sigma$
DG33E.5.1	524	92	46	0.18	0.058	0.002	0.060	0.005	0.729	0.066	0.090	0.007	102	548	81
DG33E.6.1	494	85	41	0.17	0.058	0.001	0.061	0.003	0.694	0.059	0.087	0.007	102	528	50
DG33E.7.1	660	99	51	0.15	0.058	0.001	0.035	0.001	0.662	0.054	0.082	0.006	94	543	24
DG33E.8.1	596	91	49	0.15	0.057	0.001	0.057	0.001	0.678	0.055	0.086	0.007	107	499	22
DG33E.9.1	526	90	44	0.17	0.058	0.001	0.061	0.002	0.683	0.056	0.086	0.007	104	511	35
DG33E.10.1	799	86	61	0.11	0.059	0.001	0.030	0.001	0.663	0.053	0.082	0.006	91	558	20
DG33E.11.1	561	93	43	0.17	0.057	0.001	0.063	0.001	0.621	0.050	0.079	0.006	101	486	25
DG33E.12.1	672	93	52	0.14	0.058	0.001	0.033	0.001	0.658	0.053	0.082	0.006	95	534	22
DG33E.13.1	529	94	43	0.18	0.057	0.001	0.047	0.001	0.668	0.054	0.085	0.007	105	500	22
Migmatitic hornblende gneiss (Sample no. DG33F)															
DG33F.33.3	137	112	58	0.82	0.156	0.002	0.279	0.004	7.139	0.411	0.331	0.018	76	2416	19
DG33F.34.1	354	90	164	0.25	0.155	0.001	0.087	0.001	9.232	0.515	0.432	0.024	96	2402	9
DG33F.35.1	462	167	191	0.36	0.154	0.001	0.103	0.001	8.134	0.453	0.382	0.021	87	2396	8
DG33F.36.1	403	226	199	0.56	0.157	0.001	0.163	0.001	9.395	0.524	0.434	0.024	96	2423	8
DG33F.36.2	156	172	88	1.10	0.158	0.001	0.309	0.002	9.672	0.547	0.443	0.024	97	2439	14
DG33F.37.1	184	34	17	0.18	0.062	0.002	0.070	0.003	0.788	0.051	0.093	0.005	87	657	62
DG33F.37.2	193	26	17	0.13	0.059	0.003	0.046	0.007	0.748	0.061	0.092	0.005	99	569	116
DG33F.37.3	228	41	31	0.18	0.102	0.001	0.088	0.001	1.890	0.106	0.135	0.007	49	1656	13
DG33F.38.1	647	172	279	0.27	0.155	0.000	0.076	0.000	8.692	0.479	0.407	0.022	92	2401	3
DG33F.39.1	558	149	190	0.27	0.147	0.001	0.087	0.001	6.476	0.361	0.319	0.018	77	2314	8
DG33F.39.2	514	143	169	0.28	0.142	0.001	0.085	0.001	6.079	0.339	0.311	0.017	77	2251	9
DG33F.40.1	178	118	81	0.66	0.153	0.001	0.212	0.002	8.099	0.454	0.384	0.021	88	2378	11
DG33F.41.1	517	140	208	0.27	0.158	0.001	0.082	0.001	8.187	0.455	0.376	0.021	85	2432	7
DG33F.42.1	242	93	94	0.38	0.147	0.001	0.111	0.001	7.272	0.408	0.358	0.020	85	2313	11
DG33F.10.2	148	69	57	0.47	0.146	0.001	0.138	0.002	6.906	0.393	0.343	0.019	83	2300	17
DG33F.43.1	170	97	28	0.57	0.106	0.002	0.161	0.004	2.217	0.135	0.152	0.008	53	1723	38
DG33F.43.2	384	156	165	0.41	0.155	0.000	0.117	0.001	8.390	0.464	0.393	0.022	89	2402	5

Table 5 continued

Points	U (ppm)	Th (ppm)	Total Pb (ppm)	Th/U	$^{207}\text{Pb}/^{206}\text{Pb}$	$\pm 1\sigma$	$^{208}\text{Pb}/^{206}\text{Pb}$	$\pm 1\sigma$	$^{207}\text{Pb}/^{235}\text{U}$	$\pm 1\sigma$	$^{206}\text{Pb}/^{238}\text{U}$	$\pm 1\sigma$	% conc.	$^{207}\text{Pb}/^{206}\text{Pb}$ age (Ma)	$\pm 1\sigma$
DG33F.42.2	111	84	52	0.76	0.162	0.001	0.210	0.002	8.915	0.499	0.399	0.022	87	2478	10
DG33F.44.1	326	119	125	0.37	0.149	0.001	0.108	0.001	7.174	0.399	0.350	0.019	83	2329	7
DG33F.45.1	343	131	109	0.38	0.145	0.001	0.128	0.001	5.754	0.319	0.288	0.016	71	2287	6
DG33F.45.2	379	237	183	0.63	0.159	0.000	0.180	0.001	9.181	0.508	0.419	0.023	92	2443	5
DG33F.45.3	344	123	151	0.36	0.149	0.001	0.106	0.001	8.322	0.469	0.404	0.022	94	2337	13
DG33F.46.1	532	167	224	0.31	0.151	0.001	0.087	0.001	8.216	0.461	0.395	0.022	91	2357	11
DG33F.25.2	327	142	120	0.43	0.147	0.001	0.129	0.001	6.771	0.384	0.333	0.018	80	2315	15
DG33F.47.1	362	42	67	0.12	0.120	0.001	0.054	0.001	3.038	0.175	0.183	0.010	55	1959	21
DG33F.48.1	191	40	19	0.21	0.062	0.003	0.232	0.007	0.755	0.059	0.088	0.005	79	689	103
DG33F.29.1	477	284	223	0.60	0.160	0.001	0.175	0.001	8.929	0.500	0.405	0.022	89	2456	10
DG33F.29.2	634	208	312	0.33	0.160	0.001	0.098	0.001	9.939	0.555	0.452	0.025	98	2452	9
DG33F.30.1	112	67	48	0.60	0.148	0.002	0.185	0.003	7.644	0.446	0.376	0.021	89	2318	24
DG33F.30.2	356	176	161	0.49	0.156	0.001	0.144	0.001	8.650	0.486	0.402	0.022	90	2412	11
DG33F.31.1	184	80	78	0.43	0.155	0.002	0.128	0.002	8.074	0.466	0.378	0.021	86	2401	21
DG33F.31.2	776	163	369	0.21	0.158	0.001	0.058	0.000	9.918	0.552	0.455	0.025	99	2437	8
DG33F.31.3	313	141	147	0.45	0.159	0.001	0.136	0.001	9.274	0.522	0.423	0.023	93	2447	12
DG33F.32.1	344	146	156	0.42	0.159	0.001	0.130	0.001	8.890	0.495	0.407	0.022	90	2440	8
DG33F.32.2	113	75	13	0.66	0.059	0.002	0.311	0.006	0.766	0.054	0.094	0.005	101	574	84
DG33F.33.1	180	115	75	0.64	0.153	0.001	0.207	0.001	7.362	0.410	0.350	0.019	81	2375	7
DG33F.33.2	393	49	67	0.12	0.126	0.001	0.060	0.001	2.913	0.166	0.168	0.009	49	2039	18
DG33F.23.1	202	100	80	0.50	0.152	0.001	0.136	0.001	7.433	0.415	0.356	0.020	83	2365	9
DG33F.23.2	468	268	181	0.57	0.146	0.001	0.170	0.001	6.838	0.380	0.339	0.019	82	2303	7
DG33F.24.1	182	92	57	0.51	0.134	0.001	0.176	0.001	5.108	0.287	0.276	0.015	73	2153	12
DG33F.24.2	217	140	83	0.65	0.148	0.001	0.203	0.001	6.720	0.376	0.330	0.018	79	2319	10
DG33F.25.1	91	78	47	0.86	0.153	0.001	0.245	0.002	9.041	0.515	0.428	0.024	96	2383	16
DG33F.26.1	228	117	69	0.51	0.132	0.001	0.166	0.001	4.901	0.276	0.270	0.015	73	2122	12
DG33F.26.2	209	95	86	0.45	0.148	0.001	0.152	0.001	7.489	0.419	0.367	0.020	87	2323	10
DG33F.27.1	353	197	183	0.56	0.154	0.001	0.159	0.001	9.742	0.542	0.459	0.025	102	2388	7

Table 5 continued

Points	U (ppm)	Th (ppm)	Total Pb (ppm)	Th/U	$^{207}\text{Pb}/^{206}\text{Pb}$	$\pm 1\sigma$	$^{208}\text{Pb}/^{206}\text{Pb}$	$\pm 1\sigma$	$^{207}\text{Pb}/^{235}\text{U}$	$\pm 1\sigma$	$^{206}\text{Pb}/^{238}\text{U}$	$\pm 1\sigma$	% conc.	$^{207}\text{Pb}/^{206}\text{Pb}$ age (Ma)	$\pm 1\sigma$
DG33F.27.2	117	76	50	0.65	0.152	0.001	0.199	0.002	7.630	0.433	0.365	0.020	85	2363	15
DG33F.28.1	553	309	274	0.56	0.156	0.001	0.163	0.001	9.374	0.519	0.436	0.024	97	2411	6
DG33F.28.2	750	210	369	0.28	0.157	0.000	0.082	0.000	9.962	0.551	0.462	0.025	101	2419	5
DG33F.18.2	470	76	169	0.16	0.148	0.001	0.044	0.001	7.132	0.396	0.350	0.019	83	2321	7
DG33F.17.3	299	75	49	0.25	0.115	0.002	0.088	0.003	2.513	0.147	0.159	0.009	51	1874	26
DG33F.17.4	639	389	290	0.61	0.156	0.001	0.172	0.001	8.482	0.472	0.395	0.022	89	2408	8
DG33F.18.1	282	148	109	0.52	0.156	0.003	0.169	0.006	6.934	0.420	0.323	0.018	75	2408	33
DG33F.19.1	251	35	21	0.14	0.064	0.007	0.065	0.015	0.699	0.090	0.080	0.004	68	727	232
DG33F.19.2	851	187	309	0.22	0.153	0.001	0.064	0.001	7.303	0.410	0.346	0.019	80	2380	11
DG33F.19.3	191	60	53	0.31	0.131	0.001	0.093	0.001	4.712	0.266	0.262	0.014	71	2106	13
DG33F.20.1	155	75	40	0.48	0.128	0.001	0.138	0.002	4.171	0.236	0.237	0.013	66	2065	15
DG33F.21.1	487	305	190	0.63	0.144	0.000	0.177	0.001	6.806	0.377	0.342	0.019	83	2278	6
DG33F.21.2	75	78	34	1.04	0.148	0.001	0.309	0.003	7.288	0.415	0.356	0.020	84	2328	16
DG33F.22.1	357	143	151	0.40	0.147	0.001	0.117	0.000	7.874	0.437	0.388	0.021	91	2313	6
DG33F.11.1	704	328	215	0.47	0.139	0.001	0.138	0.002	5.288	0.299	0.276	0.015	71	2213	14
DG33F.11.2	1243	435	544	0.35	0.156	0.001	0.106	0.001	8.650	0.480	0.402	0.022	90	2415	7
DG33F.12.1	347	190	180	0.55	0.159	0.001	0.152	0.002	10.021	0.565	0.457	0.025	99	2446	12
DG33F.13.1	609	273	259	0.45	0.154	0.001	0.126	0.001	8.199	0.460	0.386	0.021	88	2393	11
DG33F.13.2	630	97	246	0.15	0.156	0.001	0.048	0.001	8.069	0.452	0.376	0.021	85	2409	11
DG33F.14.1	112	86	46	0.77	0.153	0.003	0.257	0.006	6.942	0.420	0.330	0.018	77	2375	32
DG33F.15.1	661	201	300	0.30	0.156	0.001	0.089	0.001	9.073	0.507	0.423	0.023	94	2409	10
DG33F.16.1	445	242	204	0.54	0.157	0.001	0.148	0.001	8.859	0.498	0.408	0.022	91	2428	11
DG33F.17.1	455	253	199	0.56	0.151	0.001	0.163	0.002	8.053	0.453	0.386	0.021	89	2362	12
DG33F.17.2	247	147	106	0.60	0.152	0.002	0.232	0.004	7.110	0.412	0.340	0.019	80	2364	21

Table 5 continued

Points	U (ppm)	Th (ppm)	Total Pb (ppm)	Th/U	$^{207}\text{Pb}/^{206}\text{Pb}$	$^{208}\text{Pb}/^{206}\text{Pb}$	$^{207}\text{Pb}/^{235}\text{U}$	$^{206}\text{Pb}/^{238}\text{U}$	% conc.	$^{207}\text{Pb}/^{206}\text{Pb}$ age (Ma)	$\pm 1\sigma$	$\pm 1\sigma$	$\pm 1\sigma$	$\pm 1\sigma$
Migmatitic quartzfeldspathic gneiss (Sample no. BP6)														
BP6-01	642	143	286	0.22	0.158	0.001	0.000	0.424	94	2435	0.004	0.104	0.006	7
BP6-02	218	152	70	0.70	0.141	0.001	0.002	0.267	68	2240	0.003	0.081	0.006	18
BP6-03	979	132	393	0.13	0.152	0.000	0.000	0.392	90	2374	0.004	0.090	0.006	5
BP6-04	1389	314	405	0.23	0.148	0.000	0.001	0.276	68	2324	0.003	0.061	0.006	5
BP6-05	1362	150	523	0.11	0.156	0.000	0.000	0.376	85	2412	0.004	0.088	0.006	5
BP6-06	2148	614	760	0.29	0.150	0.000	0.000	0.329	78	2344	0.003	0.073	0.006	5
BP6-07	1607	460	518	0.29	0.147	0.001	0.000	0.300	73	2314	0.003	0.067	0.006	6
BP6-08	1901	532	886	0.28	0.161	0.001	0.000	0.436	95	2464	0.004	0.108	0.006	6
BP6-09	304	219	163	0.72	0.161	0.001	0.001	0.458	98	2469	0.005	0.129	0.006	10
BP6-10	1164	241	448	0.21	0.147	0.001	0.000	0.366	87	2315	0.004	0.084	0.006	7
BP6_2_01	1548	248	619	0.16	0.156	0.000	0.000	0.387	88	2409	0.005	0.116	0.006	2
BP6_2_02	343	132	116	0.38	0.140	0.001	0.001	0.307	77	2227	0.004	0.090	0.006	8
BP6_4_01	1309	1059	693	0.81	0.159	0.000	0.000	0.432	94	2450	0.006	0.134	0.006	3
BP6_4_02	437	198	215	0.45	0.152	0.000	0.001	0.445	100	2372	0.006	0.135	0.006	5
BP6_6_01	2301	1553	1185	0.67	0.159	0.000	0.000	0.436	95	2450	0.006	0.134	0.006	2
BP6_9_01	773	155	344	0.20	0.150	0.000	0.000	0.428	98	2345	0.006	0.126	0.006	4
BP6_13_01	1926	184	913	0.10	0.159	0.000	0.000	0.462	100	2445	0.006	0.142	0.006	2
BP6_13_02	563	90	228	0.16	0.154	0.000	0.000	0.389	89	2387	0.005	0.118	0.006	4
BP6_10_01	1823	259	836	0.14	0.159	0.000	0.000	0.445	97	2443	0.006	0.136	0.006	2
BP6_14_01	75	66	43	0.88	0.166	0.001	0.002	0.467	98	2515	0.007	0.171	0.007	11
BP6_15_01	494	148	136	0.30	0.132	0.001	0.001	0.242	66	2123	0.003	0.067	0.003	9
BP6_15_02	1850	358	825	0.19	0.155	0.000	0.000	0.427	96	2397	0.006	0.128	0.006	3
BP6_16_01	449	239	232	0.53	0.163	0.000	0.001	0.458	98	2487	0.006	0.148	0.006	5
BP6_16_02	3212	185	258	0.06	0.058	0.000	0.000	0.087	102	525	0.001	0.010	0.001	9
BP6_17_01	1374	318	603	0.23	0.159	0.000	0.000	0.416	92	2442	0.006	0.128	0.006	2
BP6_15_03	3664	129	354	0.04	0.076	0.000	0.000	0.102	57	1103	0.001	0.016	0.001	6
BP6-16_03	2897	174	245	0.06	0.058	0.000	0.000	0.091	109	514	0.001	0.011	0.001	8

Table 5 continued

Points	U (ppm)	Th (ppm)	Total Pb (ppm)	Th/U	$^{207}\text{Pb}/^{206}\text{Pb}$	$^{208}\text{Pb}/^{206}\text{Pb}$	$^{207}\text{Pb}/^{235}\text{U}$	$^{206}\text{Pb}/^{238}\text{U}$	% conc.	$^{207}\text{Pb}/^{206}\text{Pb}$ age (Ma)
					$\pm 1\sigma$	$\pm 1\sigma$	$\pm 1\sigma$	$\pm 1\sigma$		$\pm 1\sigma$
BP6-20_01	1233	278	563	0.23	0.157	0.068	9.393	0.433	95	2428
BP6_19_01	1857	128	169	0.07	0.062	0.025	0.829	0.096	86	688
BP6_21_02	2219	1099	1023	0.50	0.158	0.155	8.877	0.407	90	2437
Foliated quartz breccia (Sample no. DG17B)										
DG17B.7.1	907	90	84	0.10	0.072	0.037	0.950	0.096	60	978
DG17B.7.2	778	103	165	0.13	0.120	0.051	3.472	0.210	63	1956
DG17B.7.3	647	99	50	0.15	0.058	0.050	0.642	0.081	97	517
DG17B.8.1	597	289	269	0.48	0.156	0.146	8.613	0.400	90	2413
DG17B.8.2	451	152	220	0.34	0.156	0.104	9.669	0.449	99	2415
DG17B.9.1	1069	243	713	0.23	0.251	0.062	20.349	0.589	94	3188
DG17B.9.2	905	22	402	0.02	0.135	0.006	8.420	0.453	111	2161
DG17B.10.1	411	98	153	0.24	0.147	0.093	7.059	0.347	83	2316
DG17B.11.1	676	117	188	0.17	0.132	0.065	4.889	0.269	73	2120
DG17B.12.1	1307	54	167	0.04	0.067	0.015	1.255	0.136	97	842
DG17B.12.2	288	56	140	0.19	0.173	0.074	10.809	0.453	93	2589
DG17B.13.1.1	664	109	233	0.16	0.149	0.055	6.921	0.337	80	2332
DG17B.13.1.2	438	73	150	0.17	0.135	0.060	6.178	0.333	86	2158
DG17B.13.2	701	81	191	0.12	0.121	0.045	4.530	0.271	78	1973
DG17B.13.3	208	126	109	0.61	0.165	0.201	10.150	0.445	95	2510
DG17B.13.4	434	132	144	0.30	0.141	0.123	5.938	0.306	77	2238
DG17B.14.1	1094	36	149	0.03	0.094	0.018	1.784	0.138	55	1504
DG17B.14.2	245	184	161	0.75	0.162	0.221	12.319	0.552	114	2475
DG17B.1.1	467	373	247	0.80	0.163	0.224	9.928	0.442	95	2485
DG17B.1.2	433	398	227	0.92	0.165	0.257	9.655	0.424	91	2507
DG17B.1.3	630	293	253	0.47	0.152	0.153	7.459	0.356	83	2367
DG17B.2.1	327	123	116	0.38	0.152	0.142	6.563	0.314	74	2364
DG17B.2.2	481	71	138	0.15	0.145	0.051	5.446	0.273	68	2285

Table 5 continued

Points	U (ppm)	Th (ppm)	Total Pb (ppm)	Th/U	$^{207}\text{Pb}/^{206}\text{Pb}$	$\pm 1\sigma$	$^{208}\text{Pb}/^{206}\text{Pb}$	$\pm 1\sigma$	$^{207}\text{Pb}/^{235}\text{U}$	$\pm 1\sigma$	$^{206}\text{Pb}/^{238}\text{U}$	$\pm 1\sigma$	% conc.	$^{207}\text{Pb}/^{206}\text{Pb}$ age (Ma)	$\pm 1\sigma$
DG17B.3.1	319	142	151	0.45	0.163	0.001	0.130	0.002	9.507	0.632	0.423	0.027	92	2486	15
DG17B.3.2	457	250	237	0.55	0.166	0.001	0.157	0.001	10.357	0.684	0.453	0.029	96	2514	12
DG17B.4.1	585	193	181	0.33	0.154	0.001	0.082	0.002	6.104	0.405	0.287	0.019	68	2391	14
DG17B.4.2	762	141	335	0.19	0.161	0.001	0.046	0.001	9.370	0.617	0.422	0.027	92	2467	11
DG17B.5.1	1390	57	283	0.04	0.114	0.001	0.012	0.001	3.290	0.217	0.209	0.014	66	1864	13
DG17B.5.2	1091	140	307	0.13	0.143	0.001	0.048	0.001	5.374	0.353	0.273	0.018	69	2259	10
DG17B.5.3	1107	92	401	0.08	0.165	0.001	0.021	0.001	8.043	0.527	0.353	0.023	78	2510	8
DG17B.5.4	885	133	383	0.15	0.164	0.001	0.052	0.001	9.284	0.609	0.411	0.027	89	2494	9
DG17B.6.1	976	35	171	0.04	0.090	0.001	0.018	0.001	2.273	0.153	0.183	0.012	75	1432	23
DG17B.6.2	170	70	98	0.41	0.159	0.002	0.121	0.003	11.359	0.779	0.518	0.034	110	2447	25
DG17B.15.1	750	144	317	0.19	0.144	0.001	0.066	0.000	8.080	0.529	0.406	0.026	96	2282	9
DG17B.16.1	733	149	255	0.20	0.134	0.001	0.071	0.000	6.191	0.407	0.335	0.022	87	2150	10
DG17B.17.1	802	75	232	0.09	0.130	0.001	0.034	0.000	5.164	0.339	0.289	0.019	78	2094	10
DG17B.17.2	224	124	118	0.55	0.151	0.001	0.169	0.001	9.632	0.638	0.464	0.030	104	2354	14
DG17B.18.1	303	282	193	0.93	0.167	0.001	0.257	0.001	11.932	0.780	0.519	0.034	107	2524	7
DG17B.18.2	1151	193	200	0.17	0.114	0.001	0.031	0.001	2.708	0.178	0.172	0.011	55	1871	11
DG17B.19.1	174	199	119	1.14	0.165	0.001	0.331	0.002	12.095	0.793	0.532	0.034	110	2505	9
DG17B.19.2	1043	58	394	0.06	0.132	0.000	0.012	0.000	6.955	0.454	0.382	0.025	98	2127	6
DG17B.20.1	520	31	43	0.06	0.058	0.001	0.018	0.001	0.716	0.048	0.090	0.006	104	529	28
DG17B.21.1	226	129	124	0.57	0.169	0.001	0.163	0.001	11.099	0.727	0.477	0.031	99	2544	8
DG17B.22.1	959	91	97	0.09	0.068	0.001	0.026	0.001	0.960	0.064	0.103	0.007	74	853	24
DG17B.22.2	1123	44	144	0.04	0.067	0.000	0.011	0.000	1.283	0.084	0.138	0.009	98	852	13
DG17B.23.1	309	83	126	0.27	0.144	0.001	0.075	0.001	7.701	0.504	0.389	0.025	93	2272	9
DG17B.24.1	404	186	239	0.46	0.158	0.001	0.133	0.001	11.591	0.756	0.533	0.034	113	2432	6
DG17B.24.2	566	151	258	0.27	0.149	0.001	0.090	0.001	8.784	0.573	0.427	0.028	98	2336	6
DG17B.25.1	186	269	121	1.45	0.161	0.001	0.400	0.002	10.741	0.704	0.484	0.031	103	2466	9
DG17B.25.2	70	81	53	1.16	0.164	0.001	0.341	0.003	13.133	0.873	0.582	0.038	119	2494	15
DG17B.26.1	638	140	220	0.22	0.137	0.001	0.080	0.001	6.230	0.407	0.329	0.021	83	2196	6

Table 5 continued

Points	U (ppm)	Th (ppm)	Total Pb (ppm)	Th/U	$^{207}\text{Pb}/^{206}\text{Pb}$	$\pm 1\sigma$	$^{208}\text{Pb}/^{206}\text{Pb}$	$\pm 1\sigma$	$^{207}\text{Pb}/^{235}\text{U}$	$\pm 1\sigma$	$^{206}\text{Pb}/^{238}\text{U}$	$\pm 1\sigma$	% conc.	$^{207}\text{Pb}/^{206}\text{Pb}$ age (Ma)	$\pm 1\sigma$
DG17B.26.2	616	51	160	0.08	0.126	0.001	0.016	0.000	4.534	0.299	0.262	0.017	74	2036	12
DG17B.26.3	411	126	159	0.31	0.146	0.001	0.124	0.001	7.122	0.470	0.354	0.023	85	2299	13
DG17B.27.1	719	753	339	1.05	0.179	0.001	0.265	0.001	9.235	0.605	0.374	0.024	77	2645	8
DG17B.27.2	522	128	244	0.25	0.165	0.001	0.085	0.000	9.870	0.648	0.433	0.028	92	2510	9
DG17B.28.1	197	91	123	0.46	0.183	0.001	0.131	0.001	13.942	0.921	0.552	0.036	106	2683	12
DG17B.28.2	550	108	213	0.20	0.158	0.001	0.063	0.000	7.998	0.526	0.368	0.024	83	2432	11
DG17B.29.1	461	316	269	0.69	0.165	0.001	0.197	0.001	11.293	0.740	0.497	0.032	104	2506	8
DG17B.30.1	1022	219	267	0.21	0.134	0.001	0.039	0.001	4.710	0.309	0.255	0.017	68	2149	9
DG17B.31.1	844	52	205	0.06	0.112	0.001	0.012	0.000	3.866	0.255	0.250	0.016	79	1832	14
DG17B.31.2	438	93	173	0.21	0.148	0.001	0.079	0.000	7.641	0.503	0.374	0.024	88	2325	11
DG17B.32.1	524	299	289	0.57	0.163	0.001	0.178	0.000	10.741	0.703	0.478	0.031	101	2487	8

* FCI (1099 \pm 0.6 Ma; Paces and Miller, 1993)) was used as a age standard.

† SL13 (U concentration = 238 ppm; Clauoué-Long et al., 1995) was used as a standard to measure U content

Table 6: Analytical results of EPMA U-Th-total Pb geochronology

Points	ThO ₂	UO ₂	PbO	SiO ₂	CaO	P ₂ O ₅	Y ₂ O ₃	La ₂ O ₃	Ce ₂ O ₃	Pr ₂ O ₃	Nd ₂ O ₃	Sm ₂ O ₃	Gd ₂ O ₃	Dy ₂ O ₃	SO ₃	Total	Age	±2σ	
Charnokitic augen gneiss (Sample no. BP1)																			
BP1_Minz17-1	8.27	0.13	0.35	1.08	1.16	29.18	0.60	14.06	28.68	2.90	9.61	3.45	0.69	0.17	0.00	100.32	904	25	
BP1_Minz17-2	8.18	0.13	0.34	1.06	1.12	29.29	0.60	14.13	28.87	2.89	9.57	3.36	0.70	0.19	0.00	100.43	909	25	
BP1_Minz17-3	8.08	0.13	0.30	1.09	1.05	29.38	0.57	14.18	29.24	2.83	9.57	3.44	0.68	0.20	0.00	100.74	809	24	
BP1_Minz17-4	8.13	0.07	0.35	1.46	0.75	28.98	0.16	15.22	30.55	2.89	9.12	3.08	0.33	0.02	0.00	101.12	940	25	
BP1_Minz17-5	10.43	0.10	0.44	2.13	0.76	28.05	0.09	14.94	29.67	2.82	8.71	2.93	0.28	0.00	0.00	101.36	941	21	
BP1_Minz17-6	9.19	0.09	0.31	1.91	0.56	28.19	0.08	15.39	30.52	2.90	8.76	2.86	0.23	0.00	0.01	100.98	759	21	
BP1_Minz17-7	9.13	0.09	0.30	1.90	0.56	28.29	0.06	15.31	29.92	2.91	8.78	2.88	0.23	0.01	0.02	100.40	723	21	
BP1_Minz16-1	7.22	0.10	0.32	0.98	0.91	29.45	0.49	15.58	30.09	2.91	9.29	3.28	0.54	0.17	0.00	101.34	959	28	
BP1_Minz16-2	7.83	0.09	0.35	1.15	0.93	29.30	0.33	15.57	29.96	2.90	9.16	3.22	0.42	0.10	0.00	101.31	984	27	
BP1_Minz16-3	8.61	0.15	0.38	1.20	1.00	28.96	0.36	14.85	29.45	2.82	9.12	3.24	0.59	0.12	0.00	100.86	953	24	
BP1_Minz16-4	7.93	0.17	0.36	0.93	1.21	29.55	1.05	13.81	28.72	2.88	9.63	3.53	0.78	0.25	0.01	100.81	965	27	
BP1_Minz16-5	8.10	0.14	0.36	0.98	1.16	29.41	0.62	14.18	29.18	2.94	9.64	3.40	0.68	0.12	0.01	100.92	953	26	
BP1_Minz16-6	7.02	0.14	0.32	0.87	1.00	29.59	0.42	14.62	30.14	2.94	9.84	3.44	0.57	0.18	0.02	101.08	958	29	
BP1_Minz16-7	7.79	0.04	0.33	0.88	1.17	29.74	0.76	15.25	29.10	2.75	9.34	3.23	0.50	0.18	0.02	101.07	943	26	
BP1_Minz16-8	10.02	0.09	0.43	1.98	0.85	28.31	0.13	14.87	30.11	2.92	9.13	3.00	0.40	0.04	0.00	102.30	952	21	
BP1_Minz16-9	10.01	0.10	0.42	1.81	0.88	28.34	0.15	14.78	29.71	2.89	9.13	3.12	0.39	0.02	0.00	101.75	924	21	
BP1_Minz16-10	10.85	0.09	0.46	2.00	0.91	28.01	0.14	14.63	29.50	2.84	8.87	2.88	0.32	0.02	0.00	101.54	951	20	
BP1_Minz15-1	8.17	0.11	0.29	1.35	0.80	29.17	0.24	14.76	29.73	2.85	9.49	3.23	0.55	0.09	0.01	100.85	786	24	
BP1_Minz15-2	7.98	0.11	0.29	1.29	0.83	29.20	0.47	14.99	29.71	2.88	9.48	3.22	0.48	0.08	0.02	101.02	781	24	
BP1_Minz15-3	9.77	0.12	0.33	1.82	0.71	28.41	0.16	14.75	29.61	2.82	9.20	3.15	0.44	0.03	0.02	101.32	736	20	
BP1_Minz15-4	9.76	0.10	0.30	2.02	0.51	28.09	0.15	15.10	30.48	2.74	9.48	2.85	0.29	0.00	0.00	101.88	689	20	
BP1_Minz15-5	11.88	0.08	0.41	2.34	0.77	27.21	0.11	14.92	29.81	2.70	9.06	2.68	0.27	0.00	0.02	102.25	777	17	

Table 6 continued

Points	ThO ₂	UO ₂	PbO	SiO ₂	CaO	P ₂ O ₅	Y ₂ O ₃	La ₂ O ₃	Ce ₂ O ₃	Pr ₂ O ₃	Nd ₂ O ₃	Sm ₂ O ₃	Gd ₂ O ₃	Dy ₂ O ₃	SO ₃	Total	Age	±2σ
BPI_Mnz15-6	10.30	0.11	0.35	2.15	0.55	27.67	0.08	15.36	30.25	2.71	8.92	2.77	0.29	0.00	0.01	101.52	752	19
BPI_Mnz14-1	6.55	0.06	0.25	0.51	0.91	29.82	0.54	15.71	30.11	1.79	9.51	3.02	0.55	0.19	0.00	99.52	838	29
BPI_Mnz14-3	7.29	0.07	0.26	0.62	0.91	29.67	0.49	15.26	29.89	1.74	9.42	3.00	0.56	0.18	0.00	99.36	774	26
BPI_Mnz14-4	7.56	0.06	0.26	0.70	1.05	29.25	0.44	15.42	29.89	1.89	9.36	3.00	0.47	0.17	0.00	99.50	778	25
BPI_Mnz14-5	14.95	0.05	0.55	1.96	1.28	25.70	0.13	13.43	27.10	1.73	8.50	2.42	0.21	0.03	0.03	98.07	835	15
BPI_Mnz14-6	10.90	0.09	0.36	1.38	1.85	27.44	0.10	14.64	29.18	1.76	8.95	2.69	0.26	0.00	0.02	99.61	733	18
BPI_Mnz14-7	10.05	0.05	0.38	1.07	1.67	28.00	0.15	14.63	29.13	1.75	9.17	2.84	0.37	0.04	0.05	99.37	852	20
BPI_Mnz1-1	7.87	0.10	0.27	0.66	0.95	29.31	0.37	14.73	29.54	1.87	9.67	3.23	0.61	0.12	0.01	99.28	745	24
BPI_Mnz1-2	8.13	0.12	0.28	0.68	1.00	29.63	0.43	14.41	29.56	1.86	9.85	3.10	0.60	0.16	0.00	99.81	748	23
BPI_Mnz1-3	10.32	0.07	0.37	1.17	0.84	28.17	0.11	14.65	29.29	1.75	9.12	2.84	0.41	0.08	0.01	99.20	800	19
BPI_Mnz1-4	10.53	0.06	0.37	1.14	0.93	28.27	0.14	14.66	29.16	1.79	9.08	2.84	0.37	0.03	0.00	99.37	787	19
BPI_Mnz1-5	10.85	0.07	0.39	1.33	0.80	27.86	0.10	14.85	29.40	1.79	8.94	2.86	0.28	0.05	0.00	99.59	799	19
BPI_Mnz1-6	9.77	0.08	0.36	1.26	0.68	28.40	0.06	15.40	30.49	1.84	9.05	2.82	0.34	0.00	0.00	100.56	830	21
BPI_Mnz1-7	7.90	0.10	0.25	1.09	0.51	28.37	0.05	16.04	31.34	1.84	9.06	2.76	0.27	0.01	0.02	99.61	694	23
BPI_Mnz1-8	12.25	0.06	0.47	1.46	0.96	27.57	0.12	14.36	28.72	1.81	8.90	2.86	0.33	0.02	0.01	99.90	857	17
BPI_Mnz1-9	15.17	0.07	0.57	1.92	1.03	26.61	0.13	13.88	27.84	1.83	8.61	2.54	0.30	0.04	0.00	100.54	842	14
BPI_Mnz1-10	10.24	0.08	0.38	1.27	0.73	27.63	0.08	14.88	29.77	1.78	8.96	2.74	0.24	0.03	0.03	98.83	827	20
BPI_Mnz2-1	7.86	0.11	0.32	0.71	0.99	29.02	0.32	14.54	29.39	1.84	9.75	3.24	0.56	0.09	0.00	98.74	872	26
BPI_Mnz2-2	7.96	0.11	0.33	0.66	1.13	29.40	0.36	14.31	29.56	1.97	9.93	3.17	0.65	0.13	0.01	99.70	894	25
BPI_Mnz2-3	8.91	0.07	0.37	0.84	0.97	28.66	0.14	14.91	29.49	1.80	9.07	3.03	0.38	0.07	0.02	98.73	913	23
BPI_Mnz2-4	9.09	0.08	0.37	0.93	0.99	28.80	0.14	14.96	29.49	1.76	9.25	2.94	0.42	0.07	0.00	99.30	897	22
BPI_Mnz2-5	19.47	0.04	0.82	2.39	1.33	25.28	0.17	12.48	25.20	1.56	7.91	2.43	0.29	0.07	0.00	99.43	953	12
BPI_Mnz2-6	7.68	0.09	0.32	0.90	0.67	28.61	0.13	15.17	30.37	1.91	9.46	2.93	0.37	0.02	0.01	98.64	918	26
BPI_Mnz2-7	10.14	0.11	0.44	1.36	0.63	27.96	0.07	15.20	30.09	1.83	8.91	2.52	0.25	0.03	0.01	99.55	950	21
BPI_Mnz2-8	8.78	0.10	0.31	1.19	0.49	28.02	0.06	15.68	30.60	1.67	8.88	2.72	0.21	0.03	0.00	98.74	783	22
BPI_Mnz2-9	4.83	0.08	0.19	0.80	0.24	29.33	0.03	16.69	32.82	1.81	9.46	2.98	0.23	0.00	0.00	99.49	834	38

Table 6 continued

Points	ThO ₂	UO ₂	PbO	SiO ₂	CaO	P ₂ O ₅	Y ₂ O ₃	La ₂ O ₃	Ce ₂ O ₃	Pr ₂ O ₃	Nd ₂ O ₃	Sm ₂ O ₃	Gd ₂ O ₃	Dy ₂ O ₃	SO ₃	Total	Age	±2σ	
BP1_Mnz3-1	8.34	0.06	0.35	0.64	1.13	29.14	0.37	15.05	29.44	1.72	9.47	3.00	0.53	0.16	0.01	99.39	925	24	
BP1_Mnz3-2	8.26	0.03	0.33	0.71	1.05	29.58	0.49	15.68	30.08	1.68	9.49	2.80	0.41	0.11	0.01	100.71	897	24	
BP1_Mnz3-3	7.96	0.04	0.32	0.62	1.06	29.74	0.39	16.03	30.38	1.63	9.38	2.91	0.40	0.09	0.01	100.97	907	25	
BP1_Mnz3-4	9.85	0.07	0.40	1.13	0.82	28.01	0.11	14.81	29.84	1.71	9.18	2.98	0.37	0.02	0.01	99.31	906	21	
BP1_Mnz3-5	9.80	0.08	0.41	1.10	0.92	28.68	0.12	15.03	30.30	1.77	9.51	2.96	0.39	0.03	0.01	101.10	920	22	
BP1_Mnz3-6	8.92	0.09	0.36	1.00	0.80	28.50	0.11	14.94	30.35	1.83	9.57	3.01	0.35	0.02	0.01	99.86	902	23	
BP1_Mnz3-7	7.99	0.12	0.31	0.96	0.72	28.23	0.12	14.99	30.63	1.77	9.64	3.05	0.44	0.02	0.00	99.00	846	25	
BP1_Mnz3-8	9.75	0.07	0.41	1.12	0.85	28.06	0.10	14.98	30.19	1.78	9.53	3.04	0.33	0.04	0.00	100.25	938	22	
BP1_Mnz4-1	8.83	0.07	0.37	1.37	0.92	28.97	0.22	15.29	30.17	2.78	9.27	2.83	0.32	0.01	0.01	101.43	941	23	
BP1_Mnz4-2	12.71	0.04	0.54	2.22	1.15	27.50	0.22	15.04	28.96	2.63	8.63	2.79	0.31	0.04	0.01	102.79	967	17	
BP1_Mnz4-3	7.64	0.08	0.32	0.99	1.08	29.76	0.59	14.93	29.84	2.68	9.66	3.23	0.52	0.15	0.01	101.49	932	27	
BP1_Mnz4-4	8.13	0.08	0.34	1.33	0.81	29.21	0.18	15.42	30.46	2.78	9.79	3.04	0.38	0.05	0.00	102.00	924	25	
BP1_Mnz4-6	8.76	0.08	0.35	1.47	0.82	29.02	0.19	15.52	30.37	2.72	9.45	2.96	0.36	0.02	0.01	102.10	882	23	
Aluminous granulite (Sample no. BP12A)																			
BP12A2-7-1	25.18	0.97	0.63	0.75	5.58	27.68	0.06	13.14	18.80	1.46	3.82	1.63	0.02	0.03	0.02	102.27	520	8	
BP12A2-7-2	25.01	0.98	0.62	0.73	5.60	28.37	0.04	13.23	18.89	1.47	3.88	1.50	0.00	0.00	0.00	100.38	510	8	
BP12A2-8-1	22.95	1.21	0.61	0.52	5.39	28.51	0.08	13.51	19.70	1.53	4.16	1.71	0.03	0.01	0.02	102.02	528	9	
BP12A2-3-1	18.05	1.33	0.50	0.36	4.37	29.60	0.10	15.43	22.52	1.83	4.89	1.98	0.14	0.00	0.05	102.67	524	10	
BP12A2-3-2	19.07	1.28	0.52	0.43	4.49	29.59	0.09	15.10	22.24	1.74	4.75	1.89	0.10	0.06	0.03	102.21	518	10	
BP12A2-3-3	21.25	1.03	0.54	0.66	4.74	28.90	0.06	14.74	21.24	1.56	4.41	1.74	0.00	0.00	0.01	102.57	510	9	
BP12A2-3-4	17.71	1.26	0.50	0.36	4.27	29.43	0.10	15.42	22.58	1.85	5.01	2.05	0.11	0.00	0.02	102.69	534	10	
BP12A2-3-5	21.63	1.16	0.57	0.55	5.04	28.76	0.08	14.21	20.53	1.68	4.37	1.83	0.01	0.00	0.03	98.88	521	9	
BP12A2-3-6	18.12	1.34	0.51	0.38	4.38	29.70	0.09	15.32	22.56	1.80	4.87	1.91	0.11	0.00	0.02	103.23	525	10	
BP12A2-3-7	20.67	1.03	0.54	0.64	4.71	28.76	0.05	14.67	21.31	1.65	4.46	1.89	0.00	0.00	0.01	101.15	519	9	
BP12A2-3-8	20.91	1.02	0.53	0.66	4.70	29.50	0.05	14.76	21.45	1.74	4.37	1.93	0.03	0.01	0.02	103.02	512	9	

Table 6 continued

Points	ThO ₂	UO ₂	PbO	SiO ₂	CaO	P ₂ O ₅	Y ₂ O ₃	La ₂ O ₃	Ce ₂ O ₃	Pr ₂ O ₃	Nd ₂ O ₃	Sm ₂ O ₃	Gd ₂ O ₃	Dy ₂ O ₃	SO ₃	Total	Age	±2σ
Aluminous granulite (Sample no. BP12C)																		
BP12C2-3-1	7.30	0.40	0.19	0.14	1.71	31.02	0.05	16.17	30.69	2.93	9.28	2.86	0.16	0.00	0.01	102.41	509	22
BP12C2-3-2	7.55	0.44	0.20	0.14	1.80	31.14	0.05	16.32	30.54	2.87	9.07	2.81	0.16	0.00	0.01	103.94	518	21
BP12C2-3-3	6.78	0.45	0.18	0.13	1.60	30.92	0.05	15.91	30.70	2.91	9.79	2.71	0.17	0.00	0.01	102.66	507	23
BP12C2-3-4	8.32	0.48	0.22	0.13	2.02	30.90	0.05	16.63	29.98	2.85	8.26	2.55	0.11	0.00	0.00	103.15	505	19
BP12C2-3-5	9.09	0.46	0.23	0.15	2.15	31.46	0.06	16.41	29.43	2.66	7.84	2.50	0.13	0.00	0.01	103.07	502	18
BP12C2-3-6	4.71	0.51	0.14	0.12	1.20	31.36	0.06	15.46	30.93	3.08	10.85	3.00	0.23	0.00	0.00	102.96	488	29
BP12C2-1-1	9.18	0.90	0.27	0.24	2.19	30.97	0.01	15.55	28.14	2.77	9.23	3.16	0.36	0.00	0.02	102.63	520	17
BP12C2-1-2	8.29	0.71	0.24	0.20	1.99	30.49	0.02	16.23	28.76	2.72	9.06	3.20	0.26	0.00	0.00	103.06	531	19
BP12C2-1-3	8.58	0.51	0.24	0.21	1.96	30.85	0.00	15.52	28.65	2.68	9.49	3.14	0.26	0.00	0.01	102.43	529	19
BP12C2-1-4	11.60	0.43	0.29	0.18	2.76	30.43	0.06	16.12	27.91	2.51	7.33	2.56	0.15	0.00	0.00	102.90	512	15
BP12C2-1-5	2.91	0.65	0.18	0.08	0.84	31.04	1.06	13.45	28.02	3.02	13.02	4.55	1.73	0.60	0.01	103.31	797	41
BP12C2-1-6	13.99	0.93	0.40	0.52	2.87	30.33	0.05	12.84	25.22	2.66	10.35	3.25	0.31	0.00	0.01	103.24	545	13
BP12C2-2-1	1.09	1.09	0.15	0.07	0.53	31.29	1.42	13.46	28.58	3.05	12.77	4.41	1.72	0.78	0.01	102.96	745	43
BP12C2-2-2	2.37	0.39	0.14	0.07	0.68	31.19	0.64	13.79	29.05	3.12	12.92	4.45	1.39	0.39	0.00	103.37	891	57
12C2_MNZ1_1	9.62	0.45	0.26	0.15	2.29	31.92	0.07	16.57	29.50	2.61	7.90	2.70	0.14	0.00	0.02	104.19	532	18
12C2_MNZ1_2	10.53	0.45	0.27	0.16	2.53	31.78	0.07	16.46	28.89	2.50	7.53	2.64	0.08	0.01	0.00	103.90	515	17
12C2_MNZ1_3	1.47	0.48	0.07	0.06	0.51	31.39	1.30	14.84	30.91	3.00	10.49	4.29	1.23	0.69	0.01	100.73	522	58
12C2_MNZ1_4	1.82	0.47	0.08	0.06	0.55	31.04	1.08	14.91	30.71	2.85	10.15	4.29	1.14	0.59	0.00	99.75	549	54
12C2_MNZ1_5	5.12	0.40	0.15	0.11	1.39	32.04	0.44	16.16	30.79	2.77	9.24	3.65	0.57	0.27	0.00	103.10	534	30
12C2_MNZ1_6	1.59	0.34	0.07	0.08	0.40	31.86	0.88	15.55	32.01	3.05	10.88	4.43	1.14	0.53	0.00	102.81	532	65
12C2_MNZ1_7	7.13	0.53	0.21	0.16	1.71	30.59	0.05	15.66	29.96	2.79	8.61	2.60	0.16	0.00	0.00	100.16	532	22
12C2_MNZ1_8	8.55	0.46	0.23	0.14	2.05	31.01	0.06	16.39	29.71	2.66	7.97	2.65	0.09	0.00	0.01	101.97	522	20

Table 6 continued

Points	ThO ₂	UO ₂	PbO	SiO ₂	CaO	P ₂ O ₅	Y ₂ O ₃	La ₂ O ₃	Ce ₂ O ₃	Pr ₂ O ₃	Nd ₂ O ₃	Sm ₂ O ₃	Gd ₂ O ₃	Dy ₂ O ₃	SO ₃	Total	Age	±2σ	
12C2_MNZ2_1	0.95	0.42	0.06	0.06	0.32	31.50	1.68	14.49	30.36	3.04	11.19	4.15	1.37	0.88	0.02	100.47	517	75	
12C2_MNZ2_2	0.62	0.26	0.04	0.04	0.28	31.44	1.16	16.07	31.63	2.96	10.56	4.07	1.14	0.62	0.00	100.87	568	116	
12C2_MNZ2_3	0.76	0.07	0.03	0.07	0.19	31.15	1.16	16.11	31.12	2.93	10.77	4.44	1.24	0.62	0.01	100.67	603	167	
12C2_MNZ2_4	0.82	0.20	0.04	0.09	0.20	31.43	1.24	15.16	31.43	3.08	11.06	4.42	1.33	0.69	0.00	101.19	576	116	
12C2_MNZ2_5	8.86	0.49	0.24	0.13	2.12	31.41	0.06	16.24	29.45	2.61	8.14	2.65	0.08	0.00	0.01	102.50	519	19	
12C2_MNZ2_6	12.33	0.52	0.33	0.21	2.87	31.54	0.10	15.34	27.08	2.41	7.50	2.74	0.16	0.00	0.01	103.14	535	15	
12C2_MNZ3_1	1.67	0.87	0.11	0.11	0.51	31.68	1.91	14.46	30.05	2.99	10.88	4.43	1.40	0.96	0.00	102.03	530	41	
12C2_MNZ3_2	0.94	0.35	0.05	0.10	0.23	31.77	1.38	15.42	30.80	3.08	11.15	4.91	1.53	0.77	0.03	102.50	502	82	
12C2_MNZ3_3	1.25	0.45	0.06	0.13	0.31	32.01	1.41	15.58	31.08	3.01	11.05	4.74	1.43	0.78	0.00	103.28	505	64	
12C2_MNZ3_4	1.49	0.80	0.10	0.11	0.51	31.98	1.84	14.43	30.06	2.97	10.99	4.46	1.52	1.00	0.01	102.29	518	44	
12C2_MNZ3_5	2.77	0.68	0.12	0.04	0.83	30.97	0.25	16.25	31.35	2.95	10.11	3.95	0.83	0.15	0.00	101.26	530	37	
12C2_MNZ3_6	3.06	0.65	0.12	0.07	0.91	31.15	0.20	16.10	31.27	3.00	10.40	3.97	0.78	0.14	0.01	101.84	500	36	
12C2_MNZ4_1	8.08	0.49	0.22	0.14	1.93	31.49	0.06	16.16	30.06	2.74	8.35	2.62	0.05	0.00	0.00	102.39	517	20	
12C2_MNZ4_2	9.17	0.47	0.25	0.14	2.17	31.85	0.07	16.42	29.31	2.55	7.93	2.88	0.18	0.03	0.01	103.43	516	19	
12C2_MNZ4_3	3.42	0.55	0.12	0.11	0.92	31.99	1.12	15.32	29.63	2.88	10.11	4.14	1.09	0.68	0.01	102.09	524	36	
12C2_MNZ4_4	4.38	0.47	0.14	0.10	1.05	31.98	1.02	15.51	29.59	2.77	9.71	4.02	1.06	0.52	0.02	102.34	511	32	
12C2_MNZ5_1	8.99	0.77	0.28	0.23	2.14	31.31	0.08	15.07	28.28	2.61	8.89	3.23	0.33	0.01	0.01	102.24	548	18	
12C2_MNZ5_2	11.27	0.53	0.31	0.25	2.65	30.70	0.07	15.14	27.18	2.44	7.67	2.85	0.33	0.04	0.02	101.45	534	16	
12C2_MNZ5_3	6.24	0.35	0.30	0.32	1.34	31.07	0.76	12.88	26.98	2.91	12.55	4.34	1.21	0.39	0.01	101.65	913	31	
12C2_MNZ5_4	3.95	0.44	0.23	0.57	0.94	30.58	1.03	12.79	26.58	2.91	12.63	4.78	1.55	0.60	0.02	99.61	928	41	
Meta-ironstone (Sample no. DG33E)																			
DG33E-Mnz1-1	7.64	0.35	0.19	0.46	1.53	31.62	1.04	17.96	30.21	2.35	6.97	3.07	0.59	0.33	0.00	104.31	488	21	
DG33E-Mnz1-2	9.56	0.33	0.23	0.65	1.71	29.90	0.93	17.44	28.77	2.33	6.59	2.87	0.50	0.29	0.00	102.12	500	18	
DG33E-Mnz1-3	6.31	0.36	0.16	0.35	1.33	30.56	0.90	18.18	30.44	2.47	6.76	3.20	0.53	0.26	0.00	101.79	484	25	
DG33E-Mnz2-1	19.53	0.34	0.45	3.05	1.89	26.09	0.38	15.84	24.27	1.88	5.17	2.57	0.31	0.07	0.00	101.84	500	10	

Table 6 continued

Points	ThO ₂	UO ₂	PbO	SiO ₂	CaO	P ₂ O ₅	Y ₂ O ₃	La ₂ O ₃	Ce ₂ O ₃	Pr ₂ O ₃	Nd ₂ O ₃	Sm ₂ O ₃	Gd ₂ O ₃	Dy ₂ O ₃	SO ₃	Total	Age	±2σ
DG33E-Mnz2-2	7.71	0.32	0.19	0.60	1.56	29.50	0.83	18.14	29.07	2.35	6.39	3.13	0.46	0.27	0.01	100.52	484	21
DG33E-Mnz2-3	12.93	0.29	0.30	1.35	1.89	28.52	0.60	17.31	27.33	2.06	5.90	2.99	0.39	0.18	0.01	102.05	498	14
DG33E-Mnz3-1	12.96	0.29	0.30	1.38	1.85	28.38	0.59	17.49	26.86	2.10	5.66	2.80	0.33	0.20	0.02	101.21	499	14
DG33E-Mnz3-2	11.93	0.29	0.29	1.15	1.84	28.44	0.62	17.68	26.90	2.05	5.53	2.81	0.37	0.14	0.01	100.05	521	15
DG33E-Mnz3-3	5.27	0.36	0.14	0.25	1.09	29.57	0.92	18.60	31.06	2.59	7.08	3.27	0.54	0.28	0.00	101.01	508	29
DG33E-Mnz4-1	2.78	0.56	0.11	0.09	0.85	30.47	0.87	17.53	32.22	2.78	8.58	3.31	0.60	0.22	0.00	100.98	524	39
DG33E-Mnz4-2	1.51	0.62	0.08	0.05	0.76	29.63	1.02	16.80	32.92	2.83	8.93	3.48	0.76	0.30	0.00	99.71	516	50
DG33E-Mnz4-3	3.10	0.49	0.10	0.12	0.86	29.32	0.79	17.28	31.76	2.74	8.26	3.28	0.60	0.22	0.01	98.92	488	38
DG33E-Mnz5-1	4.13	0.32	0.12	0.16	1.06	30.62	0.40	19.27	32.58	2.64	7.25	3.22	0.44	0.15	0.00	102.37	500	35
DG33E-Mnz5-2	4.02	0.39	0.12	0.15	1.24	30.65	0.44	18.91	32.51	2.68	7.38	3.27	0.41	0.13	0.01	102.32	503	34
DG33E-Mnz5-3	3.19	0.41	0.10	0.12	0.98	30.76	0.47	18.88	32.75	2.64	7.64	3.29	0.41	0.12	0.02	101.79	498	39
DG33E-Mnz6-1	7.68	0.30	0.19	0.52	1.52	29.98	0.36	18.74	30.33	2.36	6.62	3.24	0.36	0.06	0.00	102.24	500	22
DG33E-Mnz6-2	7.18	0.33	0.17	0.44	1.44	30.47	0.38	18.58	30.89	2.49	6.94	2.97	0.39	0.09	0.02	102.77	481	22
DG33E-Mnz7-1	1.32	0.56	0.06	0.05	0.86	30.64	0.64	18.61	33.70	2.82	8.43	3.41	0.57	0.18	0.00	101.85	455	54
DG33E-Mnz7-2	1.07	0.48	0.06	0.04	1.06	30.95	0.61	18.04	33.96	3.05	9.02	3.36	0.53	0.16	0.01	102.40	529	65
DG33E-Mnz7-3	1.46	0.61	0.07	0.05	1.04	30.53	0.69	17.85	33.28	2.85	8.82	3.44	0.60	0.16	0.01	101.46	476	50
DG33E-Mnz8-1	2.08	0.69	0.10	0.05	1.16	29.71	0.71	17.48	32.44	2.81	8.47	3.13	0.56	0.21	0.01	99.62	500	41
Foliated quartz breccia (Sample no. DG17B)																		
DG17B-Mnz2-1	7.61	1.56	0.54	0.19	2.12	30.04	2.59	14.88	26.07	2.41	7.49	2.80	0.68	0.56	0.01	99.54	940	21
DG17B-Mnz2-2	8.34	0.54	0.24	1.58	0.61	27.53	3.96	15.41	26.62	2.40	7.54	2.93	0.69	0.72	0.00	99.09	524	20
DG17B-Mnz4-1	6.22	0.55	0.19	1.04	0.70	28.69	4.82	15.41	26.34	2.46	7.46	3.11	0.78	0.81	0.01	98.60	528	25
DG17B-Mnz4-2	7.07	0.49	0.27	1.46	0.71	29.39	3.61	15.99	27.79	2.55	7.75	3.25	0.70	0.67	0.11	101.79	689	25
DG17B-Mnz4-3	6.96	0.57	0.20	1.28	0.69	29.25	3.75	15.68	27.55	2.46	7.92	3.19	0.80	0.69	0.00	100.97	509	22
DG17B-Mnz4-4	7.13	0.57	0.20	1.40	0.60	29.05	3.92	15.50	27.27	2.46	7.79	3.11	0.81	0.74	0.00	100.55	497	22
DG17B-Mnz5-1	8.95	0.76	0.26	0.53	1.83	30.25	3.35	14.74	26.25	2.49	7.45	2.87	0.76	0.69	0.01	101.18	511	18

Table 6 continued

Points	ThO ₂	UO ₂	PbO	SiO ₂	CaO	P ₂ O ₅	Y ₂ O ₃	La ₂ O ₃	Ce ₂ O ₃	Pr ₂ O ₃	Nd ₂ O ₃	Sm ₂ O ₃	Gd ₂ O ₃	Dy ₂ O ₃	SO ₃	Total	Age	±2σ	
DG17B-Mnz5-2	8.12	0.59	0.23	1.67	0.54	28.47	5.10	14.56	26.58	2.38	7.59	3.10	0.81	0.86	0.00	100.61	507	20	
DG17B-Mnz5-3	8.66	0.40	0.22	1.46	0.87	28.79	3.53	15.59	27.01	2.45	7.58	3.15	0.75	0.74	0.00	101.19	501	20	
DG17B-Mnz5-4	8.54	0.44	0.22	1.78	0.50	29.02	4.77	15.27	26.82	2.38	7.43	3.15	0.79	0.83	0.01	101.93	494	20	
DG17B-Mnz5-5	7.76	0.43	0.21	1.58	0.52	29.11	4.53	15.04	26.65	2.44	7.85	3.13	0.78	0.81	0.00	100.84	505	22	
DG17B-Mnz5-6	8.20	0.45	0.21	1.52	0.69	29.13	4.18	15.14	26.79	2.45	7.70	3.29	0.77	0.78	0.01	101.29	495	20	
DG17B-Mnz5-7	8.10	0.58	0.23	1.67	0.53	28.57	4.80	14.91	26.81	2.38	7.41	3.18	0.76	0.84	0.00	100.75	506	20	
DG17B-Mnz7-1	14.32	0.57	0.36	3.23	0.51	25.82	3.15	13.98	24.59	2.27	7.11	2.80	0.63	0.56	0.00	99.91	504	13	
DG17B-Mnz7-2	11.59	0.37	0.30	2.24	0.75	27.40	2.56	14.63	26.18	2.35	7.71	3.04	0.65	0.51	0.01	100.30	526	16	
DG17B-Mnz7-3	8.70	1.90	0.63	0.33	2.32	29.64	2.53	14.15	25.31	2.23	7.05	2.81	0.78	0.56	0.00	98.93	925	18	
DG17B-Mnz8-1	2.91	0.17	0.22	0.25	0.56	31.03	1.32	18.18	31.11	2.78	8.88	3.58	0.75	0.39	0.02	102.15	1365	71	
DG17B-Mnz8-2	7.14	0.30	0.81	0.67	1.71	30.64	3.06	15.20	27.05	2.46	7.97	3.20	0.73	0.63	0.61	102.18	2120	44	
DG17B-Mnz8-3	7.42	0.30	0.19	1.45	0.53	29.02	3.68	15.80	27.87	2.49	7.97	3.23	0.78	0.69	0.00	101.41	507	23	
DG17B-Mnz8-4	7.63	0.44	0.20	1.46	0.59	29.15	3.64	15.71	27.58	2.47	7.71	2.99	0.77	0.65	0.01	100.99	502	22	
DG17B-Mnz8-5	6.89	0.39	0.18	1.17	0.68	29.82	4.49	14.88	27.28	2.54	8.04	3.10	0.88	0.83	0.02	101.19	503	24	
DG17B-Mnz8-6	7.37	0.44	0.20	1.32	0.68	29.67	3.61	15.86	27.57	2.53	7.77	3.24	0.79	0.71	0.00	101.75	499	22	
DG17B-Mnz9-1	14.46	0.27	0.36	2.82	0.83	25.57	2.23	13.98	25.62	2.34	7.34	2.69	0.65	0.42	0.00	99.58	520	14	
DG17B-Mnz9-2	15.92	0.27	0.38	3.53	0.45	25.34	2.07	14.09	25.88	2.37	7.51	2.62	0.57	0.42	0.01	101.42	514	13	
DG17B-Mnz9-3	20.11	0.29	0.48	4.69	0.48	23.53	1.94	12.90	23.62	2.15	7.06	2.39	0.53	0.36	0.00	100.53	511	10	
DG17B-Mnz6-1	9.76	0.54	0.27	0.75	1.76	29.82	4.32	14.06	25.35	2.32	7.17	2.88	0.72	0.79	0.01	100.50	525	18	
DG17B-Mnz6-2	11.57	0.41	0.29	2.37	0.61	27.26	3.59	14.41	26.16	2.39	7.57	2.90	0.76	0.62	0.01	100.91	499	16	
DG17B-Mnz6-3	11.19	0.43	0.28	2.19	0.67	27.75	3.75	14.47	26.19	2.31	7.49	2.81	0.66	0.69	0.00	100.88	505	16	
Migmatitic quartzofeldspathic gneiss (Sample no. BP6)																			
BP6_Mnz6-1	10.73	0.94	0.30	2.62	0.41	27.16	0.12	16.78	30.36	2.49	7.13	2.96	0.32	0.04	0.00	102.37	507	15	
BP6_Mnz6-2	10.07	0.90	0.29	2.41	0.46	27.57	0.13	16.84	30.59	2.57	7.21	3.03	0.40	0.02	0.01	102.50	505	15	
BP6_Mnz6-3	14.74	1.37	0.42	3.67	0.47	25.90	0.13	15.72	28.48	2.38	6.93	2.73	0.32	0.01	0.01	103.28	502	11	

Table 6 continued

Points	ThO ₂	UO ₂	PbO	SiO ₂	CaO	P ₂ O ₅	Y ₂ O ₃	La ₂ O ₃	Ce ₂ O ₃	Pr ₂ O ₃	Nd ₂ O ₃	Sm ₂ O ₃	Gd ₂ O ₃	Dy ₂ O ₃	SO ₃	Total	Age	±2σ
BP6_Mnz6-4	15.42	1.43	0.44	3.85	0.51	25.37	0.13	15.66	27.73	2.37	6.76	2.68	0.37	0.02	0.02	102.75	511	11
BP6_Mnz6-5	10.31	0.80	0.28	2.46	0.43	27.77	0.12	16.78	30.78	2.54	7.32	3.03	0.28	0.06	0.01	102.99	498	15
BP6_Mnz6-6	18.98	1.68	0.53	4.76	0.52	23.72	0.16	14.58	26.16	2.24	6.60	2.34	0.33	0.08	0.01	102.67	504	9
BP6_Mnz6-7	20.67	1.92	0.60	5.31	0.51	22.63	0.13	13.94	25.19	2.14	6.46	2.42	0.34	0.04	0.03	102.32	513	9
BP6_Mnz6-8	13.41	1.21	0.38	3.28	0.46	26.21	0.13	15.95	28.74	2.34	6.96	2.77	0.35	0.04	0.00	102.23	509	12
BP6_Mnz6-9	13.21	1.19	0.37	3.30	0.47	26.11	0.15	16.03	28.97	2.43	7.04	2.86	0.40	0.06	0.02	102.61	498	12
BP6_Mnz6-10	8.72	0.83	0.24	1.93	0.58	28.02	0.22	17.54	30.57	2.48	7.13	3.41	0.58	0.05	0.01	102.32	486	17
BP6-Mnz9-1	10.90	0.83	0.30	2.60	0.46	26.98	0.18	17.05	30.33	2.47	7.11	2.93	0.34	0.02	0.02	102.52	511	15
BP6-Mnz9-2	10.33	0.94	0.30	2.50	0.42	26.78	0.17	16.91	30.13	2.51	7.02	2.86	0.36	0.06	0.00	101.29	517	15
BP6-Mnz9-3	9.10	0.52	0.24	2.16	0.38	27.10	0.17	17.24	31.03	2.61	7.21	2.98	0.41	0.05	0.01	101.21	513	18
BP6-Mnz9-4	7.38	0.53	0.20	1.70	0.38	28.12	0.18	17.76	31.90	2.61	7.33	3.16	0.28	0.06	0.00	101.58	495	21
BP6-Mnz9-5	9.46	0.46	0.25	2.22	0.39	27.61	0.15	17.38	31.20	2.60	7.36	2.97	0.32	0.01	0.01	102.41	519	18
BP6-Mnz16-1	5.08	0.62	0.16	1.10	0.43	28.97	0.25	17.92	32.69	2.73	7.58	3.28	0.51	0.03	0.00	101.35	514	26
BP6-Mnz16-2	4.99	0.62	0.15	1.08	0.46	29.25	0.25	18.01	33.20	2.74	7.68	3.20	0.51	0.07	0.01	102.22	496	26
BP6-Mnz16-3	5.68	0.64	0.16	1.27	0.54	29.00	0.23	18.21	33.02	2.69	7.57	3.28	0.43	0.04	0.00	102.77	478	23
BP6-Mnz16-4	7.97	0.70	0.23	1.93	0.40	27.60	0.23	17.77	31.78	2.63	7.19	3.06	0.34	0.03	0.00	101.85	508	19
BP6-Mnz17-1	13.71	0.82	0.35	3.21	0.50	25.95	0.23	15.94	28.65	2.54	6.77	2.80	0.37	0.08	0.01	101.94	499	13
BP6-Mnz17-2	24.47	1.43	0.66	5.97	0.43	21.56	0.24	12.79	23.67	1.97	5.97	2.27	0.35	0.09	0.00	101.89	520	8
BP6-Mnz17-3	23.64	1.71	0.65	5.86	0.46	21.64	0.31	12.90	23.36	1.97	6.03	2.20	0.41	0.10	0.01	101.23	517	8
BP6-Mnz17-4	28.04	1.58	0.74	6.97	0.46	19.71	0.45	11.92	21.85	1.89	5.57	2.23	0.39	0.09	0.01	101.90	516	7
BP6-Mnz17-5	16.43	1.16	0.45	4.05	0.47	24.97	0.32	15.14	27.02	2.29	6.61	2.73	0.35	0.13	0.02	102.13	513	11
BP6-Mnz17-6	8.02	0.58	0.22	1.89	0.35	28.19	0.19	17.49	31.35	2.58	7.13	3.11	0.44	0.02	0.00	101.55	501	19
BP6-Mnz17-7	7.74	0.64	0.22	1.85	0.40	28.57	0.26	18.31	31.23	2.46	6.71	3.09	0.43	0.08	0.01	101.99	514	20
BP6-Mnz31-1	8.16	0.70	0.23	1.77	0.56	28.63	0.46	17.67	31.31	2.59	7.12	3.15	0.45	0.13	0.01	102.96	502	18
BP6-Mnz31-2	8.99	0.57	0.24	2.09	0.44	28.11	0.33	16.67	31.17	2.63	7.55	3.08	0.46	0.10	0.02	102.44	504	18
BP6-Mnz31-3	11.41	0.60	0.30	2.71	0.43	26.92	0.31	16.38	30.08	2.44	7.18	2.89	0.40	0.09	0.01	102.15	514	15

Table 6 continued

Points	ThO ₂	UO ₂	PbO	SiO ₂	CaO	P ₂ O ₅	Y ₂ O ₃	La ₂ O ₃	Ce ₂ O ₃	Pr ₂ O ₃	Nd ₂ O ₃	Sm ₂ O ₃	Gd ₂ O ₃	Dy ₂ O ₃	SO ₃	Total	Age	±2σ
BP6-Mnz31-4	8.28	0.68	0.23	1.85	0.56	28.20	0.44	17.31	30.87	2.48	6.96	3.13	0.50	0.10	0.01	101.58	493	18
BP6-Mnz31-5	19.53	1.41	0.54	4.77	0.49	23.45	0.47	14.08	25.64	2.15	6.35	2.39	0.40	0.15	0.00	101.82	515	9
BP6-Mnz32-1	8.17	0.68	0.23	1.75	0.52	27.71	0.46	17.27	30.81	2.59	6.94	3.07	0.50	0.15	0.00	100.84	504	19
BP6-Mnz32-2	11.45	0.78	0.31	2.57	0.55	26.65	0.40	16.13	29.37	2.48	7.27	2.92	0.43	0.15	0.01	101.48	514	15
BP6-Mnz32-3	8.26	0.67	0.22	1.81	0.57	28.88	0.47	17.89	30.96	2.49	7.01	3.29	0.52	0.13	0.00	103.18	481	18
BP6-Mnz32-4	15.48	0.92	0.40	3.63	0.57	25.46	0.41	14.94	27.65	2.36	6.88	2.91	0.53	0.18	0.00	102.33	502	11
BP6-Mnz32-5	13.60	0.84	0.36	3.14	0.55	26.36	0.46	15.45	28.66	2.45	7.09	2.76	0.45	0.17	0.00	102.34	509	13
BP6-Mnz32-6	21.91	1.63	0.61	5.42	0.49	22.47	0.61	13.41	24.50	2.08	6.34	2.37	0.42	0.18	0.01	102.47	515	9
BP6-Mnz32-7	21.39	1.08	0.56	5.14	0.48	22.70	0.32	13.59	25.57	2.15	6.46	2.45	0.39	0.15	0.00	102.43	516	9
BP6-Mnz32-8	25.51	1.95	0.72	6.20	0.46	20.39	0.63	12.17	22.70	1.92	5.77	2.14	0.38	0.16	0.02	101.13	523	8
BP6-Mnz32-9	11.27	0.78	0.31	2.57	0.52	26.68	0.44	16.34	29.37	2.47	6.82	2.82	0.39	0.13	0.01	100.92	520	15
BP6-Mnz32-10	11.68	0.64	0.30	2.73	0.42	26.55	0.32	16.09	29.72	2.52	6.99	2.86	0.39	0.10	0.01	101.30	509	15
BP6-Mnz15-1	10.08	0.37	0.25	2.33	0.41	27.64	0.13	17.24	31.12	2.53	7.15	2.89	0.30	0.05	0.01	102.48	509	17
BP6-Mnz15-2	11.86	0.85	0.33	2.81	0.44	26.84	0.18	16.33	29.96	2.47	7.16	2.94	0.37	0.08	0.00	102.61	511	14
BP6-Mnz15-3	9.44	0.43	0.24	2.17	0.38	27.41	0.15	17.44	31.48	2.64	7.36	2.97	0.30	0.02	0.01	102.43	508	18
BP6-Mnz15-4	19.19	0.55	0.47	4.53	0.41	23.91	0.13	14.75	26.89	2.30	6.46	2.35	0.31	0.05	0.02	102.31	515	10
BP6-Mnz15-5	27.61	1.45	0.72	6.76	0.48	20.30	0.38	12.38	22.36	1.87	5.87	2.17	0.27	0.07	0.00	102.69	517	7
BP6-Mnz15-6	8.55	0.60	0.23	2.06	0.37	27.48	0.18	17.43	31.05	2.57	7.11	3.09	0.35	0.02	0.01	101.08	506	18
BP6-Mnz15-8	9.12	0.63	0.24	2.15	0.38	27.23	0.20	17.47	30.52	2.45	7.00	2.94	0.39	0.05	0.01	100.79	503	17

*Namaqualand monazite (1033 Ma; Hokada and Motoyoshi, 2006) was used as an age standard

Chapter 7:

DISCUSSIONS AND CONCLUSIONS

Eight different deep-crustal rocks (granulites) were studied in the present research work in detail to understand the textural evolution and the ages of different tectonothermal events. Apart from the deep-crustal granulites, the detailed petrological and geochronological investigation were carried out on two mid-crustal cratonic rocks and one shallow-crustal marginal rock from the western boundary of the EGB. Multiple age-peaks in between ~3190 Ma and ~484 Ma are recorded from these rocks. The tectonothermal significance of these geochronological data is discussed in the following sections.

7.1 Significance of the Mesoarchean to Mesoproterozoic ages

Mesoarchean to Mesoproterozoic ages are obtained from the deep-crustal granulites, mid-crustal cratonic rocks and shallow-crustal sedimentary rocks from the western boundary of the EGB.

7.1.1 Mafic granulite

The spot dates in between ~2915–2470 Ma were recorded from a variety of mafic granulite, namely sample BP4 (Table 5). These spot dates were observed to spread on the concordia line without yielding any population age (Fig. 15d). It is noteworthy that the neoblastic zircon grain, once formed, does not move along the concordia line even if it suffers Pb-loss. However, the near-

concordant data-points from the inherited grains can spread along the concordia line (Krogh, 1993), which reflects the age of the protolith. The zircon grains of the studied mafic granulite record the older protolith ages, even if these rocks experienced anatexis during the high-temperature metamorphism. The survival of such older zircon grains of these rocks at the time of anatexis depend not only on the ambient pressure, temperature, and fluid condition, but also on the bulk-rock composition and zirconium saturation of the protolith (Kelsey et al., 2008). Hence, there is a possibility that these protoliths evolved in such a system where Zr saturation was high enough for the survival of few older zircon grains by increasing the melting temperature. Considering all these points, it can be inferred that these older zircon grains are the pre-Grenvillian metamorphic inherited grains, which represents the age of the older crustal components.

The origin and the evolution of this mafic granulite are, somehow, obscured as the rock experienced the multiple phases of deformation and metamorphism. One possibility is the mafic rock was emplaced at ~2900 Ma, and, then experienced an early phase of granulite facies metamorphism at ~2450 Ma. However, the fact combining the textural evidence, field relationship and, so far known tectonic setting of the EGB does not validate the possibility of Paleoproterozoic granulite facies metamorphism. The internal texture of the inherited zircon grains suggests that its protolith was most probably of magmatic origin, which emplaced possibly at ~2450 Ma with inherited zircon grains of ~2900–2500 Ma. It is also possible that the formation of this rock by

the multiple stages of magmatic events occurred between ~2900 and 2450 Ma, which later suffered UHT-HT metamorphism at ~1000–900 Ma as this rock preserve the same regional-scale metamorphic foliation associated with the Grenvillian orogeny. The latter two possibilities are geologically more plausible from the present set of data.

7.1.2 Migmatitic hornblende gneiss and migmatitic quartzofeldspathic gneiss

Both the cratonic gneisses yield the similar upper intercept and lower intercept ages at ~2450 Ma and ~550 Ma, respectively (Fig. 18b and 19b). Normally, the age data near the upper intercept is considered to provide the age of crystallization (contextually, as the age of protolith), whereas the age data near the lower intercept reflects the recrystallization age (contextually, as the age of metamorphism) (Mezger and Krogstad, 1997). Emplacement of the granitoids within the BC occurred during ~2500–2200 Ma (Sarkar et al., 1981; Krishnamurthy et al., 1988; Pandey et al., 1989; Saha et al., 2016), which coincides with the upper intercept age recorded in the migmatitic hornblende gneiss and the migmatitic quartzofeldspathic gneiss. The well-constrained age data near the upper intercept, high Th/U (>0.1) and the oscillatory zoned zircon grains of the migmatitic hornblende gneiss and the migmatitic quartzofeldspathic gneiss also vindicate the possibility in favor of magmatic origin. Hence, the upper intercept age constrains the emplacement age of these granitoid gneisses within the BC. The small spread of concordant ages at the

upper intercept may result from the multiple stages of igneous activity occurring between ~2500 and 2450 Ma. The cratonic gneisses, on the present day erosional surface, are exposed within the EGB as a “tectonic window” that represents the cratonic basement which buried under the thrust sheets of the EGB (Bhadra et al., 2004) during the final amalgamation of the EGB with the Proto-India.

7.1.3 Foliated quartz breccia

The detrital zircon grains and monazite grains exhibit multiple older age-peaks in between ~3200 Ma and ~1350 Ma, apart from the Neoproterozoic to Late Cambrian ages [Fig. 20c and 24d(II)]. The similar ages are well-documented from the detrital zircon and monazite grains (Saha et al., 2016 among others) studied from the adjacent craton-hosted basins (e.g., Chhattisgarh Main Basin, Khariar Basin, Ampani Basin, Sukma Basin and Indravati Basin). The highly angular quartz grains in this rock suggest that the degree of transportation was low as the sediments were supplied from the nearby areas. Thus, the combination of the geochronological data with textural evidence suggest that the sources(s) of Mesoarchean to Mesoproterozoic sediments located within the BC.

7.2 Significance of the Neoproterozoic to Late Cambrian ages

The three dominant age-peaks in between ~1000–900 Ma, ~850–775 Ma and ~550–495 Ma are recorded from the deep-crustal granulites and shallow-

crustal sedimentary rock. The mid-crustal cratonic rocks record only the ~550–525 Ma ages.

7.2.1 ~1000–900 Ma ages

The three textural variants of the charnockitic augen gneisses yield the dominant age cluster from both zircon (sample BP1, BP2, and BP3) and monazite grains (sample BP1) in between ~950 and ~930 Ma. One monazite grain yielding ~950 Ma age (grain 16 in sample BP1) shares the straight boundary with garnet, whereas another monazite grain is included within the porphyroblastic garnet grain (Fig. 21c). These texturally well-constrained geochronological data indicate that the porphyroblastic garnet grew during ~950 Ma. Two spot dates of 928 ± 41 Ma and 913 ± 31 Ma are also recorded from the monazite grain of aluminous granulite (sample BP12C). These dates are similar to the age of granulite metamorphism (~1060–900 Ma) described previously by Simmat and Raith (2008) from monazite of this area. The most prominent granulite facies (UHT-HT) metamorphism in the Eastern Ghats Province (northern and central parts of the EGB) occurred during 1030–900 Ma (Shaw et al., 1997; Mezger and Cosca, 1999; Simmat and Raith, 2008; Upadhyay et al., 2009; Bose et al., 2011; Das et al., 2011; Korhonen et al., 2013). The spot date of 1034 ± 16 Ma from the core of the zircon grain of charnockitic augen gneiss (sample BP3) coincides with the upper-limit of this age bracket which is the timing of UHT granulite facies metamorphism. The Tera-Wasserburg concordia diagram (Fig. 12d) for the charnockitic augen

gneiss (sample BP1) suggests the older core formation at approximately 1000–980 Ma, which is partially reset during the later thermal event at approximately 950–900 Ma. This later thermal event was responsible for the wide scattering of core ages (in between ~1000–850 Ma; Fig. 12d). The age imprint of the younger (~950–900 Ma) thermal event is mostly recorded from the rim of older cores of the zircon grains that exhibit the comparatively well-constrained age cluster. These zircon grains preserved oscillatory-zoned older core which is rimmed by a younger homogenous rim [Fig. 12a(III)]. This suggests that the crystallization of the protolith of the charnockitic augen gneiss occurred at ~1000–980 Ma, possibly as a result of the charnockite magmatism contemporaneous with the UHT metamorphism reported from the domain 2 of the EGB (Bose et al., 2011; Das et al., 2011; Korhonen et al., 2013). Thus, the evidence collected from this area and the adjacent crustal domain 2 suggest that the younger age (~950–900 Ma) bracketed the age of the HT granulite facies metamorphic overprint(s), which produced the porphyroblastic garnet in the charnockitic augen gneiss (sample BP1) during the M₂ metamorphic event (Fig. 26).

The detrital monazite grains of foliated quartz breccia also yielded spot dates of 940 ± 21 Ma and 925 ± 18 Ma. These characteristic ages of the EGB are completely missing in the adjacent BC, which imply that sediments were supplied both from the BC (Mesoarchean to Mesoproterozoic sources) and the EGB (Mesoproterozoic to Late Cambrian sources). The spot dates from the zircon grains of the charnockitic augen gneiss (sample BP3) as 884 ± 21 Ma (Table 5) and the monazite grains of the aluminous granulite (sample BP12C) as

891 ± 57 Ma probably reflect the mixed ages. The spot dates from the monazite grains of another variety of the charnockitic augen gneiss (sample BP1) were obtained in between ~900 and 850 Ma. These age peaks may suggest either the age of different tectonothermal events in between ~900 and ~850 Ma, or the mixing of the older (~950 Ma) and the younger (~775–850 Ma) ages.

7.2.2 ~850–775 Ma ages

The strong peak at 772 ± 13 Ma is recorded in the monazite grains of the charnockitic augen gneiss (sample BP1; Fig. 21d). The ~775 Ma monazite grains exist close to the porphyroblastic garnet and co-exist with plagioclase and/or orthopyroxene. The textural relationship suggests that plagioclase and/or orthopyroxene formed due to breakdown of the porphyroblastic garnet. Thus, the associated monazite grains with the plagioclase and/or orthopyroxene possibly grew during breakdown of the porphyroblastic garnet. The concordant spot date of 773 ± 22 Ma is also obtained from the core of a single zircon grain of this rock [Fig. 12a(I)]. The other two varieties of charnockitic augen gneisses (sample BP2 and BP3) also documented two spot dates in the zircon grains as 847 ± 48 Ma and 841 ± 21 Ma (Table 5). The textural evidence of breakdown of porphyroblastic garnet, i.e., development of plagioclase and orthopyroxene intergrowth at the boundary of the garnet, is reported in the sample BP3 (Fig. 7d). The foliated quartz breccia contains two detrital zircon grains of 852 ± 13 Ma and 842 ± 12 Ma age (Fig. 20b and 20c). The spot date as 797 ± 41 was recorded from one monazite grain of the deformed variety of aluminous

granulite (sample BP12C) in addition. The analyzed monazite is located at the exterior part of the porphyroblastic garnet. The ~800 Ma age from the grain was documented from the Y-rich part of the monazite (Fig. 23b(III) and 23c). This high-Y domain in the monazite grain is interpreted to form due to destabilization of garnet during decompression, as the latter is considered as the only sink for heavy rare earth elements (HREE), including Y (Pyle and Spear, 2003; Yang and Pattison, 2006). Therefore, the Y-rich monazite grain exhibits the age of the possible garnet instability during decompression. Some of the porphyroblastic garnet grains with the silicate mineral inclusions in between the interior and exterior portion possibly indicate the presence of an early garnet, and Y-rich monazite grain grew at ~800 Ma along the boundary of the early garnet. The overgrowth of garnet occurred during later metamorphism. Neither the charnockitic augen gneiss nor the aluminous granulite show the textural evidence of classical garnet breakdown intergrowths. However, the prominent garnet breakdown texture, i.e., symplectic intergrowth is developed in the adjacent mafic granulite (BP12B, Fig. 8b). It is important to note that the symplectic intergrowth might be formed either due to Na-metasomatism (Špaček et al., 2013) or due to decompressive instability of the garnet grains (Gupta et al., 2000). The symplectic intergrowth due to Na-metasomatism can be ruled out in the present sample as the plagioclase grains at the site of symplectite show the similar An-content compared to the porphyroblastic phase formed at the peak metamorphic condition. Thus, the symplectite texture in the mafic granulite was formed due to near-isothermal decompression, which is

also vindicated by the conventional geothermobarometric calculation and thermodynamic modeling (M_3 of Fig. 11). The absence of such decompression-related texture in the adjacent aluminous granulites is due to the highly Fe-rich restitic bulk-rock composition. Hence, it is logical to suggest that the decompression by exhumation (M_3) of the lower-crust occurred ~ 800 Ma (Fig. 26) by combining all the textural evidence with in-situ and bulk-separated geochronological data.

7.2.3 ~ 550 – 495 Ma ages

The deep-crustal granulites, mid-crustal cratonic gneisses, and shallow-crustal sedimentary rock preserve the age imprints of ~ 550 – 495 Ma. Age imprints of ~ 550 – 495 Ma are exclusively recorded in the rocks which were collected in a E-W transect across the EGB-BC boundary. The granulites of this region record the youngest age as ~ 530 – 500 Ma of both zircon and in-situ monazite grains. The ~ 530 – 500 Ma aged neoblastic zircon grains from the aluminous granulites (sample BP12A and BP12C) reveals that the sillimanite (fibrolite) is present as inclusion (Fig. 16a and 16c). The fibrolite could be formed in the pelitic rock as a lower temperature variety of sillimanite (Sassi et al., 2004). Moreover, Georgieva et al. (2002) conclude that the fluid-driven fibrolite can grow in the shear zone at amphibolite facies. The ingress of aqueous fluid in the presence of quartz enlarges the stability field of sillimanite (fibrolite) at the expense of plagioclase in a lower pressure-temperature than granulite facies condition (Amano and Kawakami, 2014). Hence, the ~ 530 – 500

Ma zircon grains grew possibly at a lower pressure-temperature than the granulite facies condition in the presence of an aqueous fluid. The role of fluid was, further, vindicated by the appearance of late-hornblende on clinopyroxene due to rehydration of the mafic granulite (Fig. 8c and M₄ of Fig. 11). Hence, all lines of evidence lead to the fact that these deep-crustal rocks were overprinted by a later granulite-amphibolite transitional facies metamorphism (M₄) during ~530–500 Ma (Fig. 26).

The neoblastic zircon growth during the granulite-amphibolite transitional facies (M₄) is intriguing. It is reported that the zircon can grow at such condition (Kelsey et al., 2008; Kohn et al., 2015). Kohn et al. (2015) explain that the zircon dissolution is possible by the generation of partial melt due to change in the *P-T* condition, i.e., during isothermal decompression, and the neoblastic zircon may crystallize from that melt during late stage exhumation and cooling. However, the zircon growth depends not only on *P-T* condition but also on the Zr-content of the rock (Kelsey et al., 2008). The dissolution-reprecipitation of zircon at a lower temperature is possible due to low Zr-content in the protolith. Such neoblastic zircon may contain the primary solid and/or fluid inclusions (Tomaschek et al., 2003). The inclusion of fibrolite and quartz in the ~530–500 Ma zircon grains of the aluminous granulites (sample BP12A and BP12C) were reported in the present study, which suggest the formation of such grains occurred at the granulite-amphibolite transitional facies. Zircon also can grow at the lower temperature compared to the granulite facies condition in the presence of aqueous fluids (Hoskin and Schaltegger,

2003; Dubińska et al., 2004; Schaltegger, 2007; Ayers et al., 2012; Wilke et al., 2012). The presence of fluids responsible not only for the growth of zircon but also fluids can reset the isotopic clock (Pidgeon, 1992; Pidgeon et al., 1998). The ingress of aqueous fluid at the granulite-amphibolite transitional facies can also be responsible for the normal and reverse discordance due to the intragranular isotopic disturbance by enhancing the Pb diffusion (Carson et al., 2002). The analyzed rocks of the present study show similar discordance [both reverse and normal; Fig. 15b(I), 16b and 16d(I)] as they possibly crystallized under the influence of aqueous fluid. The presence of porphyroblastic (pegmatoidal) garnet and aluminosilicate minerals further vindicate the role of the fluid (Crowe et al., 2003). The similar pegmatoidal garnet (Fig. 5e) and sillimanite in the granulites from the orogen-boundary are reported in the present study. This garnet contains abundant secondary fluid inclusions (sample BP12A), which possibly suggest that the pegmatoidal growth was fluid-assisted. Such pegmatoidal growth of minerals are not reported in the interior of the orogen, which imply that the fluid invasion was facilitated through the thrust planes and exclusively affected the rocks adjacent to the thrust boundary. The contemporaneous rehydration reactions, i.e., the formation of the late hornblende in the mafic granulite (sample BP12B) also validate the role of fluid during ~530–500 Ma restricted near the thrust boundary. Thus, the mineral inclusions of fibrolite and quartz within the neoblastic zircon grains, discordant age data points and fluid-assisted pegmatoidal growth of minerals suggest the neoblastic growth of zircon grains (or total resetting of the older isotopic clock)

at ~530–500 Ma. Such neoblastic growth might have occurred either due to the dissolution-precipitation during granulite-amphibolite overprinting or due to the influence of aqueous fluids, or a combination of both.

Both the mid-crustal cratonic gneisses (sample DG33F and BP6) record the age imprints of ~550–500 Ma in the monazite and the zircon grains. The monazite grains of the migmatitic quartzofeldspathic gneiss (sample BP6) yield a very strong age-peak at 511 ± 3 Ma. The rim of the zircon grains from the migmatitic hornblende gneiss (sample DG33F) and the migmatitic quartzofeldspathic gneiss (sample BP6) yield the lower intercept ages of the discordia lines in the Tera-Wasserburg concordia diagrams as ~550 Ma, whereas the core of the zircon grains yield ~2450–2400 Ma ages as the upper intercepts (Figs. 18a, 18b, 19a and 19b). The lower intercepts of the discordia lines in the Tera-Wasserburg concordia diagrams indicate that these rocks were overprinted by a thermal event at ~550 Ma. This age coincides with the previously documented age of ~550–500 Ma from the boundary region (Biswal et al., 2007; Simmat and Raith, 2008; Upadhyay, 2008). However, the several craton-hosted Mesoproterozoic sedimentary basins, as well as, the mid-crustal cratonic gneisses in the further tens of kilometer westward within the craton did not record any imprint of this ~550–500 Ma event (Saha et al., 2016; Das et al., 2016). Thus, the influence of the top-to-the-west thrusting of the “hot” EGB over the “cold” BC (Gupta et al., 2000; Bhadra et al., 2004; Gupta, 2012) during the ~550–500 Ma is also restricted along the narrow zone adjacent to the boundary even in the cratonic side. The textural evidence, such as the

appearance of orthopyroxene on hornblende, also imply the change from the amphibolite facies metamorphism to the amphibolite-granulite transitional facies metamorphism due to the thrusting the “hot” EGB over the “cold” BC. Metamorphic overgrowths of ~550 Ma rims are found in the zircon grains, which record the timing of the amphibolite-granulite transitional facies metamorphism due to the thrusting of the “hot” EGB over the BC.

The detrital zircon grains and the monazite grains in the foliated quartz breccia (sample DG17B) preserve the very strong age imprints of ~530–495 Ma. The youngest spot date retrieved from the detrital zircon grain is 517 ± 23 Ma, whereas the detrital monazite grain yields the youngest spot date as 494 ± 20 Ma. The maximum depositional age of this sedimentary basin is calculated as $484 (+10/-18)$ Ma from the monazite age data (Fig. 27). The field evidence, such as the presence of conformable thrust-related regional foliation (Fig. 5i), combined with the geochronological data (zircon and monazite grains of ~530–495 Ma) suggests for the first time that the thrust-related deformation was post- to syn-depositional of this shallow-crustal component. This implies that the thrusting might have continued at least, up to, ~484 Ma.

7.3 Age-zonation across the boundary of orogen

It is interesting to note that the superposition of granulite-amphibolite transitional facies metamorphism (M_4) on ~950–930 Ma granulite facies metamorphic rocks (M_2) are widely documented from several regions within the EGB. The present study indicates that the extensive neoblastic growth of minute

zircon grains (or completely resetting the isotopic clock) during the granulite-amphibolite transitional facies metamorphism erased almost all the earlier age memory from the granulites (in and around the Parla village) near the thrust contact between the EGB-BC. The age signatures of ~550 Ma on the cratonic gneisses are also restricted very close to the western boundary of the EGB in the cratonic counterpart. Such age imprints on the cratonic rocks are completely absent at the farther away (westward) from the western boundary of the EGB (Saha et al., 2016; Das et al., 2016). On the other hand, the granulites outcropped ~60 km away from the boundary towards the interior of the orogen, only preserve the older age imprints of ~950 Ma exclusively (in and around Bhawanipatna town), with no record of ~530–500 Ma zircon growth/resetting. Thus, the high-resolution zircon age data from the systematically sampled rocks collected in a ~60 km long E-W transect across the EGB-BC boundary unveil an age zonation across the western boundary of the EGB. Such spatial variation of the metamorphic events and their corresponding ages in a E-W transect across the boundary is depicted in Figure 28.

This spatial variation of the geochronological data of the extensive zircon growth or resetting requires the unique physico-chemical environment prevalent along the narrow zone adjacent to the both side of the thrust-bound boundary. Such prevalence of the physico-chemical environment may be due to the effect of the thrusting of the EGB on the BC during its amalgamation. The influence of the thrust-related physico-chemical environment completely diminished towards the interior of the orogen (in and around the Bhawanipatna

town). Thus, no age imprints of ~550-500 Ma are found from the rocks near the Bhawanipatna town, ~60 km away towards the east of the thrust boundary.

7.4 Age-integrated tectonic modeling

Three distinct tectonothermal pulses are recorded in between ~950–500 Ma from different areas within the northern EGB. The texturally well-constrained and high-resolution age data demonstrates that the three age peaks at ~950–930 Ma, ~850–775 Ma, and ~550–485 Ma are correlated with all the corresponding tectonothermal events, which are recorded exclusively from the western boundary of the EGB. Such correlation of the age peaks with respective tectono-metamorphic events allows to propose the comprehensive age-integrated tectonic model (modified after Bhadra and Gupta, 2016 and among others) encompassing deep- to shallow-crustal events started from its Early Neoproterozoic granulite facies metamorphism till the final amalgamation of the EGB at the Late Cambrian period.

The stable mineralogical assemblage of garnet, orthopyroxene, K-feldspar and quartz in the charnockitic augen gneisses reflect the deep-crustal granulite facies metamorphism, which were collected at about ~60 km eastward from the postulated boundary between the EGB and the BC. The zircon U-Pb age dating method and the texturally well-constrained in-situ monazite U-Th-total Pb dating method constrain the time of the granulite facies metamorphism between ~950–930 Ma. It is noteworthy that no petrochronological signatures of the granulite facies metamorphism are recorded from the adjacent Bastar

Craton during ~950–930 Ma in the published literature, as well as, in the present study. Such absence of the petrochronological signatures in the adjacent rocks of BC suggests that the EGB was not co-evolving with the Proto-India during ~950–930 Ma. Hence, along the western boundary of the EGB, the evolution of the EGB with respect to the Proto-India is less understood during ~950–930 Ma (Fig. 29a).

The near-isothermal decompression of the EGB rocks was followed by the post-peak granulite facies metamorphism at ~800 Ma. Such fact implies that the initial phase of exhumation of the deep-crust to, at least, up to mid-crustal level occurred during ~800 Ma. However, the published literature and the present study revealed that the adjacent BC did not record any geochronological signature of ~800 Ma event as well, which brings further uncertainty regarding the evolution of the EGB with respect to the Proto-India during this period (Fig. 29b).

The juxtaposition of the EGB with the Proto-India was achieved by the top-to-the-west thrusting during ~550–500 Ma. The combination of textural evolution and geochronological data from the cratonic rocks suggest that this thrusting caused the heating and the deformation in the footwall block (the BC) due to the presence of the “hot” EGB on its top (Gupta et al., 2000; Bhadra et al., 2004; Gupta, 2012; Bhadra and Gupta, 2016). Additionally, the thrusting was responsible for the development of the small basin adjacent to the thrust front and caused the brecciation of the nearby source rocks, which supplied the

sediments from both sides of the thrust plane (the BC and the EGB) during the final stage of thrusting up to, at least, ~484 Ma (Fig. 29c).

7.5 Supercontinent correlation

The EGB co-evolved with its Precambrian neighbors, such as East Antarctica, Australia, China and parts of Laurentia, during three supercontinental cycles including the Columbia, Rodinia and the Gondwana. The strategic position of the EGB between the Archean Proto-India and its Precambrian neighbors made it the suitable candidate to study the supercontinental evolution with respect to the Proto-India. The present study was carried along the western boundary of the northern EGB which separates the Archean Proto-India from the Proterozoic orogenic belt. This study reveals that the northwestern boundary of the EGB experienced the granulite facies metamorphism at ~950–930 Ma during the Rodinia assembly, which was contemporaneous with the granulite facies metamorphism in Rayner Complex of East Antarctica (Harley et al., 2013; Morrissey et al., 2015). However, no petrochronological signature of the thermal event is recorded from the adjacent cratonic gneisses of the EGB. This suggests that during the Rodinia assembly the northern EGB was not contiguous with the Proto-India, but co-evolving with the East Antarctica. The northern EGB witnessed the early-phase of exhumation in between ~850–775 Ma after the granulite facies metamorphism. The similar age imprints are also reported from the East Antarctica. For example, Black et al. (1987) reported granitic and pegmatitic magmatism at

~770 Ma in the Rayner Complex. The U-Pb zircon age of 772 ± 48 Ma in the mafic granulite from the northern Mirror Peninsula, Prydz Bay is also reported by Tong et al. (1995), which was explained as the age of the probable tectonothermal event in response to the granulite facies metamorphism or possibly reflecting a resetting age due to the overprint of Pan-African metamorphism. High-grade metamorphism and mylonitic fabric development have been reported at ~800 Ma at the cratonic interior part of the East Antarctica (U-Th-Pb monazite age; Nichols and Fahey, 1996). Shiraishi et al. (2008) reported similar ages of metamorphism between ~800–700 Ma at the western Rayner Complex. The time-frame between ~850–775 Ma is regarded as the breakup period of the Rodinia supercontinent (Li et al., 2008). However, no age imprints of ~850–775 Ma during the Rodinia breakup recorded in the cratonic counterpart of the northern EGB, which further suggests that during the Rodinia breakup the northern EGB was co-evolving with the East Antarctica but not with the Proto-India.

The geochronological signature, as well as, the petrological evidence in the cratonic gneisses suggest firmly that the amalgamation of the northern EGB with the Proto-India initiated at ~550 Ma during the final phase of the Gondwana assembly. The Gondwana assembly was achieved by two phases of orogenesis. The initial phase is known as the East Africa Orogeny (~750–620 Ma) and the final phase is known as the Kuunga Orogeny (~570–530 Ma; Meert, 2003). Thus, the amalgamation of the northern EGB was achieved through the Kuunga Orogeny. However, the data of this study suggest that the

amalgamation of the northern EGB during Gondwana assembly was continued, at least, up to ~484 Ma, which post-dates the Kuunga Orogeny. Hence, the span of the thrust-related tectonics during the amalgamation of the northern EGB oversteps the Precambrian-Cambrian boundary and continued up to the Late Cambrian period.

7.5 Conclusions

The detailed petrological and the geochronological investigations on the deep- to shallow-crustal rocks collected at the western boundary of the northern EGB reveal that the entire crustal segment participated actively during and prior to the amalgamation with the Proto-India. The geochronological data coupled with the petrological observations constrain the timing of various tectono-metamorphic events ranging in between Mesoarchean to Late Cambrian. The outcomes of this study are summarized below:

- The inherited zircon grains of ~2915–2470 Ma in mafic granulite (sample BP4) represent the Late Archean to the Early Paleoproterozoic protolith ages, which was metamorphosed under the granulite facies condition during the Grenvillian time.
- The petrological and the geochronological evidence of the granulite facies metamorphism during ~950–930 Ma was recorded exclusively in the granulites, which are located at ~60 km eastward from the boundary between the EGB and the BC. The granulite facies metamorphism

during ~950–930 Ma suggests that the EGB was co-evolving with the East Antarctica during the Rodinia assembly, but not with the Proto-India as suggested by the available geochronological data.

- The early-phase of exhumation of the deep-crust of the EGB occurred between ~800 Ma during the Rodinia breakup.
- The amphibolite-granulite transitional facies overprinting at ~530–500 Ma erased all the earlier geochronological histories in the granulites near the boundary between the EGB-BC. On the other hand, the rocks farther to the east and west of the thrust boundary did not record the age imprints of ~530–500 Ma. Such spatial variation of the age imprints confined along a narrow zone adjacent to the both sides of the thrust boundary due to the effect of thrust-related tectonics.
- The foliated quartz breccia preserves the conformable thrust-related regional foliation. The maximum depositional age for deposition of the foliated quartz breccia was calculated as 484 (+ 10/- 18) Ma.
- The geochronological signatures, as well as, the petrological evidence in the cratonic gneisses suggest firmly that the amalgamation of the northern EGB with the Proto-India initiated at ~550 Ma during the final phase of Gondwana assembly, which continued up to ~485 Ma and post-dates Gondwana assembly.

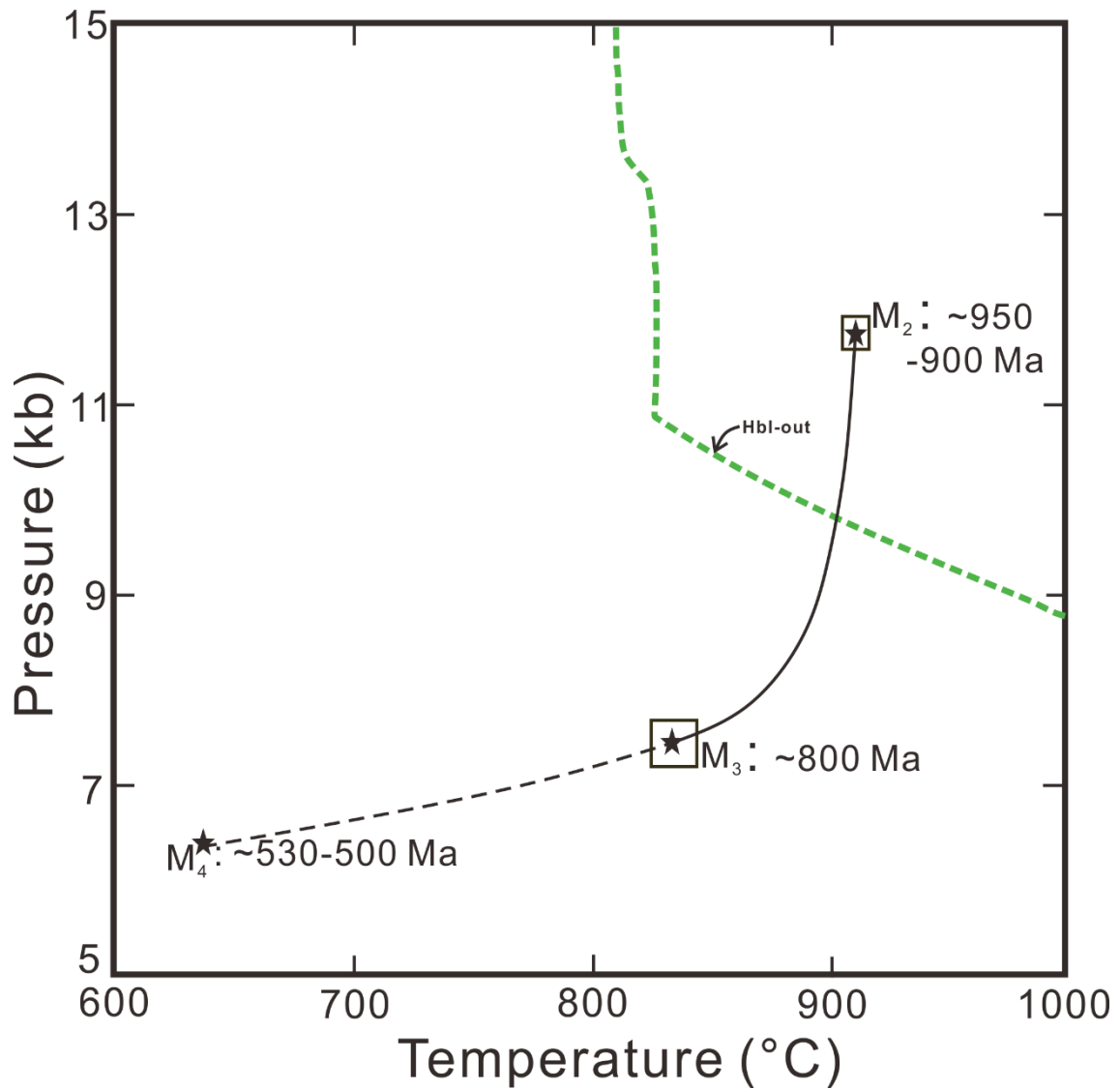


Figure 26: Different metamorphic stages on P - T space correlated with high-resolution and texturally well-constrained geochronological data. The granulite facies metamorphism (M_2) occurred between ~950–900 Ma, followed by an exhumation (M_3) at ~800 Ma. Granulite-amphibolite transitional facies metamorphism (M_4) took place during ~530–500 Ma.

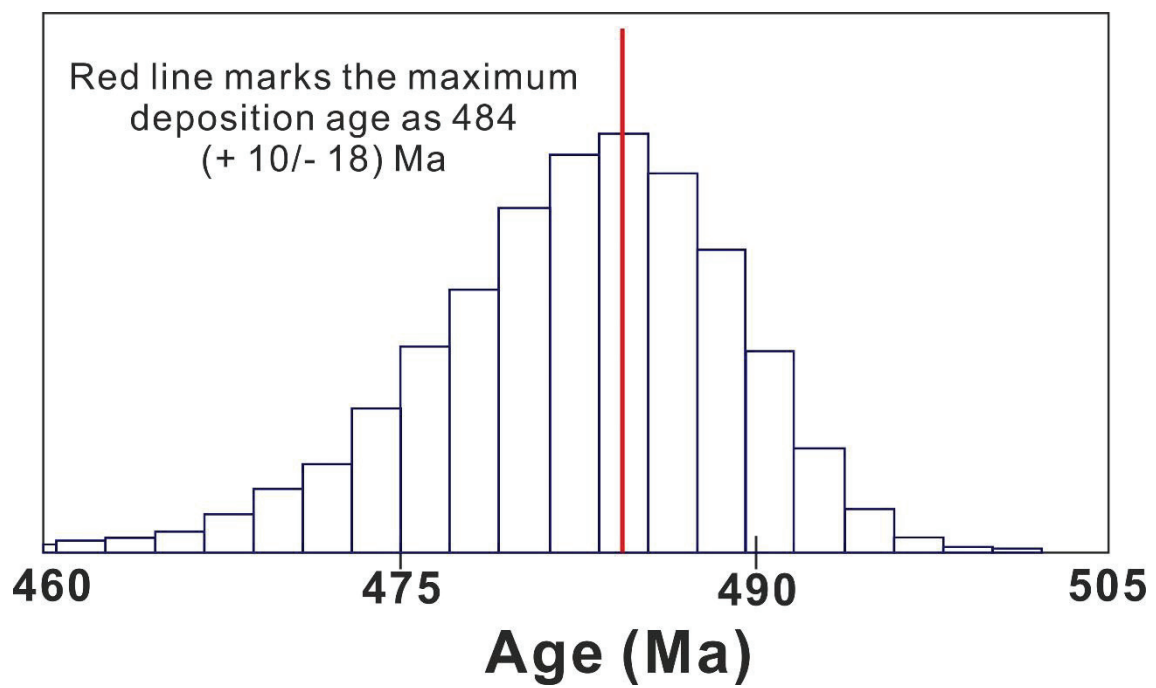


Figure 27: The maximum depositional age of the foliated quartz breccia is calculated as 484 (+ 10/- 18) Ma using the detrital monazite geochronology.

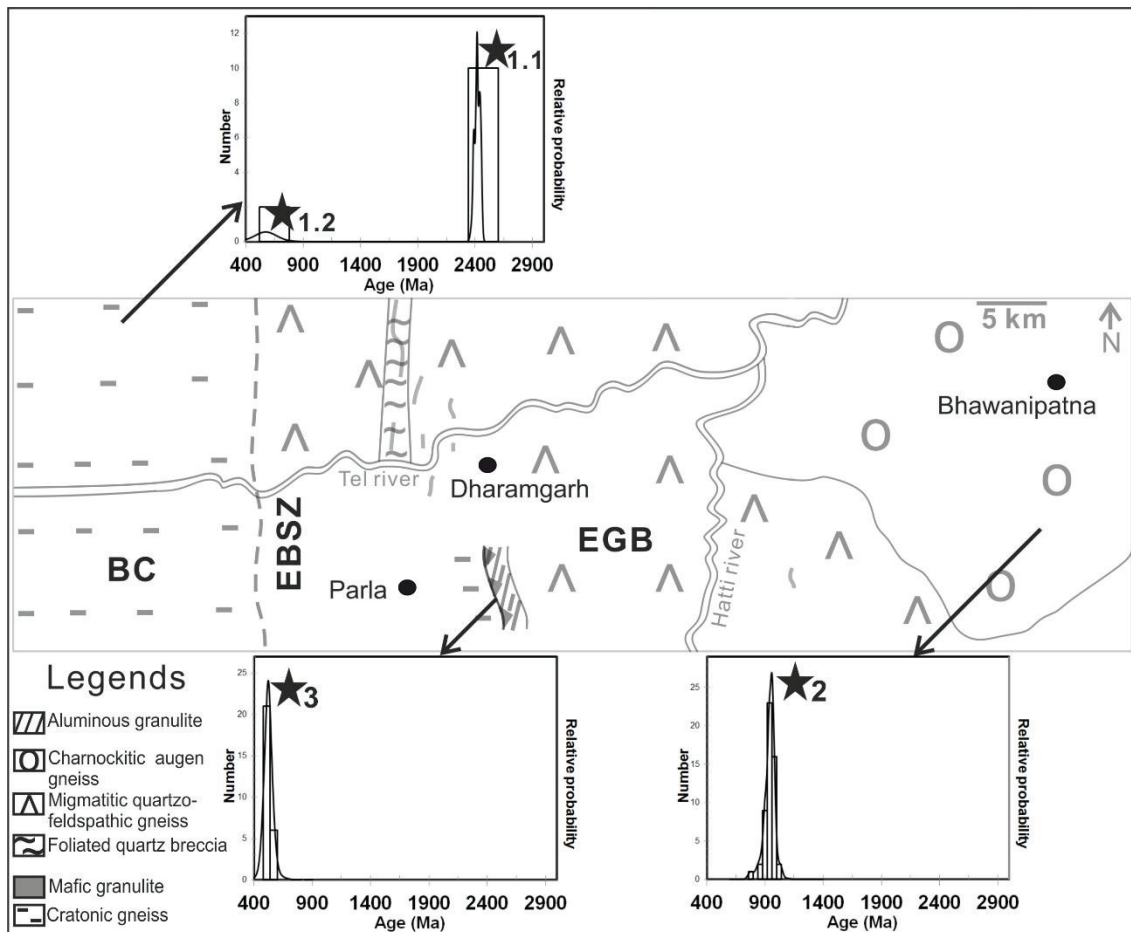


Figure 28: The probability density diagrams showing the spatial variation of the zircon $^{207}\text{Pb}/^{206}\text{Pb}$ ages of the different geological events in the transect across the western boundary of the EGB. “★1.1” age-peak denotes the protolith age of the cratonic gneiss (migmatitic hornblende gneiss), which is later overprinted by a weak ~550 Ma thermal event (“★1.2” age-peak). Note that the cratonic rock of the current study (migmatitic hornblende gneiss) exposed within the EGB as “tectonic window” (Bhadra et al., 2004). The granulite facies metamorphism at ~950 Ma is denoted by the strong “★2” age-peak recorded ~60 km eastward from the boundary. Near the margin, “★3” age-peak attests a strong overprinting of ~550–500 Ma granulite-amphibolite transitional facies.

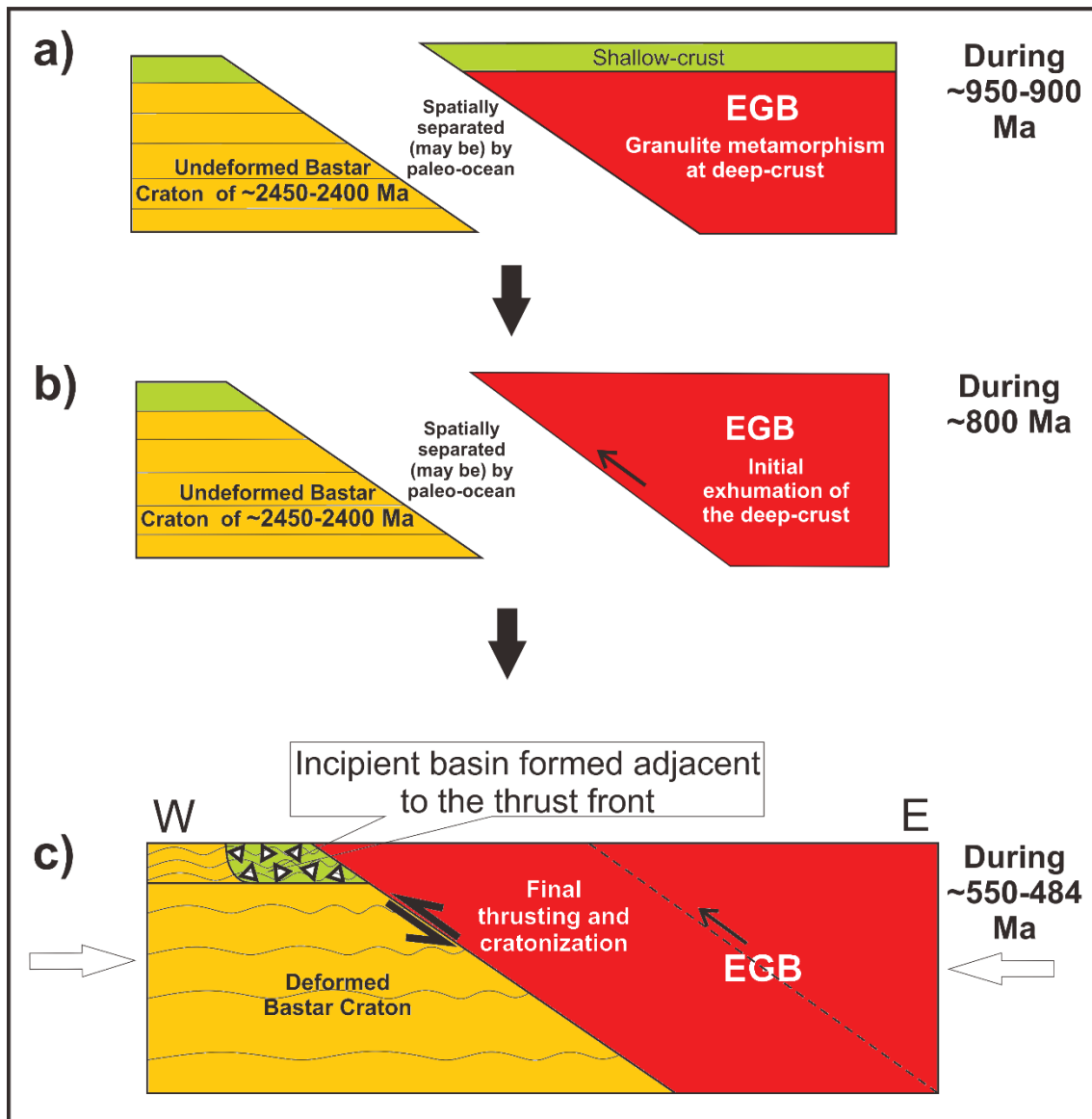


Figure 29: The tectonic evolutionary model of the EGB during and before its amalgamation with the Proto-India (contextually, the BC). (a) ~950–930 Ma granulite facies metamorphism of EGB. The position of the EGB with respect to the Proto-India during that time is uncertain. (b) The initial exhumation of the EGB at ~850–775 Ma. The position of the EGB with respect to the Proto-India during the time is inconclusive. (c) The EGB amalgamated with the Proto-India during ~550–500 Ma. The cratonic rocks of ~2450–2400 Ma subsequently suffered the deformation and the metamorphism due to the thrusting. The linear basin was formed adjacent to the thrust front and syn- to post-tectonic sedimentation initiated and continued up to ≤ 484 Ma.

REFERENCES

- Aftalion, M., Bowes, D.R., Dash, B. and Fallick, A.E. (2000) Late Pan-African thermal history in the Eastern Ghats terrane, India from U-Pb and K-Ar isotopic study of the Mid-Proterozoic Khariar alkali syenite, Orissa. *Geological Survey of India, Special Publication, 57*, 26–33.
- Amano, S. and Kawakami, T. (2014) Fluid related origin of sillimanite veins in polymetamorphic rocks from the Ryoke Belt, Japan. *Abstract, JpGU annual meeting*, SMP46-14.
- Ayers, J.C., Zhang, L., Luo, Y. and Peters, T.J. (2012) Zircon solubility in alkaline aqueous fluids at upper crustal conditions. *Geochimica et Cosmochimica Acta, 96*, 18–28.
- Bhadra, S. (2003) Tectonometamorphic evolution of a craton-mobile belt assembly: The Bhawanipatna-Deobhog transect, Orissa, India. Unpublished PhD thesis, Indian Institute of Technology, Kharagpur, India.
- Bhadra, S., Gupta, S. and Banerjee, M. (2004) Structural evolution across the Eastern Ghats Mobile Belt - Bastar craton boundary, India: hot over cold thrusting in an ancient collision zone. *Journal of Structural Geology, 26*, 233–245.
- Bhadra, S. and Gupta, S. (2016) Reworking of a basement - cover interface during Terrane Boundary shearing: An example from the Khariar basin, Bastar craton, India. In: Mukherjee, S. and Mulchrone, K.F. (Eds.) Ductile shear zone from micro to macro-scale. John Wiley & Sons, 164–181.

- Bhattacharya, S. (2004) High-temperature crustal scale shear zone at the western margin of the Eastern Ghats granulite belt, India: Implications for rapid exhumation. *Journal of Asian Earth Science*, 24, 281–290.
- Biswal, T.K., De Waele, B. and Ahuja, H. (2007) Timing and dynamics of the juxtaposition of the Eastern Ghats mobile belt against the Bhandara Craton, India: A structural and zircon U-Pb SHRIMP study of the fold-thrust belt and associated nepheline syenite plutons. *Tectonics*, 26, TC4006.
- Black, L.P., Harley, S.L., Sun, S.S. and McCulloch, M.T. (1987) The Rayner Complex of East Antarctica: complex isotopic systematics within a Proterozoic mobile belt. *Journal of Metamorphic Geology*, 5, 1–26.
- Bose, S., Fukuoka, M., Sengupta, P. and Dasgupta, S. (2000) Evolution of high-Mg-Al granulites from Sunkarametta, Eastern Ghats, India: Evidence for a lower crustal heating-cooling trajectory. *Journal of Metamorphic Geology*, 18, 223–240.
- Bose, S., Dunkley, D.J., Dasgupta, S., Das, K. and Arima, M. (2011) India-Antarctica-Australia-Laurentia connection in the Paleoproterozoic-Mesoproterozoic revisited: Evidence from new zircon U-Pb and monazite chemical age data from the Eastern Ghats Belt, India. *Bulletin of the Geological Society of America*, 123, 2031–2049.
- Bose, S., Das, K., Kimura, K., Hidaka, H., Dasgupta, A., Ghosh, G. and Mukhopadhyay, J. (2016a) Neoproterozoic tectonothermal imprints in the Rengali Province, eastern India and their implication on the growth of Singhbhum Craton:

- Evidence from zircon U-Pb SHRIMP data. *Journal of Metamorphic Geology*, 34, 743–764.
- Bose, S., Das, K., Torimoto, J., Arima, M. and Dunkley, D.J. (2016b) Evolution of the Chilka Lake granulite complex, northern Eastern Ghats Belt, India: First evidence of ~780 Ma decompression of the deep crust and its implication on the India-Antarctica correlation. *Lithos*, 263, 161–189.
- Brown, M. (2007) Metamorphism, Plate Tectonics, and the Supercontinent Cycle. *Earth Science Frontier*, 14, 1–18.
- Carson, C.J., Ague, J.J., Grove, M., Coath, C.D. and Harrison, T.M. (2002) U-Pb isotopic behaviour of zircon during upper-amphibolite facies fluid infiltration in the Napier Complex, East Antarctica. *Earth and Planetary Science Letters*, 199, 287–310.
- Cawood, P. A., Kröner, A., Collins, W.J., Kusky, T.M., Mooney, W.D. and Windley, B.F. (2009) Accretionary orogens through Earth history. In: Cawood, P. A. and Kröner, A. (Eds.) *Earth Accretionary Systems in Space and Time. Geological Society London, Special Publication*, 318, 1–36.
- Chakraborty, P.P., Saha, S. and Das, P. (2015) Geology of Mesoproterozoic Chhattisgarh Basin, central India: current status and future goals. In: Mazumder, R. and Eriksson, P. G. (Eds.) *Precambrian Basins of India: Stratigraphic and Tectonic Context. Geological Society London, Memoirs*, 43, 185–205.
- Chattopadhyay, S., Upadhyay, D., Nanda, J.K., Mezger, K., Pruseth, K.L. and Berndt, J. (2015) Proto-India was a part of Rodinia: Evidence from Grenville-age suturing of

the Eastern Ghats Province with the Paleoproterozoic Singhbhum Craton.

Precambrian Research, 266, 506–529.

Claoue-Long, J. C., Compston, W., Roberts, J. and Fanning, C. M. (1995) Two Carboniferous ages: a comparison of SHRIMP zircon dating with conventional zircon ages and $^{40}\text{Ar}/^{39}\text{Ar}$ analysis. In: Berggren, W. A., Kent, D. V., Aubry, M. P. and Hardenbol, J. (Eds.) *Geochronology Time Scales and Global Stratigraphic Correlation. SEPM (Society for Sedimentary Geology), Special Publication, 4*, 3–21.

Compston, W. (1999) Geological age by instrumental analysis: The 29th Hallimond Lecture. *Mineralogical Magazine*, 63, 297–311.

Condie, K.C. (2005) *Earth as an evolving planetary system*, first ed. Elsevier, Amsterdam, p.p. 350.

Connolly, J.A.D. (2005) Computation of phase equilibria by linear programming: A tool for geodynamic modeling and its application to subduction zone decarbonation. *Earth and Planetary Science Letters*, 236, 524–541.

Connolly, J.A.D. and Petrini, K. (2002) An automated strategy for calculation of phase diagram sections and retrieval of rock properties as a function of physical conditions (0.4 Mb). *Journal of Metamorphic Geology*, 20, 697–708.

Crowe, W.A., Nash, C.R., Harris, L.B., Leeming, P.M. and Rankin, L.R. (2003) The geology of the Rengali Province: implications for the tectonic development of northern Orissa, India. *Journal of Asian Earth Science*, 21, 697–710.

Dale, J., Powell, R., White, R.W., Elmer, F.L. and Holland, T.J.B. (2005) A thermodynamic model for Ca-Na clin amphiboles in $\text{Na}_2\text{O}-\text{CaO}-\text{FeO}-\text{MgO}-\text{Al}_2\text{O}_3-$

- SiO₂-H₂O-O for petrological calculations. *Journal of Metamorphic Geology*, 23, 771–791.
- Das, K., Yokoyama, K., Chakraborty, P.P. and Sarkar, A. (2009) Basal tuffs and contemporaneity of the Chattisgarh and Khariar Basins based on new dates and geochemistry. *The Journal of Geology*, 117, 88–102.
- Das, K., Bose, S., Karmakar, S., Dunkley, D.J. and Dasgupta, S. (2011) Multiple tectonometamorphic imprints in the lower crust: First evidence of ca. 950 Ma (zircon U-Pb SHRIMP) compressional reworking of UHT aluminous granulites from the Eastern Ghats Belt, India. *Geological Journal*, 46, 217–239.
- Das, K., Chakraborty, P.P., Hayasaka, Y. and Kayama, M. (2015) 1450 Ma regional felsic volcanism at the fringe of the East Indian Craton: constraints from geochronology and geochemistry of tuff beds from detached sedimentary basins. *Geological Society London, Memoirs*, 23, 207–221.
- Das, K., Chakraborty, P.P., Horie, K., Tsutsumi, Y., Saha, S. and Balakrishnan, S. (2016) Detrital Zircon U-Pb Geochronology, Nd Isotope Mapping, and Sediment Geochemistry from the Singhora Group, Central India: Implications Toward Provenance, Its Shift, and Regional Stratigraphic Correlation. In: Mazumder, R. (Eds.) Influences on Compositional Change from Source to Sink. *Sediment Provenance 1*, 15, 403–451.
- Das, S., Bhattacharya, A., Raith, M.M., Bhadra, S. and Banerjee, M. (2006) Aluminous sapphirine granulites from the Eastern Ghats Belt (India): Phase

- relations and relevance to counterclockwise P-T history. *European Journal of Mineralogy*, 18, 35–48.
- Das, S., Nasipuri, P., Bhattacharya, A. and Swaminathan, S. (2008) The thrust-contact between the Eastern Ghats Belt and the adjoining Bastar craton (Eastern India): Evidence from mafic granulites and tectonic implications. *Precambrian Research*, 162, 70–85.
- Dasgupta, S., Sengupta, P., Ehl, J., Raith, M. and Bardhan, S. (1995) Reaction textures in a suite of spinel granulites from the Eastern Ghats belt, India: Evidence for polymetamorphism, a partial petrogenetic grid in the system KFMASH and the roles of ZnO and Fe₂O₃. *Journal of Petrology*, 36, 435–461.
- Dasgupta, S., Bose, S. and Das, K. (2013) Tectonic evolution of the Eastern Ghats Belt, India. *Precambrian Research*, 227, 247–258.
- Dasgupta, S., Bose, S., Bhowmik, S.K. and Sengupta, P. (2017) The Eastern Ghats Belt, India, in the context of supercontinent assembly. In: Pant, N.C. & Dasgupta, S. (Eds.) *Crustal Evolution of India and Antarctica: The Supercontinent Connection. Geological Society, London, Special Publications*, 457.
- DeCelles, P.G. and Giles, K.A. (1996) Foreland basin systems. *Basin Research*, 8, 105–123.
- Dobmeier, C.J. and Raith, M.M. (2003) Crustal architecture and evolution of the Eastern Ghats Belt and adjacent regions of India. In: Yoshida, M., Windley, B.F.,

- Dasgupta, S. (Eds.) Proterozoic East Gondwana: Supercontinent Assembly and Breakup. *Geological Society London, Special Publication, 206*, 145–168.
- Dobmeier, C., Hammerschmidt, K. and Mezger, K. (2006) Emplacement and deformation of the Vinukonda meta-granite (Eastern Ghats, India) - Implications for the geological evolution of peninsular India and for Rodinia reconstructions. *Precambrian Research, 146*, 165–178.
- Dubińska, E., Bylina, P., Kozłowski, A., Dörr, W., Nejbort, K., Schastok, J. and Kulicki, C. (2004) U-Pb dating of serpentinization: Hydrothermal zircon from a metasomatic rodingite shell (Sudetic ophiolite, SW Poland). *Chemical Geology, 203*, 183–203.
- Ellis, D.J. and Green, D.H. (1979) An experimental study of the effect of Ca upon garnet-clinopyroxene Fe-Mg exchange equilibria. *Contributions to Mineralogy and Petrology, 71*, 13–22.
- Ennih, N. and Liégeois, J.P. (2008) The boundaries of the West African craton, with special reference to the basement of the Moroccan metacratonic Anti-Atlas belt. In: Ennih, N., Liégeois, J.P. (Eds.) The boundaries of the West African craton. *Geological Society London, Special Publication, 297*, 1–17.
- Fujii, M., Hayasaka, Y. and Terada, K. (2008) SHRIMP zircon and EPMA monazite dating of granitic rocks from the Maizuru terrane, southwest Japan: Correlation with East Asian Paleozoic terranes and geological implications. *Island Arc, 17*, 322–341.
- Georgieva, M., Cherneva, Z., Kolcheva, K., Gerdjikov, I. and Voinova, E., 2002. P-T metamorphic path of sillimanite-bearing schists in an extensional shear zone,

- Central Rhodopes, Bulgaria. *Geochemistry, Mineralogy and Petrology*, 39, 95–106.
- Ghosh, G., Bose, S., Das, K., Dasgupta, A., Yamamoto, T., Hayasaka, Y., Chakrabarti, K. and Mukhopadhyay, J. (2016) Transpression and juxtaposition of middle crust over upper crust forming a crustal scale flower structure: Insight from structural, fabric, and kinematic studies from the Rengali Province, eastern India. *Journal of Structural Geology*, 83, 156–179.
- Ghosh, J.G. (2004) 3.56 Ga tonalite in the central part of the Bastar Craton, India: Oldest Indian date. *Journal of Asian Earth Sciences*, 23, 359–364.
- Gray, D.R., Foster, D. A. and Bucher, M. (1997) Recognition and definition of orogenic events in the Lachlan Fold Belt. *Australian Journal of Earth Sciences*, 44, 489–501.
- Gupta, S. (2012) Strain localization, granulite formation and geodynamic setting of “hot orogens”: A case study from the Eastern Ghats Province, India. *Geological Journal*, 47, 334–351.
- Gupta, S. and Bhattacharya, A. (2000) Granulites of the ‘Transition Zone’: implications for the western reach of the Eastern Ghats Belt. *Geological Survey of India, Special Publications*, 57, 57–66.
- Gupta, S., Bhattacharya, A., Raith, M. and Nanda, J.K. (2000) Contrasting pressure-temperature-deformation history across a vestigial craton-mobile belt boundary: The western margin of the Eastern Ghats Belt at Deobhog, India. *Journal of Metamorphic Geology*, 18, 683–697.

- Gupta, S., Nanda, J., Mukherjee, S.K. and Santra, M. (2005) Alkaline magmatism versus collision tectonics in the Eastern Ghats Belt, India: Constraints from structural studies in the Koraput Complex. *Gondwana Research*, 8, 403–419.
- Harley, S.L. (1984) An experimental study of the partitioning of Fe and Mg between garnet and orthopyroxene. *Contributions to Mineralogy and Petrology*, 86, 359–373.
- Harley, S.L., Fitzsimons, I.C.W. and Zhao, Y. (2013) Antarctica and supercontinent evolution: historical perspectives, recent advances and unresolved issues. *Geological Society, London, Special Publications*, 383, 1–34.
- Hokada, T. and Motoyoshi, Y. (2006) Electron microprobe technique for U-Th-Pb and REE chemistry of monazite, and its implications for pre-, peak- and post-metamorphic events of the Lutzow-Holm Complex and the Napier Complex, east Antarctica. *Polar Geoscience*, 19, 118–151.
- Holland, T. and Powell, R. (1998) An internally consistent thermodynamic data set for phases of petrological interest. *Journal of Metamorphic Geology*, 16, 309–343.
- Holland, T. and Powell, R. (2003) Activity-compositions relations for phases in petrological calculations: An asymmetric multicomponent formulation. *Contribution to Mineralogy and Petrology*, 145, 492–501.
- Hoskin, P.W.O. and Schaltegger, U. (2003). The composition of zircon and igneous and metamorphic petrogenesis. *Reviews in Mineralogy and Geochemistry*, 53, 27–62.

- House, W.M. and Gray, D.R. (1982) Cataclasites along the Saltville thrust, U.S.A. and their implications for thrust-sheet emplacement. *Journal of Structural Geology*, 4, 257–269.
- Kale, V. S. and Phansalkar, V. G. (1991) Purana basins of peninsular India: a review. *Basin Research*, 3, 1–36.
- Kanazawa, T., Sager, W.W. and Escuita, C. (2001) Explanatory notes. Proceedings of the Ocean Drilling Program, *Initial Report*, 191, 46.
- Kelly, N.M., Clarke, G.L. and Fanning, C.A.M. (2002) A two-stage evolution of the Neoproterozoic Rayner structural episode: New U-Pb sensitive high resolution ion microprobe constraints from the Oygarden Group, Kemp Land, East Antarctica. *Precambrian Research*, 116, 307–330.
- Kelsey, D.E., Clark, C. and Hand, M. (2008) Thermobarometric modelling of zircon and monazite growth in melt-bearing systems: examples using model metapelitic and metapsammitic granulites. *Journal of Metamorphic Geology*, 26, 199–212.
- Kohn, M.J., Stacey, L.C. and Christopher, M. (2015) The fall and rise of metamorphic zircon. *American Mineralogist*, 100, 897–908.
- Korhonen, F.J., Clark, C., Brown, M., Bhattacharya, S. and Taylor, R. (2013) How long-lived is ultrahigh temperature (UHT) metamorphism? Constraints from zircon and monazite geochronology in the Eastern Ghats orogenic belt, India. *Precambrian Research*, 234, 322–350.

- Kovach, V.P., Simmat, R., Rickers, K., Berezhnaya, N.G., Salnikova, E.B., Dobmeier, C., Raith, M.M., Yakovleva, S.Z. and Kotov, A.B. (2001) The Western charnockite zone of the Eastern Ghats Belt, India - An independent crustal province of Late Archean (2.8 Ga) and Paleoproterozoic (1.7–1.6 Ga) terrains. *Gondwana Research*, 4, 666–667.
- Krishnamurthy, P., Chaki, A., Pandey, B.K., Chimote, J.S. and Singh, S.N. (1988) Geochronology of the granite rhyolite suite of the Dongargarh Supergroup, Central India. *Proceeding of 4th National Symposium on Mass Spectrometry*, EPS-2/1-3.
- Krogh, T.E. (1993) High precision U-Pb ages for granulite metamorphism and deformation in the Archean Kapuskasing structural zone, Ontario: implications for structure and development of the lower crust. *Earth and Planetary Science Letters*, 119, 1–18.
- Lal, R.K., Ackermann, D. and Upadhyay, H. (1987) P-T-X relationships deduced from corona textures in sapphirine - spinel - quartz assemblages from Paderu, Southern India. *Journal of Petrology*, 28, 1139–1168.
- Lee, H.Y. and Ganguly, J. (1988) Equilibrium compositions of coexisting garnet and orthopyroxene: Experimental determinations in the system FeO-MgO-Al₂O₃-SiO and applications. *Journal of Petrology*, 29, 93–113.
- Li, Z.X., et al. (2008) Assembly, configuration, and break-up history of Rodinia: A synthesis. *Precambrian Research*, 160, 179–210.
- Ludwig, K.R. (2012) User's Manual for Isoplot 3.7. *Berkeley Geochronology Centre*, 1–72.

- Mallikarjuna Rao, J., Bhattacharji, S., M., Rao, N. and Hermes, O. D. (1995) ^{40}Ar - ^{39}Ar ages and geochemical characteristics of dolerite dyke around the Proterozoic Cuddapah Basin, south India, *Memoirs of the Geological Society of India*, 33, 307–328.
- Meert, J.G. (2003) A synopsis of events related to the assembly of the eastern Gondwana. *Tectonophysics*, 362, 1–40.
- Mezger, K. and Krogstad, E. (1997) Interpretation of discordant U-Pb zircon ages: An evaluation. *Journal of Metamorphic Geology*, 15, 127–140.
- Mezger, K. and Cosca, M.A. (1999) The thermal history of the Eastern Ghats Belt (India) as revealed by U-Pb and ^{40}Ar - ^{39}Ar dating of metamorphic and magmatic minerals: implications for the SWEAT correlation. *Precambrian Research*, 94, 251–271.
- Misra, S., Moitra, S., Bhattacharya, S. and Sivaraman, T.V. (2000) Archean granitoids at the contact of eastern Ghats Granulite Belt and Singhbhum–Orissa Craton, in Bhubaneswar-Rengali sector, Orissa, India. *Gondwana Research*, 3, 205–213.
- Moecher, D.P., Essene, E.J. and Anovitz, L.M. (1988) Calculation and application of clinopyroxene-garnet-plagioclase-quartz geobarometers. *Contributions to Mineralogy and Petrology*, 100, 92–106.
- Mondal, M.E.A., Hussain, M.F. and Ahmad, T. (2006) Continental growth of Bastar craton, Central Indian shield during precambrian via multiphase subduction and lithospheric extension/rifting: Evidence from geochemistry of gneisses, granitoids and mafic dykes. *Journal of Geosciences*, 49, 137–151.

- Morrissey, L.J., Hand, M. and Kelsey, D.E. (2015) Multi-stage metamorphism in the Rayner-Eastern Ghats Terrane: P-T-t constraints from the northern Prince Charles Mountains, east Antarctica. *Precambrian Research*, 267, 137–163.
- Nanda, J.K. and Pati, U.C. (1989) Field relations and petrochemistry the granulites and associated rocks in the Ganjam-Koraput sector of the Eastern Ghats belt. *Indian Minerals*, 43, 247–264.
- Nanda, J., Gupta, S. and Dobmeier, C.J. (2008) Metamorphism of the Koraput Alkaline Complex, Eastern Ghats Province, India - Evidence for reworking of a granulite terrane. *Precambrian Research*, 165, 153–168.
- Nelson, D.R. (2006) CONCH: A Visual Basic program for interactive processing of ion-microprobe analytical data. *Computers and Geosciences*, 32, 1479–1498.
- Neogi, S. and Das, N. (2000) Lithotectonic domains and metamorphic history of the boundary zone of the Eastern Ghats mobile belt and the Bastar craton, Deobhog area, Central India. *Geological Survey of India, Special Publication*, 57, 180–204.
- Newton, R.C., Charlu, T. V. and Kleppa, O.J. (1980) Thermochemistry of the high structural state plagioclases. *Geochimica et Cosmochimica Acta*, 44, 933–941.
- Newton, R.C. and Perkins, D. (1982) Thermodynamic calibration of geobarometers based on the assemblages garnet - plagioclase - orthopyroxene (clinopyroxene) - quartz. *American Mineralogist*, 67, 203–222.

- Nichols, G. T. and Fahey, A. (1996) Preliminary monazite ages of second generation mylonites, Prince Charles Mountains, East Antarctica. *Abstract, 13th Australian Geological Convention, Canberra Geological Society of Australia*, 316.
- Paces, J.B. and Miller, J.D. (1993) Precise U-Pb ages of the Duluth Complex and related mafic intrusions, northeastern Minnesota: geochronological insights to physical, petrogenetic, paleomagnetic, and tectonomagmatic processes associated with the 1.1 Ga midcontinent rift system. *Journal of Geophysical Research*, 98, 13997–14013.
- Pandey, B.K., Prasad, R.N., Krishna, V., Sagar, S., Gupta, J.N. and Saraswat, A.C. (1989) Early Proterozoic Rb-Sr ages of granitic rocks from parts of Koraput district of Orissa, India. *Indian Minerals*, 43, 273–278.
- Patranabis-Deb, S., Bickford, M.E., Hill, B., Chaudhuri, A.K. and Basu, A. (2007) SHRIMP ages of zircon in the uppermost tuff in Chattisgarh Basin in Central India require ~500-Ma adjustment in Indian Proterozoic stratigraphy. *The Journal of Geology*, 115, 407–415.
- Pattison, D.R.M. (2003) Petrogenetic significance of orthopyroxene-free garnet + clinopyroxene + plagioclase ± quartz-bearing metabasites with respect to the amphibolite and granulite facies. *Journal of Metamorphic Geology*, 21, 21–34.
- Perkins, D. and Chipera, S.J. (1985) Garnet-orthopyroxene-plagioclase-quartz barometry: Refinement and application to the English River Subprovince and the Minnesota River Valley. *Contributions to Mineralogy and Petrology*, 89, 69–80.

- Pidgeon, R.T. (1992) Recrystallisation of oscillatory zoned zircon: some geochronological and petrological implications. *Contribution to Mineralogy and Petrology*, 110, 463–472.
- Pidgeon, R.T., Nemchin, A.A. and Hitchen, G.J. (1998) Internal structures of zircon from Archean granites from the Darling Range batholith: implications for zircon stability and the interpretation of zircon U-Pb ages. *Contribution to Mineralogy and Petrology*, 132, 288–299.
- Pyle, J.M. and Spear, F.S. (2003) Yttrium zoning in garnet: Coupling of major and accessory phases during metamorphic reactions. *American Mineralogist*, 88, 708.
- Ramakrishnan, M., Nanda, J.K. and Augustine, P.F. (1998) Geological evolution of the Proterozoic Eastern Ghats mobile belt. *Geological Survey of India, Special Publication*, 44, 1–21.
- Ratre, K., Waele, B.D., Biswal, T.K. and Sinha, S. (2010) SHRIMP geochronology for the 1450 Ma Lakhna dyke swarm: Its implication for the presence of Eoarchean crust in the Bastar Craton and 1450-517 Ma depositional age for Purana basin (Khariar), Eastern Indian Peninsula. *Journal of Asian Earth Sciences*, 42, 1440–1441.
- Rickers, K., Mezger, K. and Raith, M.M. (2001) Evolution of the Continental Crust in the Proterozoic Eastern Ghats Belt, India and new constraints for Rodinia reconstruction: implications from Sm-Nd, Rb-Sr and Pb-Pb isotopes. *Precambrian Research*, 112, 183–210.

- Rosenberg, C.L. and Stünitz, H. (2003) Deformation and recrystallization of plagioclase along a temperature gradient: an example from the Bergell tonalite. *Journal of Structural Geology*, 25, 389–408.
- Saha, S., Das, K., Hidaka, H., Kimura, K., Chakraborty, P.P. and Hayasaka, Y. (2016) Detrital zircon geochronology (U-Pb SHRIMP and LA-ICPMS) from the Ampani Basin, Central India: Implication for provenance and Mesoproterozoic tectonics at East Indian cratonic margin. *Precambrian Research*, 281, 363–383.
- Sarkar, A., Nanda, J.K., Paul, D.K., Bishui, P.K. and Gupta, S.N. (1989) Late Proterozoic alkaline magmatism in the Eastern Ghats Belt: Rb-Sr isotopic study on the Koraput complex, Orissa. *Indian Minerals*, 43, 265–272.
- Sarkar, A. and Paul, D. K. (1998) Geochronology of the Eastern Ghats Precambrian Mobile Belt - a review. *Geological Survey of India, Special Publication*, 44, 51–86.
- Sarkar, G., Corfu, F., Paul, D.K., McNaughton, N.J., Gupta, S.N. and Bishui, P.K. (1993) Early Archean crust in Bastar Craton, Central India-a geochemical and isotopic study. *Precambrian Research*, 62, 127–137.
- Sarkar, S.N., Gopalan, K. and Trivedi, J.R. (1981) New data on the geochronology of the Precambrians of Bhandara-Drug, central India. *Indian Journal of Earth Sciences*, 8 (2), 131–151.

- Sarkar, T. and Scheck, V. (2016) Early Mesoproterozoic (1.6–1.5 Ga) granulite facies events in the Ongole domain: geodynamic significance and global correlation. *Journal of Metamorphic Geology*, 34, 765–784.
- Sarkar, T., Schenk, V., Appel, P., Berndt, J. and Sengupta, P. (2014) Two-stage granulite formation in a Proterozoic magmatic arc (Ongole domain of the Eastern Ghats belt, India): Part 2. LA-ICP-MS zircon dating and texturally controlled in-situ monazite dating. *Precambrian Research*, 255, 467–484.
- Sassi, R., Mazzoli, C., Spiess, R. and Cester, T. (2004) Towards a Better Understanding of the Fibrolite Problem: The Effect of Reaction Overstepping and Surface Energy Anisotropy. *Journal of Petrology*, 45, 1467–1479.
- Schaltegger, U. (2007) Hydrothermal zircon. *Elements*, 3, 51–52.
- Schwans, P. (1988) Depositional response of Pigeon Creek Formation, Utah, to initial fold-thrust belt deformation in a differentially subsiding foreland basin. *Geological Society of America Memoir*, 171, 531–556.
- Sengupta, P., Dasgupta, S., Bhattacharya, P.K., Fukuoka, M., Chakraborti, S. and Bhowmick, S. (1990) Petro-tectonic imprints in the sapphirine granulites from Anantagiri, Eastern Ghats mobile belt, India. *Journal of Petrology*, 31, 971–996.
- Sengupta, P., Sen, J., Dasgupta, S., Raith, M., Bhui, U.K. and Ehl, J. (1999) Ultra-high Temperature Metamorphism of Metapelitic Granulites from Kondapalle, Eastern Ghats Belt: Implications for the Indo-Antarctic Correlation. *Journal of Petrology*, 40, 1065–1087.

- Shaw, R.K., Arima, M., Kagami, H., Fanning, C.M., Shiraishi, K. and Motoyoshi, Y. (1997) Proterozoic Events in the Eastern Ghats Granulite Belt, India: Evidence from Rb-Sr, Sm-Nd Systematics, and SHRIMP Dating. *The Journal of Geology*, 105, 645–656.
- Shiraishi, K., Dunkley, D.J., Hokada, T., Fanning, C.M., Kagami, H. and Hamamoto, T. (2008) Geochronological constraints on the Late Proterozoic to Cambrian crustal evolution of eastern Dronning Maud Land, East Antarctica: a synthesis of SHRIMP U-Pb age and Nd model age data. *Geological Society, London, Special Publications*, 308, 21–67.
- Sibson, R.H. (1986) Brecciation processes in fault zones: Inferences from earthquake rupturing. *Pure and Applied Geophysics*, 124, 159–175.
- Simmat, R. and Raith, M.M. (2008) U-Th-Pb monazite geochronometry of the Eastern Ghats Belt, India: Timing and spatial disposition of poly-metamorphism. *Precambrian Research*, 162, 16–39.
- Špaček, P., Ackerman, L., Habler, G., Abart, R. and Ulrych, J. (2013) Garnet breakdown, symplectite formation and melting in basanite-hosted peridotite xenoliths from Zinst (Bavaria, Bohemian Massif). *Journal of Petrology*, 54, 1691–1723.
- Spry, A. (1969) *Metamorphic Textures*. Pergamon, Oxford, p.p 352.
- Stipp, M., Stünitz, H., Heilbronner, R. and Schmid, S.M. (2002) The eastern Tonale fault zone: A “natural laboratory” for crystal plastic deformation of quartz over a temperature range from 250°C to 700°C. *Journal of Structural Geology*, 24, 1861–1884.

- St-Onge, M.R., van Gooi, J.A.M., Garde, A.A. and Scott, D.J. (2009) Correlation of Archean and Paleoproterozoic units between northeastern Canada and western Greenland: constraining the pre-collisional upper plate accretionary history of the Trans-Hudson orogen. *Geological Society London, Special Publication*, 318, 193–235
- Subramanyam, C. and Verma, R.K. (1986) Gravity field, structure and tectonics of Eastern Ghats. *Tectonophysics*, 126, 195–212.
- Suzuki, K. and Adachi, M. (1991) The chemical Th-U-total Pb isochron ages of zircon and monazite from the Gray Granite of the Hida terrane, Japan. *Journal of Earth Science, Nagoya University*, 38, 11–37.
- Tomaschek, F., Kennedy, A.K., Villa, I.M., Lagos, M. and Ballhaus, C. (2003) Zircons from Syros, Cyclades, Greece - recrystallization and mobilization of zircon during high pressure metamorphism. *Journal of Petrology*, 44, 1977–2002.
- Tong, L., Liu, X., Zhang, L. and Chen, H. (1995) The U-Pb zircon chronology of mafic granulite from the Larsemann Hills, East Antarctica and its possible geological implications. *Terra Antarctica*, 2, 123–126.
- Upadhyay, D. (2008) Alkaline magmatism along the southeastern margin of the Indian shield: Implications for regional geodynamics and constraints on craton-Eastern Ghats Belt suturing. *Precambrian Research*, 162, 59–69.
- Upadhyay, D. and Raith, M.M. (2006) Intrusion age, geochemistry and metamorphic conditions of a quartz-monzosyenite intrusion at the craton - Eastern Ghats Belt contact near Jojuru, India. *Gondwana Research*, 10, 267–276.

- Upadhyay, D., Gerdes, A. and Raith, M.M. (2009) Unravelling Sedimentary Provenance and Tectonothermal History of High-Temperature Metapelites, Using Zircon and Monazite Chemistry: A Case Study from the Eastern Ghats Belt, India. *The Journal of Geology*, 117, 665–683.
- Vielzeuf, D. and Schmidt, M.W., 2001. Melting relations in hydrous systems revisited: application to metapelites, metagreywackes and metabasalts. *Contribution to Mineralogy and Petrology*, 141, 251–267.
- Vijaya Kumar, K., Leelanandam, C. and Ernst, W.G. (2011) Formation and fragmentation of the Palaeoproterozoic supercontinent Columbia: evidence from the Eastern Ghats Granulite Belt, southeast India. *International Geology Review*, 53, 1297–1311.
- Whitney, D. L. and Evans, B. W. (2010) Abbreviations for names of rock-forming minerals. *American Mineralogist*, 95, 185–187.
- Wilke, M., Schmidt, C., Dubraille, J., Appel, K., Borchert, M., Kvashnina, K. and Manning, C.E. (2012) Corrigendum to Zircon solubility and zirconium complexation in $\text{H}_2\text{O}+\text{Na}_2\text{O}+\text{SiO}_2\pm\text{Al}_2\text{O}_3$ fluids at high pressure and temperature. *Earth and Planetary Science Letters*, 373, 242–243.
- Wolf, M.B. and Wyllie, P.J. (1994) Dehydration-melting of amphibolite at 10 kbar: the effects of temperature and time. *Contribution to Mineralogy and Petrology*, 115, 369–383.
- Yang, P. and Pattison, D. (2006) Genesis of monazite and Y zoning in garnet from the Black Hills, South Dakota. *Lithos*, 88, 233–253.

Zegers, T.E., De Wit, M.J., Dann, J. and White, S.H. (1998) Vaalbara, Earth's oldest assembled continent? A combined structural, geochronological, and palaeomagnetic test. *Terra Nova*, 10, 250–259.

Thesis Supplements

(1) Zircon U-Pb SHRIMP and monazite EPMA U-Th-total Pb geochronology of granulites of the western boundary, Eastern Ghats Belt, India: new possibility for Neoproterozoic exhumation history. Amitava Chatterjee, Kaushik Das, Sankar Bose, Proloy Ganguly, Hiroshi Hidaka.

Geological Society London, Special Publication, 457 (2017), DOI: <https://doi.org/10.1144/SP457.1>

(2) Age-integrated tectonic modelling across the orogen-craton boundary: Age zonation and shallow- to deep crustal participation during Late Cambrian cratonization of Eastern Ghats Belts, India.

Amitava Chatterjee, Kaushik Das, Sankar Bose, Hiroshi Hidaka
Lithos, (2017) (in press) DOI: 10.1016/j.lithos.2017.07.020.

Reference papers

(1) Neoproterozoic transpression and granite magmatism in the Gavilgarh-Tan Shear Zone, central India: Tectonic significance of U-Pb zircon and U-Th-total Pb monazite ages.

Anupam Chattopadhyay, Amitava Chatterjee, Kaushik Das, Arindam Sarkar.

Journal of Asian Earth Science, 147 (2017), 485-501.

DOI:10.1016/j.jseaes.2017.08.018

(2) Mechanism of formation of water-escape structure due to seismogenic fluidization: an experimental revelation.

Prabir Dasgupta and Amitava Chatterjee.

Proceedings of the Indian National Science Academy, under review.